Synthetic aperture application for the focusing and interferometry of buried structures

Robert Kedzierawski

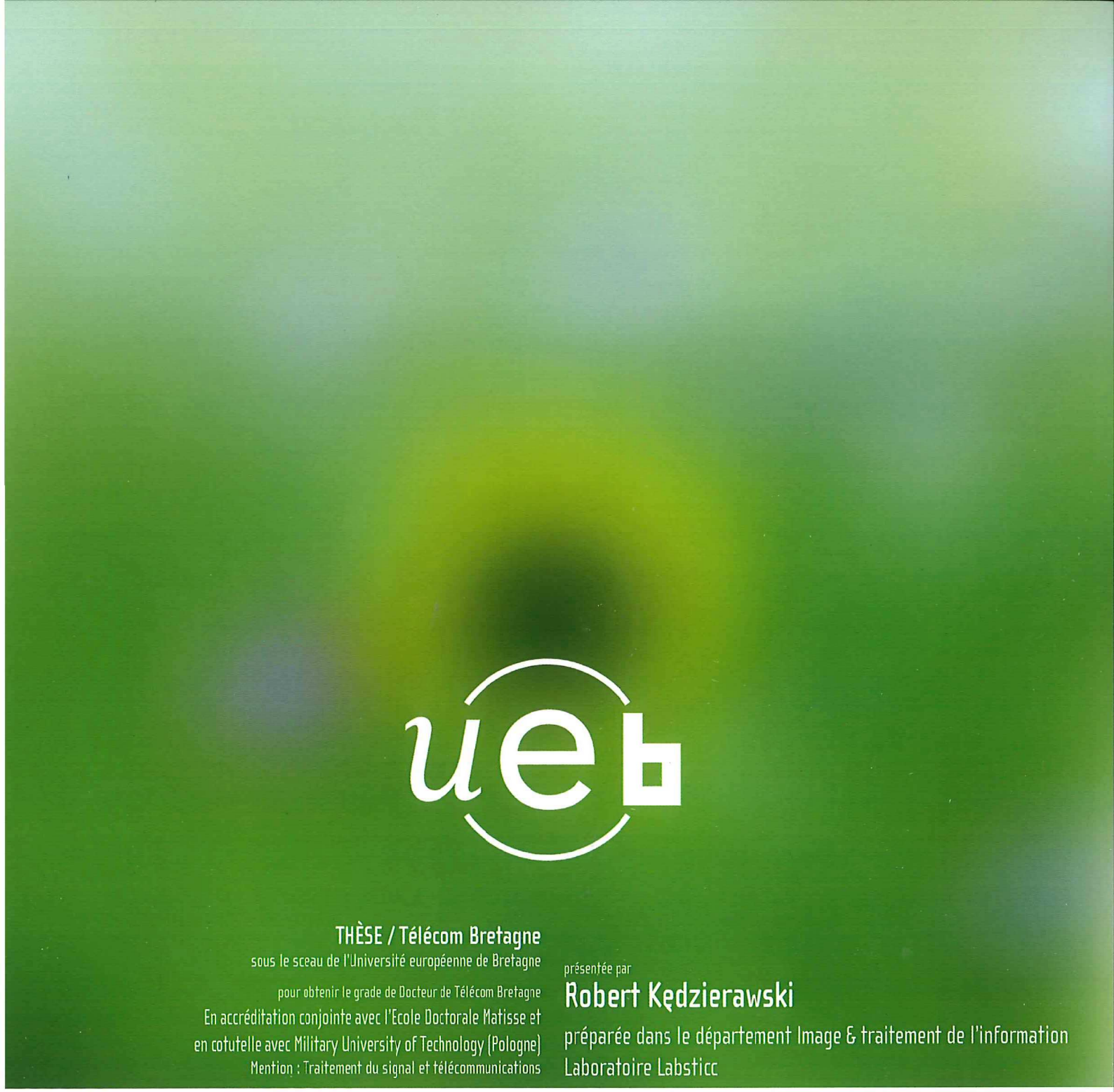

THÈSE / Télécom Bretagne
sous le sceau de l'Université européenne de Bretagne

pour obtenir le grade de Docteur de Télécom Bretagne
En accréditation conjointe avec l'Ecole Doctorale Matisse et
en cotutelle avec Military University of Technology (Pologne)
Mention : Traitement du signal et télécommunications

présentée par
Robert Kędzierawski
préparée dans le département Image & traitement de l'information
Laboratoire Labsticc

Synthetic aperture application for the focusing and interferometry of buried structures

Thèse soutenue le 19 janvier 2016
Devant le jury composé de :

David Blacknell
Professeur, Cranfield University - Royaume-Uni / président et rapporteur

Udo Uschkerat
Directeur de recherche, Fraunhofer Institut – Allemagne / rapporteur

Witold Czarnecki
Professeur, Military University of technology (Pologne) / co-directeur de thèse

Jean-Marc Le Caillec
Professeur, Télécom Bretagne / directeur de thèse

N° d'ordre : 2016telb0383

Sous le sceau de l'Université européenne de Bretagne

Télécom Bretagne

En accréditation conjointe avec l'Ecole Doctorale Matisse

En cotutelle avec l'Université Militaire de Varsovie

Ecole Doctorale – MATISSE

SYNTHETIC APERTURE APPLICATION FOR THE FOCUSING AND INTERFEROMETRY OF BURIED STRUCTURES

Thèse de Doctorat

Mention : Traitement du signal et Télécommunications

Présentée par **Robert Kędzierawski**

Département : ITI

Laboratoire : Lab-STICC/ Pôle Connaissance, Information et Décision

Directeurs de thèse : Witold Czarnecki et Jean-Marc Le Caillec

Jury :

M. David Blacknell (Rapporteur)
M. Udo Uschkerat (Rapporteur)
M. Witold Czarnecki (Directeur de thèse)
M. Jean-Marc Le Caillec (Directeur de thèse)

Résumé

Le but de ces travaux de thèse est de développer une approche par renversement temporel (RT) pour des radars à synthèse d'ouverture (RSO), aéroportés ou satellitaires, pour imager la structure du sol et les cibles enfouies grâce à des méthodes d'interférométrie. Les radars pénétrants aéroportés (Airborne Ground Penetrating Radar, AGPR), « essaient » d'imager la sous surface (invisible aux autres types de capteurs que les radars) sur de très grandes échelles, ce qui a de très nombreuses applications potentielles que cela soit dans le domaine militaire, avec l'imagerie de cibles enfouies telles que les mines, mais aussi de très nombreuses applications civiles comme la surveillance et la caractérisation de pollution ou l'estimation des ressources en eau. Plusieurs expériences ont montré que les radars à synthèse d'ouverture conventionnels basses fréquences (bande P ou L) pouvaient imager la sous-surface sur quelques mètres, mais dans des conditions optimales où le sol est presque entièrement sec. A notre connaissance, il n'existe pas de systèmes RSO (qu'ils soient aéroportés ou satellitaires) opérant avec du Renversement Temporel, solution technique que nous proposons pour l'imagerie de la sous surface (pour des conditions réalistes) et qui a suscité ces travaux, pionniers dans le domaine des radars pénétrants. Pour cette raison, ces travaux de thèse sont principalement basés sur des simulations numériques. Cette démarche nécessite la définition et la validation des paramètres d'une mission RSO pour des radars pénétrants, mais aussi une modélisation physique poussée, que cela soit du point de vue hydrologique ou géologique afin de dériver les constantes diélectriques (ainsi que leurs variations), ce qui est fait dans un premier chapitre du manuscrit. Le deuxième chapitre est consacré à la validation, ou plus exactement à la connaissance des limitations des hypothèses d'application du Renversement Temporel pour une onde se propageant dans le sol avec les modélisations physiques déduites du premier chapitre. Dans ce deuxième chapitre nous proposons des techniques de compensation permettant de corriger les pertes électromagnétiques, lesquelles sont normalement une violation des hypothèses de Renversement Temporel. Enfin le troisième chapitre propose et valide numériquement la conception d'un système RSO complet opérant en renversement temporel. Le renversement temporel nécessite de repenser le système d'acquisition, mais aussi de redéfinir les algorithmes de focalisation (radial/azimutale). Les simulations se concluent sur les résultats de focalisation de cibles enfouies à différentes profondeurs dans différent types de sol et pour des RSO opérant à différentes porteuses. Ce dernier chapitre présente aussi une première reconstruction de cibles enfouies à partir d'images RSO obtenus par renversement temporel.

Comme nous l'avons dit, le premier chapitre introduit les propriétés électromagnétiques du sol, la géométrie de l'imagerie de la sous-surface à partir de capteurs aéroportés ainsi que les problèmes relatifs à la pénétration de l'onde électromagnétique, engendrés par la structure inhomogène du sol. Puisque les propriétés électromagnétiques du sol dépendent de sa structure géologique ainsi que de son profil d'humidité, les données géophysiques collectées dans les profils du « Soil Typological Unit» (STU) sont utilisées afin d'approcher le plus possible une structure réaliste tridimensionnelle du sous sol présentant une surface (c'est-à-dire l'interface entre le sol et l'espace libre) nue et plate, cette structure devant être la plus représentative possible de la diversité du sous-sol. En effet, les bases de données géophysiques sont une source fiable d'information sur la texture du sol à des profondeurs importantes et sur de larges étendues spatiales (c'est-à-dire sur l'étendue de la mission du radar), en particulier sur l'homogénéité des sous sols inspectés, ce qui est un aspect important de la planification de mission d'acquisition sur de vastes zones, ce qui en général le cas des missions des radars à synthèse d'ouverture. En effet, un principe implicite de ce type de mission d'observation de la sous surface est que la forme d'onde s'adapte au fur et à mesure de l'acquisition, en particulier lorsque la structure du sol change. De plus, bien que le problème de l'estimation du profil d'humidité ne soit pas le cœur de ces travaux de thèse, un simple calcul numérique du profil d'humidité (équation de Richards) montre que ce profil est fortement dépendant du type de sol (car les paramètres hydrologiques varient fortement d'un type de sol à l'autre). Les profils d'humidité montrent en général des discontinuités importantes aux interfaces des différentes natures de terrain constituant le sous sol.

A partir des calculs numériques du profil d'humidité, les propriétés électromagnétiques, telles que la permittivité relative complexe et la conductivité sont calculées grâce à une fonction de pedotransfert (traduisant ainsi l'approche conjointe géologique et hydrologique). Les caractéristiques liées à la

rétrodiffusion et à l'imagerie de la sous surface sont détaillées avec une attention particulière portée à la modélisation de la propagation dans un milieu multicouche et sur la capacité de pénétration de l'onde électromagnétique. La propagation des impulsions électromagnétiques est analysée en fonction de plusieurs paramètres tels que la fréquence ou la polarisation, lesquelles dépendent des caractéristiques intrinsèque du Radar à Ouverture de Synthèse. En effet, à cause de la dispersion fréquentielle du sous sol, des atténuations non uniformes le long de la rampe fréquentielle (c'est-à-dire pour le chirp, forme d'onde habituelle pour obtenir une image très haute résolution) ainsi que de la variation de vecteur d'onde électromagnétique (due au gradient des constantes diélectriques), l'enveloppe de l'impulsion rétrodiffusée est déformée et des atténuations irrégulières apparaissent lors de la propagation de l'onde dans un sol présentant des structures fortement inhomogènes. Ces déformations dénaturent l'enveloppe de l'impulsion, comme nous l'avons dit, et modifient la longueur effective de cette impulsion. Ces différents effets conduisent à une dissipation de l'énergie qui, conjointement à la distorsion de l'enveloppe, modifient profondément la sortie du filtrage adapté (qui sert à créer la partie radiale de l'image) et dégradent fortement la résolution spatiale le long de cet axe radial (distance/profondeur). La modulation de l'enveloppe donne aussi naissance à des cibles « fantômes » qui introduisent une ambigüité sur l'estimation de la profondeur des rétrodiffuseurs (c'est-à-dire sur leur localisation), mais surtout conduisent à de fausses détection de cibles enfouies, ce qui est très préjudiciable à l'utilisation de l'information fournie par le radar à synthèse d'ouverture. De plus, comme nous l'avons déjà dit, le temps de propagation (aller et retour) de l'impulsion à travers la sous surface dépendent des propriétés électromagnétiques mais aussi de la hauteur des différentes couches consécutives. L'estimation de la véritable localisation des potentielles cibles est un problème de première importance en particulier pour l'imagerie de la sous surface à des incidences obliques pour lesquelles la profondeur relative de la cible (c'est-à-dire le ratio entre la véritable profondeur et la profondeur estimée) peut être relativement grande. Pour ces incidences obliques, le mauvais placement de la cible a lieu conjointement sur l'axe vertical et dans le plan horizontal, pénalisant encore l'utilisation de l'information radar pour la localisation des cibles enfouies. Enfin, les effets de dispersion et d'atténuation se cumulant sur le trajet aller-retour, plus le rétrodiffuseur (cible) est profond, plus ces effets sont prononcés et donc la localisation de cette cible est rendue difficile.

Le deuxième chapitre analyse et valide l'hypothèse du Renversement Temporel (RT) dans un milieu inhomogène dispersif et à pertes. Après une courte introduction sur le principe du renversement temporel associé aux ondes électromagnétiques, les limitations de cette approche pour son application à de l'imagerie de la sous-surface sont détaillées. Le renversement temporel consiste à émettre une forme d'onde (dans notre cas un chirp) puis à enregistrer l'écho de cette onde émise, à renverser cet échos puis à le réémettre. La technique du renversement temporel utilise la propagation multi trajet dans un milieu hautement dispersif afin d'obtenir une très haute résolution et donc d'améliorer les performances de détection des cibles. Dans le domaine fréquentiel, le renversement temporel est équivalent à une conjugaison de phase. Cependant la conjugaison de phase s'applique à des ondes monochromatiques, alors que le renversement temporel s'applique à des impulsions larges bandes (fréquentielles) dans le domaine temporel. Par conséquent, en opérant dans le domaine temporel, le renversement temporel peut opérer sur des signaux à très larges bandes et donc fournir des images à très haute résolution dans des milieux à pertes avec, dans notre cas, des porteuses située à des fréquences basses. Ce concept de refocalisation utilise la réversibilité (autrement dit la réciprocité) du milieu où se propage l'onde électromagnétique, ce qui signifie que l'onde électromagnétique, ainsi que sa renversée temporelle peuvent se propager tous les deux dans le milieu de manière symétrique (du point de vue temporel). En absence de pertes (c'est-à-dire avec une conductivité nulle, ce qui n'est pas le cas du sous sol), les équations de Maxwell vérifient cette réciprocité. L'algorithme de focalisation basé sur le Renversement Temporel est alors décrit dans ce chapitre ainsi que les conditions nécessaires à son application. En effet, l'approche par renversement temporel nécessitant deux émissions et deux réceptions, les schémas d'acquisition par un radar (pas nécessairement à synthèse d'ouverture) doivent alors être repensés. Un schéma opérationnel est proposé dans ce chapitre pour un système d'imagerie de la sous surface dans une configuration double impulsion-écho avec dans notre cas un possible allongement du premier écho dû aux effets dispersifs de la sous surface, comme nous l'avons dit. Ceci nécessite d'ajouter un temps supplément « de garde » afin de s'assurer que la réception de ce premier écho n'est pas perturbé par la réémission lors du renversement temporel. Les différences avec les systèmes de radars pénétrants

habituels ainsi que les développements de ce nouveau système d'acquisition sont discutés en détail dans ce chapitre. Enfin, l'algorithme proposé est validé numériquement pour des cibles modélisées par des diffuseurs isotropes distribués aléatoirement dans le sol. A la fin de ce chapitre, la refocalisation est présentée pour toutes les structures de sol considérées (avec la même localisation pour tous les rétrodiffuseurs ponctuels) et pour différentes configurations de radars.

Le troisième chapitre présente le cadre général de l'imagerie de la sous surface à partir de renversement temporel pour un radar aéroporté avec synthèse d'ouverture. Bien que le renversement temporel ait été appliqué dans une grande variété de systèmes de télédétection (qui ont confirmé expérimentalement les avantages des approches par renversement temporel), l'application du renversement temporel pour l'imagerie haute résolution de la sous surface (avec notamment les limitations théoriques détaillées dans le deuxième chapitre) nécessite une modification des méthodes d'imagerie utilisées par les capteurs mentionnés ci-dessus avec un effort particulier a porté sur le développement de nouveaux algorithmes de traitement du signal pour la création de l'image radar haute résolution (notamment sur l'axe azimutal). L'impact de la dispersivité et des pertes électromagnétiques est discuté du point de vue spectral, larguer de bande, pour deux cibles ponctuelles et isotropes avec trois largeurs de bandes de fréquences différentes. En effet, l'utilisation d'un signal présentant une bande de fréquences étroite (hypothèses généralement faite pour les systèmes habituels à filtrage adapté), ne permet, à causes des conditions de propagation déjà mentionnées, d'obtenir une information exploitable de la sous surface en particulier pour faire une synthèse d'antenne le long de l'axe azimutal. L'élargissement de la bande fréquentielle du signal permet d'obtenir une information plus précise sur la nature du sol, mais se traduit par deux effets, la première étant une atténuation irrégulière de d'enveloppe de l'impulsion, la seconde une distorsion de la structure interne de l'impulsion électromagnétique. Une analyse de ces effets a conduit à la reconstruction de la propagation initiale avec une amplification adaptative du signal, permettant ainsi la restauration de la structure interne de l'impulsion. L'utilisation d'un filtrage non linéaire, adapté au milieu que l'on cherche à imager, accentue les capacités d'imagerie de l'approche par renversement temporel.

En effet, le schéma des mesures en renversement temporel est décrit dans ce chapitre pour des Radars pénétrants aéroportés dans une configuration monostatique comme nous l'avons dit c'est-à-dire dans un mode de réflexion. Ce schéma diffère significativement des systèmes habituels utilisant le renversement temporel, qui sont utilisés en mode de transmission et qui ont des objectifs très différents du système décrit dans ces travaux de thèse. En particulier, au lieu de focaliser l'énergie sur la cible (autrement dit un récepteur pour un mode transmission), le but est d'obtenir une restauration de l'impulsion cumulative au cours du temps. Le schéma proposé a été validé sur une structure de sol approximée pour deux RSO opérant à deux fréquences porteuses différentes (bande P et L) avec 200 Mhz de bande. Le phénomène de refocalisation a été vérifié sur les simulations pour chacune des structures de sol considérées et toutes les localisations de cibles définies dans le chapitre précédent. Sur ces simulations, il a été observé que, bien que les sols aient des structures différentes avec des couches de nature et de profondeurs différentes qui affectent l'impulsion de manières très différentes, la restauration de l'impulsion est bien effective pour tous les types de sols testés et pour toutes les fréquences de porteuses. De plus, dans une acquisition avec renversement temporel, la confiance que l'on peut avoir dans l'acquisition du signal lors de la première étape dépend des paramètres de la mission définis pour cette acquisition initiale. Donc, une définition précise de ces paramètres est nécessaire pour des missions de RSO pénétrants aéroportés (avec retournement temporel) devant être menées pour tout type de structures de sol, en particulier sur des larges zones non arides.

Dans ce dernier chapitre du manuscrit, les données brutes (raw data) ont été simulées pour six différents types de sol et deux radars (bande L et P). La géométrie de la mission a été dérivée de systèmes d'acquisition de radar à synthèse d'ouverture existants, de manière à être le plus réaliste possible pour l'acquisition (future) des données et pour le test du nouveau concept de RSO proposé (c'est-à-dire fonctionnant avec un mode de renversement temporel) ainsi que pour la validation des algorithmes qui découlent de ce nouveau mode d'acquisition particulier. Les résultats de ce chapitre montrent que les radars en bande P ont une plus grande possibilité d'imagerie que les radars en bande L (alors que la conclusion était inverse pour les RSO travaillant en mode usuel, sans retournement temporel). En effet,

pour les RSO classiques, les radars en bande P présentent de plus grandes distorsion que ceux en bande L, alors que les atténuations (dues aux pertes) soient plus faibles en bande P et permettent donc de meilleurs acquisition (rétrodiffusion plus forte). Par conséquent, les acquisitions avec renversement temporel sont mieux adaptées au milieu imagé pour la bande P. En effet, plus l'écho de la première émission est distordu (cas de la bande P), plus le signal est restauré lors de la seconde acquisition si le niveau d'énergie est suffisant. Du point de vue de la synthèse d'antenne le long de l'axe azimutal, un algorithme habituel, le RDA (Range-Doppler Algorithm), a été appliqué afin de vérifier la possibilité de synthétiser une image RSO avec une acquisition en mode de renversement temporel (pour l'axe radial). Dans ce chapitre, lorsque la compression d'impulsion sur l'axe radial est effectuée avec le réplica normal, (c'est-à-dire le chirp émis) après le retour du second écho, la correction de trajectoire (Range Cell Migration, RCM) et la fonction de référence azimutale doivent être changées afin de tenir compte de l'intensification du déphasage dans l'étape d'exploitation de l'émission du renversement temporel (Time Reversal Probing, TRP). Par conséquent, le renversement temporel à des effets conjoints sur la compression radiale, mais aussi sur la compression azimutale dans la formation de l'image que nous proposons, ces nouveaux algorithmes conduisant à des images mieux focalisées que celles issues des algorithmes usuels. La comparaison des profils azimutaux montre alors une restauration de la résolution azimutale la plus fine. L'intensification du déphasage pourrait aussi affecter d'autre type de formation de l'image (c'est-à-dire dans l'étape de synthèse d'antenne), mais cela n'a pu être testé dans le cadre de ces travaux de thèse.

Ce dernier chapitre se conclue par un premier test d'interférométrie à partir des images RSO générées par des techniques de renversement temporel, montrant ainsi l'intérêt de cette approche pour la surveillance de structure enfouies. L'intensification du déphasage, introduit par le renversement temporel, accentue la différence de phase dans l'interférogramme. Pour un scénario avec un rétrodiffuseur ponctuel, la reconstruction, avec un processus de renversement temporel, est meilleure que celle des algorithmes classiques avec une seule émission. Cependant, une analyse complète des possibilités de la reconstruction de cibles enfouies à partir d'interférogrammes extraits d'images RSO produite par renversement temporel nécessite la définition d'une hauteur d'ambiguïté par rapport à la longueur de la ligne de base (afin d'éviter la décorrelation), cette analyse devant être effectuées en relation avec des données réelles.

Les principaux résultats de cette thèse peuvent se résumer en 4 points

-Nous avons proposé un modèle réaliste des propriétés diélectriques du sol prenant en compte son inhomogénéité tant du point de vue géologique qu'hydrologique.

-Nous avons proposé une méthode qui permet de compenser les effets dispersifs de la structure (inhomogène) du sol lors de la propagation de l'impulsion électromagnétique dans ce sol en utilisant le renversement temporel. Nous avons aussi proposé une technique de compensation des pertes électromagnétiques (qui théoriquement perturbe le renversement temporel).

-Nous avons proposé un nouveau schéma d'acquisition d'un RSO opérant avec du renversement temporel, la double émission nécessitant de redéfinir ces paramètres d'acquisition.

-Enfin nous avons retravaillé les algorithmes de formation de l'image que cela soit pour l'axe radial (renversement temporel), mais aussi pour l'axe azimutal.

Bien entendu, ces travaux de thèse doivent être validés sur des données réelles. Les modifications des algorithmes de synthèses doivent être aussi définies pour d'autres algorithmes que celui utilisé dans cette thèse (RDA). Enfin l'interférométrie à partir d'images RSO obtenues par renversement temporel doit étudiée plus en profondeur.

ABSTRACT

Synthetic aperture application for the focusing and interferometry of buried structures

This dissertation addresses the problem of the application of synthetic aperture and interferometry techniques for low frequencies (VHF, UHF, P, L bands) airborne/satellite-borne radars imaging over non-arid (in general, unknown) areas for civilian and defence applications. The experimental results, published so far, shown that the airborne Synthetic Aperture Radar (SAR) reached the sufficient penetration depth in soil structure down to several meters in homogeneous and dry soil. Hence, whereas such areas with homogeneous and dry soil rarely occur in natural environment, the convenience of SAR application decreases significantly due to the soil effect on electromagnetic wave as pulse distortion and envelope deformation caused by dispersion and frequency-dependent attenuation. When soil is considered as inhomogeneous medium and modelled based on the pedotransfer (geologically and hydrologically-motivated) approach, the Time-Reversal (TR) technique, through its refocusing ability, can be used for pulse regeneration and for restoration of undisturbed range resolution required for the essential azimuth processing by SAR methods.

We start by soil modelling based on the real geological data and assumed meteorological history to obtain as realistic as possible soil structures. Using the pedotransfer approach, the dielectric constants and conductivity are modelled. Then the mission geometry is defined and features related to subsurface imaging are analysed. We continue with the TR concept and its limitations for inhomogeneous media. The TR-based acquisition method is proposed for airborne platform with the analysis of its differences, challenges and expectations. Then, the proposed method of scanning is investigated in two different radar band (P, L) under several assumptions. The refocusing and pulse restoration effects are presented for all considered soil structures and location of buried objects. When the proposed algorithm is verified, the acquisitions is repeated along the synthetic aperture line over bare and flat soil with inhomogeneous-in-depth properties. The image formation method is applied to verify the TR impact on SAR processing in azimuth direction. Finally, interferometric phase method is applied for soil structure reconstruction.

Although we only consider imaging from airborne platform, the proposed algorithm and all contributions presented in this dissertation can be directly adapted for satellite-borne system or modified for Ground Penetrating Radar (GPR) systems.

RÉSUMÉ

Application de la synthèse d'ouverture pour la focalisation et l'interférométrie de structure enfouies

Ce manuscrit aborde le problème de l'application de la synthèse d'ouverture radar et des techniques d'interférométrie, pour des radars (sur satellites ou aéroporté) ayant pour but d'imager la sous surface de zones non-arides (zones dont les caractéristique sont en général inconnues) pour des applications soit de défense, détection de mines, soit civiles, comme la surveillance de structures dans le sol. Les résultats expérimentaux, publiés jusqu'ici, montrent que les radars à synthèse d'ouverture aéroportés peuvent atteindre des profondeurs de pénétration de plusieurs mètres dans un sol homogène et sec. Ceci est suffisant pour les applications usuelles militaires ou civiles visées par la surveillance de zones par des radars à synthèse d'ouverture (RSO). Cependant, de telles zones, présentant un sol homogène et sec, se rencontrent rarement dans la nature, et donc l'intérêt d'appliquer les techniques usuelles d'imagerie RSO décroît fortement pour les autres types de surface et de sol à cause des distorsions de l'enveloppe de l'onde électromagnétique par les effets de dispersion et d'atténuation dans des sols humides. Si l'on considère le sous sol comme un milieu inhomogène et qu'on lui applique conjointement un modèle basé sur une fonction de pedotransfert (avec des sous jacents géologiques et hydrologiques), l'approche par Renversement Temporel, grâce à ses capacités de refocalisation adaptative pour être utilisée pour la refocalisation/régénération de l'impulsion électromagnétique afin de préserver la résolution radiale. Ceci est une condition primordiale afin d'appliquer les algorithmes de traitement d'antenne synthétique pour obtenir une résolution radiale la plus haute possible comme cela est nécessaire pour obtenir une résolution azimutale satisfaisante.

Une première partie de ce manuscrit est consacrée à la modélisation du sol basée sur des données géophysiques réelles et en supposant un historique météorologique connu afin de d'obtenir une modélisation du sous sol la plus réaliste possible. Les constantes diélectriques ainsi que la conductivité sont alors déduites par une approche par fonction de pédotransfert. La géométrie d'acquisition des données est alors définie et les caractéristiques de l'image du sous sol sont ensuite analysées. Le manuscrit se poursuit par une présentation du concept de renversement temporel ainsi que de ses limitations pour un milieu inhomogène, dispersif et à pertes. Si la dispersivité ne pose pas de problèmes fondamentaux, les pertes dues à la conductivité sont une violation importante des hypothèses de renversement temporel, car dans ce cas, les équations de propagation ne sont plus réciproques du point de vue temporel.

Dans une seconde partie, le concept de RSO basé sur ce concept de renversement temporel TR-based acquisition est alors proposé pour un radar aéroporté. L'utilisation d'une forme d'onde adaptative implique en particulier de diminuer la répétition de l'émission des impulsions électromagnétique (connue sous l'acronyme anglo saxon de PRF) car chaque ac-

quisition sur l'axe radial (temps rapide) nécessite deux émissions. Cette réduction implique en particulier de diviser, au minimum par la résolution azimutale (temps lent). Cette perte de résolution peut être supérieure car des marges doivent être prises en considération à cause des effets de dispersion qui peuvent allonger la durée effective de l'impulsion, cet étirement étant inconnu. La méthode ainsi proposée a été testée pour deux radars (en bande P et L, respectivement). Les effets de restauration de l'impulsion et de sa refocalisation sont présentés pour tous les types de sol considérés ainsi que pour diverses localisations d'objets dans le sous sol. Quand la méthode proposée permet la refocalisation radiale, les acquisitions sont répetées le long de la ligne de synthèse d'antennes sur des sols nus présentant des inhomogénéités le long de l'axe vertical. La méthode de formation de l'image est alors appliquée afin de vérifier l'impact du renversement temporel sur la refocalisation le long de la direction azimutale. Dans une dernière partie de ce manuscrit la méthode de reconstruction des images à synthèse d'ouverture est appliquée sur deux images interférométriques afin de vérifier la reconstruction sur de structures étendues dans le sous sol.

Bien que nous ayons considéré l'imagerie à partir des algorithmes proposés et toutes les contributions présentées ici peuvent directement être adaptées pour des images d'imageries satellitaires ou modifiée pour des systèmes GPR (Gound Penetrating Radars).

STRESZCZENIE

Zastosowanie techniki syntetyzowania apertury anteny w technologii penetracji gruntu

Rozprawa doktorska podejmuje problematykę opracowania algorytmu wykorzystującego technikę syntetyzowania apertury anteny (SAR - Synthetic Aperture Radar) i techniki interferometryczne do radarowego obrazowania optycznie niewidocznej struktury gruntu z pokładu powietrznych platform w zakresie niskich częstotliwości mikrofalowych (VHF, UHF, P, L). Dotychczas opublikowane wyniki pomiarów przeprowadzonych eksperymentalnie wykazują, że w sprzyjających warunkach geologicznych możliwa jest penetracja i obrazowanie przypowierzchniowej struktury gruntu z wykorzystaniem algorytmów SAR do głębokości kilkunastu metrów. Z uwagi na fakt, że obszary o geologicznie jednorodnej i suchej teksturze gruntu występują bardzo rzadko w naturalnym środowisku, nie jest możliwe pełne wykorzystanie możliwości algorytmów SAR do obrazowania dowolnego obszaru Ziemi. Dyspersyjna i stratna natura przypowierzchniowych warstw gruntu wpływa na strukturę czasowo - częstotliwościową i obwiednię sygnału sondującego silnie ją deformując i zniekształcając, co prowadzi do pogorszenia wyników filtracji optymalnej ze względu na niedopasowanie między sygnałem echa radarowego a funkcją referencyjną. Rozważając strukturę gruntu jako silnie niejednorodną i modelując jej parametry elektromagnetyczne z wykorzystaniem funkcji transferu (bazującej na jej parametrach geologicznych i hydrologicznych) możliwe jest zastosowanie techniki odwróconego czasu (TR - Time-Reversal) do odtworzenia struktury czasowo-częstotliwościowej sygnału. Jest to warunkiem koniecznym do zastosowania algorytmów SAR, a zapewnienie wysokiej rozróżnialności w dziedzinie odległości jest kluczowe dla uzyskanie wysokiej rozróżnialności w dziedzinie azymutu.

Pierwsza część rozprawy poświęcona jest zagadnieniu modelowania parametrów geofizycznych przypowierzchniowych warstw gruntu w oparciu o rzeczywiste dane geologiczne i założoną historię opadów meteorologicznych. Celem modelowania jest opracowanie struktur geologicznych odzwierciedlających przypowierzchniowe warstwy gruntu w możliwie najwierniejszy sposób. Parametry elektromagnetyczne gruntu obliczono z wykorzystaniem funkcji transferu. Następnie przeanalizowano geometrię funkcjonowania systemów SAR wykorzystywaną do sondowania przypowierzchniowych struktur gruntu i scharakteryzowano właściwości radarowego obrazowania gruntu. Przedstawiono założenia wykorzystania techniki TR do odtworzenia struktury czasowo - częstotliwościowej sygnału wraz z analizą ograniczeń jej zastosowania w ośrodku niejednorodnym, dyspersyjnym i stratnym.

W drugiej części rozprawy przedstawiono koncepcję zastosowania algorytmów SAR wykorzystujących technikę TR do radarowego obrazowania z pokładu platform lotniczych. Jednym z warunków zastosowania techniki TR jest odpowiednie dopasowanie częstotliwości powtarzania impulsów sondujących (ang. PRF), która w ogólnym przypadku musi

być zmniejszona, aby zapewnić dwukrotną transmisję sygnałów. Redukcja PRF wpłynie niekorzystnie na jakość syntetyzowania apertury anteny i rozróżnialność azymutalną zobrazowania. Wartość PRF musi być odpowiednio dobrana, by zapewnić akceptowalną rozróżnialność oraz poprawną akwizycję sygnałów z nieznanego ośrodka. Proponowana metoda została przetestowana dla dwóch radarów pracujących w różnych pasmach częstotliwości (w paśmie P i L). Efekt odtworzenia struktury czasowo - częstotliwościowej sygnału oraz ponownego zogniskowania energii został przedstawiony dla wszystkich rozważanych struktur geologicznych gruntu i różnej lokalizacji ukrytych obiektów. Pozytywne zweryfikowanie proponowanej metody skanowania i przetwarzania sygnałów pozwolił na jej powtórzenie wzdłuż toru lotu platformy nad obszarami o niejednorodnej strukturze gruntu. Następnie zweryfikowano wpływ techniki TR na jakość syntezy zobrazowania wzdłuż syntetycznej apertury. Na przykładzie algorytmu RDA (Range-Doppler Algorithm) wykazano, że zastosowanie techniki TR wymusza modyfikację parametrów wykorzystywanych do syntezy funkcji referencyjnej. Ponadto, zastosowano techniki interferometryczne do zweryfikowania możliwości rekonstrukcji przypowierzchniowych warstw gruntu.

Mimo, że przedstawione w tej rozprawie rozważania i wnioski dotyczą radarowego obrazowania z pokładu powietrznych platform latających, mogą zostać one zaadaptowane w systemach satelitarnego obrazowania lub zmodyfikowane na potrzeby systemów georadarowych (GPR - Ground Penetrating Radar).

CONTENTS

LIST OF FIGURES

LIST OF TABLES

LIST OF ACRONYMS

AGPR	Airborne Ground Penetrating Radar
AIRSAR	Airborne SAR
CMF	Cross Matched Filtering
CREP	Complex Relative Effective Permittivity
CSA	Chirp Scaling Algorithm
CW	Continuous Waveform
DBS	Doppler Beam Sharpening
DEM	Digital Elevation Model
DLR	Deutschen Zentrum für Luft-und Raumfahrt
DORT	Decomposition of the Time Reversal Operator (*French: Decomposition de l'Operateur de Retournement Temporel*)
E-SAR	Experimental SAR
EM	Electromagnetic
EN	Energy Normalization
FDTD	Finite-Difference Time-Domain
FLGPR	Forward-Looking Ground Penetrating Radar
FP	Forward Probing
GPR	Ground Penetrating Radar
IDE	Improvised Explosive Device
InSAR	Interferometric SAR
JPL	Jet Propulsion Laboratory
LFM	Linear Frequency Modulation
LOS	Line-of-Sight
MBSDM	Mineralogically Based Spectroscopy Dielectric Model
MF	Matched Filtering
MIMO	Multiple-Input Multiple-Output
MUSIC	Multiple Signal Clasifitation
NASA	National Aeronautics and Space Administration
ONERA	Office National d'Études et de Recherches Aérospatiales

Pol-InSAR	Polarimetric SAR Interferometry
PolSAR	Polarimetric SAR
PRF	Pulse Repetition Frequency
PRI	Pulse Repetition Interval
PSR	Pulse Spread Response
RAMSES	Radar d'Analyse MultiSpectral et d'Etude des Signatures
RCM	Range Cell Migration
RCS	Radar Cross Section
RDA	Range-Doppler Algorithm
RMA	Range Migration Algorithm
SAR	Synthetic Aperture Radar
SCR	Signal-to-Clutter Ratio
SIR	Shuttle Imaging Radar
SLAR	Side-Looking Airborne Radar
SNR	Signal-to-Noise Ratio
SPADE-2	Soil Profile Analytical Database for Europe
STU	Soil Typological Unit
TE	Transverse Electric
TM	Transverse Magnetic
TR	Time-Reversal
TR-AGPR	Time-Reversal Airborne Ground Penetrating Radar
TRA	Time-Reversal Array
TRAIC	Time-Reversal Adaptive Interference Cancellation
TRM	Time-Reversal Mirror
TRO	Time-Reversal Operation
TRP	Time-Reversal Probing
TSL	Target Surface Location
TSR	Target Surface Refraction
TTW	Through-The-Wall
UHF	Ultra High Frequency
UWB	Ultrawideband
VHF	Very High Frequency
VNA	Vector Network Analyzer

CHAPTER 1

INTRODUCTION

1.1 Problem Statement

The thrust of this dissertation is to develop Time-Reversal (TR)-based Synthetic Aperture Radar (SAR) algorithm for airborne/space-borne imaging of buried targets leading further to soil structure reconstruction with interferometric method. The airborne radar system, referred to as Airborne Ground Penetrating Radar (AGPR), intended for the subsurface imaging of optically invisible soil structure over a large scale, potentially has several meaningful applications in a broad range, starting from above-mentioned buried targets imaging, through many civilian applications, including detection and characterization of pollution and ground water resources, and up to defence/military applications, as minefields localization.

To the best of our knowledge, the current SAR systems (airborne or space-borne) do not operating in time-reversed mode, hence, this dissertation is based on simulations and assumes that the imaging geometry and parameters of the AGPR as well the soil dielectric constant are all sufficient to give acceptable ground penetration. Experimental results, published so far, show that the penetration depth over few meters is possible.

Moreover, to ensure the soil effect as realistic as possible, this dissertation aims at the soil modelling as a geologically inhomogeneous, dispersive and lossy medium with isotropic electromagnetic properties. In contrast to assumptions on homogeneous soil widely encountered in related literature, the efforts were made to use the textural soil profiles from geological database for approximation of the three-dimensional soil structure with small and non-uniform height of successive layer, and to calculate the dielectric constant based on the pedotransfer (geologically- and hydrologically-motivated) approach. Approximated soil structures and parameters are used for exact estimation of backscattered returns in both conventional SAR acquisitions and TR reflection mode.

1.2 Motivations and Literature Review

From the radar paradigm [1], the Synthetic Aperture Radar (SAR) has become one of the most important engineering inventions in the remote sensing domain of the last century. This radar [2] imaging technique, based on combining the theory of antenna and signal processing methods and leading to improvement of the azimuthal resolution [3], is being continuously developed and has found innumerous fields of applications in the modern world. Until now, different operating modes, various signal processing algorithms and image reconstruction methods have been developed: starting from the conventional single-polarization single-path operation modes, such as the Strip-map SAR, the Spotlight SAR and the ScanSAR [4–13], leading to reconstruction of the surface reflectivity image based on Range-Doppler or

frequency-wavenumber ($\omega - k$) domain algorithms [14,15]; through the advanced image processing methods applied in order to improve the quality of SAR image, e.g., reduction of the speckle [16], which is a signal dependent granular noise that visually degrades the appearance of SAR focused image; and up to sophisticated operating mode and robust signal processing algorithms developed in order to extract quantitative information about observed area from mutually correlated (at least two) complex SAR images [17,18], as Interferometric SAR (InSAR) [19–23], Polarimetric SAR (PolSAR) [24–26] and Polarimetric SAR Interferometry (Pol-InSAR) [17,27]. InSAR retrievals terrain topography from an interferogram, which represents the phase difference between two complex SAR images of the same scene acquired at various look angles. PolSAR uses various polarization channels to extracts information about different backscattering mechanisms from a terrain surface highly related to orientation, geometrical reflectivity and geophysical properties such as roughness and humidity. Pol-InSAR is based on the coherent combination of inteferograms acquired at different polarizations [17]. Several SAR space-borne (for instance: RADARSAT-2, TerraSAR-X) or airborne systems are being operated today, and another will be launched soon, to ensure unique imaging capabilities independent from daylight, clouds and weather conditions. Moreover, nowadays the space-borne systems are widely organized in satellite constellation for improving spatial resolution and bistatic imaging. Generally, these systems operate in a wide frequency range: VHF (30 MHz – 300 MHz), UHF (300 MHz – 1000 MHz), L (1.0 GHz – 2.0 GHz), S (2.0 GHz – 4.0 GHz), C (4.0 GHz – 8.0 GHz), X (8.0 GHz – 12.0 GHz) and with different bandwidth [2], as well in various mode of scan, in co- or/and cross-polarized channels, and provide the purpose-dependent resolution (from a few meters to tens of centimetres) and area of the observed swath (from a hundreds to thousands squares metres).

Although that the area of SAR application is vast and mainly focused on terrain surface imaging in many fields as geology, agriculture, forestry, cartography, hydrology, urban and disaster monitoring, many recent research activities deals with subsurface parameters retrieval. These activities are focused around the surface moisture and subsurface wet structure retrieval [28,29], with different frequency bands, polarizations and incident angles as well as different correlation results between estimated and real values of soil moisture [29, Table 2]. Moreover, subsurface imaging and its parameters estimation is a constantly growing field of interest in the whole remote sensing domain, not limited only to the SAR systems. Nowadays, the Ground Penetrating Radar (GPR) [2,30,31] is the leading radar technology intended for non-destructive microwave imaging of subsurface structure of the soil. These surface-based systems are typically mounted on a van or remotely operated vehicle. The transmitter and receiver antennas (bistatic mode) are placed at the height up to several centimetres and mostly directed perpendicularly (down-looking) to the terrain surface. GPR directly sends the Ultra-wideband (UWB) [32] Electromagnetic (EM) waveform toward the soil structure through the air-terrain interface, and records backscattered energy from the soil's inhomogeneities in the form of so called A-scan. The GPR frequency range spreads from several megahertz to a few gigahertz. Although the exact bandwidth of GPR frequency is not precisely defined, for the effective, in other words, the deeper penetration into the soil as low as possible frequencies are used, because the attenuation in the soil increases as the frequency increases. Thus, the low frequency band (in general VHF, UHF, P, L band) are referred to as GPR frequency [2], and allows the imaging of ground down to few meters, which is suitable for buried object detection and localization. A typical GPR image, referred to as the B-scan, is formed from coherently collected A-scans along the displacement path and recorded in uniformly spaced positions along movement direction, with constant Pulse Repetition Interval (PRI). Thus, the B-scan image is defined in the coordinates identified with ground displacement axis and delay time axis (recognized as the depth). Unfortunately, due to finite beam width of the main lobe of the antennas, the B-scans exhibit defocused characteristics in movement direction. The data collection scheme, i.e., Pulse Repetition Frequency (PRF), constant and low vehicle

velocity, beam width of the transmitter and receiver antennas and the mounting height of the antennas, result in hyperbolic curves characteristic for buried targets. However, several imaging methods were applied for shallowly buried objects localization. In recent years, various GPR system, e.g., the stepped frequency [33–36] or impulse [37], more often use the SAR-based processing for focusing the GPR images [38, 39]. For example, in time-space domain [33, 35, 37, 40] or frequency-wavenumber ($\omega - k$) domain [41, 42] as well as with Stolt Migration [36], Range Migration [43], Time Migration [44] and Multiple Signal Clasifitation (MUSIC) [45] algorithms. Moreover, the SAR algorithm based on the wavelength reduction in reconstruction process [46] (with constant ε_r in entire illuminated soil structure) was proposed for subsurface imaging, as well the interferometric technique has been applied for SAR-based algorithms for GPR images [47]. Although, the SAR was originally invented for airborne/space-borne high-resolution imaging of terrain surface, a common feature between SAR and GPR imaging processes, i.e., they are formed as a result of antenna movement above the surface at constant height, allows one to apply the SAR-based focussing technique for improving the quality of B-scan images. Furthermore, similarly to improving the SAR images quality, by a speckle reduction, the improving of GPR images is performed by surface reflection (surface clutter) removal [48–50]. For deeply located objects, the backscattered signal arrived later than ground reflection and gating the time signal allows one to remove the ground clutter. Unfortunately, the shallowly buried objects are blurred and masked [51] due to strong backscattering from ground surface. Hence, the correct clutter reduction enhances the shallowly buried object detection, in particular, with regard to small and non-metallic land mines or IDE detection. In contrast to the speckle reduction in focused SAR images, which is post-processing method, the surface clutter reduction is a preprocessing method resulting in improving the unfocused B-scan quality.

However, besides to the fully proven capabilities of subsurface imaging and soils' parameter retrieval, the GPR technique has a several drawbacks limiting its functionality. Firstly and foremost, GPR has a limited area of imaging, thus significantly reducing the ability to image complex and vast buried structures only to local-scale applications. Even in laboratory conditions, the imaging of large areas using GPR is highly lobar investment and time consuming. The area of the GPR imaging process depends on three factors, i.e., on the width of footprint over the surface (antenna pattern and height), on the total displacement length, and on the effective penetration depth of soil. Since the antenna pattern and total displacement length can be both selected in dependence on system requirements, the effective penetration depth of soil is a physically-dependent issue. Secondly, different soil types affecting the dielectric contrast between buried objects and surrounding soil structure [52] (i.e., dielectric constant of the soil can be similar to dielectric constant of the buried object), and in results, affecting the GPR signature [53] as well as the detection performance of GPR system [54]. And finally, propagation speed and attenuation of EM wave in the soil depends on may factors, including soil geological texture and moisture profile, and thus the SAR-based focussing is degraded by unpredicted phase errors along the synthetic aperture [55] due to the inevitability of propagation velocity uncertainty. In fact, limitation of the GPR functionality can be identified with operating volume limitation. More specifically, for GPR system both the maximum survey depth and terrain surface area under simultaneous investigation are limited. The maximum depth of GPR imaging is physically-dependent issue, however, the area under simultaneous investigation can be significantly extended by increasing the height and/or aperture of antennas as well as changing the incident angle. Some of the down-looking ground-based system operates with array antenna (one-dimensional (1-D) or two-dimensional (2-D) aperture). For instance, the Polish consortium of the Military University of Technology and the Bumar Electronika S.A. has developed the platform HABUB with Continuous Waveform (CW) radar [56] designed for hazardous object detection. Another type of ground-based system functioning as Forward-Looking Ground Penetrating Radar (FLGPR), for example, the ALARIC Radar

System [57, 58] designed and developed by the US Army. Both systems provide an increase in the width of the observed area, which is highly important for imaging the road lying in the waysides of the military convoy. Furthermore, in the recent years some tests have been made to mount the GPR on a helicopter-borne platform [59, 60] in the down-looking configuration. This solution leads to a significant increase of the simultaneously investigated area, but requires robust positioning algorithm of the antenna system due to the antennas hanging on the lines a few meters below the helicopter. The results of on-field helicopter-based GPR experiment using the tomographic approach were presented in [61]. Moreover, an analysis of a space system operating as a GPR and aimed at achieving adequate penetration depth and accuracy was performed in [62]. However, as mentioned earlier, both GPR and SAR imaging processes are formed as antenna movements over the surface. A lot of efforts have been performed to combine those imaging processes into a system working in the Side-Looking Airborne Radar (SLAR) configuration and using the SAR technique for imaging the subsurface structure. The essential attribute of the Airborne Ground Penetrating Radar (AGPR) system lies in the combining the advantages and key features of the both well-known imaging techniques, as airborne SAR and ground-based GPR, and operating over a large scale and to adequate penetration depth as well as providing a high resolution imaging capabilities.

Some early attempts at AGPR concept have been already performed with the use of Shuttle Imaging Radar (SIR) imaging instruments in the 80s of the last century. Firstly, in 1982, the SIR-A [63] has been used in the pioneering experiment in order to reveal the subsurface valleys [64] over the Eastern Sahara at a constant look angle of 47°. Two years later, in 1984, the SIR-B [65] has been used over the Eastern Sahara for subsurface imaging of a sand-buried landscape [66] and for controls on signal penetration and subsurface scattering [67] as well as for study on microwave penetration and attenuation in Nevada desert soil [68]. While both SIR-A and SIR-B operated as SAR system in L-band (23 cm wavelength) with HH polarization, i.e., both H-polarization for transmission and reception, the SIR-B was improved by a mechanically tilting antenna for imaging at selectable look angles between 15° and 60° [65]. One decade later, in 1994, the SIR-C/X-Band SAR, has been used for snow mapping in the Alps region [69]. In contrast to the previous SIR imaging instrument, the SIR-C has been enhanced with additional X-band and quad-polarization (HH, HV, VH, VV) modes [29]. Successively to the use of shuttle-based imaging instruments, at the turn of the centuries, the aircraft platforms were being applied more frequently as a carrying platform for SAR systems. For instance, in 1998, the P-3 airborne platform, developed by the National Aeronautics and Space Administration (NASA), was used in the polar ice thickness measurements along the south-west Greenland 2000-contour line [70]. Furthermore, several SAR systems operating in the low frequency band (P- or L-band) have been developed and used for subsurface imaging and parameters retrieval. Selected configurations of those system ware compared in Tab. 1.1. The French agency Office National d'Études et de Recherches Aérospatiales (ONERA) have developed the Radar d'Analyse MultiSpectral et d'Etude des Signatures (RAMSES) [71]. In 2001, the RAMSES was used for P-band [72, 73] and for polarimetric L-band [28, 74] data collection over Pyla Dune in France. Later, the RAMSES has been used for L-band subsurface imaging in south-central Egypt [75], i.e., over the same site investigated previously by the SIR-A [64] and SIR-B [67]. Moreover, the German agency Deutschen Zentrum für Luft-und Raumfahrt (DLR) have designed the Experimental SAR (E-SAR) four-band sensor [76], that was used for the analysis of physical backscattering properties of the imaged area [24], and the Jet Propulsion Laboratory (JPL) have developed the Airborne SAR (AIRSAR) that was used, for instance, to investigate the sand thickness effect on radar backscatter from subsurface structure [77] based on the L-band data acquired over the Dumont Dunes area. In outlined above AGPR experiments the estimated penetration depth varies from 1.5 m down to several meters. However, these SAR experiments have been carried out over the so-called arid areas, mostly over desserts [64, 66–68, 75], dunes [28, 72, 74, 77] and over snow

Table 1.1 Comparison of selected airborne SAR systems operating in low frequency range and used for subsurface imaging and parameters retrieval: f_c is the centre frequency, B_f is the bandwidth.

Radar ID	System & Band	f_c [GHz]	B_f [MHz]	Source
Radar1	P-3, VHF	0.150	20	[70]
Radar2	E-SAR, P	0.360	30	[76]
Radar3	RAMSES, P	0.435	70	[72]
Radar4	AIRSAR, L	1.200	75	[77]
Radar5	E-SAR, L	1.300	75	[24,76]
Radar6	RAMSES, L	1.600	200	[28,74]

[69] and glacier [70]. Due to the natural environmental conditions, the structures of desert sands and glaciers are strongly similar to a homogeneous structure (dry sand, snow or ice) with almost constant EM properties in the investigated site. Hence, the propagation medium can be approximated as two homogeneous half-spaces, i.e., free space (radar space) and a material medium. A similar homogeneous approach of the soil geological structure and nearly optimal conditions for EM wave propagation, with constant values of permittivity ε and conductivity σ, was used for AGPR concept in theoretical analysis and design considerations [78–80], numerical simulations and processing [46,81–84] and laboratory experiment [85,86]. Theoretical aspects of imaging targets buried below earth's surface addresses the dispersion and reflection, side lobe attenuation, usable bandwidth of the radar and dynamic range [78]; resolution and antenna size, signal bandwidth and processing capability [79] as well as impact of altitude and swath wide on averaged power and waveform shape [80]. The comparison between surface and buried point targets imaging, in side-looking mode and with chirp signal, has been presented in [81] and the numerical results of tunnels detection for two general cases of soil type, i.e., nondispersive sandy soil and dispersive clay loam soil, are shown in [82]. Furthermore, the results of AGPR numerical simulation with various surface roughness was conducted in [83], and with different bistatic antenna arrangements and flight heights in [84]. The results of laboratory experiment and numerical modelling of AGPR concept was presented in [85]. In [86], the InSAR technique was used for topography of sand-covered bedrocks in homogeneous media (arid and deserts areas) and was confirmed by in laboratory-scale model with dual-frequency InSAR (VHF, Ka). All the above-mentioned efforts [63–86] are based almost completely on homogeneous and well-know soils structure. However, such a broad interest in the problem of soil structure imaging encourages to further research of solutions, that can be universal and soil independent.

Unfortunately, such a homogeneous approximation of the soil structure, in all the above-mentioned works considering airborne subsurface imaging, does not correspond to the vast majority of lands, which are a mixture of different soil types, arranged in horizontal-layered structures with varied texture and parameters inside a geological soil's horizons. Due to the inhomogeneous, dispersive and lossy nature of the soil, the backscattered signal derived from multi-reflections of the electromagnetic waveform transmitted through the soil is disturbed by dispersion and lossy effects. In general, wave propagation in soil structure can be considered as wave propagation into rich scattering channel, where soil discontinuities represents secondary scatterers (clutter). Furthermore, multipath components of wave imposed on each other and on the transmitted radar waveform thus leading to envelope modulation and phase fluctuation in the received signal. This, in consequence, leads to energy dissipation and received pulse distortion strongly affecting the output of the matched filtering and significantly degrading the range (depth) resolution (the replica of transmitted signal is not well matched to received signal). Detailed analysis of the low frequency SAR focusing problems was carried out in [87] with special emphasis of attenuation, range defocusing and misplacement. Foremost, the most

important problem is the strong defocussing of the backscattered signal in range (depth) dimension, which decreases the detection capabilities, since the energy level of the focusing point is much weaker than expected. Due to the velocity changes in soil, the target is not correctly focused in its origin location (depth misplacement), the energy dissipation leads to the occurrence of the ghost (apparent) targets. Moreover, the information contained in the phase of the backscattered signal is difficult to extract in order, for example, to measure the height of buried structure. Therefore, the primary step to take advantage of the SAR processing should be firstly the neutralization (or compression) of the defocusing effects in depth dimension.

Since the soil can be approximated as a cluttered channel, because of the geological discontinuities between consecutive soil horizons and its natural belongings as rocks and underground water fields, the method to overcome the defocusing effect and to provide a significant enhance of detection gain is the use of time-reversal approach. The Time-Reversal (TR) technique was introduced by Fink *et al.* [88,89] to focus an ultrasonic wave on a target through an inhomogeneous channel with the use of a Time-Reversal Mirror (TRM). In TR technique, the backscatter echo of an initially transmitted signal into a scattering medium is recorded, energy normalized and retransmitted through the same scattering medium. Basic principles of the TR [90] state that the spatial-temporal Matched Filtering (MF) performed by Time-Reversal Array (TRA) is optimal and self-adaptive technique that compensate any propagation distortions through inhomogeneous media. In practice, TR exploits the multipath propagations in a highly scattering medium to achieve supperresolution, i.e., resolution which is better (finer) than the classical diffraction limit (Rayleigh resolution) [91]. The TR focusing is obtained by constructive interference of multipath components of the wave at the scatterer location. Assumptions of the TR have been verified experimentally [92], and later, applied and confirmed, for instance, in ultrasound medical imaging [93]. Recently, the positive result of TR studies in propagation of acoustic waves and ultrasound in randomly layered media [94], resulted in growth of interest research groups (lead by M. Fink, J. M. F. Moura and F. L. Teixeira) in the use of TR-based focusing methods for EM waves [95, 96]. In particular, for the experimental and numerical investigation on UWB waves propagation and focusing at initial source location in random media [97–99] using either TRA or single antenna, and in active and passive mode. TR experiments with single antenna [100] and antenna arrays [101] confirmed, that the TR detection provides increase of the detection gain and Signal-to-Noise Ratio (SNR) over conventional radar detection, also for targets immersed in cluttered environment [102]. Moreover, besides the significant increase in the detection gain, the TR approach allows one for the best match of the probing signal to the intervening medium in retransmission. Overall, in the last years, the TR technique has been incorporated (mostly numerically) into wide number of remote sensing applications to improve their imaging efficiency and detection performances [103]. For example, the FDTD-based microwave breast cancer detection [104], the space-frequency UWB imaging [105] and the Multiple-Input Multiple-Output (MIMO) radar [106]. Contrary to the *standard TR* technique allowing the re-focusing simultaneously on all scatterers and more strongly on the dominant scatterers, the Decomposition of the Time Reversal Operator (*French: Decomposition de l'Operateur de Retournement Temporel*) (DORT) [107] has been developed to overcomes the problem of simultaneous focusing. DORT provides *selective* focusing on particular scatterers over the others by using eigenvalues of multistatic data matrix measure by the TRA of N elements [98, 108]. However, DORT method requires that the number of TRA elements should be not less than the considered number of well resolved scatterers in investigated medium. Moreover, Time-Reversal Adaptive Interference Cancellation (TRAIC) [109] method was developed for clutter channel cancellation using the TR nulling. In contrary to the TR focussing, the TR nulling provides destructive interference in nulling spot centred around scatterer location. In addition, the TR were incorporated into a large number of existing detection and imaging techniques using EM waves. For instance,

the TR were used for target localization in highly scattering and cluttered environments [110, 111], for instance, using frequency selection TR method [112], as well as in the combination with the MUSIC algorithm [113]. Furthermore, the TR methods were applied for the SAR processing in the indoor laboratory environment for ghost image cancellation [114–116], numerical simulation for TR imaging of shielded targets [117] hidden in cluttered environment as well as in the outdoor experiment for change detection assessment [118]. Finally, but not the least important, the TR technique was applied for TR-based focusing algorithm for Through-The-Wall (TTW) imaging [119–121] and for GPR imaging and depth estimation [122,123]. Hence, as follows from the above-described works, the Time-Reversal technique has enriched existing remote sensing methods for greater performance and efficiency of detection and localization in a multipath media (or cluttered channel).

Thus, while the aircraft platforms with the SAR system operating in the SLAR configuration provide an enhanced usability and reconfigurability comparable to the space-borne platform as well as the broader area of simultaneous observation than the GPR, the expansion of SAR functionality with a new method of scanning along a modern TR-based signal focusing algorithm may result in novel and uncommon capabilities for high-resolution imaging of optically invisible soil structure over large-scale and down to purpose-required depth. A validation of the TR-based focusing algorithm would provide new broad-area imaging capabilities. The above-mentioned idea is fraught with challenges and constrains related to the physical aspects of subsurface imaging and to the features of the AGPR functionality [124]. For instance, the platform altitude, PRF, transmitted power, look angle and antenna beam width, radar centre frequency and band; or maximum penetration depth, which is physically-dependent. Foremost, the inhomogeneous dispersive and lossy soil affects the transmitted signal causing its strong deformation during the propagation. Thus the hypothesis about soil dielectric constant may be critical to determine the SAR system features, which, in turn, may provide a highly directed and minimally disturbed energy propagation down to a predetermined depth and significant increase of the level of the backscattered signal energy. Furthermore, the TR approach leads to a signal which is internally best matched to rich scattering medium, which is modelled as an inhomogeneous, dispersive and lossy soil. The mirrored retransmission of the time-reversed signal provides spatial-temporal matching to the soil structure. Therefore, the Time-Reversal Airborne Ground Penetrating Radar (TR-AGPR) system, unlike conventional airborne SAR system, by taking advantages of the internal complex scattering phenomenon provides range/depth focal of the backscattered energy, which results in the high-resolution imaging capabilities of the soil structure. Hence, the successful coupling of the SAR and TR techniques leads to new imaging capabilities of the subsurface soil structure, which would be usable in many fields, such as soil-resource mapping (ground water, oil fields), environmental protection and monitoring as well as military surveillance and recognition. What is the most important, the successful coupling of these techniques can provide universal imaging capabilities of the soil structure, which are adaptive to inhomogeneous soil conditions. And, therefore, the subsurface imaging can mainly depend on the radar resources only, without the strong dependence on soil conditions.

1.3 Synthetic Aperture Radar Background

The term of the Synthetic Aperture Radar [1–27] refers to a family of radar systems and processing techniques extensively used for obtain high-resolution and two-dimensional image of illuminated scene representing their directional reflectivity. While mostly, the SAR is considered only as a group of image formation algorithms, in fact, it is also a family of data collection schemes, that determine further processing algorithms and potential resolution. Fig. 1.1 shows a flow chart of the SAR system. During a single acquisition the selected scene

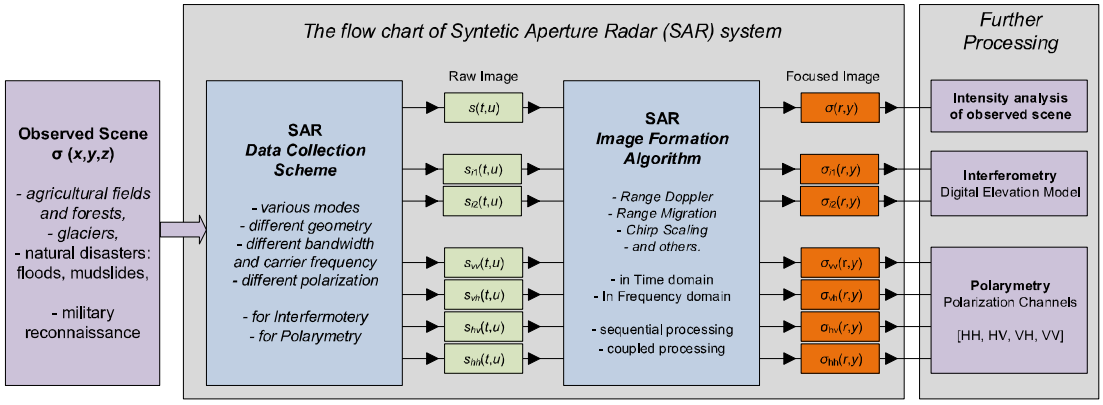

Figure 1.1 Sketch of data acquisition and signal processing in the SAR system.

$\sigma(x, y, z)$ can be illuminated in various scan modes, which may differ from each other in geometry, carrier frequency and bandwidth of the radar waveform as well as in polarization. For a particular application of SAR (as Interferometric SAR (InSAR), Polarimetric SAR (PolSAR)), several acquisitions should be carried out in correlated manner. The result of the single acquisition is the raw image $s(t, u)$, whereas, for the correlated acquisitions the raw images should be grouped mutually for further processing: $s_{i1}(t, u)$ and $s_{i2}(t, u)$ for InSAR and $s_{vv}(t, u)$, $s_{vh}(t, u)$, $s_{hv}(t, u)$ and $s_{hh}(t, u)$ for PolSAR. The t denotes fast-time, and u the slow-time. After acquisition, each raw image (even from mutually correlated) is processed based on the image formation algorithm leading to a focused image $\sigma(r, y)$. Finally, the focused images can be analysed (interpreted) or further processed by InSAR or PolSAR in order to extract quantitative information about observed areas. Fig. 1.2 presents a geometry of the Stripmap SAR system.

The focused SAR image $\sigma(r, y)$ reveals high spatial resolution in both range r direction and azimuth (or cross-range) y direction. This determines the use of SAR systems as a tool for imaging in a wide range of applications and weather conditions, that are adversed for optical imaging (compare [9, Fig. 1.1 and Fig. 1.2]). A high resolution in SAR image is achieved by using two-dimensional processing, divided into two data processing each in orthogonal direction as the distance (slant range) and azimuth (cross-range) direction. High resolution in range direction directly depends on the bandwidth B_f of used radar signal [2, 4, 12, 13]

$$\Delta r = \frac{c}{2\ B_f} \tag{1.1}$$

and long pulses with the internal wideband modulation are more often used than short pulses. For instance, signal with the Linear Frequency Modulation (LFM), which is a common radar waveform. By the use of a replica of transmitted signal (MF approach), the high slant resolution is achieved over each backscattered signal recorded at every u_n position. Thus, range compression produces a 1-D complex range profile of entire area located in the antenna footprint on the ground. The 1-D complex range profile conveys information about relative slant range between the point on the terrain and radar. Then, later, the high resolution in azimuth direction is synthesised along the distance that airborne platform flew over the observed area, which is know as the synthetic aperture, and with the use of all 1-D complex range profiles (amplitudes and phases) that are coherently recorded during the flight along L_{sar} in every uniformly spaced u_n positions. While for real aperture radar the fine cross-range resolution at range r_s requires a very large antenna L of several hundred meters long [2, 4, 12, 13]

$$\Delta a_r = \frac{\lambda}{L} r_s \tag{1.2}$$

the SAR systems use a small antenna of horizontal dimension L_R carried by an airborne platform over the flight distance to successively illuminate the observed area at different u_n positions and record backscattered signals. Instead of parallel processing as for a long real aperture, high azimuth resolution is mathematically synthesised by coherent processing of the data collected during a flight and taking into account the quadratic phase history spread over multiple pulses recorded in successive u_n positions along platform trajectory. The collection of 1-D range profiles is transformed into a matrix and fine resolution in azimuth is synthesized along a second dimension (parallel to flight trajectory). For the considered scan mode, i.e., Stripmap SAR, the lower bound of the cross-range resolution equals [2, 4, 12, 13]

$$\Delta a_s = \frac{L_R}{2} \tag{1.3}$$

which states that the fine resolution is independent of range and is much better than Δa_r real-beam resolution (Eq. 1.2).

While the operation of the SAR system seems to be intuitively simple and clear (Fig. 1.1), in fact, it is very complex. First of all, range and azimuth processing are coupled and high resolution in azimuth direction requires providing firstly a high resolution in range direction. In turn, while a high range resolution is provided by method known from other radar systems (for instance, long-range radar), the aperture synthesizing technique refers to a processing that improves a cross-range resolution only. During the flight over time T_s and with v_p velocity (i.e., N_s scans each at $n \times PRI = n/PRF$ seconds) the slant range $r(u)$ between airborne platform and target on the ground change over the flight (see Fig. 1.2) as follows [4, 9, 12, 17]

$$r(u) = \sqrt{r_s^2 + v_p^2(u - u_c)^2} = \sqrt{r_s^2 + \frac{v_p^2}{PRF^2}(n - n_c)^2} \tag{1.4}$$

where the u is slow-time along flight path, the $u_c = T_s/2$, the n is position along flight path and the $n_c = N_s/2$. Due to the nonzero azimuth beamwidth θ_{az} of the antenna, the backscattered response is spread in set of the 1-D complex range profiles. Hence, after range compression the targets are focused in different range cells along the hyperbola, whose shape depends on the target location in slant range direction. For these targets located around the near edge of the swath, the hyperbola is more curved (more bent ends) and progressively flattens for targets lying close to the far edge of swath. However, longer dwell time at far slant distances results in an increase of its length. At far ranges, the target is longer exposed in the antenna azimuth beamwidth than in near ranges. Rearranging of Eq. 1.4 leads to [4, 12, 13]

$$r(u) = r_s\sqrt{1 + \frac{v_p^2(u - u_c)^2}{r_s^2}} \tag{1.5}$$

which can be further simplified as [4, 12, 13]

$$r(u) \approx r_s\left[1 + \frac{1}{2}\frac{v_p^2(u - u_c)^2}{r_s^2}\right] \tag{1.6}$$

based on the expansion of the square root $\sqrt{1+x} = 1+\frac{1}{2}x+\frac{1}{8}x^2+...$ and keeping only the first two terms. The required assumptions $\frac{v_p^2 \mid u - u_c \mid^2}{r_s^2} < 1$ is satisfied when $(L_R/2)^2 \ll r_s^2$ [13], which is correct for Stripmap SAR where synthetic aperture length L_R is much shorter than slant range to the observed scene in its entire area. Furthermore, the phase of backscattered

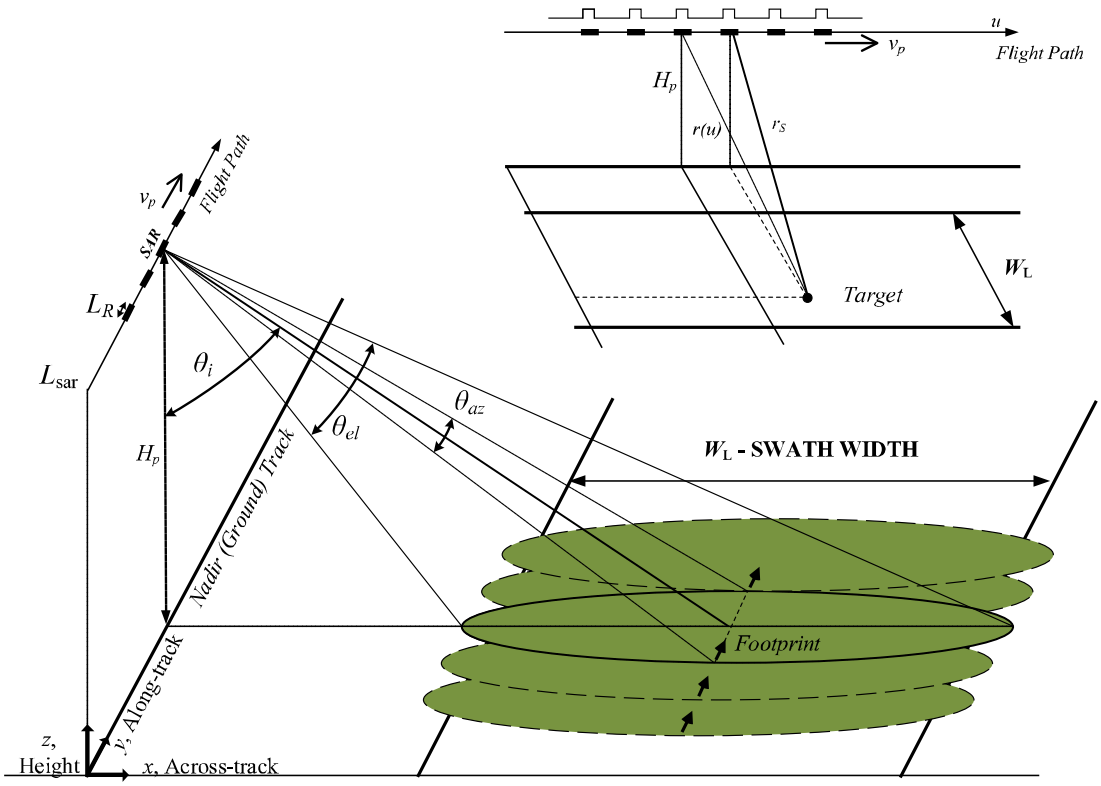

Figure 1.2 Geometry of the Stripmap SAR system.

returns changes as follows over two-way slant range $r(u)$ [4,17]

$$\phi(u) = -\frac{2\pi}{\lambda} \cdot 2 \cdot r(u) \tag{1.7}$$

Substituting Eq. 1.6 into Eq. 1.7 gives [4]

$$\phi(u) \approx -2\pi \left[\frac{2\ r_s}{\lambda} + \frac{v_p^2 (u - u_c)^2}{\lambda\ r_s} \right] \approx -\frac{4\pi\ r_s}{\lambda} - \frac{2\pi}{\lambda\ r_s} v_p^2 (u - u_c)^2 \tag{1.8}$$

which shows that phase of backscattered echo varies approximately quadratically along L_{sar} with constant shift proportional to the nominal slant range r_s. Considering $(u - u_c) = t_u$, where $\mid t_u \mid \leq T_s/2$, the Eq. 1.8 changes as [4]

$$\phi(t_u) \approx \phi_{CPA} - 2\pi \frac{v_p^2}{\lambda\ r_s}\ t_u^2 \tag{1.9}$$

The Doppler frequency equals [4,17]

$$f_D(t_u) \approx \frac{1}{2\pi} \frac{d\ \phi(t_u)}{dt_u} \tag{1.10}$$

which after substitution of Eq. 1.9 gives [4]

$$f_D(t_u) \approx -\frac{2v_p^2}{\lambda\ r_s} t_u \approx -\frac{2v_p^2}{\lambda\ r_s} (u - u_c) \tag{1.11}$$

where the instantaneous Doppler frequency is proportional to the u slow time. Fig. 1.3 shows the changes of relative two-way phase and Doppler frequency along the flight trajectory in

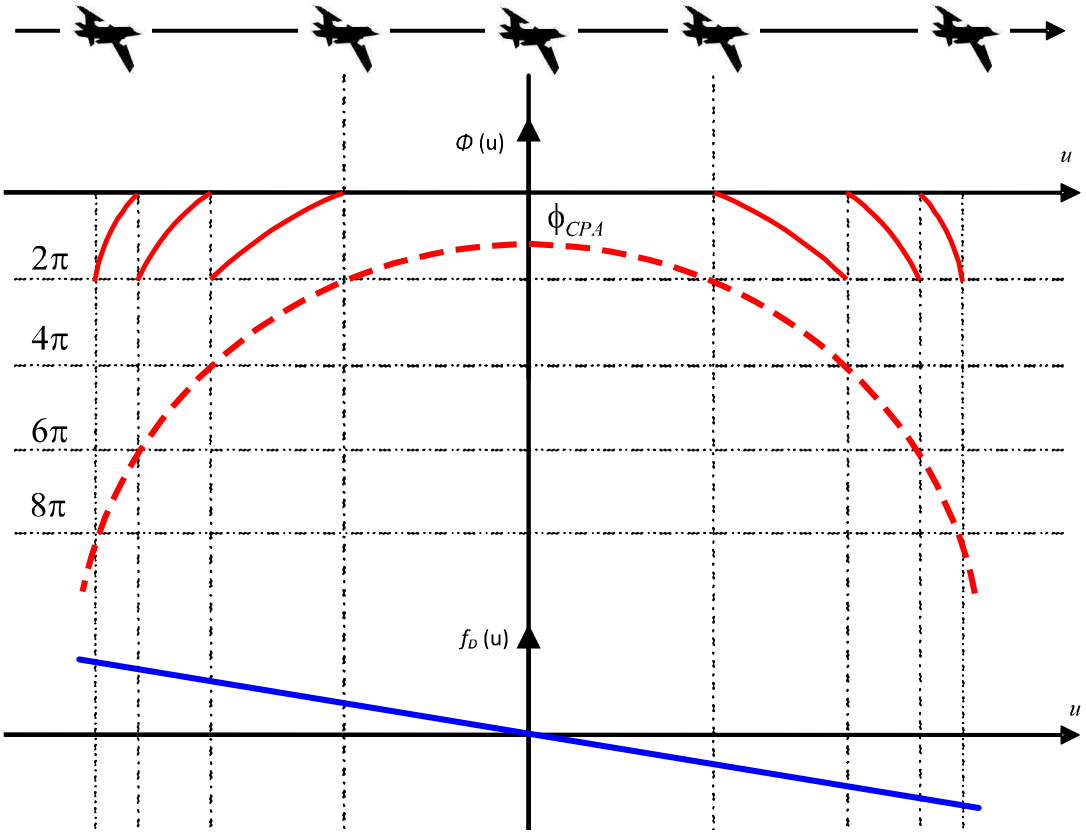

Figure 1.3 Changes of the relative two-way phase $\phi(u)$, the Doppler frequency $f_D(u)$ and azimuth reference function along the flight trajectory.

relation to the theoretical point target located at the surface (see Fig. 1.2). The Doppler frequency rate equals [4, 9, 13]

$$K_u(t_u) = \frac{d\ f_D(t_u)}{dt_u} \approx -\frac{2v_p^2}{\lambda\ r_s} \tag{1.12}$$

Considering minimum and maximum value of slow time, $-T_s/2$ and $+T_s/2$, the Doppler bandwidth along the L_{sar} synthetic aperture line equals

$$B_D = \max[f_D(t_u)] - \min[f_D(t_u)] \approx \frac{2v_p^2}{\lambda\ r_s} T_s \tag{1.13}$$

When the observation time T_s at slant range r_s it defined as

$$T_s = \frac{\lambda}{L_R}\ r_s\ v_p^{-1} \tag{1.14}$$

hence, the Doppler bandwidth

$$B_D \approx 2\frac{v_p}{L_R} \tag{1.15}$$

Finally, using Eq. 1.1 (over one way distance along L_{sar}), the lower limit of cross-range resolution for the Stripmap SAR equals (as previously defined by Eq. 1.3) [2, 4, 12, 13]

$$\Delta a_s = \frac{v_p}{B_D} = \frac{L_R}{2} \tag{1.16}$$

Due to the large number of raw data collection modes the potential cross-range resolution differs between modes and the size of the investigated areas varies as well. For instance, the circular Spotlight SAR [6] provide finer resolution that the Stripmap SAR with the disadvantage that it provides a smaller observation area. These dependencies determine the application for SAR systems. Another important issues linked to SAR systems can be found in related literature [1–27] starting from the description of data collection modes and accurate specification of focussing algorithms, through the geometric distortion of the radar images and the visualisation and comparison of a focussed image, finally ending at examples of SAR applications.

1.3.1 Interferometric SAR

When focused SAR image represents only the magnitude of surface reflection coefficient in a plane dimension (2-D image), it omits information about changing the relative height of observed area. To extract quantitative information about observed area, the Interferometric SAR (InSAR) technique analyses the phase of at least two complex SAR images (mutually correlated, $s_{i1}(t,u)$ and $s_{i2}(t,u)$ from Fig. 1.1) and, for instance, it can produce information about the target elevation, surface reflectivity change and other topics [19–23]. To achieve this InSAR, for instance, uses complex images of the same area collected at the same time (parallel imaging) at slightly different angles (referred to as Across-track InSAR) or collected at the same angle after intervals of time (referred to as Repeat-pass InSAR). Beyond obtaining quantitative information about observed area, InSAR systems are most often used to generate the Digital Elevation Model (DEM), which represents a high-quality digital topographic map (3-D image). Moreover, the InSAR technique, in particular in repeat-pass mode, is used for change detection, for instance, analysis of the growth of forests or agricultural crops or glacier movements. Due to the operational conditions and requirements for constant interferometric baseline as well as for the platform trajectory the InSAR imaging is mostly performed from a space-borne platforms rather than from airborne, however, the available results show that airborne InSAR imaging also leads to correct results over smaller areas.

Fig. 1.4 shows the essential steps of InSAR as a further processing of two mutually acquired and formed SAR images (see the right side of sketch presented in Fig. 1.1). These steps will be later, in Chapter 4, discussed and applied to compressed images. The respective coregistered and focused master $\sigma_M(r,y)$ and slave $\sigma_S(r,y)$ images are defined in complex form as [13, 19, 20]

$$\sigma_M(r,y) = |\sigma_M(r,y)| \exp\left[\mathrm{j}\ \phi_M(r,y)\right] \tag{1.17}$$

$$\sigma_S(r,y) = |\sigma_S(r,y)| \exp\left[\mathrm{j}\ \phi_S(r,y)\right] \tag{1.18}$$

The interferogram $\chi(r,y)$ is formed as [22, 23]

$$\chi(r,y) = \sigma_M(r,y) \cdot \sigma_S^*(r,y) = |\sigma_M(r,y)|\,|\sigma_S(r,y)| \exp\left[\mathrm{j}\ \psi(r,y)\right] \tag{1.19}$$

where the $\psi(r,y)$ is the interofermetric phase difference

$$\psi(r,y) = \phi_M(r,y) - \phi_S(r,y) \tag{1.20}$$

which represent the phase difference between each pixel of coregistred images. Assuming the phase of backscattered returns as a result of the contribution of individual terms arising from radar pulse propagation [20, 22, 23]

$$\phi(r,y) = -\frac{2\pi}{\lambda} r_s(r,y) + \phi_\sigma(r,y) - \frac{2\pi}{\lambda} r_s(r,y) \tag{1.21}$$

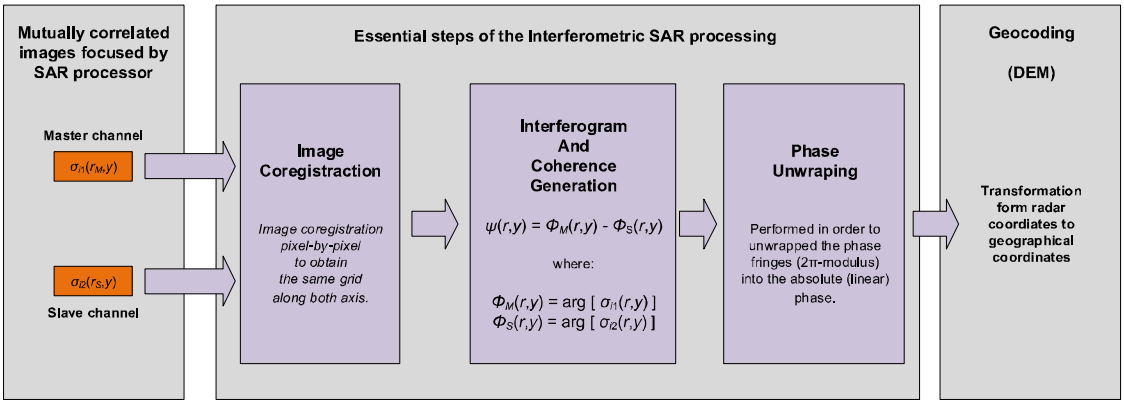

Figure 1.4 The sketch with essential steps of InSAR processing.

where $\phi_\sigma(r,y)$ incorporates all the phase contributions from the RCS of the scatterer and $r_s(r,y)$ represents the one-way slant range. For slightly different geometries, $\phi_\sigma^M(r,y) \cong \phi_\sigma^S(r,y)$, then the interferometric phase simplifies to

$$\psi(r,y) = -\frac{4\pi}{\lambda}(r_s^M(r,y) - r_s^S(r,y)) = -\frac{4\pi}{\lambda}\Delta r_s \tag{1.22}$$

Furthermore, the interferometric phase $\psi(r,y)$ consists of several factors that affect its final form. In general, assuming no temporal deformation between two complex images (images acquired in the same time) and identical influence of atmosphere, the $\psi(r,y)$ can be expressed as [20, 22, 23]

$$\psi(r,y) = \psi_t(r,y) + \psi_n(r,y) + \psi_f(r,y) \tag{1.23}$$

where the ψ_t represents topographic deformation (related to terrain reflectivity), the ψ_f is flat-earth phase and the ψ_n is phase shift caused by independent noise of both radars (or other factors related to processing). Assuming the $\psi_n(r,y) \approx 0$, Eq. 1.23 simplifies to

$$\psi(r,y) \approx \psi_t(r,y) + \psi_f(r,y) \tag{1.24}$$

where only ψ_f distorts the topographic interferogram. Simply assuming the perfectly flat surface (no topography in observed scene), the flat-earth phase model is formed as a phase difference between two points on the same height with different slant distances to radar. This phase difference is given by [23]

$$\psi_f(r,y) = -\frac{4\pi}{\lambda}B_{in}\cos(\psi + \beta_{in}) \tag{1.25}$$

and interferogram flattening can be simply realize as [23]

$$\psi^{wr}(r,y) \cong \arg\ [\ \chi(r,y) \times \exp(\ \mathrm{j}\psi_f(r,y)\ )\ ] \tag{1.26}$$

The $\psi^{wr}(r,y)$ represents the topographic interferogram wrapped into interval of $(-\pi,\pi)$ (interferegram can been seen as a image of isolevel curves which reflects the height changes). The height amiability of terrain h_{amb} (i.e., heigh difference that produce interferometric phase change of 2π) is inversely proportional to th perpendicular baseline B_p [17, 20, 22]

$$h_{amb} = \frac{\lambda\ r_s \sin(\theta_{in})}{2\ B_p} \tag{1.27}$$

and is one of the factors influencing the choice of the baseline length. The other one, refereed to as the critical perpendicular baseline $B_{p,c}$ (defined in terms of incident angle θ_{in}) [23]

$$B_{p,c} = \frac{\lambda\ r_s \tan(\theta_{in})}{2\ \Delta r} = \frac{\lambda\ B_f\ r_s \tan(\theta_{in})}{c} \tag{1.28}$$

limits the baseline length over which the correlation between two SAR images completely vanished (they become uncoupled for InSAR processing due to $\sigma^M(r,y) \neq \sigma^S(r,y)$, thus, $\phi_\sigma^M(r,y) \neq \phi_\sigma^S(r,y)$). θ_{in} is the local incident angle and Δr is the slant range resolution inversely proportional to radar bandwidth B_f (Eq. 1.1). Considering that h_{amb} responds to full phase rotation, the interferometric phase is first unwrapped to its instantaneous form [20]

$$\psi^{uwr}(r,y) = 2\pi l_p + \psi^{wr}(r,y) \tag{1.29}$$

where l_p is a integer value, and later, the phase-to-height conversion performed by scaling factor, which is defined as [20]

$$\zeta_\psi^h = \frac{\lambda\ r_s \sin(\theta_{in})}{4\pi B_p} \tag{1.30}$$

and geocoding lead to the DEM, which is determined in relation to reference or true height.

1.4 Outline of the Dissertation

This dissertation has five chapters and two additional appendices, it begins with the problem statement, literature review and motivations as well the SAR background presented in **Chapter 1**.

Chapter 2 presents the electromagnetic nature of soil, the geometry of subsurface imaging from airborne platform and the problems related to EM wave propagation through soil structure. Since the EM properties of soil depend on its geological structure and moisture profile, firstly, the real geological data collected in the Soil Typological Unit (STU) profiles are used to approximate the three-dimensional (3-D) soil structure with the bare and flat surface and the intentionally added geological inclusions to diversify the inner soil structure. Afterwards, the soil electromagnetic properties, i.e., the complex relative permittivity and conductivity, are calculated based on the pedotransfer function (geologically- and hydrologically-motivated approach). Results of modelling are presented and discussed. Furthermore, the subsurface imaging geometry is described with taking into account the relationship between the height of airborne platforms and the maximum depth of considered soil structure. The features related to subsurface backscattering and imaging are analysed with the special emphasis of propagation in multi-layer medium and penetration capabilities. Finally, the backscattered pulses are analysed for various radar parameters.

Chapter 3 validates the Time-Reversal (TR) hypothesis in inhomogeneous, dispersive and lossy medium. After a short introduction to the Time-Reversal technique for EM waves, the differences and limitations are presented. The dispersion and loss effects are described through an analysis of the spectrum of backscattered pulses at different carrier frequencies. Then, the TR-based focusing algorithm is described along the hypothesis of its application. A TR measurements scheme is proposed for the airborne system using for subsurface imaging in monostatic pulse-echo configuration. Differences, potential development and expectations regarding to the proposed method of measurement are discussed. The proposed acquisition methods has been verified over one soil structure from developed in **Chapter 2**. Later, developed algorithm is numerically validated for six buried point-like targets freely distributed

in the soil structure. Finally, the refocusing phenomenon is presented for all considered soil structure with the same location of the objects and for different radar parameters.

Chapter 4 addresses the efforts of synthetic aperture application for focussing and interferometry of buried structure. Based on the introduction to SAR concept (Section 1.3), the motivations of TR-based SAR imaging of subsurface structures are presented. When the fine azimuth resolution requires the undistorted range resolution (regardless of its exact value depending of signal bandwidth), in inhomogeneous structures the TR reveals the azimuth resolution by restoration of the fine range resolution initially disturbed by impact of the soil. The imaging geometry in InSAR mode is presented with mission parameters as well the raw SAR images simulated in assumed geometry are shown and described. To verify the TR impact on image fomentation method the raw SAR images were focused with the Range-Doppler Algorithm (RDA) under the assumptions about the unknown soil parameters. As shown in **Chapter 3**, when the TR impact on range compression enhance the range resolution, its applications along L_{sar} results in the narrowing and reinforcement of target trajectory over the clutter background. However, the parameters used for synthesis of azimuth reference function changed under TR acquisitions. Finally, based on the same assumption about the unknown soil, the InSAR method has been applied for soil structure reconstruction.

Chapter 5 concludes this dissertation, summarising all performed works and contributions as well as indicates the future works.

Appendix A, which is an introduction to **Chapter 2**, highlights for the readers the geological structure of the soil on the basis of the Soil Profile Analytical Database for Europe (SPADE-2), the real geological database created and provided on-demand by the European Commission Joint Research Centre (The Institute for Environment and Sustainability).

Appendix B presents the basic TR measurements scheme in transmission mode where the source and TRA are located at the opposite side of the investigated medium.

CHAPTER 2

EM NATURE OF THE SOIL AND SUBSURFACE IMAGING FEATURES

This chapter presents the electromagnetic nature of soil, the geometry of subsurface imaging from airborne platform and the problems related to EM wave propagation through soil structure. Since the EM properties of soil depend on its geological structure and moisture profile, firstly, the real geological data collected in the Soil Typological Unit (STU) profiles are used to approximate the three-dimensional (3-D) soil structure with the bare and flat surface and the intentionally added geological inclusions to diversify the inner soil structure. Afterwards, the soil electromagnetic properties, i.e., the complex relative permittivity and conductivity, are calculated based on the pedotransfer function (geologically- and hydrologically-motivated approach). Results of modelling are presented and discussed. Furthermore, the subsurface imaging geometry is described with taking into account the relationship between the height of airborne platforms and the maximum depth of considered soil structure. The features related to subsurface backscattering and imaging are analysed with the special emphasis of propagation in multi-layer medium and penetration capabilities. Finally, the backscattered pulses are analysed for various radar parameters.

The introduction to geological soil texture is presented in ***Appendix A****, based on the STU from the Soil Profile Analytical Database for Europe (SPADE-2), provided by the European Commissions Joint Research Centre (The Institute for Environment and Sustainability).*

2.1 Soil Modelling

From the geological point of view, the soil is a composition of the mineral particles, organic matter (both decomposed and undecomposed one), water and air [125, 126]. The real geological databases (refer to Appendix A for introduction to geological soil structure presented based on real data) are a valuable source of information about the soil textural composition, its inhomogeneous and layered nature [127]. However, an information arranged in textural profiles represent only average values inside successive soil horizons. Thus, to obtain the models of soil structure as realistic as possible, firstly, the approximation of textural composition should be carried out in depth dimension. In many works, for instance [87, 127–131], the soil has been modelling as structure, which consists of homogeneous and planar layers with different height, inner textural composition and EM properties. Since the horizontal approach to the soil texture seems to be correct, the problem lies in the proper choice of the number and heigh of soil horizons as well as the number and height of consecutive layers. In laboratory condition, individual layer can have a height up to several centimetres and can be filled with precisely known type of soil. For instance, a dry sand with homogeneous moisture profile. But, in realistic conditions the soil texture varies strongly and height of theoretically homogeneous layer may be as less as a few millimetres. Moreover, the moisture profile is dependent upon the type of soil, and its shape results from the long-time internal processes. Therefore, the natural phenomenon of soil inhomogeneity has to be taken into account in modelling of soil structure, in particular, in depth dimension.

In this section, the emphasis is focus on the soil structure modelling having regard several aspect as reality of the geological layers and moisture profile. Hence, the modelling is performed based on the real Soil Typological Unit (STU) profiles from the Soil Profile Analytical Database for Europe (SPADE-2). The results of modelling are then used to estimate the EM properties of soil structure, i.e., complex relative permittivity ε_r and conductivity σ, as well as in modelling of EM wave propagation in soils structure with inconstant in depth and frequency-dependent $\varepsilon_r(z, f)$ and $\sigma(z, f)$.

2.1.1 Geological Layers

Since the STU profile from the SPADE-2 represents one-dimensional soil textural composition averaged in z depth dimension, defined between z_{up} and z_{down} and over land parcel, firstly, the depth vector is formed with not uniform step, and then the soil texture is approximated at the calculated depths. For all selected profiles the maximum depth was increased to $Z_{max} = 15.00$ m. The h_n height of successive layers was modelled as a Gaussian distribution with the mean value equals $\mu_h = 0.01$ m and standard deviation $\sigma_h \approx 0.0017$ m. The probability density function of h_n layer height, $f(h_n; \mu_h, \sigma_h)$, is given by

$$f(h_n; \mu_h, \sigma_h) = \frac{1}{\sigma_h \sqrt{2\pi}} \exp\left(\frac{-(h_n - \mu_h)^2}{2\sigma_h^2}\right) \tag{2.1}$$

and it is shown in Fig. 2.1(a). The z depth vector starts at $z_0 = 0.0$ m and is iteratively sampled as follows

$$z_{n+1} = z_n - h_n \tag{2.2}$$

where n is layer number. When $h_0 \approx 1.14$ cm, hence $z_1 \approx -0.0114$ m, etc. Total number of layers is $N_z = 1509$ and maximum considered depth of the soil is $Z_{max} = 15.0317$ m, as presented in Fig. 2.1(b). The root mean square of layers height $h_{n,rms} \approx 0.0101$ m. While Eq. 2.2 indicates only the depth at which the interface between successive layers is defined, the individual soil layer l_n is modelled as the geologically uniform, thin and planar layer

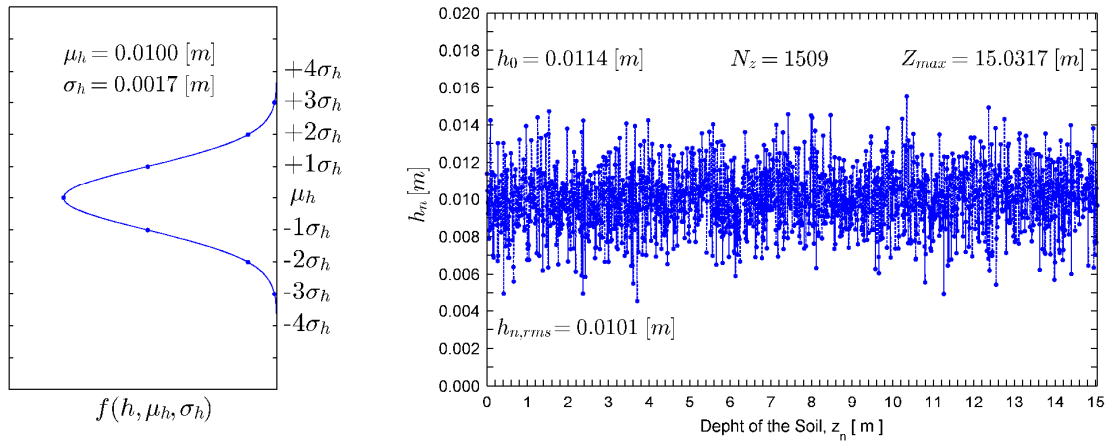

(a) PDF h_n (b) Height of consecutive layers

Figure 2.1 Unevenly approximation of the depth vector: a) the probability density function of layer height, b) the layer height vs. unevenly sampled depth vector (absolute value) of the soil.

located between following interfaces

$$l_n \in [z_n, z_{n+1}) \tag{2.3}$$

The l_n starts at z_n and ends just above z_{n+1}, since z_{n+1} begins next layer l_{n+1}. The last soil layer l_{N_z} starts at the Z_{max} and $l_{N_z} \in [Z_{max}, -\infty)$.

Although the STU profile has various number of soil horizons with a diverse inner geological texture, the approximation method was used similar to Eq. 2.1, with taking into account a different values of c_l clay and s_d sand content in consecutive horizons. Since the $c_l(z)+s_t(z)+s_d(z) = 100\%$, the $c_l(z)$ and $s_d(z)$ were chosen as independent variable, and $s_t(z)$ silt content is calculated as fulfilment to 100% at z_n selected points. The probability density function of clay $c_l(z)$ and sand $s_d(z)$ content are given by

$$f(c_l(z), \mu_{k,c_l}, \sigma_{k,c_l}) = \frac{1}{\sigma_{k,c_l}\sqrt{2\pi}} \exp\left(\frac{-(c_l(z) - \mu_{k,c_l})^2}{2\sigma^2_{k,c_l}}\right) \tag{2.4}$$

$$f(s_d(z), \mu_{k,s_d}, \sigma_{k,s_d}) = \frac{1}{\sigma_{k,s_d}\sqrt{2\pi}} \exp\left(\frac{-(s_d(z) - \mu_{k,s_d})^2}{2\sigma^2_{k,s_d}}\right) \tag{2.5}$$

respectively. The μ_{k,c_l} (μ_{k,s_d}) is a mean value of clay (sand) content in k^{th} soil horizon. The σ_{k,c_l} and σ_{k,s_d} are the standard deviation of clay $c_l(z)$ and sand $s_d(z)$ content in k^{th} soil horizon, respectively, and $\sigma_{k,c_l} = \sigma_{k,s_d} \approx 0.17$ %. Additionally, the STU contains information about the ρ_b averaged value of bulk density of the dry soil in each horizon. However, due to the approximation of soil texture at z_n selected points, the $\rho_b(z)$ is calculated based on clay $c_l(z)$ and sand $s_d(z)$ content as follows [132]

$$\rho_b(z) = 3.455 \ / \ R(z) \tag{2.6}$$

where

$$R(z) = [\ 25.1 - 0.21\ s_d(z) + 0.22\ c_l(z)\ ]^{0.3018} \tag{2.7}$$

Hence, the $p(z)$ porosity is defined by [126, 132]

$$p(z) = 1 - \frac{\rho_b(z)}{\rho_s} = \frac{\rho_s - \rho_b(z)}{\rho_s} \tag{2.8}$$

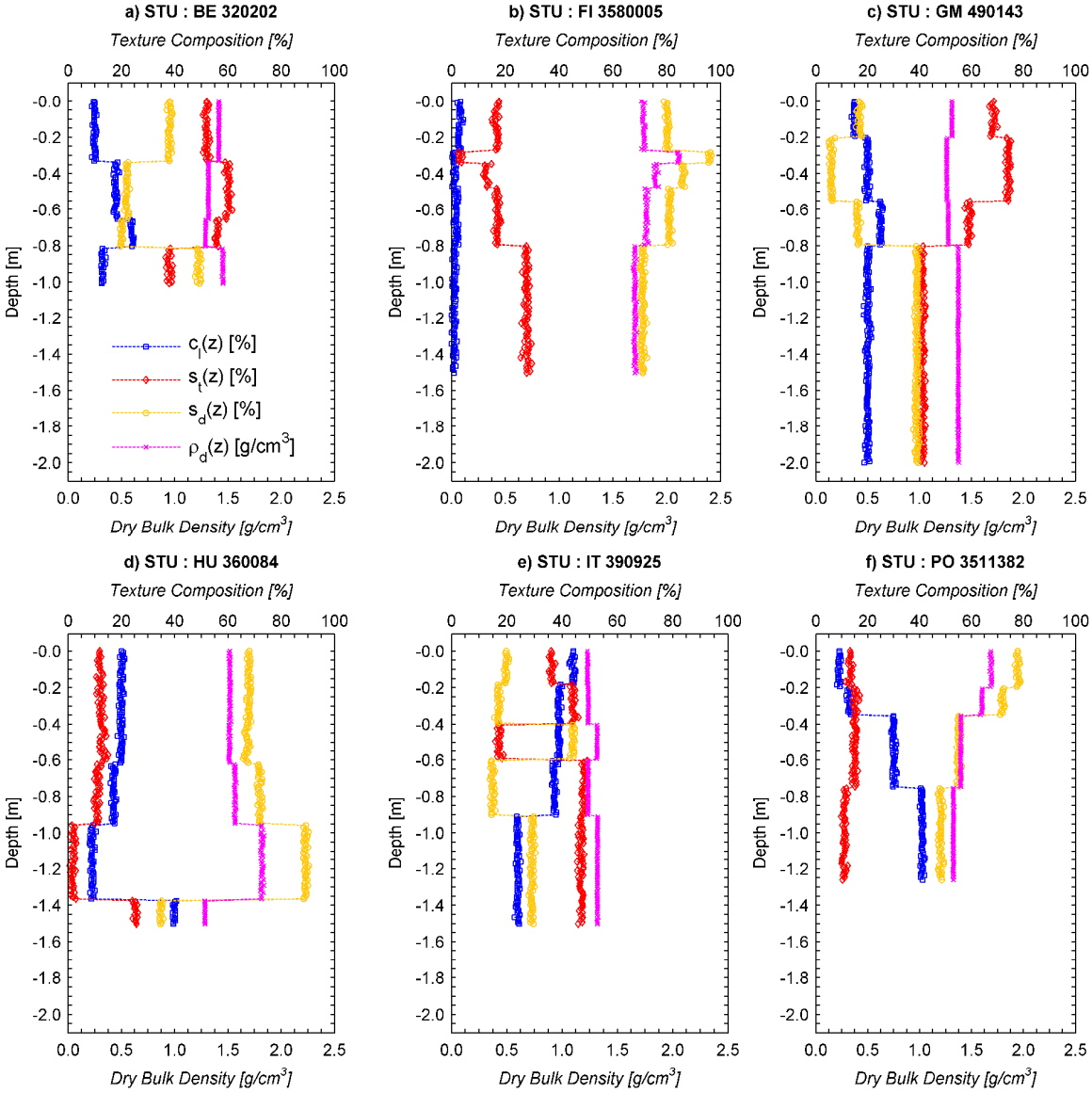

Figure 2.2 Approximated soil texture composition of six chosen STU profiles from the SPADE-2: percentage content of c_l clay, s_t silt and s_d sand, and value of bulk density ρ_b at selected points z_n (down to original STU profiles depth).

where ρ_s is the density of the rock in the soil. Its value varies from 2.6 g/cm^3 to 2.75 g/cm^3 depending soil type. The result of approximation of the soil texture at z_n selected points for six chosen STU profiles is shown in Fig. 2.2. Since the soil texture is approximated down to the 15.00 m, the plots are drawn down to the depth of which the STU profile has been originally defined (as in Appendix A, Fig. A.4). For all STU profiles the slight changes in the soil texture, proportional to σ_{k,c_l} (σ_{k,s_d}), are visible. Moreover, the $\rho_b(z)$ better reflects the change of soil texture, and its layered nature is clearly visible (comparing to Fig. A.4). Introduction of the randomness of soil texture leads to change of soil type in few cases. The changes of soil type after approximation between consecutive soil layers are presented in Fig. 2.3 on the soil textural triangle[1]. Crossings between soil types are now visible, since in Fig. A.5 the textural compositions in soil horizons are uniform. For STU profile whose texture lies close to the border between two soil types, after approximation, the differentiation in the soil types is observed. For examples, *FI* 358005 shows the changes between *loamy sand*, *sand*

[1]Soil Textural Triangle available at: `http://ims.eid.org/homepage/Images/SoilTriangle.jpg`

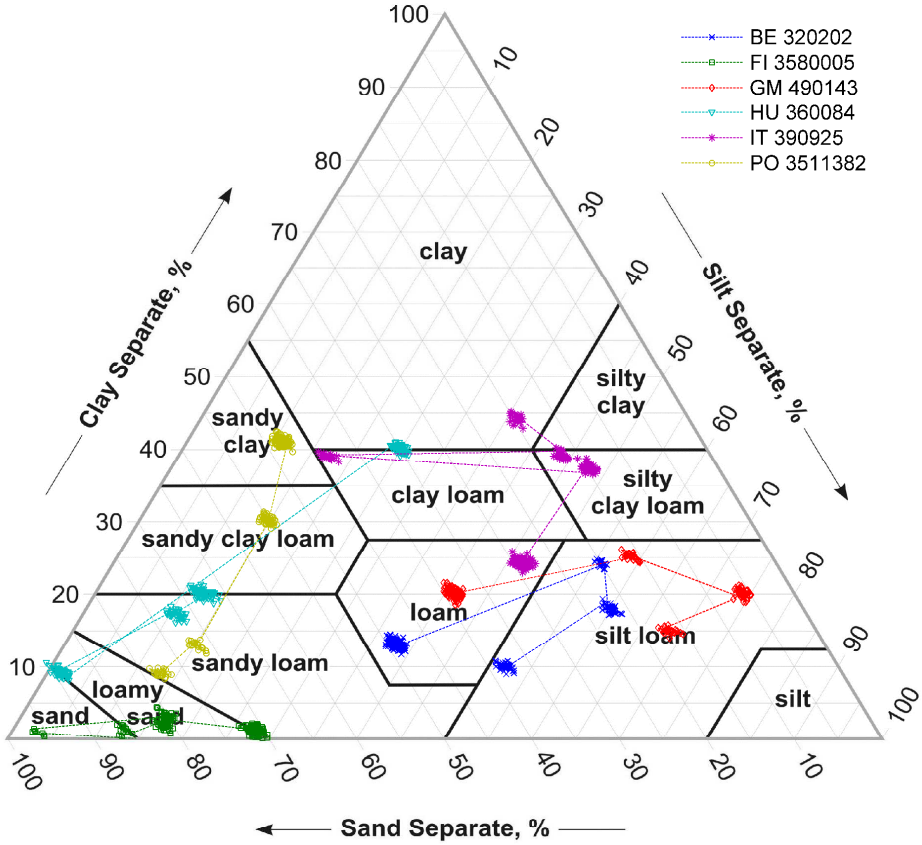

Figure 2.3 Approximated soil texture composition represented on the soil textural triangle (developed by the US Department of Agriculture (USDA)[1]).

and *sandy loam*, as well as the *HU* 360084 shows the changes between *sandy clay loam*, *sandy loam*, *loamy sand*, *sand*, *clay loam* and *clay* in consecutive soil layers. Mainly, the changes in the type of soil stem from the composition of the original texture which lies on the border of two or three types of soil. The scale of texture changes and change of the soil types depends on the assumed values of the σ_{k,c_l} and σ_{k,s_d}. However, for *BE* 320202 and *GM* 490143 the approximation of soil texture has not changed the type of soil, only their inner textural compositions was changed. Nevertheless, for different textural triangle, i.e., with various number of soil types of different area (see [133, Fig. 1]), the soil texture changes will have another form on textural triangle for the same original soil composition and values of σ_{k,c_l} and σ_{k,s_d}.

The approximated STU profiles, however, still represent soil texture composition only in z depth dimension. As stated in Appendix A, the most significant and crucial changes of the soil structure are observed in depth z dimension. In the remaining dimension, i.e. along x and across y axis, soil structure shows a less significant variations. Thus, to create three-dimensional structure of the soil, the percentage content of $c_l(z)$ clay, $s_d(z)$ sand, and $\rho_b(z)$ bulk density, have to be simply multiplied in both along x and across y dimension, as follows

$$\begin{aligned} c_l(x,y,z) &= c_l(z) \\ s_d(x,y,z) &= s_d(z) \\ \rho_b(x,y,z) &= \rho_b(z) \end{aligned} \tag{2.9}$$

and for fulfilment to 100% at selected points z_n

$$s_t(x, y, z) = 100\% - s_d(x, y, z) - c_l(x, y, z) \tag{2.10}$$

The Eq. 2.9 and Eq. 2.10 (keeping in mind the Eq. 2.4 - Eq. 2.8) present fairly realistic model of soil structure, which is based on a randomly varying height of consecutive thin and planar layers of constant inner soil compositions.

The particle composition represents only quantitative information about soil texture and can be obtained after examining the structure of the soil. The natural information, however, about soil structure, obtained after digging a hole in the soil down to few meters, is the colour of consecutive horizons in soil structure (see Fig. A.3). The three-dimensional soil structures created based on the approximation of chosen STU profiles are presented in Fig. 2.4, in colour scale identified with the type of soil, as shown on colour bar. Similarly as before, the structures are plotted only down to limited depth, but now to 3.0 m for each one. For the sake of simplicity, a bare and flat soil surface is assumed, thus avoiding taking into account the surface shape (roughness) and vegetation on the surface. Now, the changes of soil type are distinguishable in colour scale. Four structures created based on *BE* 320202, *GM* 490143, *IT* 395025 and *PO* 3511382 show smooth changes of soil colours through the consecutive horizons. However, in *PO* 3511382 one thin layer located at the depth of $z_n = 0.2$ m represents different type of soil as in layers above and under it. The *FI* 3580005 shows smooth changes of soil colours only through the three first horizons, and then it has a high variability between *loamy sand* and *sandy loam* as can be observed in Fig. 2.3. Finally, the approximation of soil composition mostly affected the *HU* 360084. For these structures, the soil type changes frequently in the first layers down to 0.55 m, between *sandy loam* and *sandy clay loam*, and later from 1.2 m between *loamy sand* and *sand*, and from 1.4 m between *clay* and *clay loam*, respectively. Comparing the six approximated STU-based soil structures, the *HU* 360084 contains the six different soil types. Although, the *FI* 3580005 has also strong variations of structure, it contains only three various soil types. On the other hand, the *IT* 395025 has regular structure and it has also three various soil types, the same as *PO* 3511382. The *BE* 320202 and *GM* 490143 contains both the same two types of soil, i.e., *silt loam* in the upper part and *loam* in the lower part of the structure. Nonetheless, as follows from a comparison of information presented in Fig. 2.2, Fig. 2.3 and Fig. 2.4, the information about the soil texture changes (Fig. 2.2, Fig. 2.3) is partly lost when the soil structure is represented in colour scale (Fig. 2.4). For a soil types of small and narrow area (as *sand*, *silt*, see Fig. 2.3) even a slight changes of soil texture lead to a change of soil type, which is not true in the case of soil types with large and wide area (for example, *clay*, *silt loam*).

2.1.2 Moisture Content and Profile

Besides the minerals particles, the soil is mostly made up of water and air, which together represent a second group in terms of the percentage content. The organic matter is a vestigial (residual) component. The θ_v moisture content is defined as the amount of water present in the soil and is expressed mostly as the percentage of volume. In other words, θ_v gives the ratio of the volume of water (in m^3) in the volume of soil (in m^3). Therefore, θ_v lies inside $[0, 1]$, but from physical reasons does not exceed 50%. Moreover, the θ_v mostly does not exceed the p porosity value, i.e., when $\theta_v = p$, all pores are filled by water and there is no air in the volume of soil, and then, the soil is said to be saturated. The θ_v represents the averaged information about water content over the volume of soil. While $\theta_v = 5\%$, it means that in 1.00 m^3 of soil (e.g. 1.00 m of depth, and 1.00 m^2 of surface area) is contained 0.05 m^3 of water (e.g. 0.05 m of depth, and 1.00 m^2 of surface area) [125]. And thus, the averaged θ_v is

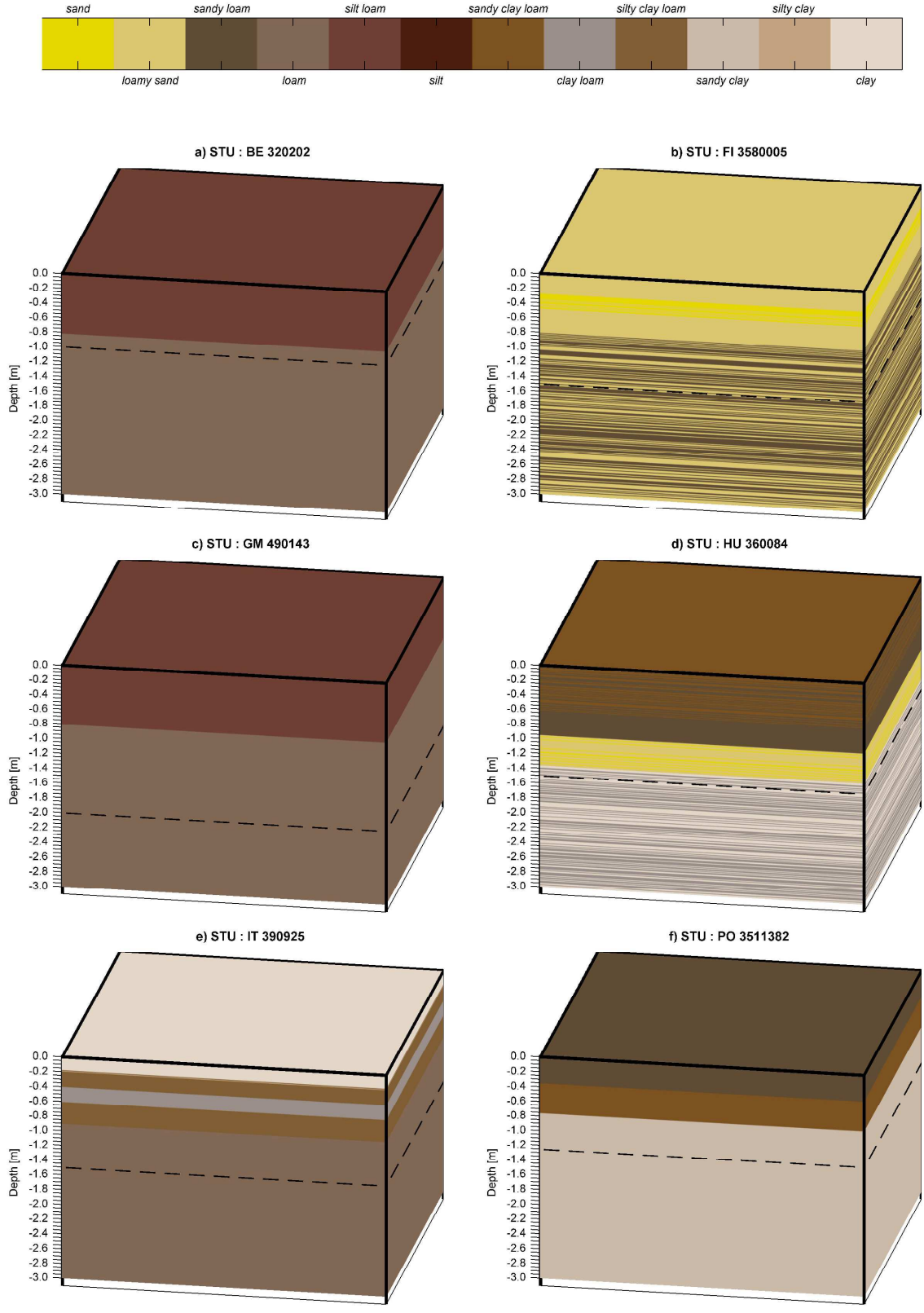

Figure 2.4 Three-dimensional soil structure created based on the approximated STU profiles from the SPADE-2 (horizontal dashed line represents the depth to which the profile was defined).

expressed by

$$\theta_v = \frac{0.05 \text{ m}^3}{1.00 \text{ m}^3} \times 100\% = 5\% \tag{2.11}$$

The amount of water stored in the soil can vary in time and spatial coordinates, for examples, due to the infiltration or evaporation. Thus, instead of θ_v moisture content the $\Theta_v(x, y, z)$ moisture profile is used, which expresses the spatial distribution of water inside the soil.

Currently many methods are used to measure or to estimate the soil moisture profile as well as surface moisture mapping. Some of the measurement method are based on the coaxial cable, or used active and passive microwave remote sensing methods [126, 134–137] as well as GPR [138]. Moreover, the SAR is an important tool for surface and soil moisture retrieval [29, 139, 140]. Additionally to measurement methods, the analytical methods are applied to estimate the Θ_v in one-dimension [141, 142] or three-dimension [143]. In fact, the Θ_v should be identified with the water flow in porous media [144]. The water flow is usually described by the Richards' equation [145], which generally can be given by [87, 146–149]

$$\frac{\partial \Theta_v(t, \bar{r})}{\partial t} = \frac{\partial}{\partial \bar{r}}\left(h(t, \bar{r}) \frac{\partial \Theta_v(t, \bar{r})}{\partial \bar{r}}\right) + \frac{\partial K(t, \bar{r})}{\partial \bar{r}} + F(t, \Theta_v(t, 0)) \tag{2.12}$$

where $\Theta_v(t, \bar{r})$ is soil moisture profile, t is time, $\bar{r}$ is spatial coordinates, $F(t, \Theta_v(t, 0))$ is a source function accounting for water exchange process at the soil interface such as precipitation, evaporation and run-off. The $K(t, \bar{r})$ is hydraulic conductivity and $h(t, \bar{r})$ is soil water pressure head. Furthermore, both $K(t, \bar{r})$ and $h(t, \bar{r})$ are highly non-linear function of soil moisture, and are expresses as [87, 149]

$$K(\Theta_v) = K_s \left(\frac{\Theta_v(t, \bar{r})}{\Theta_s}\right)^{2b+3} \tag{2.13}$$

$$h(\Theta_v) = K(\Theta_v) \frac{\partial \Psi(\Theta_v)}{\partial \Theta_v} \tag{2.14}$$

where $\Psi(\Theta_v)$ is soil water tension, given by

$$\Psi(\Theta_v) = \Psi_s \left(\frac{\Theta_v(t, \bar{r})}{\Theta_s}\right)^{-b} \tag{2.15}$$

The K_s, Θ_s, Ψ_s and b are saturated hydraulic conductivity, saturated water content, saturated soil water tension and curve-filtering (shape) parameter, respectively, and all of these parameters depend on the soil types (textural class). Following [150, see Table 3], for each of these parameters the means and standard deviations are given for twelve soil types defined in USDA soil textural triangle.

Although the problem of the efficient and fast numerical solution of moisture profile is outside the scope of this dissertation, a simple finite difference method was used to calculate soil moisture profile only for one-dimensional vertical flow in depth (as in [87]). Thus, the Eq. 2.12 reduces to

$$\frac{\partial \Theta_v(t, z)}{\partial t} = \frac{\partial}{\partial z}\left(h(t, z) \frac{\partial \Theta_v(t, z)}{\partial z}\right) + \frac{\partial K(t, z)}{\partial z} + F(t, \Theta_v(t, 0)) \tag{2.16}$$

and now $K(t, z)$ and $h(t, z)$. The vertical water flow is calculated at z_n points, the same in which the soil texture was approximated (see Fig. 2.2). Moreover, three additional cases should be taken into account in the simulation, i.e., rainfall, evaporation coefficient and initial moisture profile. In general, the rainfall periods and monthly precipitation depend on the climate [151], thus the fairly realistic approximation, taking into account the variability

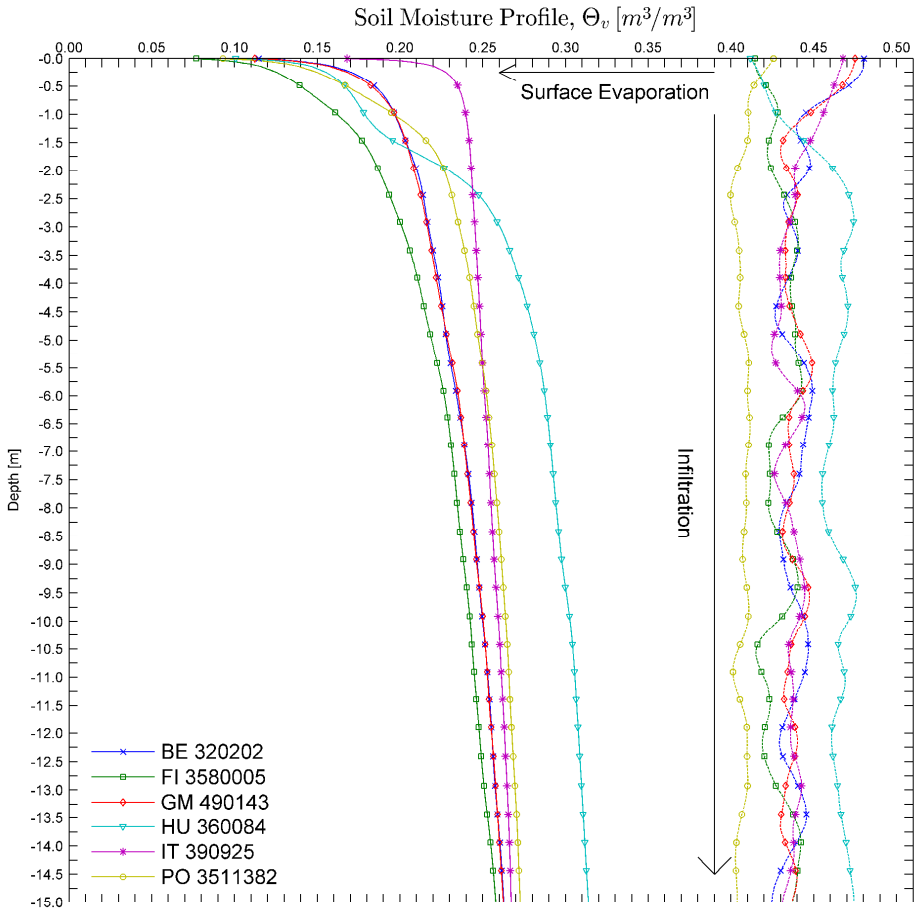

Figure 2.5 Simulated 1-D soil moisture profile for six STU profiles from SPADE-2.

of rainfall in time and its maximum value, is needed, however, it may be difficult to model. Furthermore, in the rainless periods, only evaporation from soil surface occurs, and it depends from temperature and wind. Various models of evaporation coefficient are presented in [152]. The influence of both rainfall and evaporation is included in the source function $F(t, \Theta_v(t, 0))$, which determines the soil non-homogeneity in the first layers. Finally, initial moisture profile must be well chosen for the simulation, i.e., adequately estimated for a given soil profile. Depending from the soil textural classes, the maximum amount of water theoretically possible to store differ significantly, and is limited by the Θ_s saturated water content or p porosity. Hence, the initial moisture profile in consecutive soil layers can be estimated based on those two quantities. Thus, namely in simulation, for each STU the initial moisture profile is assumed as a result of very long rainfall, and its value in consecutive layers is smaller than Θ_s. The simulation period equals $T_r = 4$ days, with simulation step $\Delta_{T_r} = 1$ s, and it was assumed as a rainless period occurring after very long rainfall. The evaporation coefficient was simply chosen as proportional to water content at the surface (similarly as in [87]). Although, these assumptions are very simply compared to real climatic conditions, they are acceptable enough for simulations.

The results of $\Theta_v(z)$ soil moisture profile simulation for six chosen STU profiles are shown in Fig. 2.5. The two sets of data are shown, and all plots are drawn down to 15.0 m. Firstly, the Θ_{init} initial moisture profiles were plotted with thin dashed lines. As can be seen, for all STU profiles the initial moisture profiles are smaller than 50 % and they reflected the inhomogeneous nature related to the soil structure. Due to the surface evaporation and infiltration into the soil (even below 15 m) the total water content decreases within the

time with respect to the hydrological properties as K_s, Θ_s, Ψ_s and b [150]. The numerically calculated Θ_v soil moisture profiles are plotted with solid lines. As it can be seen, the obtained profiles are smoothed compared to the initial ones. Only the *HU* 360084 retained curves in the initial layers. *FI* 3580005 and *PO* 3511382 are slightly curved, since other profiles were completely smoothed, where *BE* 320202 and *GM* 490143 are almost identical. Except the *HU* 360084, remaining profiles tend to a constant value with depth. Comparing both processes, i.e., surface evaporation and infiltration, the surface evaporation more strongly effects moisture profile since it is proportionally dependent to surface water. Evaporation interacts faster on the amount of water in the first layer (i.e., at surface) than infiltration rate causing water penetration down to the second layer. Infiltration mostly depends on hydraulic properties, especially on K_s (expressed in m/h or cm/s), that describes the speed with which a water can penetrate through porous soil.

2.1.3 Dielectric Properties

Up to day, several models or mixing equations of EM properties have been proposed for soil-water mixture [126, 153–163]. Besides the difference in the number of factors taken into account, these models are mostly based on the pedotransfer approach allowing the calculation of EM properties as a function of soil textural composition (c_l, s_d and ρ_b), Θ_v moisture profile, f frequency and T_c temperature. Hence, the pedotransfer modelling of EM properties can be expressed generally as

$$\left\{ \underbrace{[\, c_l,\ s_d,\ \rho_b,\ \Theta_v]}_{\text{from or based on SPADE-2}},\ f,\ T_c \right\} \ \Rightarrow\ \left\{ \varepsilon,\ \mu,\ \sigma \right\} \tag{2.17}$$

Pedotransfer function shows a mathematical relation between one or more measured soil parameters and non-measurable ones. Such modelling allows the translation of data available in geological database into EM properties.

The common areas of the aforementioned models and mixing equations are as following:

1. In all models, the emphasis is focused only on the ε permittivity and σ conductivity, while the μ permeability is assumed as for the free space, i.e., the relative permeability is assumed as a real value $\mu_r = 1$ and

$$\mu = \mu_r \mu_0 = \mu_0 \tag{2.18}$$

   where μ_0 is the permeability of free space and $\mu_0 = 4\pi \times 10^{-7}$ H/m [31].

2. Since soil is characterized as a lossy material, the ε_r relative permittivity is generally expressed in a complex form [31, 164–167]

$$\varepsilon_r = \varepsilon_r' - \varepsilon_r'' i \tag{2.19}$$

   Thus, the permittivity

$$\varepsilon = \varepsilon_r \varepsilon_0 = \varepsilon' - \varepsilon'' i \tag{2.20}$$

   where ε_0 is the permittivity of free space and from definition $\varepsilon_0 = \dfrac{1}{c^2 \mu_0} \approx 8.854 \times 10^{-12}$ F/m $\approx \dfrac{1}{36\pi} \times 10^{-9}$ F/m, and the speed of light in free space equals $c = 299792458$ m/s. Moreover, the ε_r' is defined as the relative dielectric constant of an equivalent lossless soil and ε_r'' is relative dielectric loss factor related to energy absorption by the moist soil [12, 126].

3. The frequency dependence of soil-water mixture is defined by the ε'_{fw} real and ε''_{fw} imaginary part of the relative dielectric constant of free water, $\varepsilon_{fw} = \varepsilon'_{fw} - \varepsilon''_{fw} i$, given by a Debye-type dispersion equation [156, 160, 161, 167, 168]

$$\varepsilon'_{fw} = \varepsilon_{w\infty} + \frac{\varepsilon_{w0} - \varepsilon_{w\infty}}{1 + (2\pi f \tau_w)^2} \tag{2.21}$$

$$\varepsilon''_{fw} = 2\pi f \tau_w \frac{\varepsilon_{w0} - \varepsilon_{w\infty}}{1 + (2\pi f \tau_w)^2} + \frac{\sigma_w}{2\pi \varepsilon_0 f} \tag{2.22}$$

where ε_{w0} is low-frequency limit of permittivity for water, $\varepsilon_{w\infty}$ is the high-frequency limit of ε'_{fw}, τ_w is relaxation time of free water, f is the frequency in hertz and σ_w is conductivity of water. According to [154], for a soil-water mixture $\varepsilon_{w\infty}$ is assumed to vary with Θ_v water profile and p porosity as follows

$$\varepsilon_{w\infty} = \varepsilon_{rock}(1 - p) + \varepsilon_a(p - \Theta_v) + 4\Theta_v \tag{2.23}$$

where $\varepsilon_{rock} \approx 5.0$ and $\varepsilon_a = 1$ are dielectric constant of rocks and air, respectively.

4. The temperature dependence of soil-water mixture is given by the temperature relationship of ε_{w0} and τ_w as follows [126, 169]

$$\varepsilon_{w0}(T_c) = 88.045 - 0.4147\ T_c + 6.295 \times 10^{-4}\ T_c^2 + 1.075 \times 10^{-5}\ T_c^3 \tag{2.24}$$

$$2\pi\ \tau_w(T_c) = 1.1109 \times 10^{-10}\ -\ 3.824 \times 10^{-12}\ T_c\ +\ 6.938 \times 10^{-14}\ T_c^2\ +\ 5.096 \times 10^{-16}\ T_c^3 \tag{2.25}$$

and at room temperature ($T_c = 20$ °C), $\varepsilon_{w0} \approx 80.1$ and $\tau_w \approx 9.2764 \times 10^{-12}$ s.

5. The σ conductivity of soil is considered as a complex value [31, 170]

$$\sigma(\omega) = \sigma'(\omega) + \sigma''(\omega) i \tag{2.26}$$

but this approach is rarely used. Mostly in GPR frequency, the σ is assumed as real and frequency-independent value. Thus, the σ equals

$$\sigma(\omega) = \sigma_{dc} \tag{2.27}$$

where σ_{dc} is static conductivity. Hoverer, the σ_{eff} complex effective conductivity [171] equals

$$\sigma_{eff}(\omega) = \sigma_{dc} + \omega \varepsilon_0 \varepsilon''_r - \omega \varepsilon_0 \varepsilon'_r i \tag{2.28}$$

6. Additionally, to marriage the polarization loss and conductivity loss, the σ is incorporated into imaginary part of ε_r complex dielectric constant, thus Eq. 2.19 changes as follows

$$\varepsilon_r(\omega) = \varepsilon'_r(\omega) - \left(\varepsilon''_r(\omega) + \frac{\sigma_{dc}}{\varepsilon_0 \omega}\right) i \tag{2.29}$$

where ω is the angular frequency measured in radians per second. Eq. 2.29 is refereed as the *complex relative effective permittivity* (CREP) [31, 171], due to the fact that it combines the relative dielectric constant ε'_r of an equivalent lossless medium as well as the polarization loss ε''_r and conductivity loss σ_{dc}. Therefore, the *complex effective permittivity* is

$$\varepsilon(\omega) = \varepsilon_0\ \varepsilon_r(\omega) = \varepsilon'(\omega) - \left[\varepsilon''(\omega) + \frac{\sigma_{dc}}{\omega}\right] i \tag{2.30}$$

and the loss tangent becomes [167]

$$\tan\delta = \frac{\omega\varepsilon_0\varepsilon_r'' + \sigma_{dc}}{\omega\varepsilon_0\varepsilon_r'} \tag{2.31}$$

While the (1)-(6) (Eq. 2.18 - Eq. 2.31) accentuate only the main objectives of EM properties modelling, the exact equations defining the complex dielectric constant and conductivity has been developed by Wang (1980, based on Schwarz model from 1962) [154], Hallikainen *et al.* (1985) [156, 157], Peplinski *et al.* (1995) [159]. These models give both real and imaginary part of complex relative permittivity as a function of f frequency and Θ_v water content. Moreover, Hallikainen *et al.* and Peplinski *et al.* models clearly show the relationship to the soil texture (c_l, s_t, s_d and ρ_b). The Schwarz-Wang and Hallikainen *et al.* models are developed for $f > 1.4$ GHz, since Peplinski *et al.* model is developed and fitted to 0.3 GHz – 1.3 GHz frequency range. Additionally, both Schwarz-Wang and Peplinski *et al.* model have been widely used in many fields. For instance, the Schwarz-Wang was used model for determination of soil moisture profile as a function of depth [136, 172] and study on the penetration depth in realistic model of dielectric constant [87]. On the other hand, Peplinski *et al.* model was used, for instance, for prediction of soil effects on GPR signature [53], for studies on thermal properties of soil [173], for retrieval the effects of salinity on the dielectric properties of geological materials [174] and for studies on the effects of bulk density on soil emission at microwave frequency [175]. For these reasons, the Peplinski *et al.* model has been chosen for dielectric constant modelling, it allows the calculation of both parts of the ε_r in wide GPR frequency range, i.e., the whole UHF band and the lower part of L band, and the information about soil texture (Section 2.1.1) and moisture profile (Section 2.1.2), can be easily applied. However, it should be noted that the Peplinski *et al.* model does not take into account the changes of dielectric properties with bound water [29]. To improve it, the Mineralogically Based Spectroscopy Dielectric Model (MBSDM) was developed by Mironov (2009) [161], which has a higher validity range than empirical models.

Besides that, since the moisture effects the dielectric properties of soil, the moisture profile can be predicted using dielectric properties [126, 176]. Thus, it shows a strong relationship between soil moisture profile and dielectric properties. Moreover, similarly to moisture retrieval from SAR data, the permittivity and conductivity can be measured using transmission line technique [177] or estimated from GPR data [178].

Complex dielectric constant in 0.3 GHz - 1.3 GHz range

The Peplinski *et al.* model [159] is based on the semi-empirical dielectric model for soil-water mixture developed by Hallikainen *et al.* [156, 157]. Since Hallikainen *et al.* model is defined in 1.4 GHz – 18.0 GHz frequency range, the Peplinski *et al.* model was modified and fitted to 0.3 GHz – 1.3 GHz frequency range over 19 sets of distinctive soil conditions and with linear correlation coefficient of 0.985. In relation to [156, 157], in [159] the simple linear adjustment of ε_r' and a new empirically expression for $\sigma_{dc,eff}$ effective static conductivity is added.

According to [159], the ε_r' real and ε_r'' imaginary part of complex dielectric constant ε_r (Eq. 2.19) are given by

$$\varepsilon_r' = 1.15\Big[1 + \frac{\rho_b}{\rho_s}(\varepsilon_s^{\zeta_P} - 1) + \Theta_v^{\beta'}\varepsilon_{fw}'^{\zeta_P} - \Theta_v\Big]^{\frac{1}{\zeta_P}} - 0.68 \tag{2.32}$$

$$\varepsilon_r'' = \Theta_v^{\frac{\beta''}{\zeta_P}}\ \varepsilon_{fw}'' \tag{2.33}$$

respectively. Where ρ_b is soil bulk density, ρ_s= 2.66 g/cm^3 is the specific density of the solid soil particles (assumed constant for all soil types), ζ_p= 0.65 is an empirically determined constant[2] and Θ_v is soil moisture profile (Eq. 2.16). The β' and β'' are empirically determined soil-type dependent constants given by

$$\beta' = 1.2748 - 0.519\ s_d - 0.152\ c_l \tag{2.34}$$

$$\beta'' = 1.33797 - 0.603\ s_d - 0.166\ c_l \tag{2.35}$$

where s_d and c_l are percentages content of sand and clay, respectively. Moreover, in Eq. 2.32, ε_s is the dielectric constant of soil particles (rocks), and is given by the empirical model

$$\varepsilon_{rock} \approx \varepsilon_s = (1.01 + 0.44\rho_s)^2 - 0.062 \tag{2.36}$$

ε'_{fw} and ε''_{fw} are given by Eq. 2.21 and Eq. 2.22, respectively, but now σ_w in Eq. 2.22 is changed by (taking into account the p porosity given by Eq. 2.8)

$$\sigma_w = \sigma_{eff}\ \frac{\rho_s - \rho_b}{\rho_s \Theta_v} = \sigma_{eff}\ p\ \Theta_v^{-1} \tag{2.37}$$

where

$$\sigma_{eff} = 0.0467 + 0.2204\ \rho_b - 0.4111\ s_d + 0.6614\ c_l \tag{2.38}$$

Hence, substitution Eq. 2.22 into Eq. 2.33, with taking into account Eq. 2.37, leads to

$$\varepsilon''_r = \frac{\omega\tau_w(\varepsilon_{w0} - \varepsilon_{w\infty})}{1 + (\omega\tau_w)^2}\Theta_v^{\frac{\beta''}{\zeta_P}} + \frac{\sigma_{eff}\ p\ \Theta_v^{\frac{\beta''}{\zeta_P}-1}}{\varepsilon_0\omega} \tag{2.39}$$

where $\omega = 2\pi f$. Comparing Eq. 2.39 with the imaginary part of Eq. 2.29, the imaginary part of complex relative permittivity, ε''_r, and conductivity, σ, equal

$$\varepsilon''_r = \frac{\omega\tau_w(\varepsilon_{w0} - \varepsilon_{w\infty})}{1 + (\omega\tau_w)^2}\Theta_v^{\frac{\beta''}{\zeta_P}} \tag{2.40}$$

$$\frac{\sigma_{dc}}{\varepsilon_0\omega} = \frac{\sigma_{eff}\ p\ \Theta_v^{\frac{\beta''}{\zeta_P}-1}}{\varepsilon_0\omega} \tag{2.41}$$

Those two equations, along Eq. 2.32, represent the EM properties of soil structure, with the assumption that $\mu_r = 1 - 0i$. Therefore, the real part of CREP (Eq. 2.29) is defined by Eq. 2.32, and the imaginary part is defined by the sum of Eq. 2.40 and Eq. 2.41.

Presented model, Eq. 2.32 - Eq. 2.36 [159], and with regard to Eq. 2.21 - Eq. 2.25, clearly shows the dependence of ε_r on soil texture, moisture profile, frequency and temperature as well as the dependence of σ_{dc} on soil texture and moisture profile. Since both the soil texture and moisture profile can be expressed as a function of depth, i.e., $c_l(z)$ (Eq. 2.4), $s_d(z)$ (Eq. 2.5), $\rho_b(z)$ (Eq. 2.6) and $\Theta_v(z)$ (Eq. 2.16), the quantities in Peplinski *et al.* model can be also defined as a function of depth. Hence, the CREP $\varepsilon_r(z, f)$ (Eq. 2.29) can be expressed as

$$\varepsilon_r(z, f) = \varepsilon'_r(z, f) - \left[\varepsilon''_r(z, f) + \frac{\sigma_{dc}(z)}{2\pi f\varepsilon_0}\right]i \tag{2.42}$$

[2]Originaly, it is denoted as α. Here, is changed to ζ_P, since α denotes the attenuation coefficient (in Eq. 2.82)

Table 2.1 Comparison of the CREP in first layer.

STU Profile	f_{min} 300 [MHz]	f_c 800 [MHz]	f_{max} 1300 [MHz]	R_{ε_r} [−]
BE 320202	7.3599-1.7387i	7.3530-0.7312i	7.3399-0.5425i	-0.0200+1.1961i
FI 3580005	8.9179-1.2319i	8.9098-0.5643i	8.8945-0.4668i	-0.0233+0.7651i
GM 490143	5.8423-1.6882i	5.8374-0.6839i	5.8279-0.4802i	-0.0145+1.2079i
HU 360084	9.4783-2.5883i	9.4687-1.0984i	9.4503-0.8252i	-0.0279+1.7631i
IT 390925	9.1743-4.4159i	9.1640-1.7859i	9.1445-1.2508i	-0.0298+3.1652i
PO 3511382	9.9933-1.7025i	9.9834-0.7709i	9.9646-0.6292i	-0.0287+1.0732i

Therefore, the $\varepsilon(z,f)$ *complex effective permittivity* is defined as

$$\varepsilon(z,f) = \varepsilon_0\ \varepsilon_r(z,f) = \varepsilon'(z,f) - \left[\varepsilon''(z,f) + \frac{\sigma_{dc}(z)}{2\pi f}\right] i \tag{2.43}$$

While $\sigma_{dc}(z)/(2\pi\varepsilon_0 f)$ varying strongly in the considered frequency range, compared to $\varepsilon''(z,f)$, the results of *complex relative permittivity* modelling, instead of *complex relative effective permittivity*, for the six chosen STU profiles based on Peplinski *et al.* model, are shown in Fig. 2.6 for $\varepsilon'(z,f)$ and in Fig. 2.7 for $\varepsilon''(z,f)$. Due to the fact that $\sigma_{dc}(z)$ is frequency-independent, it will be discussed later ($\sigma_{dc}(z)$ is shown in Fig. 2.9c). In these figures, the z depth vector is given by Eq. 2.2 (Section 2.1.1), and the f frequency vector is simply defined in 0.3 GHz − 1.3 GHz range over N_f= 2001 uniformly spaced points, with the frequency step Δf= 0.5 MHz. The T_c temperature of the soil has been assumed constant in z depth, $T_c(z)$ = 20 °C. The results are drawn just down to depth of 3.0 m and for comparison the plots on each figure are represented in the same colour scale. The vertical lines represent the frequency band of the three airborne systems compared in Tab. 1.1 (Section 1.2), whose bandwidth completely lies in the range of applicability of the Peplinski *et al.* model. The Radar2 is marked with maroon lines, the Radar3 is marked with dark green lines and the Radar4 is marked with grey lines. Moreover, the centre frequency of 800 MHz is marked with white dashed line. Additionally, the plots include the area above the ground $z > 0.0$ m, which represent the air (free space) where ε_r= 1.0 − 0i, i.e, $\varepsilon_r'' = 0$ and $\sigma_{dc} = 0$. Comparing all plots in both figures, the difference between free space and first layer are evident, in particular, in the case of ε_r' (Fig. 2.6). The values of real and imaginary part of *complex relative permittivity* in the first layer are marked at each plots (see black dots) for 800 MHz. Moreover, Fig. 2.8 shows the $\varepsilon'(f)$, $\varepsilon''(f)$ and $\sigma_{dc}/(2\pi\varepsilon_0 f)$ of the first soil layer in considered frequency range, i.e., for $z \in [0.0, -h_0)$. The value of the CREP in the first layer for 300 MHz, 800 MHz and 1300 MHz were presented in Tab. 2.1 for the chosen STU profiles. The joint change of ε_r' real and ε_r'' imaginary part of the ε_r in given frequency range are expressed by the R_{ε_r} change ratio, defined in complex form by

$$R_{\varepsilon_r} = \Delta\varepsilon_r'(f_{max}, f_{min})\ + \Delta\varepsilon_r''(f_{max}, f_{min})i \tag{2.44}$$

where f_{min} and f_{max} is minimum and maximum frequency, respectively. Thus, for BE 320202, the R_{ε_r} equals

$$R_{\varepsilon_r} = (7.3399 - 7.3599)\ + (-0.5425 - (-1.7387))i \approx -0.0200\ + 1.1961i \tag{2.45}$$

Relative changes of both parts of the ε_r in the assumed frequency range differ considerably between STU profiles. An analysis of Fig. 2.6, Fig. 2.7, Fig. 2.8 and Tab. 2.1 gives the following observations:

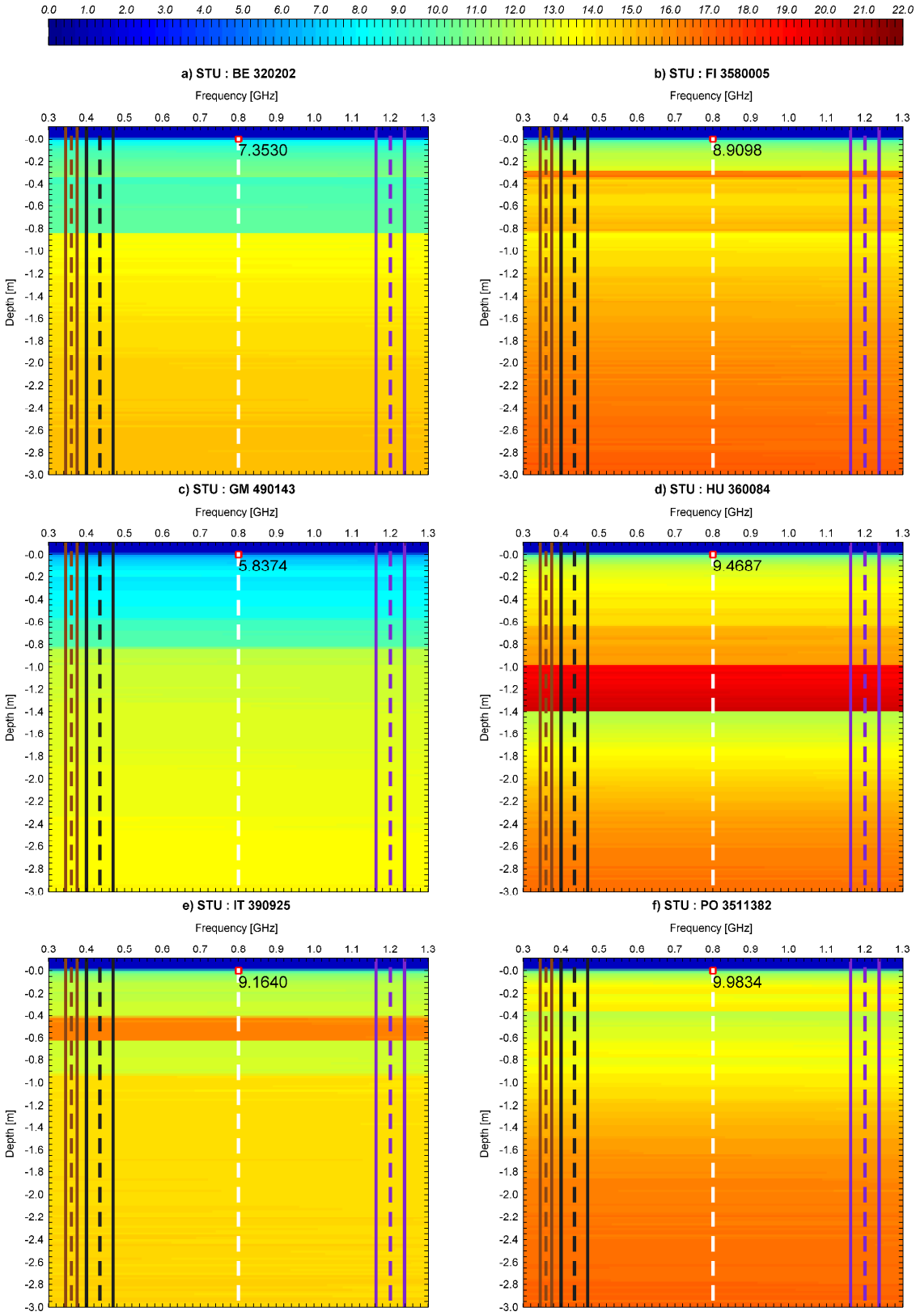

Figure 2.6 Comparison the results of $\varepsilon'_r(z, f)$ real part of CREP (Eq. 2.19) as a function of z depth and f frequency for the six STU profiles using the mode of Peplinski *et al.*

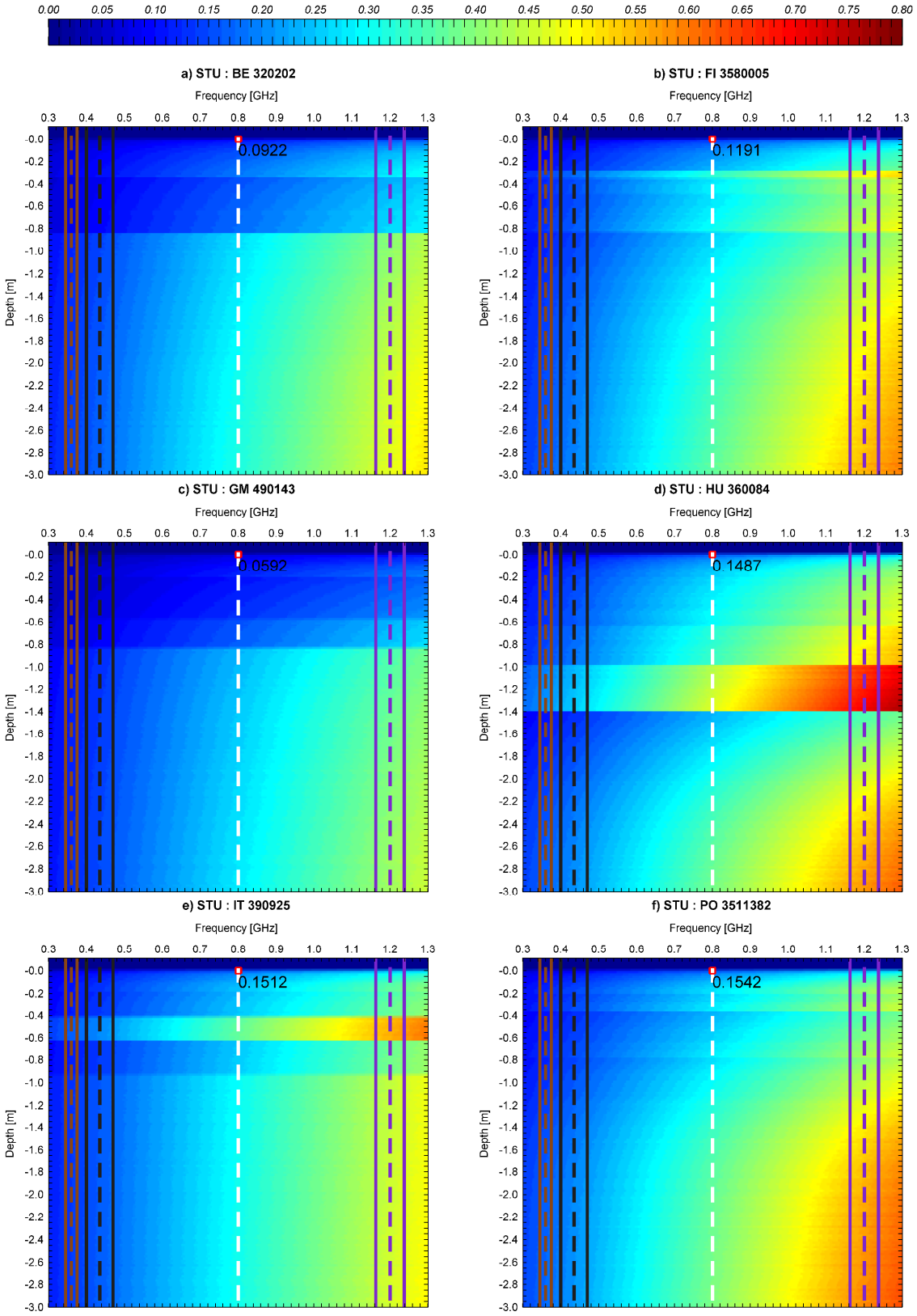

Figure 2.7 Comparison the results of $\varepsilon_r''(z, f)$ imaginary part of CREP (Eq. 2.19) as a function of z depth and f frequency for the six STU profiles using the mode of Peplinski *et al.*

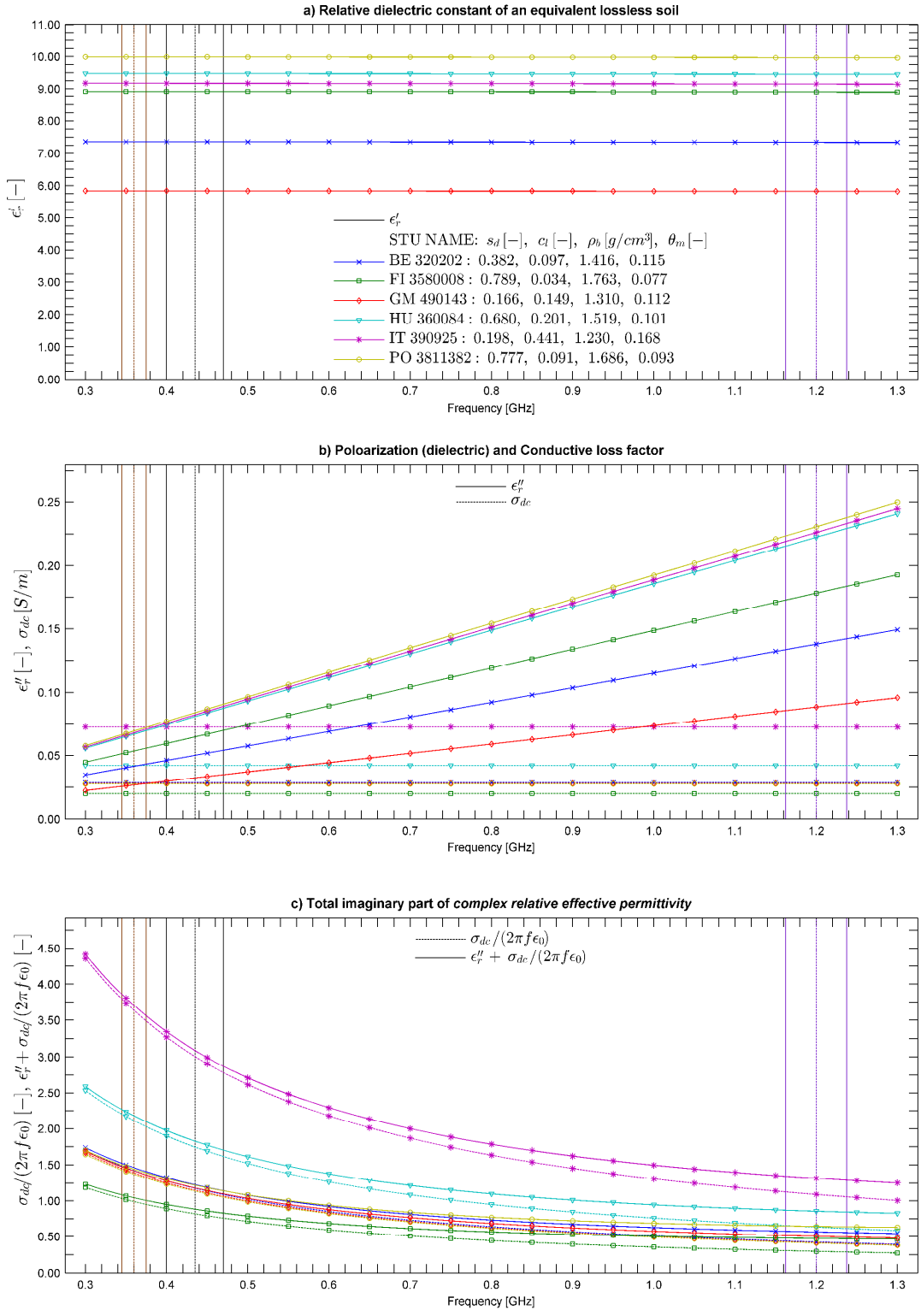

Figure 2.8 Comparison the results of $\varepsilon'(f)$, $\varepsilon''(f)$ and $\sigma_{dc}/(2\pi\varepsilon_0 f)$ of the first soil layer ($z \in [0.0, -h_0)$) in considered frequency range for the six STU profiles using the mode of Peplinski *et al.*

- In general, the horizontally layered nature of ε'_r (Fig. 2.6) and ε''_r (Fig. 2.7) is maintained in relation to the geological horizons (compare with Fig. 2.4).
- In depth dimension, based on results for all profiles it can be said that the shape of the complex relative permittivity for a given frequency can be described as a process, the

shape of which being similar to the shape of Θ_v soil moisture profile, but it amplitude is modulated by the soil composition, i.e., relations between the s_d and c_l as well as the ρ_b. According to Eq. 2.34 and Eq. 2.35, the s_d sand content have a greater effect on ε_r than c_l clay content.

- Furthermore, the dependence on the frequency is also visible, clearly in the case of ε_r'' and less for ε_r'. According to Fig. 2.8 and Tab. 2.1 the ε_r' decreases slightly at the level of a few hundredths, while the ε_r'' increase more significantly at the level of a few tenths. Thus, variability of both parts of the ε_r shows dispersive and loss nature of soil, which is not uniform. The non-zero value of $\Delta\varepsilon_r'$ indicates the dispersion affecting the EM waveform. Frequency-dependent attenuation (non-uniform energy absorption in frequency domain) is represented by the relatively high value of $\Delta\varepsilon_r''$.

In addition to Fig. 2.6, Fig. 2.7 and Fig. 2.8, the two parts of the ε_r as well as σ_{dc} were plotted in Fig. 2.9, only in depth dimension, down to $z = 3.0$ m and for constant frequency $f_c = 800$ MHz (along white lines in these figures). The ε_r' is defined by Eq. 2.32, and ε_r'' is defined by Eq. 2.40. As results from Eq. 2.41, σ_{dc} is frequency independent. Now, the relationship between the geological soil horizons (and their inner textural compositions) (Fig. 2.2), the soil moisture profile (Fig. 2.5) and the ε_r complex dielectric constant as well as σ_{dc} static conductivity is clearly visible. As stated before, the shape of both parts of the ε_r reproduce the shape of the Θ_v moisture profile. Moreover, the amplitude is determined by mutual relation between the s_d and c_l. Further, as follows from Eq. 2.32 and Eq. 2.39, the ε_r' is more influenced by the textural composition than ε_r''. Since the soil texture only affects ε_r'' through β'' (Eq. 2.35), ε_r' is affected through β' (Eq. 2.34) and ρ_b bulk density. When the Θ_v moisture profile (Fig. 2.5) is completely monotonically increasing function, i.e., the moisture content increases when depth increases, the ε_r shows piecewise nature of length associated with the height of consecutive soil horizons. Moreover, in Fig. 2.9 the height of first layer h_0 is marked as well as the free space above the ground $z > 0.0$ m where $\varepsilon_r = 1.0 - 0i$. Now, the dielectric contrast between free space and soil surface is more visible. In fact, this contrast effects on the surface reflection coefficient. While, the higher reflection coefficient is desired for conventional surface imaging systems, for subsurface imaging its higher value results in less amount of energy that can penetrate into the soil. Therefore, although the moisture profile can have unlimited shape in natural environment, it seems desirable that in the near subsurface layers the moisture profile should slightly increase from dry (about 5 %) at surface down to its natural value. Thus, the slight change of the ε_r between air and surface (low EM reflection coefficient), as well as between near-surface layers, will results in the high EM transmission coefficient of energy into the soil. As following from Eq. 2.41 (and Eq. 2.38), the static conductivity σ_{dc} (Fig. 2.9c) is strongly associated with sand s_d and clay c_l content. The *FI* 3580005 has the dominant s_d content in all horizons, in which it is defined (Fig. 2.2b), thus, it has the lowest σ_{dc}. On the other hand, the *IT* 390925 has dominant c_l content, hence its σ_{dc} is the higher.

Similarly to the approximated soil structures presented in Fig. 2.4, the results of $\varepsilon_r(z, f)$ modelling (see Eq. 2.42) are duplicated in both x along and y across dimension as follow:

$$\varepsilon_r(x, y, z, f) = \varepsilon_r(z, f) \tag{2.46}$$

and shown in Fig. 2.10. As before, the results are drawn down just to depth of 3.0 m and in the same colour scale, but now they are presents for one frequency $\varepsilon_{r,f}(x, y, z) = \varepsilon_r(x, y, z, f)$, since Eq. 2.46 is four-dimensional. For differentiation, the a) *BE* 320202 and b) *FI* 3580005 show the $|\varepsilon_r|$ for $f_c = 360$ MHz (Radar2, the dashed maroon lines in Fig. 2.6 and Fig. 2.7). The $|\varepsilon_r|$ for $f_c = 435$ MHz (Radar3, the dashed green lines) is shown in c) *GM* 490143 and d) *HU* 360084, and the e) *IT* 390925 and f) *PO* 3511382 show the $|\varepsilon_r|$ for $f_c = 1200$ MHz

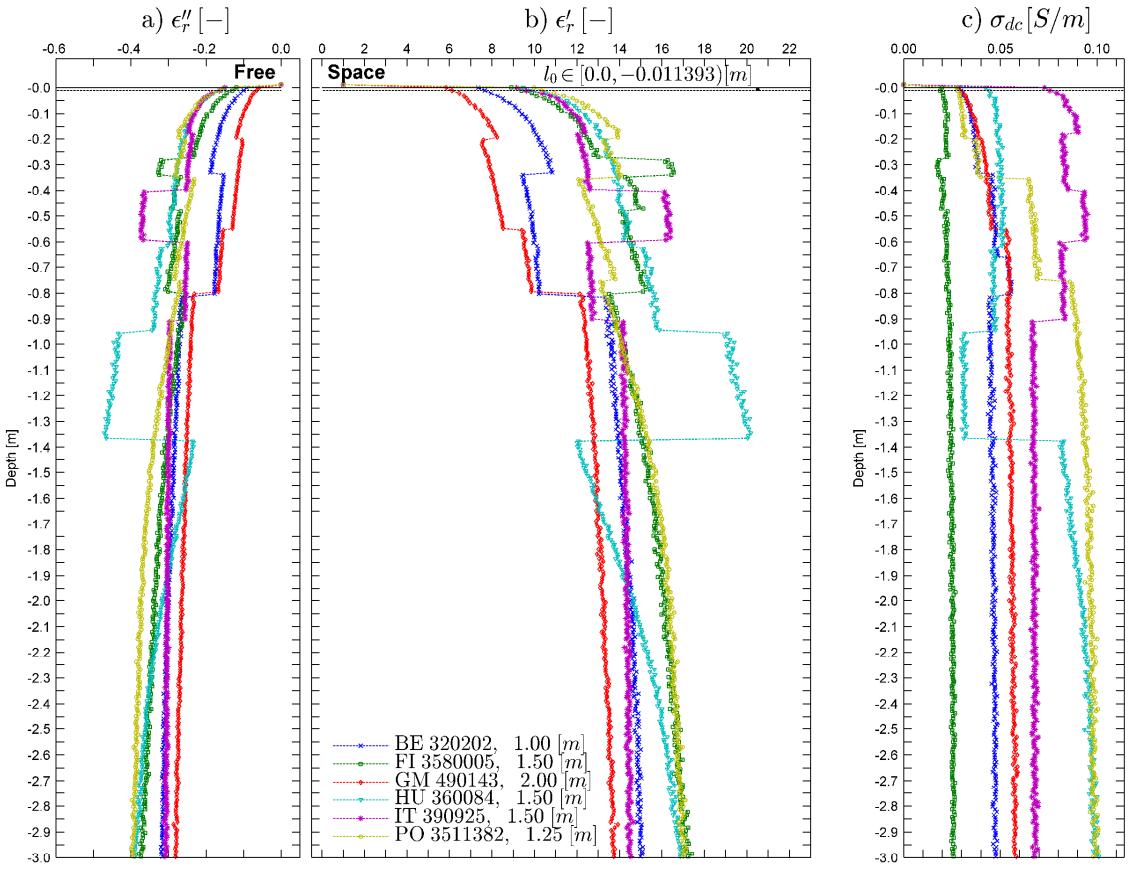

Figure 2.9 Comparison the results of modelling of the a) $\varepsilon_r''(z)$ and b) $\varepsilon_r'(z)$ of the soil complex dielectric constant, and c) $\sigma_{dc}(z)$, as a result of z depth, for $f = 800$ MHz and the six STU profiles using the mode of Peplinski *et al.*

(Radar4, the dashed grey lines). Additionally, value of the ε_r in the first layer is given at the top of structure. Comparison of Fig. 2.10 and Fig. 2.4 shows that the structure of the relative permittivity is not totally equivalent to the geological structure represented in colour scale. The soil colour indicates only the textural information, and slight changes in soil composition within the same soil horizon (which are invisible in Fig. 2.4) firstly results in different moisture content and then in the changes of dielectric constant.

2.1.4 Summary

Presented in this section, considerations on modelling of the soil EM nature are based on the assumption that textural composition of the soil affects both the soil moisture profile and EM properties. Thus, the pedotransfer (geologically- and hydrologically-motivated) approach is applied to calculate the complex relative permittivity and conductivity of soil structure, which both are recognized as complex relative effective permittivity (CREP). Firstly the real geological information, stored in the SPADE-2 database, has been used for the approximation of soil layered structure with an uniform height of the successive layers and with a random inner soil composition. However, to improve the soil structure interpolation in assumed grid the geophysics based interpolation method, like Inverse Distance Weighting, or Kriging based interpolation might be used. The empirical model proposed by Peplinski *et al.* was used for calculation of the EM properties in GPR frequency range (0.3 GHz – 1.3 GHz) and down to the sufficient depth of 15.00 m, which is much greater than the assumed maximum depth of subsurface imaging.

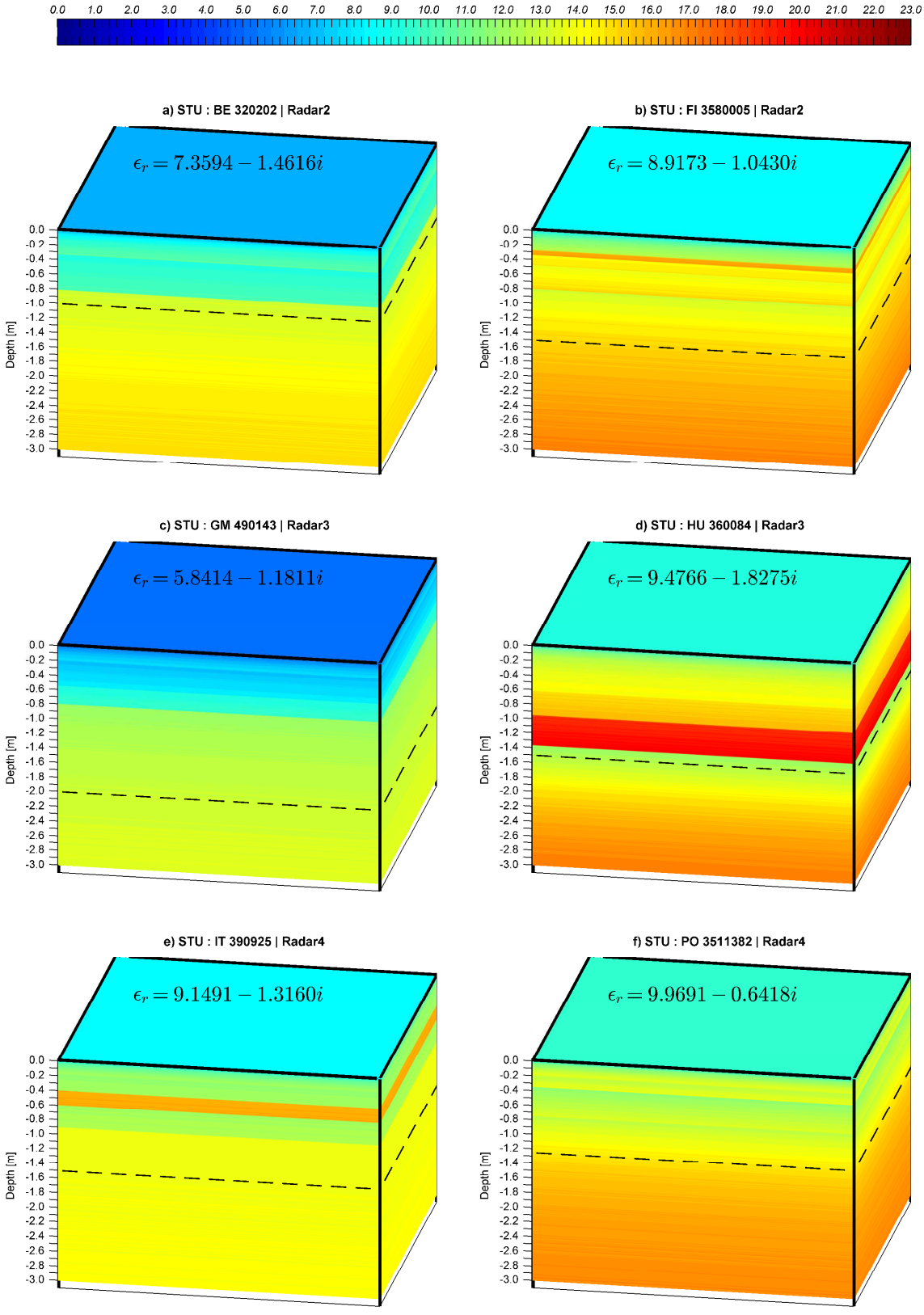

Figure 2.10 Three-dimensional approximation of the $|\varepsilon_r|$ CREP of soil structures created based on the chosen STU profiles from SPADE-2 (for comparison, see Fig. 2.4).

The obtained results clearly show that the geological structure is not fully tantamount to the structure of complex dielectric constant, and moisture profile is a parameter which links geological and EM nature of soil. Therefore, the exact information about the geological nature of the soil can be a key parameter for microwave subsurface imaging, in particular, performed on a large scale from the airborne platforms over non-arid areas. Moreover, as depicted in Fig. 2.10, the EM soil structure is not monotonic volume, wherein the permittivity constantly increasing with changing step in depth dimension up to a fixed constant value, but rather the non-periodical structure, in which permittivity significant changes between successive horizons (causing a not negligible discontinuity at the border of the following horizons).

2.2 Airborne Subsurface Imaging Geometry

Compared to the satellite-borne SAR and ground-based GPR platforms, the airborne platform provides high reconfigurability and vast, purpose-dependent area for imaging of an optically invisible soil structure. In addition, the imaging process may be repeated several times in short periods, with various radar features (carrier frequency and band, polarization) and/or at different geometry (different height and look angle). Thus, assuming a high stability and also repeatability of airborne platform trajectory, the imaging process over the area under investigation can be carried out as conventional SAR acquisition, or extended with additional acquisitions and leading to InSAR or Pol-InSAR processing.

Overall, from the geometrical point of view, the AGPR imaging configuration is based on the SLAR configuration, with typical parameters of radars used in conventional airborne SAR mission (presented in Tab. 1.1). The key difference lies in a different purposes of observation [124]. Classical airborne SAR systems are devoted to imaging the terrain surface and a typical high-resolution SAR image represents only a directional (backscattered) reflectivity of the terrain surface. On the other hand, AGPR intends to image the optically invisible soil structure located under the surface and process backscattered terrain returns as clutter, which blurs the image. Fig. 2.11 presents an adequate geometry of a AGPR mission (in SLAR, broadside Stripmap SAR with zero squint angle) with an example location of typical objects buried in the soil. The AGPR subsurface imaging mission is performed at height H_p of several thousands of meters, where $H_p \gg h_n \ \forall \ n$, where n is the index of l_n layer (see Section 2.1.1), and $H_p \gg Z_{max}$; along the straight and parallel to Earth surface line with υ_p velocity and at θ_i oblique incidence over the distance L_S in the flight time T_S. The Earth is assumed as locally flat. The real antenna of length L_R, with 3dB azimuth θ_{az} and 3dB elevation θ_{el} beam-width, is oriented at an incident angle θ_i. The antenna gain G_a equals [11,13]

$$G_a = \frac{4\pi}{\theta_{az}\theta_{el}}\alpha_a^2 \tag{2.47}$$

where θ_{az} and θ_{el} are in radians and $\alpha_a = 0.88$ is the antenna factor providing -13 dB peak sidelobe level. When $\alpha_a = 1.30$ gives the -45 dB, but then the antenna dimensions increases, that it is impractical and decreases the theoretical azimuth resolution. The grazing angle ψ_g, defined between the line of sight and ground plane, equals $\psi_g = \frac{\pi}{2} - \theta_i$, the near slant range to swath is R_{sn} and the far slant range is R_{sf}. The area of the footprint at the ground, A_F (shown in Fig. 2.12(a)), defined by the intersection of the antenna beam in ground plane, depends on R_{sc} slant range to swath centre, 3dB antenna beam-width in θ_{az} azimuth and θ_{el} elevation as well from ψ_g grazing angle. The size of footprint on the soil surface is defined as [13]

$$A_{F,a} = R_{sc}\theta_{az} \tag{2.48}$$

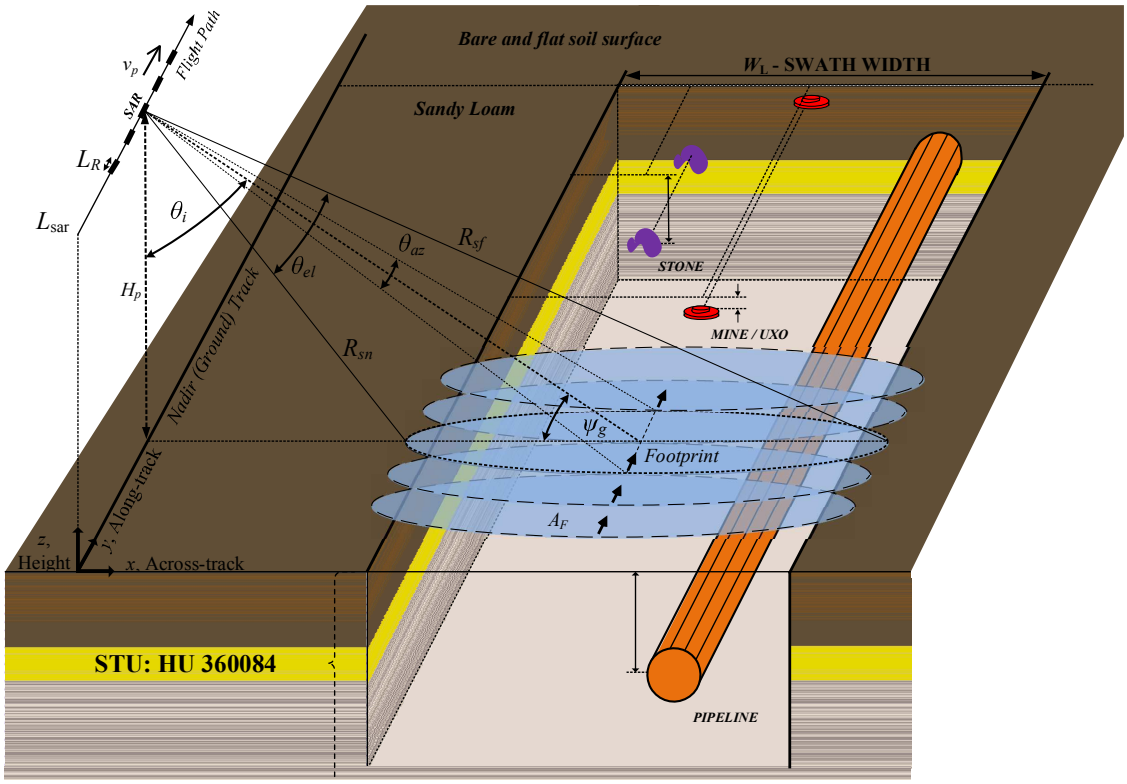

Figure 2.11 The airborne subsurface imaging geometry over flat and bare soil surface (*sandy loam*) of approximated soil structure (based on STU *HU* 360084) with typical objects buried at different depths and locations: pipeline, stone and mine.

$$A_{F,e} = R_{sc}\theta_{el}\csc\psi_g = \frac{R_{sc}\theta_{el}}{\sin\psi_g} \tag{2.49}$$

in the $A_{F,a}$ azimuth and $A_{F,e}$ ground direction, respectively. The T_{dwell} dwell time at R_{sc} centre slant range equals (see Eq. 1.14)

$$T_{dwell}^{R_{sc}} = \frac{\lambda R_{sc}}{\upsilon_p L_R} \tag{2.50}$$

meaning that the target located on soil surface in the middle of L_S will be exposed in $T_{dwell}^{R_{sc}}$ seconds ($T_{dwell}^{R_{sc}}$ is also referred to as the exposure time). The ΔR slant range resolution, which proportional to τ pulse duration, equals $\Delta R = c\tau/2$, and pulse stretch on the ground (shown in Fig. 2.12(b)) equals

$$\Delta R_g = \frac{\Delta R}{\cos\psi_g} \tag{2.51}$$

which decreases with decreasing ψ_g (increasing θ_i). For modern SAR systems, which transmit a chirp signal, the $\Delta R = c/(2B_f)$ is inversely proportional to the pulse bandwidth B_f. During an acquisition along the L_S and over bare and flat terrain surfaces, the AGPR system observes swath about W_L width and length dependent on the acquisition (or mission) time. The low PRF_{low} and high PRF_{high} limit of PRF is given by [4, 12]

$$PRF_{low} = \frac{v_p}{L_R/2} \tag{2.52}$$

$$PRF_{high} = \left[2\tau + 2\frac{R_{sf} - R_{sn}}{c}\right]^{-1} \tag{2.53}$$

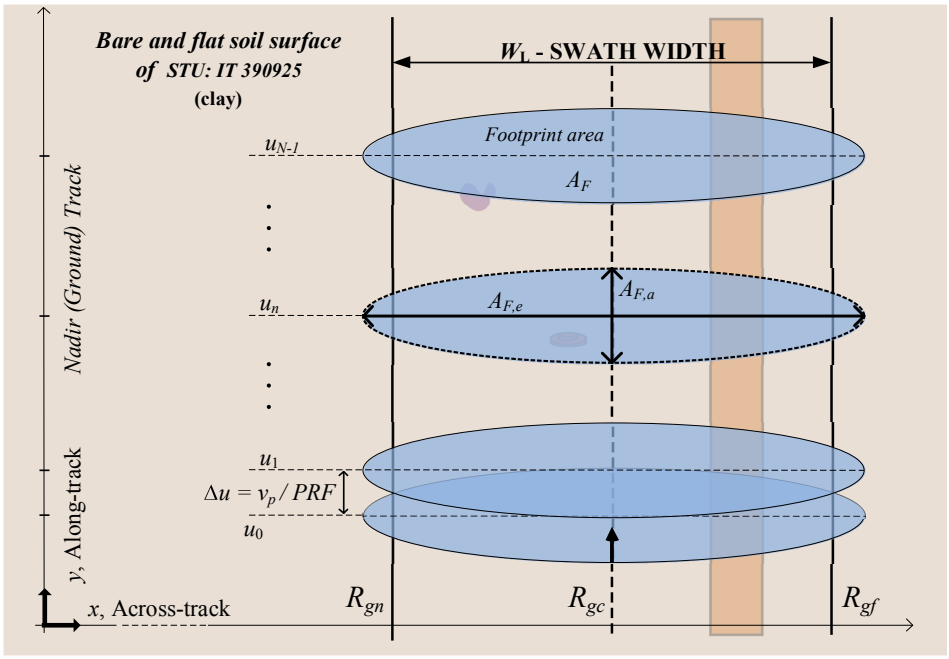

(a) Ground-plane xy view

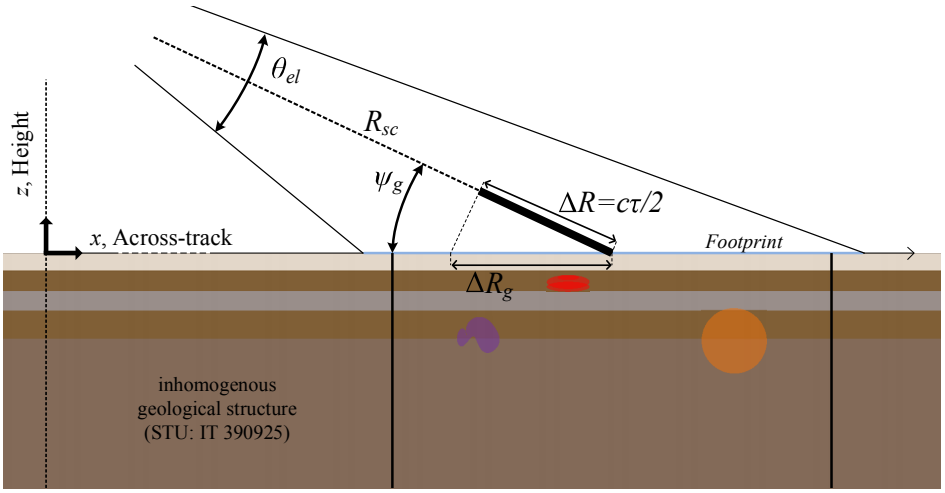

(b) Elevation xz view

Figure 2.12 The airborne subsurface imaging geometry in ground and elevation plane (soil structure is approximated based on STU *IT* 390925).

which means that the radar should send the next pulse before moving half of the along-track antenna length (Eq. 2.52), moreover, the leading edge of $u+1$ transmitted pulse cannot reach a near swath range R_{sn} before the travelling edge of u pulse reached a far slant range R_{sf} (Eq. 2.53). In other words, in the observed area, between R_{sn} and R_{sf}, only one pulse can propagate to avoid range ambiguity.

The soil structure in Fig. 2.11, created based on STU *HU* 360084 (Fig 2.4d), contains three types of usual objects located at typical depths for each. Anti-personnel mines are mostly placed just below the surface, pipelines (or underground installations) are usually located down to several meters and stones (or rocks) which can lie at every depth. Such objects have their own dielectric constants, defined by the material from which they are

made (see [31, Table 2.1] for instance). Moreover, as stated early, the soil discontinuities and underground water tanks are natural scatterers inside its structure. For simplicity, only one approximated geological soil structure from Fig. 2.4 is shown in Fig. 2.11. Although all created structures have the same number of layers, i.e., N_z, *HU* 360084 structure stands out the most inhomogeneous geological structure in depth dimension among others, i.e., it has the largest number of different soil types (six, from top: *sandy loam*, *sandy clay loam*, *loamy sand*, *sand*, *clay*, *clay loam*) and the greatest number of changes in soil types between consecutive layers (above 700). This STU consists of, in an original form, the most varied horizontal composition, and after the approximation and application of pedotransfer approach it gained the most unforeseen changes of the CREP in depth dimension. However, other approximated soil structures, presented in Fig 2.4, can replace the *HU* 360084 in Fig. 2.11, such as the *IT* 390925 (Fig 2.4e) is shown in Fig. 2.12.

2.3 Subsurface Backscattering Features

Unlike to conventional SAR systems, the AGPR intends to subsurface imaging. Thus, the subsurface backscattering features have to be correctly mapped to the adequate multi-layer model, taking into account both the reflection and transmission of EM waves at a consecutive planar interfaces as well as attenuation of EM waves during its propagation through a stack of piecewise homogeneous and thin layers [130, 131]. The Fig. 2.13 shows a reflection and transmission of EM wave in an isotropic stratified medium made up from the consecutive, homogeneous, planar and thin layers l_n of various h_n height (Eq. 2.1) and with different $\varepsilon_{r,n}$ complex relative permittivity (Eq. 2.19), $\mu_{r,n}$ relative permeability (Eq. 2.18) and conductivity σ_n (Eq. 2.41). The boundary between consecutive layer l_n and l_{n+1} are defined at z_{n+1} (Eq. 2.2), where $h_n = z_{n+1} - z_n$ and $h_n \neq h_{n+1}$. As follows from Eq. 2.3, the last layer $l_{N_z} \in [Z_{max}, -\infty)$ is modelled as semi-infinite homogeneous region. In this half-space, only downward transmitted field exists since there in no reflection from the bottom of down-infinite homogeneous half-space [179–182]. Similarly, the air is modelled as upper-infinite half-space $l_a \in (+\infty, 0)$, but with the difference that in this half-space both the downwards transmitted E^i and upwards backscattered E^b fields exist. The index of refraction n_n for a l_n layer in non-magnetic dielectric stratified medium, where $\mu_{r,n} = \mu_{r,n+1} = 1+0i$, is defined as [167,180]

$$n_n = \sqrt{\mu_{r,n}\varepsilon_{r,n}} = \sqrt{\varepsilon_{r,n}} \tag{2.54}$$

and the relative refractive index $n_{n,n+1}$ from layer l_n to layer l_{n+1} is

$$n_{n,n+1} = \frac{n_n}{n_{n+1}} = \sqrt{\frac{\varepsilon_{r,n}}{\varepsilon_{r,n+1}}} \tag{2.55}$$

and $n_{n+1,n} = (n_{n,n+1})^{-1}$. Hence, the relative refractive index $n_{a,0}$ from air l_a, where dielectric constant $\varepsilon_{r,a} = 1.0$, to first soil layer l_0, where $\varepsilon_{r,0}$, is $n_{a,0} = \sqrt{\frac{\varepsilon_{r,a}}{\varepsilon_{r,0}}} = \frac{1}{\sqrt{\varepsilon_{r,0}}}$. Furthermore, substitution of the calculated values of $\varepsilon_{r,n}$ (Section 2.1.3, Fig. 2.9) into Eq. 2.55 results in non-monotonic changes of $n_{n,n+1}$. Inside soil horizon the value of $n_{n,n+1}$ will fluctuate around 1.0, since $\varepsilon_{r,n}$ and $\varepsilon_{r,n+1}$ differs slightly. The largest deviation from the $n_{n,n+1} \approx 1.0$ occurs at the border of horizons, where epsilon is changing significantly. In general, both the inward (when $n_n < n_{n+1}$) and outward (when $n_n > n_{n+1}$) refraction occur during wave propagation, even in the same soil horizon. Moreover, since relative permittivity is assumed to be complex valued, the index of refraction is also complex and can be expressed in general form as $n_n = n'_n - n''_n i$. Beside that, in each layer l_n the magnitude k (i.e., angular wavenumber) of

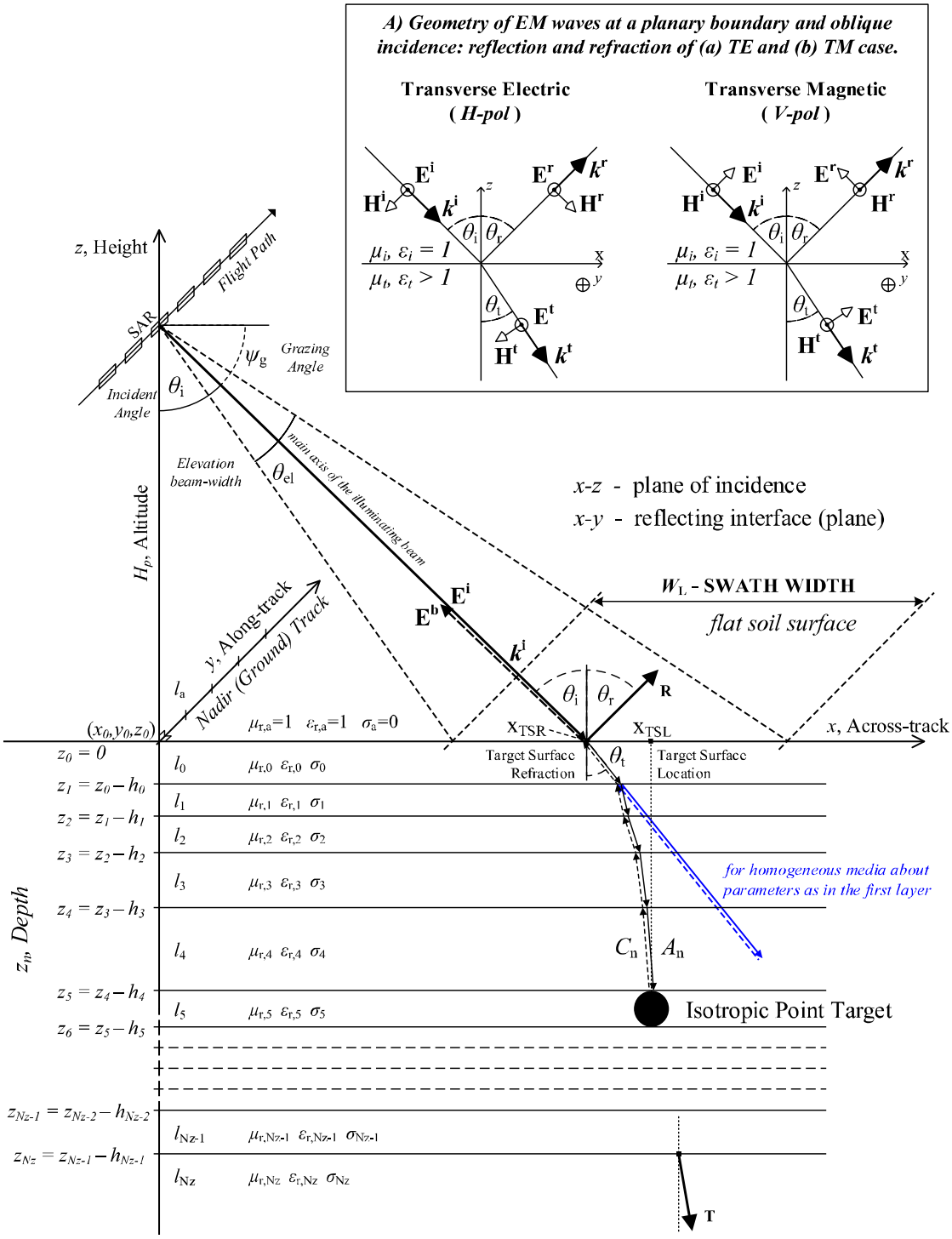

Figure 2.13 The reflection and transmission of the obliquely incident EM wave in stratified isotropic medium made up from N_z homogeneous, planar and thin layers: A) geometry of EM waves at a planar boundary and oblique incidence (not to scale for clarity).

the $\boldsymbol{k}$ wave vector equals [179, 180]

$$k_n = \frac{2\pi}{\lambda} = \frac{2\pi f}{\upsilon_{p,n}} = \frac{\omega}{\frac{c_0}{\sqrt{\varepsilon_{r,n}\mu_{r,n}}}} = \omega\sqrt{\varepsilon_n\mu_n} = \omega\sqrt{\varepsilon_0\mu_0}\sqrt{\varepsilon_{r,n}} \tag{2.56}$$

where $\varepsilon_n = \varepsilon_0\varepsilon_{r,n}$, $\mu_n = \mu_0\mu_{r,n} = \mu_0$, λ is wavelength, $\upsilon_{p,n}$ is the phase velocity. Moreover, the $\boldsymbol{k_n}$ wave vector in l_n can be decomposed into three components (k_n^x, k_n^y, k_n^z) which satisfied

the relations [167]

$$\boldsymbol{k_n} = \boldsymbol{n}k_n = \hat{\boldsymbol{x}}k_n^x + \hat{\boldsymbol{y}}k_n^y + \hat{\boldsymbol{z}}k_n^z \tag{2.57}$$

$$\left(k_n\right)^2 = \left(k_n^x\right)^2 + \left(k_n^y\right)^2 + \left(k_n^z\right)^2 \tag{2.58}$$

where $\hat{\boldsymbol{x}}$, $\hat{\boldsymbol{y}}$ and $\hat{\boldsymbol{z}}$ are the unit vectors in their respective directions, and $\boldsymbol{n}$ is the unit vector of propagation direction. However, assuming the component $k_n^y = 0$, and using Eq. 2.56, the Eq. 2.58 change as follow [167, 179–182]

$$\left(k_n^x\right)^2 + \left(k_n^z\right)^2 = \omega^2 \varepsilon_n \mu_n \tag{2.59}$$

Eq. 2.59 is more often known as the dispersion equation. For oblique incidence and propagation at $\theta_{i,n}$ (as depicted in Fig. 2.13A) through l_n layer

$$\begin{aligned} k_n^x &= k_n \sin\theta_{i,n} \quad \textit{(along x-axis)} \\ k_n^z &= k_n \cos\theta_{i,n} \quad \textit{(along z-axis)} \end{aligned} \tag{2.60}$$

2.3.1 Reflection and Transmission in Stratified Medium

Reflection and transmission of EM waves at plane boundaries are governed by Fresnel coefficients of R^{TE} (R^{TM}) reflection and T^{TE} (T^{TM}) transmission, respectively for transverse electric (TE) or transverse magnetic (TM) waves. In general, for oblique incidence at θ_i from i incidence medium to t transmission medium (see Fig. 2.13A), the R^{TE} reflection and T^{TE} transmission coefficients for perpendicular polarization (i.e., reflection and transmission coefficients of electric field) and the R^{TM} reflection and T^{TM} transmission coefficients for parallel polarization (i.e., reflection and transmission coefficients of magnetic field) are given by [167]

$$R_{i,t}^{TE} = \frac{\eta_t \cos\theta_i - \eta_i \cos\theta_t}{\eta_t \cos\theta_i + \eta_i \cos\theta_t} \tag{2.61}$$

$$T_{i,t}^{TE} = 1 + R_{i,t}^{TE} = \frac{2\eta_t \cos\theta_i}{\eta_t \cos\theta_i + \eta_i \cos\theta_t} \tag{2.62}$$

$$R_{i,t}^{TM} = \frac{-\eta_i \cos\theta_i + \eta_t \cos\theta_t}{\eta_t \cos\theta_t + \eta_i \cos\theta_i} \tag{2.63}$$

$$T_{i,t}^{TM} = \left(1 + R_{i,t}^{TM}\right) \frac{\cos\theta_i}{\cos\theta_t} = \frac{2\eta_t \cos\theta_i}{\eta_t \cos\theta_t + \eta_i \cos\theta_i} \tag{2.64}$$

where η_i (η_t) is wave impedances of i incident (t transmission) medium. For the oblique incidence, however, at boundary between non-magnetic dielectric media, where $\mu_{r,n} = \mu_{r,n+1} = 1 + 0i$, i.e., from upper l_n layer to bottom l_{n+1} layer (as depicted in Fig. 2.13), the Eq. 2.61-Eq. 2.64 becomes [181, 182]

$$R_{n,n+1}^{TE}\Big|_{\mu_n=\mu_{n+1}=1} = \frac{\cos\theta_{i,n} - \sqrt{\frac{\varepsilon_{n+1}}{\varepsilon_n}}\sqrt{1 - \left(\frac{\varepsilon_n}{\varepsilon_{n+1}}\right)\sin^2\theta_{i,n}}}{\cos\theta_{i,n} + \sqrt{\frac{\varepsilon_{n+1}}{\varepsilon_n}}\sqrt{1 - \left(\frac{\varepsilon_n}{\varepsilon_{n+1}}\right)\sin^2\theta_{i,n}}} \tag{2.65}$$

$$T_{n,n+1}^{TE}\Big|_{\mu_n=\mu_{n+1}=1} = \frac{2\cos\theta_{i,n}}{\cos\theta_{i,n} + \sqrt{\frac{\varepsilon_{n+1}}{\varepsilon_n}}\sqrt{1 - \left(\frac{\varepsilon_n}{\varepsilon_{n+1}}\right)\sin^2\theta_{i,n}}} \tag{2.66}$$

$$R^{TM}_{n,n+1}\Big|_{\mu_n=\mu_{n+1}=1} = \frac{-\cos\theta_{i,n} + \sqrt{\frac{\varepsilon_n}{\varepsilon_{n+1}}}\sqrt{1-\left(\frac{\varepsilon_n}{\varepsilon_{n+1}}\right)\sin^2\theta_{i,n}}}{\cos\theta_{i,n} + \sqrt{\frac{\varepsilon_n}{\varepsilon_{n+1}}}\sqrt{1-\left(\frac{\varepsilon_n}{\varepsilon_{n+1}}\right)\sin^2\theta_{i,n}}} \tag{2.67}$$

$$T^{TM}_{n,n+1}\Big|_{\mu_n=\mu_{n+1}=1} = \frac{2\sqrt{\frac{\varepsilon_n}{\varepsilon_{n+1}}}\cos\theta_{i,n}}{\cos\theta_{i,n} + \sqrt{\frac{\varepsilon_n}{\varepsilon_{n+1}}}\sqrt{1-\left(\frac{\varepsilon_n}{\varepsilon_{n+1}}\right)\sin^2\theta_{i,n}}} \tag{2.68}$$

respectively. The $\theta_{i,n}$ is angle of incident in l_n (upper) layer. The magnitude of the $|R^{TE}_{a,0}|$, $|T^{TE}_{a,0}|$, $|R^{TM}_{a,0}|$, $|T^{TM}_{a,0}|$ for oblique incidence from air l_a to first layer l_0 of the soil structure are shown in Fig. 2.14, with respect to the incidence angle and radar carrier frequency, and separately for chosen STU profiles. The vertical lines indicate incident angles used by radar systems. While $\varepsilon_{r,0}$ of first soil layer depends on frequency (for a given STU profile), for each radar unit (of different carrier frequency) the $|R^{TE}_{a,0}|$, $|T^{TE}_{a,0}|$, $|R^{TM}_{a,0}|$ and $|T^{TM}_{a,0}|$ have slightly different shape. As presented in Section 2.1.3, the real part of $\varepsilon_{r,0}$ changes slightly in the considered frequency range, therefore, the diversity of shape results from strongly varying imaginary part of $\varepsilon_{r,0}$. For Radar2 and Radar3, which carrier frequency lies close to each other, the plots strongly overlapping, almost completely for *FI* 3580005 and *PO* 3511382. However, little differences occur for *IT* 390925. For Radar4, with a higher carrier frequency, plots can be clearly distinguished for *IT* 390925. For *FI* 3580005, they overlap with the other two systems. While the magnitude $|\varepsilon_{r,0}|$ of the complex relative permittivity decreases in frequency (see Tab. 2.1) in the first layer,the $n_{a,0}$ (Eq. 2.55) increases, the magnitude of $|R_{a,0}|$ decreases whereas the magnitude of $|T_{a,0}|$ increase. Hence, more energy can pass through the air-soil interface to its interior structure. However, since the frequency decreases, the module of ε_r significantly increases, and in consequence, the reflection losses at first soil surface increases. Moreover, comparing between the STU profiles, the reflection coefficient is higher for clayey soils as for *IT* 390925 than in sandy soils *BE* 320202 and *GM* 490143 (compare left column). Extending the analysis through further interfaces, i.e., consecutively on interface between l_0 and l_1, the $|R^{TE}_{0,1}|$ and $|R^{TM}_{0,1}|$ almost equal zero, and $|T^{TE}_{0,1}|$ and $|T^{TM}_{0,1}|$ equals approximately one, since $\varepsilon_{r,0} \approx \varepsilon_{r,1}$ (Fig. 2.9). The most significant departures from $|R^{TE}_{n,n+1}| \approx |R^{TM}_{n,n+1}| \approx 0$ and $|T^{TE}_{n,n+1}| \approx |T^{TM}_{n,n+1}| \approx 1$ occur at the interface between different soil horizons (their lower and upper layer).

2.3.2 EM Field in Multi-Layer Medium

Overall, although that the soil layer l_n is modelled as thin, planar and homogeneous (as depicted in Fig. 2.13) the total electric field in it can be written as [167, 179, 182]

$$E_{y,n} = \left(A_n e^{-\mathrm{j}k^z_n \cdot z} + C_n e^{\mathrm{j}k^z_n \cdot z}\right) e^{\mathrm{j}k^x_n \cdot x} \tag{2.69}$$

where A_n is magnitude of fields traversing downward (transmitted or reflected from upper interface defined at z_n) and C_n is magnitude of fields traversing upward (reflected or transmitted from lower interface defined at z_{n+1}), and (k^x_n, k^z_n) are wave number components along x and z axis (Eq. 2.60). Since there are multiple reflection (double bounce) in each l_n layer, A_n represents all wave components that travelling downwards, and C_n represents those wave components that travelling upwards. Assuming the TE plane wave $\vec{E} = \vec{y}E_0$, which obliquely incident at soil surface (reflecting plane in x-y), the total field in l_a air becomes

$$E_a = \left(1 \cdot E_0 e^{-\mathrm{j}k^z_a \cdot z} + \widetilde{R}_{a,0} E_0 e^{\mathrm{j}k^z_a \cdot z}\right) e^{\mathrm{j}k^x_a \cdot x} \tag{2.70}$$

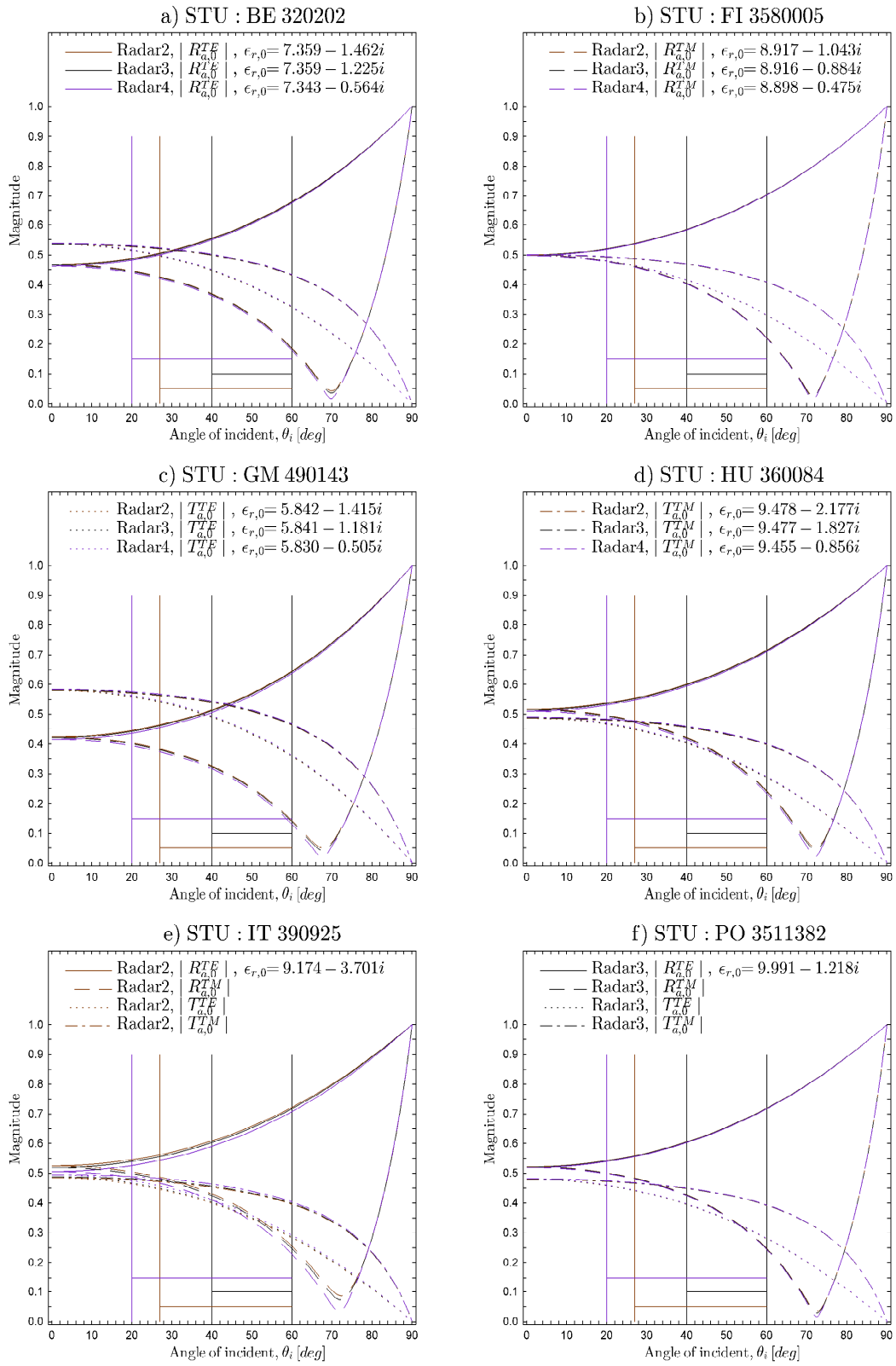

Figure 2.14 Magnitude of $|R^{TE}_{a,0}|$, $|R^{TM}_{a,0}|$ reflection and $|T^{TE}_{a,0}|$, $|T^{TM}_{a,0}|$ transmission coefficients for approximated soil structures as a function of θ_i incident angle, polarization (TE, TM) and frequency: Radar2 (f_c = 360 MHz, 20° $\leq \theta_i \leq$ 60°), Radar3 (f_c = 435 MHz, 40° $\leq \theta_i \leq$ 60°), Radar4 (f_c = 1200 MHz, 27° $\leq \theta_i \leq$ 60°); the $\varepsilon_{r,0}$ represents CREP in the first soil layer, its depends on frequency.

since there are no downwards wave except the E_0, so $A_a = 1 \cdot E_0$, and $C_a = \widetilde{R}_{a,0} E_0$, where $\widetilde{R}_{a,0}$ represents generalized reflection coefficient from soil surface. In turn, the total field in th last layer l_{N_z} becomes

$$E_{N_z} = (\widetilde{T}_{N_z-1,N_z} E_{N_z-1}\ e^{-\mathrm{j}k^z_{N_z}\cdot z} + 0 \cdot e^{\mathrm{j}k^z_{N_z}\cdot z})\ e^{\mathrm{j}k_{x,N_z}\cdot x} \tag{2.71}$$

with $C_{N_z} = 0$ because there are no upwards field, E_{N_z-1} is total field in l_{N_z-1} and $\widetilde{T}_{N_z-1,N_z}$ is generalized transmission coefficient from layer l_{N_z-1} to layer l_{N_z}. Furthermore, both $\widetilde{R}_{a,0}$ and $\widetilde{T}_{N_z-1,N_z}$, in addition to $R_{a,0}$ surface reflection in l_a and T_{N_z-1,N_z} transmission in l_{Nz}, include the effect of subsurface internal reflection $R_{a\rightarrow\!\!\!\!\rightarrow N_z}$ and internal transmission $T_{a\rightarrow\!\!\!\!\rightarrow N_z}$ in multilayer medium. Hence, they can be expressed in general form as [180]

$$\widetilde{R}_{a,0} = R_{a,0} + R_{a\rightarrow\!\!\!\!\rightarrow N_z} \tag{2.72}$$

$$\widetilde{T}_{N_z-1,N_z} = T_{N_z-1,N_z} + T_{a\rightarrow\!\!\!\!\rightarrow N_z} \tag{2.73}$$

and their close-form solution can be found iteratively [180]. However, this straightforward procedure is highly time-consuming, particularly when the $N_z \gg 1$, and it cannot be simplified when $h_n \neq h_{n+1}$ (according to Eq. 2.1). Nevertheless, as result from the boundary conditions of continuity of tangential electric and magnetic fields at each interface, the magnitudes of total upwards and downwards wave component in a given layers l_n and l_{n+1}, i.e., A_n, C_n, A_{n+1}, C_{n+1} are coupled as follow [179]

$$\begin{bmatrix} A_n e^{-\mathrm{j}k^z_n\cdot z_n} \\ C_n e^{\mathrm{j}k^z_n\cdot z_n} \end{bmatrix} = B_{(n,n+1)} \begin{bmatrix} A_{n+1} e^{-\mathrm{j}k^z_{n+1}\cdot z_{n+1}} \\ C_{n+1} e^{\mathrm{j}k^z_{n+1}\cdot z_{n+1}} \end{bmatrix} \tag{2.74}$$

by the backward-propagating matrix $B_{(n,n+1)}$, which gives the ratio of the fields in upper l_n layer to fields in lower l_{n+1} layer. For TE wave, $B_{(n,n+1)}$ is given by

$$B_{(n,n+1)} = \frac{1}{2}\left(1 + \frac{\mu_n\ k^z_{n+1}}{\mu_{n+1}\ k^z_n}\right) \times \begin{bmatrix} e^{-\mathrm{j}k^z_{n+1}h_{n+1}} & R_{(n,n+1)}\ e^{\mathrm{j}k^z_{n+1}h_{n+1}} \\ R_{(n,n+1)}\ e^{-\mathrm{j}k^z_{n+1}h_{n+1}} & e^{\mathrm{j}k^z_{n+1}h_{n+1}} \end{bmatrix} \tag{2.75}$$

where h_{n+1} (Eq. 2.1) is the heigh of lower l_{n+1} layer. Moreover, the Fresnel reflection coefficient $R_{(n,n+1)}$ at the interface z_{n+1} equals

$$R_{(n,n+1)} = \frac{1 - \dfrac{\mu_n\ k^z_{n+1}}{\mu_{n+1}\ k^z_n}}{1 + \dfrac{\mu_n\ k^z_{n+1}}{\mu_{n+1}\ k^z_n}} = \frac{\mu_{n+1}\ k^z_n - \mu_n\ k^z_{n+1}}{\mu_{n+1}\ k^z_n + \mu_n\ k^z_{n+1}} \tag{2.76}$$

Based on $B_{(n,n+1)}$, the wave amplitudes in any region m can be express in terms of those in region p, where $m < p$. Therefore, for $m = a$ (air) and $p = N_z$ (semi-infinite soil layer), and $a < d_n \ll N_z$, where d_n is isotropic target location (see Fig. 2.13), the Eq. 2.74 can be literally expanded through all considered layers, even much deeper than the location of the object, as follow [179]

$$\begin{bmatrix} 1 \\ \widetilde{R} \end{bmatrix} = B_{(a,0)} B_{(0,1)} \ \ldots\ B_{(d_n-1,d_n)} B_{(d_n,d_n+1)} \ \ldots\ B_{(Nz-1,Nz)} \begin{bmatrix} \widetilde{T} e^{\mathrm{j}k^z_{N_z}\cdot z_{Nz}} \\ 0 \end{bmatrix} \tag{2.77}$$

where $\widetilde{R}$ and $\widetilde{T}$ are two unknowns. Since the exact soil model is known, i.e., $\mu_a = \mu_n = \mu_{n+1} \equiv \mu_0$, d_n depth of each interface, h_n height of each layer as well as its $\varepsilon_{r,n}$ complex dielectric constant and σ_n conductivity, the $B_{(n,n+1)}$ can be found based on disper-

sion relation. As follows from Eq. 2.59, in each layer the two wave vector components (k_n^x, k_n^z) satisfied the equation of dispersion. Thus, using the method of the tangential filed continuity (phase matching conditions) at the interface of two layers [179]

$$k_i \sin\theta_i = k_a^x = k_0^x = k_1^x = ... = k_d^x = k_{d+1}^x = ... = k_{Nz-1}^x = k_{Nz}^x \tag{2.78}$$

where k_i is magnitude of wave vector of incident E^i wave in air. Then, the k_n^z can be deduced from the equation of dispersion (Eq. 2.59)

$$k_n^z = \sqrt{\omega^2 \varepsilon_n \mu_n - \left(k_i \sin\theta_i\right)^2} \tag{2.79}$$

Based on the ray-tracing method [183,184] (applied also in [21]), the downward scattering component of the electric filed can be calculate for each layer l_n. Assuming an isotropic point scatterer at depth d_n, where $0 < d_n \ll Z_{max}$, the upward backscattering component of the electric field can be obtained by changing the wavenumber sign [87]. Although this method of ray-tracing used for calculation of target backscattered response is very simple, it allows one to understand the distortion, i.e., irregular attenuation and dispersion effect, leading to envelope fluctuations of the backscattered signal, in an easier way. Despite the other methods developed for modelling of EM wave propagation and fitted for GPR, as a method using finite differences, the ray-tracing method allows to consider only the backscattered EM filed. In addition, the advantage of this method is the ability to calculate both propagation angles ($\theta_{i,n}$, $\theta_{t,n}$) as well as the propagation time τ_n of radar chirp through a layer l_n. Hence, based on τ_n the global two-way delay time of radar chirp, transmitted by radar at H_p and θ_i through the soil structure down to the d_n depth and return, can be calculated as well. Moreover, as follows from Snell's law, $\theta_{t,n} = \theta_{i,n}$. Finally, this computational formalism can be easily applied for TM polarization by replacing $\mu_{n,r}$ by $\varepsilon_{n,r}$ in backward-propagation matrix (Eq. 2.75 and Eq. 2.76).

2.3.3 Penetration Capabilities

The problems affecting the EM wave propagation in soil structure result from dispersive and lossy nature of the soil expressed in complex effective permittivity (Eq. 2.30). Since $\boldsymbol{k}$ wave vector is complex, the $\gamma = ki$ propagation coefficient [167, 182] is complex as well. As results from Eq. 2.59, k can be expressed in general form as $k = \beta - \alpha i$. Hence

$$\gamma = ki = (\beta - \alpha i)i = \alpha + \beta i \tag{2.80}$$

In Eq. 2.80, the α is the attenuation coefficient (Np/m), and β is the phase coefficient (rad/m), and 1 Np = $20/\ln 10 \approx 8.6859$ dB. The α depicts the attenuation (propagation loss) affecting wave propagation in layer, and it does not include reflection loss occurring when wave incident on the interface between two layers (see Section 2.3.1). The β represents additional phase shift. Including relative parameters (Eq. 2.18 and Eq. 2.29) into Eq. 2.59, leads to [167]

$$k^2 = k_x^2 + k_z^2 = \omega^2 \mu_0 \varepsilon_0 \left[\varepsilon_r' - \left(\varepsilon_r'' + \frac{\sigma_{dc}}{\omega \varepsilon_0}\right) i\right] \equiv (\beta^2 - \alpha^2) - 2\alpha\beta i \tag{2.81}$$

where the real and imaginary parts must be equals to each other. Therefore, the α attenuation coefficient equals

$$\alpha \text{ [dB/m]} = 8.6859\ \omega \sqrt{\varepsilon_0 \mu_0} \sqrt{\frac{\varepsilon_r'}{2}\left[\sqrt{1 + \left(\frac{\omega \varepsilon_0 \varepsilon_r'' + \sigma_{dc}}{\omega \varepsilon_0 \varepsilon_r'}\right)^2} - 1\right]} \tag{2.82}$$

and β phase coefficient equals

$$\beta \text{ [rad/m]} = \omega\sqrt{\varepsilon_0\mu_0}\sqrt{\frac{\varepsilon_r'}{2}\left[\sqrt{1+\left(\frac{\omega\varepsilon_0\varepsilon_r''+\sigma_{dc}}{\omega\varepsilon_0\varepsilon_r'}\right)^2}+1\right]} \tag{2.83}$$

Both parameters are determined by polarization loss (when $\varepsilon_r'' \neq 0$) and conductivity loss (when $\sigma_{dc} \neq 0$). However, for $\varepsilon_r = \varepsilon_r' - 0i$, and $\sigma_{dc} = 0$, the Eq. 2.82 and Eq. 2.83 reduce to

$$\alpha \text{ [dB/m]} = 0 \tag{2.84}$$

$$\beta \text{ [rad/m]} = \omega\sqrt{\mu_0\varepsilon_0\varepsilon_r'} \tag{2.85}$$

Taking into account that $\varepsilon'(z,f)$ and $\varepsilon''(z,f)$ depend on depth and frequency as well as $\sigma(z)$ depends only on depth, the attenuation coefficient can be calculated in l_n layer as a function of depth and frequency. The Fig. 2.15 shows the one-way α attenuation coefficient calculated for approximated soil structures. As before, the plots are drawn down to depth smaller that Z_{max} and for three various frequency: 360 MHz, 435 MHz and 1200 MHz, i.e., the carrier frequency of Radar2, Radar3 and Radar4, respectively (see Tab. 1.1). These plots present the attenuation (in dB) at the distance of 1 m in the homogeneous medium about the parameters exactly as in l_n layer. The horizontal changes are clearly visible. These changes result from the value of CREP (Eq. 2.29, Fig. 2.10) estimated for the approximated geological texture (Fig. 2.4) with the use of pedotransfer function. The α_n (in n^{th} layer) significantly grows with frequency. For constant frequency is has lower value in sandy soils (horizons) than in clayey soils (horizons), with the assumption about the same moisture content. Characteristically, while mainly in all approximated structures the shape of α is similar among considered frequency (proportionally shifted), the α_n for Radar4 behaves differently just below the surface for *FI* 3580005, *HU* 360084 and *PO* 3511382 (see left column of Fig. 2.15).

Furthermore, the α_n indicates how the EM wave drops (decay per metre) during propagation in a lossy medium. The quantity δ, defined as depth of penetration [12, 126, 167] or *skin depth*, express a concept leading to the depth over which the wave amplitude decays to $1/e \approx 0.369$ (-8.69 dB) of its value just under the interface (i.e., at $z = 0_-$, also defined as immediate sub-surface value). The δ is defined as

$$\delta \text{ [m]} = \frac{1}{\alpha} = \frac{1}{\omega\sqrt{\varepsilon_0\mu_0}\sqrt{\frac{\varepsilon_r'}{2}\left[\sqrt{1+\left(\frac{\omega\varepsilon_0\varepsilon_r''+\sigma_{dc}}{\omega\varepsilon_0\varepsilon_r'}\right)^2}-1\right]}} \tag{2.86}$$

As results from the analysis of Eq. 2.86, for homogeneous and loss half-space the δ increases with wavelength (the lower frequency, the higher penetration depth). Moreover, when $\varepsilon_r'' = 0$ and $\sigma_{dc} = 0$, the $\alpha = 0$ dB/m, hence, the $\delta = \infty$ m. This useful concept of δ shows the effect of soil EM properties (determined by soil composition and moisture profile) and wavelength on the maximum depth contributing to backscattered signal registration [126]. Although theoretically, shorter wavelengths and drier soils provide greater depth of propagation, in practice, the precise value of δ is difficult to compute or even estimate. In particular, outside of laboratory conditions or for real soil field. In Fig. 2.16, the computed values of δ_n are shown for approximated structures and for the same set of frequencies. In these plots, the estimated value of δ_n in layer l_n (at depth d_n) represents the depth (below theoretical interface) at which the EM wave decay to $1/e$ of its value below this interface, with the assumption that EM wave entered and propagates through a medium (unlimited from the bottom and homogeneous) with parameters of layer l_n. Estimated values of δ_n are much greater than the height of each layer (Eq. 2.1) assumed in soil model. Horizontal changes are still presents, but now it is clearly

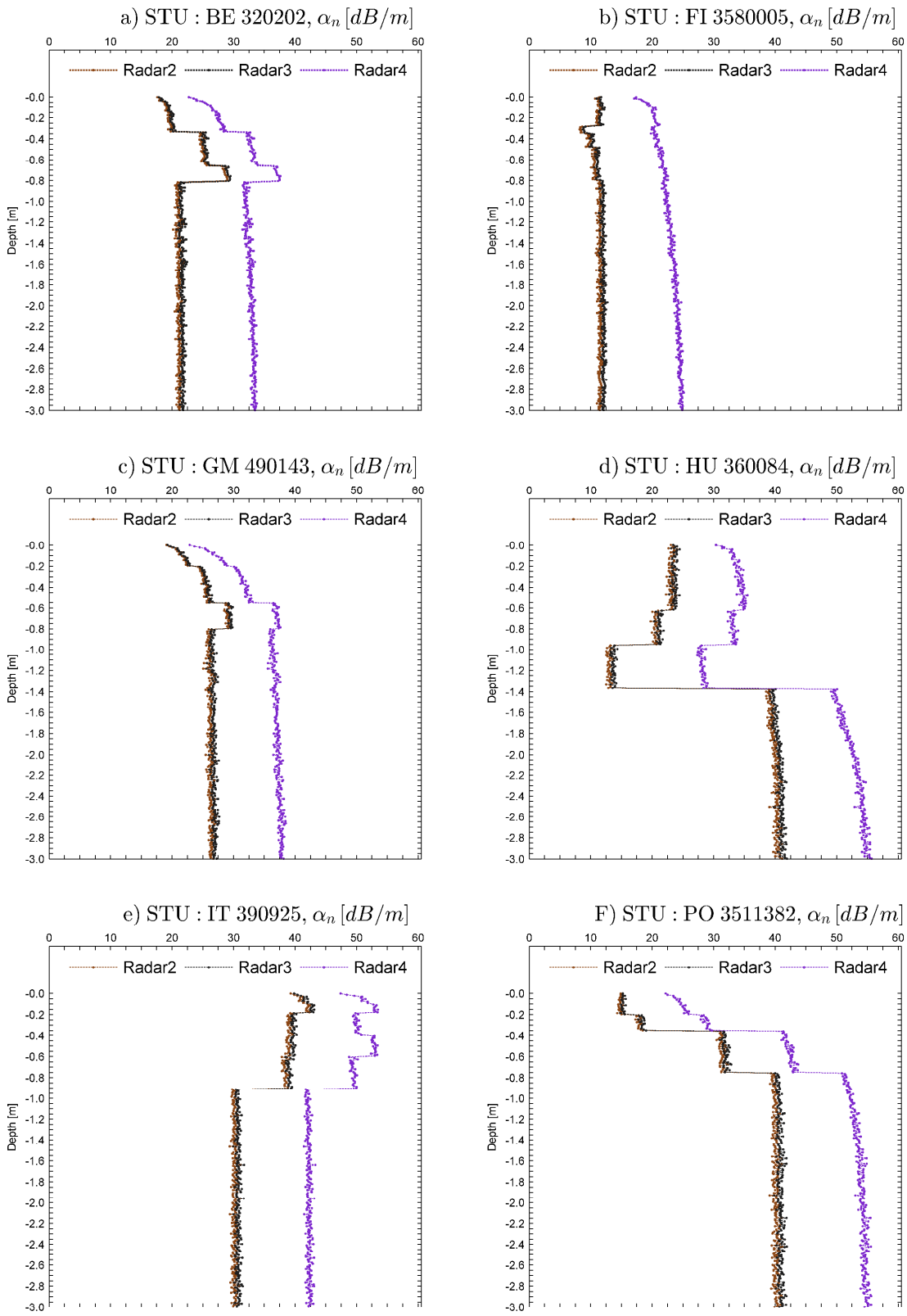

Figure 2.15 The one-way attenuation α_n [dB/m] in soil layers for various carrier frequency of SAR system in considered STU-based soil structures.

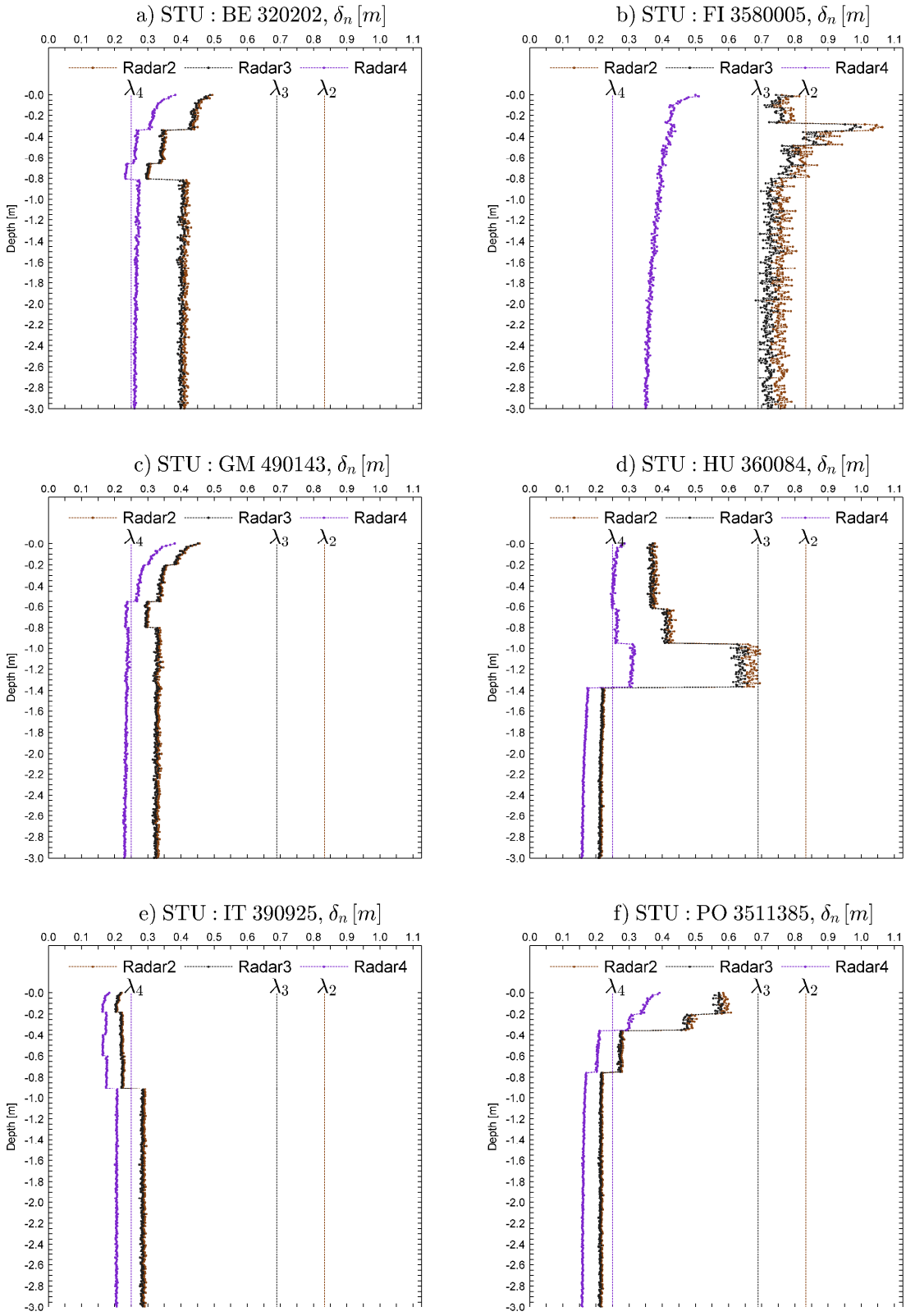

Figure 2.16 The penetration depth δ_n [m] in soil layers for various carrier frequency of SAR system in considered STU-based soil structures.

shown that in homogeneous medium the deeper penetration depth is obtained for longer wavelengths and sandy soils. For highly clayey composition (as in first layers of *IT* 390925), attenuation α is significantly high, and the penetration depth δ_n is the lowest among the considered STU-based soil structures. On the other hand, although that *FI* 3580005 has relatively high complex dielectric constants (i.e., its real part, see Fig. 2.9a,b), it has the lowest α_n and the deepest δ_n, since it has the lowest σ (see Fig. 2.9c). In addition, thin dashed vertical lines in Fig. 2.16 represents the wavelength of radar waveform $\lambda_r = c_0/f_{c,r}$. Mostly, the *skin depth* for given radar is less than or close to the wavelength of radar pulse. Only for *FI* 3580005 it is deeper than the wavelength, or slightly less. Comparing, however, the ratio of δ_n/λ_r it is clearly shown that for Radar4 this ratio is close to one, and in *FI* 3580005 reaches the maximum value of $\delta_n/\lambda_r \approx 2.00$ (in first two layer). For Radar2 and Radar3, the ratio of δ_n/λ_r is generally less than 0.6, expect *FI* 3580005, where it oscillate around 1.0, while the ratio of δ_n/λ_r for Radar4 in the all approximated structures is not less than 0.5. Whereas, the *skin depth* is widely considered as equal to wavelength, the Fig. 2.16 shows that it strongly depend on soil EM nature. Contrary to many experiments, performed in nearly optimal conditions, in real scenario, i.e., over wide areas in different places of the Earth, the penetration depth can vary strongly. Hence, small buried targets can be easily observed with higher frequency radar at deeper depths than large buried structures located at shallow depths.

For oblique incidence at θ_i, the effective propagation distance in layer l_n is proportional to the height h_n of layer and transmission angle $\theta_{t,n}$. Therefore, although that the α is not negligible, it affects the magnitude of EM wave only at very short distance during its propagation in l_n layer. Hence, in highly inhomogeneous medium, consisting of thin planer and homogeneous layers (Fig. 2.13), the equivalent propagation loss and theoretical penetration depth result from individual contributions of attenuation of the successive layers as well as from transmission losses at boundary between consecutive layers. Fig. 2.17 shows the one-way total attenuation L_α affecting the magnitude of EM wave propagate through approximated STU-based soil structures only for 40° and both polarization. The estimated $\delta_{1/e}$ penetration depths are presented in Tab. 2.2 and are marked (in thin vertical lines) for various carrier frequencies. In calculations, the θ_i incident angle was equal to 20°, 40° and 60°, respectively, for these three airborne SAR systems presented earlier in Section 2.3.1. For 20° and 60°, the one-way total attenuation L_α retains its shape and is proportionally shifted due to different transmission loss at air-soil interface, relatively small decrease in L_α for 60° and relatively high increase L_α for 20° (as results from assumed model of CREP). From this reasons, the plots for 20° and 60° are not shown in the Fig. 2.17. While $\delta_{1/e}$ is defined with respect to immediate sub-surface value, the transmission losses at air-soil interface are taken into account. These losses are identified as part of the energy that do not penetrate through interface between layer. Without taking this losses into consideration, the $\delta_{1/e}$ does not exceed a few centimetres below soil surface (see the $1/e \approx 0.369$ (−8.69 dB) limit marked by dashed horizontal line). As can be seen, the attenuation is nearly linear through soil horizon and it changes significantly at interface between the soil horizons. The deflection of curves occurred at the boundary between soil horizons (compare with Fig. A.4 presented in Appendix A), in particular, when the soil composition changes radically between two different types. Moreover, the relation between level of α_n attenuation in layer (Fig 2.15) and transmission losses revealed in first soil layer. While ε_r decreases with frequency (Fig. 2.8) and at carrier frequency of Radar4 the transmission losses are smaller than for Radar3 and Radar2, the attenuation in all layer is significantly higher for Radar4. Hence, despite the fact that just below the surface the $L_\alpha(z_{0-})$ is lower for Radar4, at the top of second soil layer the $L_\alpha(z_{1-})$ is higher for Radar4 and smaller for other. While through the original soil horizon, the $\varepsilon_{r,n} \leqq \varepsilon_{r,n+1}$, the attenuation α_n strongly affects the EM wave. However, when $\varepsilon_{r,n}$ is significantly higher than $\varepsilon_{r,n+1}$ (as around $z_n = -0.3$ m for *FI* 3580005, $z_n = -1.4$ m for *HU* 360084 and $z_n = -0.6$ m for

Table 2.2 Estimated value of $\delta_{1/e}$ [m] penetration depth of EM wave in considered soil structures for various carrier frequency.

STU Profile	Radar2 360 [MHz]	Radar3 435 [MHz]	Radar4 1200 [MHz]	$\Delta\delta_{1/e}$ [m]	$\Delta\delta^B_{1/e}$ [m/MHz]
BE 320202	0.3942	0.3942	0.2985	-0.0956	-9.565e-05
FI 3580005	0.7179	0.6843	0.3742	-0.3437	-3.437e-04
GM 490143	0.3471	0.3381	0.2822	-0.0649	-6.485e-05
HU 360084	0.3381	0.3291	0.2438	-0.0943	-9.426e-05
IT 390925	0.1938	0.1938	0.1584	-0.0354	-3.538e-05
PO 3511382	0.4328	0.4328	0.3083	-0.1245	-1.245e-04

IT 390925), the amplitude of EM wave at the top of the layer $n+1$ increases relatively more than the attenuation that occurs at distance $h_{n+1}(\cos\theta_{i,n+1})^{-1}$. From this reason, at the boundary between optically more n and less $n+1$ denser layers, the L_α distinguish decreases. An analysis of the total attenuation along the propagation path in soil can be equated to analysis of the wave attenuation caused by vegetation or tree canopy (stalks or trunks, and leafs, see [185, Fig. 11-19, Fig. 11-53]), with the difference that soil surface stands uniform septation between air and soil structure, whereas vegetation or tree crown is not so uniform and cohesive surface (area). Hence, which results in rapid attenuation below soil surface (Fig. 2.17) in contrast to a slight fluctuation in the first few centimetres of vegetation canopy ([185, Fig. 11-19]). The estimated values of $\delta_{1/e}$ differs for various carrier frequencies, are similar for Radar2 and Radar3 and distinctly lower for Radar4. In addition, throughout the considered frequency bandwidth, the $\Delta\delta_{1/e}$ penetration depth deviation takes negative values. Those negative values of the $\Delta\delta_{1/e}$ show that higher frequency are attenuated strongly (which was predictable when analysing Fig. 2.15). As results from Tab. 2.2, the values of $\delta_{1/e}$ and $\Delta\delta_{1/e}$ depend on soil composition in consecutive layers (horizons). However, $\Delta\delta_{1/e}$ for *BE* 320202 and *HU* 360084 as well for *GM* 490143 and *IT* 390925 takes similar values, and is smaller than 10 cm or 7 cm, respectively. Hence, for UWB system (e.g., of 1.0 GHz bandwidth as the frequency range of Peplinski *et al.* model) small deviation of the penetration depths may possibly occur in the highly lossy soil, even if the penetration depth is much shallower than in the "easily penetrating" soils, where $\Delta\delta_{1/e}$ may be an order of magnitude greater (compare maximum and minimum of $\delta_{1/e}$ and $\Delta\delta_{1/e}$ for *FI* 3580005 and *IT* 390925). The $\Delta\delta^B_{1/e}$ expresses a slope of the change in depth penetration over the frequency range. Large $\delta_{1/e}$ required for the dedicated mission purposes can lead to large variation of penetration depth $\Delta\delta^B_{1/e}$ over instantaneous frequency of UWB radar pulse, and thus, to significant deformation of the backscattered pulse envelope. The ratio of δ_n/λ_r shows that the penetration depth is more degraded by increasing the dielectric constants and conductivity than decreasing wavelength.

2.3.4 Surface-Volume Backscattering Coefficient

The area investigated by AGPR is rather represented as soil volume than only as soil surface. Hence, both surface reflection and volume scattering contribute to backscattering coefficient but with various degrees. For planar or weakly rough surfaces (Fig. 2.11), the backscattering coefficient is directly proportional to Fresnel reflection coefficient (Fig. 2.14). Beyond the dependence on incident angle θ_i, polarization and radar wavelength λ, the surface backscattering coefficient is strongly dependent on the roughness, type of ground cover (bare or vegetation-covered), moisture content and soil composition [186–188]. The limit between planar or rough

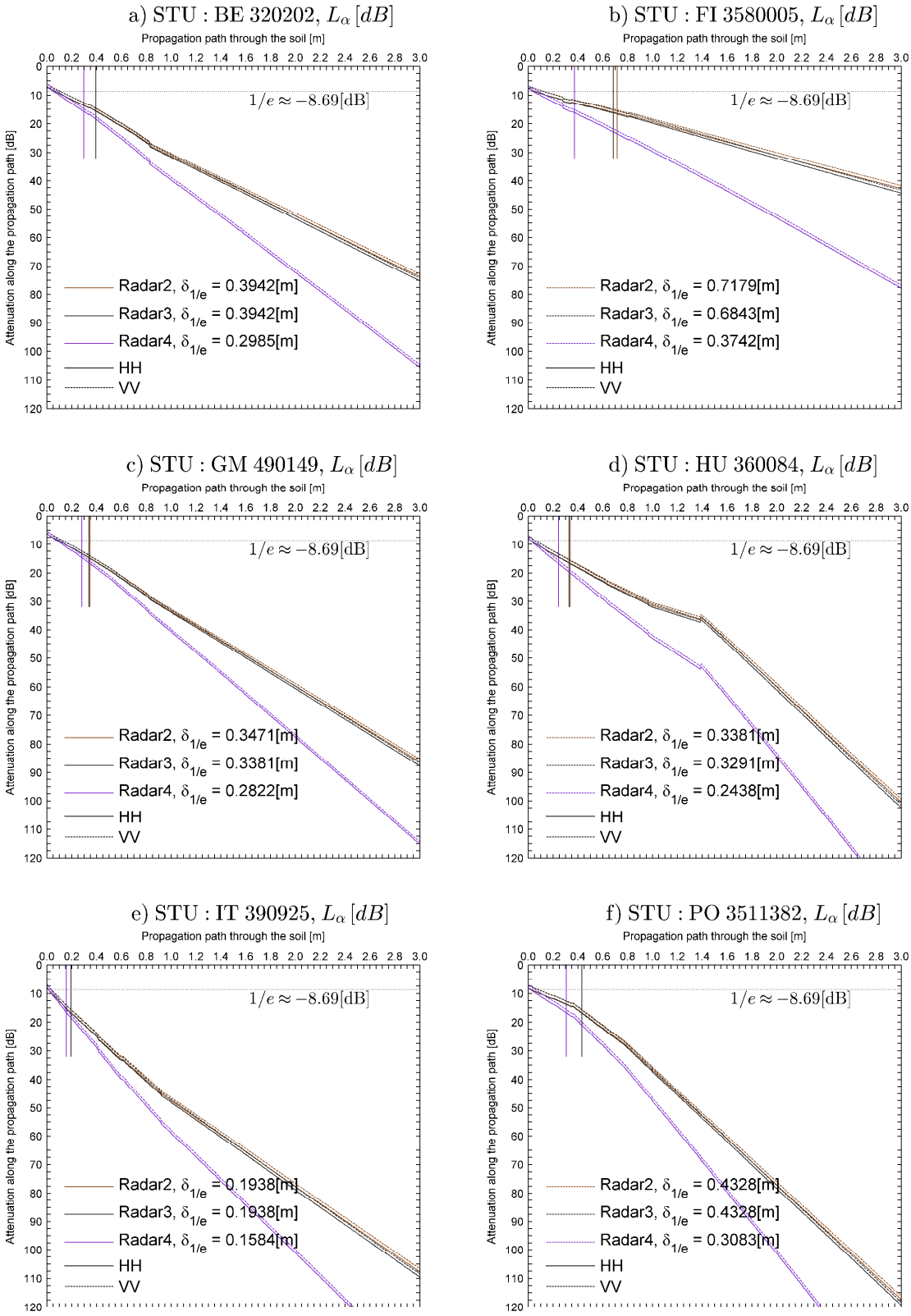

Figure 2.17 The total one-way total attenuation L_α [dB] for various carrier frequency and two polarization of SAR systems in considered STU-based soil structures, $\theta_i = 40°$.

surface is defined by the Rayleigh criterion [12]

$$\frac{2\pi}{\lambda}\, 2h_{rms} \sin\psi_g < \frac{\pi}{2} \tag{2.87}$$

where h_{rms} is the root mean square of a surface height irregularity, and $\psi_g = (\frac{\pi}{2} - \theta_i)$ is the grazing angle. From Eq. 2.87 results that the surface can be considered as flat, when the phase variation caused by vertical variations of the surface does not exceed $\pi/2$. For considered λ (i.e., λ_2, λ_3 and λ_4) and assuming weakly rough surface $h_{rms} = \sigma_h$ (see Section 2.1), Eq. 2.87 is satisfied over the whole range of observation angles $\theta_i \in [0°, 90°]$. Hence, the backscattering coefficient, σ^0 Normalized Radar Cross Section, in m^2/m^2 or dB, can be considered only in surface plane as for an area backscattering case [13]. Nevertheless, having regard to a small deformation of a flat surface $h_{rms} = h_{n,rms}$ (see Section 2.1), σ^0 (σ^0_{hh} or σ^0_{vv}) can be calculated with semi-empirical model [189,190], which is considered to be applicable to a wider range of surface roughness [12]. Fig. 2.18 shows general behaviour of σ^0 as a function of incident angle θ_i, and for λ_2 (Radar2), λ_3 (Radar3) and λ_4 (Radar4), for two different values of h_{rms} (i.e., σ_h and $h_{n,rms}$) and two polarization. Vertical lines represent the range of observation angles of considered radar units (as in Fig. 2.14). In general, the σ^0 is polarization sensitive, the σ^0_{vv}(*solid lines*)> σ^0_{hh}(*dashed lines*) for given λ, θ_i and h_{rms}. Further, σ^0 (both σ^0_{vv} and σ^0_{hh}) are stronger for higher value of h_{rms} ($h_{n,rms}$ (marked as $\triangledown$) > σ_h (marked as □)). The σ^0 depends also on λ. For constant h_{rms}, decreasing λ induces a higher ratio between h_{rms} and λ, and more energy is backscattered from the rough surface. Finally, σ^0 decreases as θ_i increases. Thus, lower frequencies and higher incident angles provide lower level of backscattered energy. Comparison of the results obtained for different soil structures show that there is no significant difference in σ^0, the same as in surface reflection and transmission coefficient. This is explained by the modelling of [189, 190] σ^0_{vv} that is proportional to the average of the horizontally and vertically polarized Fresnel reflectivities (i.e., $\Gamma_h(\theta) = |R^{TE}_{a,0}(\theta)|^2$ and $\Gamma_v(\theta) = |R^{TM}_{a,0}(\theta)|^2$, Fig. 2.14). And σ^0_{hh} is found based on the co-polarized coefficient. Therefore, while the dielectric properties of the soil upper layer may slightly vary over the considered soils structures (see Fig. 2.10, as well as in real scenario), the inner propagation phenomenon (refraction at interfaces and attenuation inside soil horizons or layers) substantially impact on the backscattered signal from buried objects. Furthermore, σ^0 is very important for InSAR simulation [21] in order to provide correlation between two raw SAR images representing the same area observed under slightly different angles.

2.3.5 Model of Backscattered Signal

Foremost, theoretically, in a rich scattering medium, the target response of a point scatterer consists of a direct amplitude-scaled and time-delay echo and multipath echoes from surrounding scatterers. On the other hand, the target response in an AGPR consists of a strong backscattered echo made up of the surface reflection and the cumulative echo from soil structure. The dominant reflection echo comes from the boundary between the radar half-space and target half-space (i.e., soil inhomogeneous structure, see Fig. 2.13). Furthermore, the cumulative echo from the soil structure contains direct amplitude-scaled, time-delayed and distorted echo from point scatterers, and superposition of every indirect multipath reflections from the point scatterers and an infinite number of multipath reflections from soil inhomogeneities (surrounding scatterers). Hence, target response $s_r(t)$ is generally expressed as [124]

$$s_r(t) = \underbrace{\sigma_c s_t(t-\tau_d)}_{\text{surface reflection}} + \underbrace{\sum_{i=1}^{\infty} h_i(t) * s_t(t-\tau_d-t_i)}_{\text{internal multireflections}}, \tag{2.88}$$

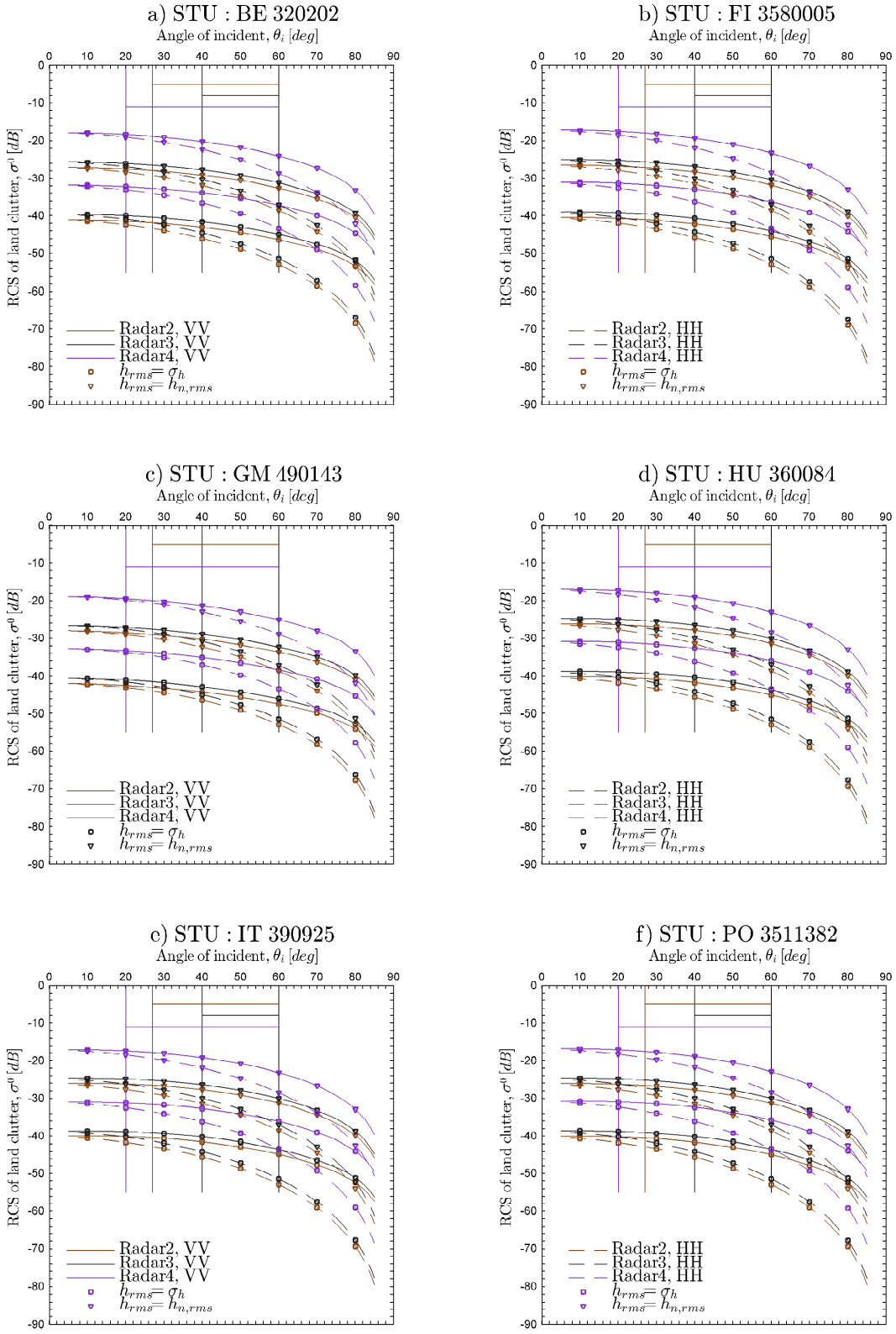

Figure 2.18 General behaviour of σ^0 [dB] as a function of angle θ_i [°] and for various $\lambda = c/f_c$, h_{rms} ($\sigma_h(\square)$, $h_{n,rms}(\triangledown)$) and polarization H (dashed lines), V (solid lines).

where σ_c is surface reflection coefficient proportional to the surface clutter area A_c, i.e., $\sigma_c = A_c\sigma^0$, $s_t(t)$ is transmitted radar signal, τ_d is the two-way time delay between radar and surface, $h_i(t)$ is impulse response of i^{th} propagation path inside the soil, t_i is propagation time of i^{th} path and $*$ denotes time convolution. Even a slight difference of EM properties (e.g. $\epsilon_{r,n}$, see Fig. 2.9) between two consecutive layers (l_n, l_{n+1}) causes energy reflection proportionally to the reflection coefficient (Eq. 2.65, Eq. 2.67). Permittivity $\epsilon_{r,n}$ affects the propagation time through the layer l_n, thus in consequence, the change of $\epsilon_{r,n}$ affects the propagation time t_i of i^{th} path. Considering the downwards and upwards propagation of the UWB pulse only through a small number of dispersive layers L in the structure presented in Figure 2.13, where $L \ll N_z$, with N_z of considered layers (see Section 2.1.1), the distortion of backscattered pulse becomes non-negligible. In addition, L decreases when the bandwidth of transmitted pulse increases. Hence, for the UWB systems the pulse distortion occurs already in the first layers, at a shallow depths. It cannot be ignored in the simulations for strongly inhomogeneous structures with thin layers. However, taking into account the high attenuation in each layer (see Fig. 2.15), the multiple specular reflection can be omitted in the simulation. Therefore, based on the ray-tracing method and model presented in Fig. 2.13, the Eq. 2.88 can be simplified only with time-delayed surface reflection and direct backscattered, amplitude-scaled, time-delay and distorted echo from point scatterers buried in the soil at a specified depth, as follows

$$s_r(t) = \underbrace{\widetilde{R}_{a,0}\ s_t(t-\tau_d)}_{\text{surface reflection}} + \underbrace{\widetilde{T}_{0,n}\ \widetilde{R}_{n,0}\ s_t(t-\tau_d-t_d)}_{\substack{\text{backscattered echo} \\ \text{from point target}}} \tag{2.89}$$

where $\widetilde{R}_{a,0} = A_c\sigma^0$, $\widetilde{T}_{0,n}$, $\widetilde{R}_{n,0}$ is the generalized surface reflection coefficient, generalized downward transmission coefficient from surface to target and generalized upward reflection coefficient from target to surface, respectively, and t_d is time delay over propagation path in soil from refraction point at surface $(X_{TSR}, Y_{TSR}, 0)$ to target location in soil (X_{TSL}, Y_{TSL}, z_d) (as depicted in Fig. 2.13, where $Y_{TSR} = Y_{TSL} = 0$). Furthermore, introducing the generalized target reflection coefficient as $\sigma_t = \widetilde{T}_{0,n}\widetilde{R}_{n,0}$ and receiver thermal noise $n(t)$, Eq. 2.89 become

$$s_r(t) = \underbrace{A_c\sigma^0 s_t(t-\tau_d)}_{\text{surface reflection}} + \underbrace{\sigma_t\ s_t(t-\tau_d-t_d)}_{\substack{\text{backscattered echo} \\ \text{from point target}}} + \underbrace{n(t)}_{\substack{\text{receiver} \\ \text{noise}}} \tag{2.90}$$

where $n(t)$ represent the additive zero mean noise with variance (power) $P_N = \sigma_N^2 = k_B T B_f$, k_B is the Boltzmann constant, T K $= 273.15 + T_C$ °C is absolute temperature and B_f is receiver bandwidth (for T_C see Section 2.1.3). The two first terms in Eq. 2.90 can be considered individually without losing the accuracy of the backscattered signal envelope analysis. Moreover, σ_c depends on dielectric properties of upper soil layer (via σ^0) and clutter area A_c, while σ_t depends on the effective length of the two-way propagation path in soil structure (i.e., through dielectric properties of consecutive layers from soil surface to target depth, the assumed height of layers and incident angle on the soil surface). The clutter area A_c represents an area in the footprint (Fig. 2.12(a)) from which distributed radar returns interfere with signal backscattered from (buried) target, i.e., the phases of individual interference (facets) are random and have uniform distribution (in $[0, 2\pi]$) and their amplitudes exhibit a Rayleigh distribution. The size of A_c in azimuth direction, i.e., $A_{c,a}$, equals to $A_{c,a} = A_{F.a}$ (Eq. 2.49), where its size in ground direction, i.e., $A_{c,e}$, should be discussed according to two cases, depending on the relation between the projection of the elevation beam-width on the ground, $A_{F,e}$ (Eq. 2.49), and the stretch of the transmitted pulse on the ground surface, ΔR_g (Eq. 2.51). If $A_{F,e} > \Delta R_g$, then the clutter area A_c is said to be pulse limited in ground direction, and $A_c < A_F$, otherwise, is said to be beam limited, and then $A_c = A_F$. Comparing

Eq. 2.49 and Eq. 2.51

$$\frac{R_{sc}\theta_{el}}{\sin\psi_g} = \frac{c\tau}{2\cos\psi_g} \tag{2.91}$$

the limit can be defined as follow [13]

$$[\text{ beam limited, } A_c = A_F \text{ }] \quad \tau\frac{c}{2R_{sc}}\tan\psi_g \gtrless \theta_{el} \quad [\text{ } A_c < A_F \text{ , pulse limited }] \tag{2.92}$$

which expresses a relation between pulse duration τ, slant range to the centre of illuminated area R_{sc}, grazing angle ψ_g and 3dB elevation beam-width θ_{el} [13]. Both cases assume that the clutter is recorded only by the main lobe of the antenna, clutter observed through the side-lose of the antenna radiation pattern is omitted. Such an assumption is correct for airborne-mounted radar operating in side-looking configuration at significant altitudes H_p, which are far higher than antenna height in ground-based air surveillance or tracking radars, where side-lobes clutter cannot be ignored. Furthermore, in calculation, instead of simple multiplication of the σ^0 by A_c (Eq. 2.90), the A_c can be decomposed into a finite number of small areas A_s (facets, of size in azimuth proportional to the lower limit of the theoretical Stripmap SAR azimuth resolution) each of statistically fluctuating σ^0, that contribute in complex way to the backscattered returns and lead to the speckle effect.

2.4 Backscattered Pulse Simulation and Analysis

Assume the linearly polarized (TE or TM) plane wave as the LFM [2, 13] pulse

$$s_t(t) = \mathrm{w}_t(t)\cdot E_0(t) = \mathrm{w}_t(t)\cdot[\, A_0(t)\, e^{\mathrm{j}(2\pi f_0 t\, +\, \pi\alpha_f t^2)}\, e^{\mathrm{j}k_x x} e^{-\mathrm{j}k_z z} e^{-\mathrm{j}\phi_0}\,], \qquad t\in[0,\tau] \tag{2.93}$$

where A_0 is the amplitude of radar pulse, f_0 is the initial frequency, ϕ_0 is the initial phase, $\alpha_f = \pm B_f/\tau$ is the LFM slope, τ is time duration of radar pulse and t is time. The w_t is time-window function used to symmetrically smooth the radar pulse at its ends. In order to ensure as realistic shape of the radar signal as possible, the Tukey window (tapered cosine window) [191] can be used with the tapers parameter $r\in[0,1]$. For $r = 0$, w_t becomes rectangular window, and for $r = 1$ it becomes a Hanning window. Table 2.3 presents the radar pulse (LFM chirp) parameters of three considered radar systems. Since f_c and B_f are known (see Tab. 1.1 for references), the $\tau = 1.00$ µs and $P_0 = 1$ kW (the RAMSES has $P_0 = 8$ kW [71]) have been assumed arbitrary and identical for all radars, where P_0 is the peak power of radar signal. While Tab. 2.3 only presents radar pulse parameters, H_p= 4000 m and θ_i= 40° for all radars, and tapers parameter $r = 0.0$ (rectangular window). Moreover, the PRF and f_s sampling frequency are assumed to be high enough to accurately perform simulation and further processing. Theoretical slant range resolution in free space equals ΔR, and is $B_f\tau$ times more finer than that resulting from a τ time duration. The P_N is the noise power proportional to σ_N^2. Figure 2.19(a) shows the LFM waveform, with positive slope a_f (up-chirp), $B_f\tau$ product and P_0 amplitude. The arrows indicate the electric field oscillations. The spectra of LFM pulses created based on the radar parameters (Tab. 2.2) are shown in Fig. 2.19(b).

Although the complete consideration about airborne subsurface imaging along L_{sar} at different carrier frequencies and bands, over various soil structure is addressed later, here, the defocusing problems, i.e., irregular attenuation, pulse distortion, envelope modulation and energy misplacement, are presented in regard to one individual probing over a identical soil structure (i.e., *HU* 360084). The AGPR simulations have been carried out taking into account the entire propagation path (radar - air - subsurface structure - air - radar) resulting from mission geometry, radar parameters and calculated EM

Table 2.3 Radar pulse parameters used in simulation

Radar Unit	f_c [MHz]	B_f [MHz]	τ [μs]	a_f [MHz][μs^{-1}]	$B_f\tau$ [−]	P_0 [kW]	ΔR [m]	P_N [dB]
Radar2	360	30	1.00	30.00	30.00	1.0	4.995	-123.14
Radar3	435	70	1.00	70.00	70.00	1.0	2.141	-119.46
Radar4	1200	75	1.00	75.00	75.00	1.0	1.998	-119.16

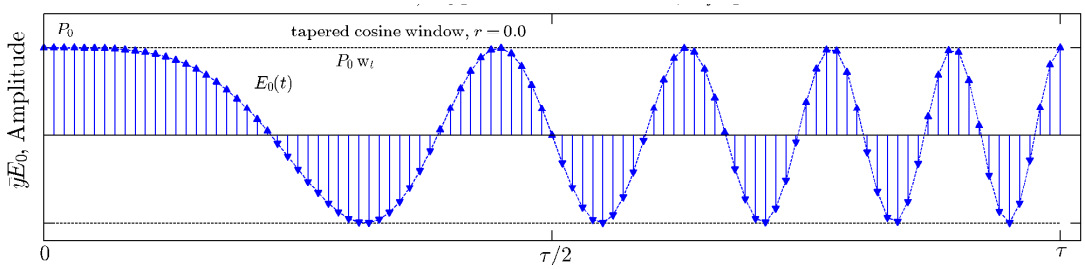

(a) Typical LFM waveform with $B_f\tau$. The amplitude is P_0, and the time-weighting function w_t is cousins tapered window, $r = 0.0$ (rectangular window).

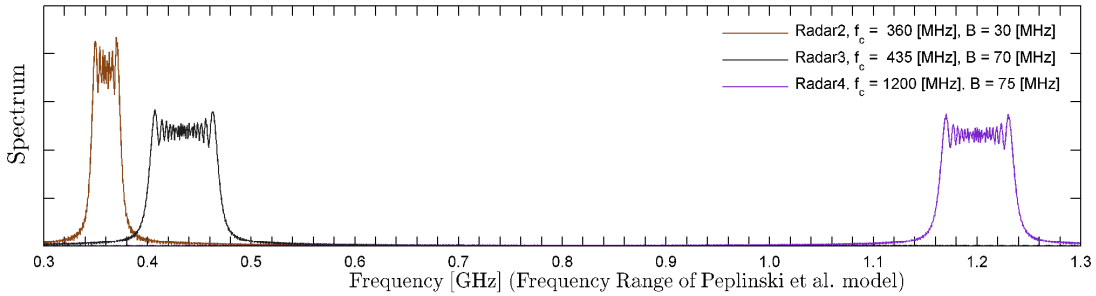

(b) Spectrum of three Airborne SAR systems (see Tab. 2.2) and its positions in the frequency range of applicability of Peplinski *et al.* model.

Figure 2.19 EM waveform used in simulation: (a) LFM pulse in time domain, (b) spectrum of three different LFM pulses created based on SAR systems parameters.

properties of soil structure. The amplitude levels of radar pulse at soil surface are determined from radar range equation [2, 192], assuming zero internal radar losses. Five isotropic point scatterers have been considered at different d_n depth, i.e., $d_1 = 0.10$ m, $d_2 = 0.50$ m, $d_3 = 1.00$ m, $d_4 = 1.75$ m and $d_5 = 2.50$ m. The coordinates of point scatterers, i.e. (x, y, z) m, are $(x_{TSL,1}, y_{TSL,1}, d_1)$ m, $(x_{TSL,2}, y_{TSL,2}, d_2)$ m, $(x_{TSL,3}, y_{TSL,3}, d_3)$ m, $(x_{TSL,4}, y_{TSL,4}, d_4)$ m and $(x_{TSL,5}, y_{TSL,5}, d_5)$ m respectively. The x_{TSL} is target surface location (TSL) in ground direction (see Fig. 2.13), and for assumed geometry parameters

$$x_{TSL,1} = \cdots = x_{TSL,5} = H_p \tan\theta_i \approx 3\ 356.4 \text{ m} \tag{2.94}$$

and y_{TSL} target surface location in azimuth direction

$$y_{TSL,1} = \cdots = y_{TSL,5} = \text{const} = y_{TSL,CPA} \tag{2.95}$$

where $y_{TSL,CPA}$ express a position along L_{sar} at which the slant distance between radar platform and buried point is the smallest, so called the closest point of approach. The point scatterers lie in one vertical line, beneath one each other at different depths. According to Snell's law and propagation path from radar to surface and between consecutive layers, for each target the surface refraction point x_{TSR} (see Fig. 2.13, the TSR abbreviates target surface refraction) is different. In general, as results from Snell's law, to reach a point at d_n depth below refraction interface, the wave for which relative refractive index n_1 is smaller should

enter into the soil earlier than the wave for each relative refractive index n_2 is higher. Thus, since $n_1 < n_2$, the $x_{TSR,1} < x_{TSR,2}$. While wave enters at oblique incidence earlier into soil, it spends less time in air, oppositely to wave which enter later. The wave travel time in soil strongly depends on its v_p propagation velocity inside soil (i.e., on $\varepsilon_{r,n}$ relative permittivity in consecutive layers) and propagation angle. Thus, total two-way delay time is the sum of total air-propagation and soil-propagation time. In strongly inhomogeneous medium, these relationships are also satisfied and they results in very curved propagation path and rapid phase changes, which are highly dependent on the incident angle θ_i at soil surface and relative refractive index $n_{n,n+1}$ between successive thin homogeneous region (many inward and outward refraction).

The Fig. 2.20 shows the normalized envelopes of backscattered signals. As can be seen, pulse distortion depends on centre (carrier) frequency f_c, bandwidth B_f and polarization as well. The irregular modulation of envelope occurs along the backscattered signal duration, and it increase when signal bandwidth increases. When the signal bandwidth is wider, the irregularities of envelope (its oscillations) are stronger. However, when the bandwidth of the Radar3 is slightly narrower than Radar4, the envelope of Radar3 backscattered signals are much more deformed (see Fig. 2.8(c) and compare the relative change of imaginary part of the CREP in operating bandwidth of these radars). Hence, the envelope modulation increases when the wider bandwidth are centralized around lower carrier frequency. In addition, attenuation increases with carrier frequency. Tab. 2.4 presents the average level of backscattered energy in relation to its average level at soil surface. While attenuation in a free spaces is similar due to slightly different slant range to $x_{TSR,d}$, the two-way attenuation in soil increases with the target depth with irregular increasing. This variability results from the changes of global impedance of the wave-guide that occurs between the ground surface and the buried scatterers. Furthermore, the T_D effective time duration of backscattered pulse (its envelope) is slightly different than the initial pulse (see Tab. 2.4 and in Fig. 2.20 the end of the envelope exceeds initial pulse duration). In general, the backscattered pulse is longer than initial radar pulse (up-chirp LFM pulse), and elongation increases non-linearly for the deeper targets. However, similarly to the envelope modulation, the relative elongation of the pulse is longer for the wider bandwidths centralized around lower carrier frequencies. The T_D is slightly varying between polarization, but the differences are less than sampling frequency. An analysis of Tab. 2.4 in comparison to Fig. 2.18 shows that for some buried objects the level of the backscattered envelope can be higher than the σ^0 surface backscattered coefficient (in particular for smooth surface case), even if σ^0 will be multiply by the nominal area of radar resolution cell. The corresponding normalized outputs of matched filter are shown in Fig. 2.21. Depending on the distortion level of the backscattered signal, the main lobe of the matched filtering output is wider, due to the mismatch between backscattered pulse and replica of transmitted signal. Additionally, the maximum of output is shifted proportionally to the changes of the effective time duration of backscattered pulse. Since for the shallowest scatterer, the output of the matched filtering beyond a slight shift is almost unaffected, the outputs for deeper scatterers are enriched with irregular side lobes. Moreover, for the deeper buried objects, the ghost target appears, with a fairly high level, and they are stronger for TM polarization.

2.5 Chapter Summary

This chapters shows the main and crucial issues, related to the EM wave propagation in highly inhomogeneous, dispersive and lossy medium, as the soil subsurface layers. Since the imaging geometry is assumed the same as for conventional SAR imaging, the considerations

Table 2.4 The average level of the envelope of backscattered pulse for three different radar and six buried targets.

T_i	Radar2. $P_N \approx -123$[dB]			Radar3, $P_N \approx -119$[dB]			Radar4, $P_N \approx -119$[dB]		
z_m[m]	P_H[dB]	P_V[dB]	T_D[μs]*	P_H[dB]	P_V[dB]	T_D[μs]*	P_H[dB]	P_V[dB]	T_D[μs]*
0.102	-22.88	-19.79	1.0002	-22.40	-22.73	1.0004	-23.28	-25.51	1.0002
0.503	-28.82	-30.70	1.0010	-29.56	-31.43	1.0020	-35.10	-36.67	1.0008
1.007	-26.90	-35.15	1.0021	-27.26	-34.30	1.0041	-32.50	-44.91	1.0016
1.756	-46.63	-47.27	1.0037	-47.33	-51.49	1.0072	-50.08	-59.22	1.0028
2.504	-51.58	-59.07	1.0053	-52.13	-60.44	1.0103	-49.36	-59.19	1.0040

*Diffrence between the $T_{D,H}$[μs] and $T_{D,V}$[μs] are smaller than the sampling period

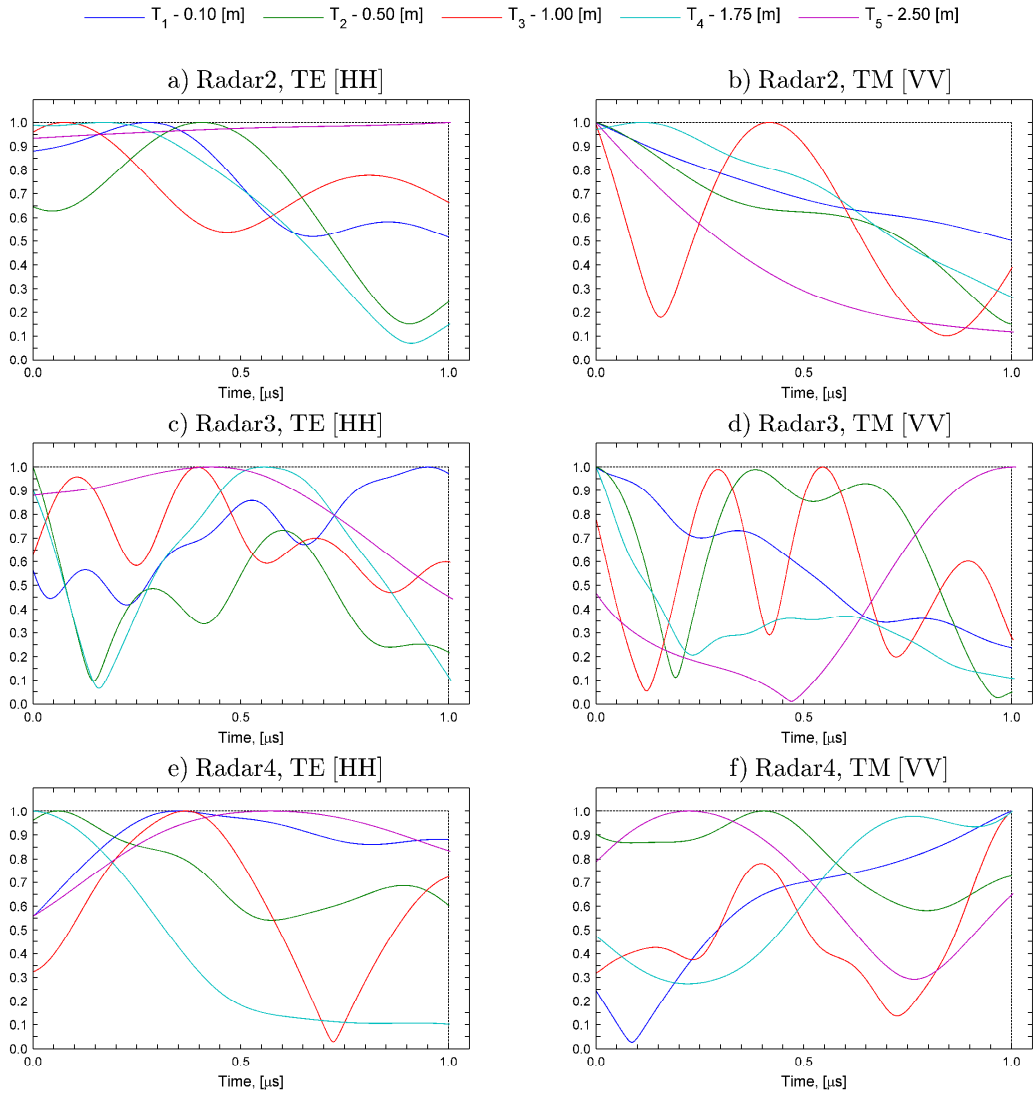

Figure 2.20 The envelope of backscattered pulse for various SAR systems for incident angle of $\theta_i = 40°$ and horizontal polarization (left) and vertical polarization (right): Radar2 (top), Radar3 (middle) and Radar4 (bottom).

are focused at the EM nature of subsurface soil layers and their impact on the radar pulse propagating inside the soil.

When the mathematical expressions defining the attenuation coefficient α (Eq. 2.82) and the phase coefficient β (Eq. 2.83) are known, the quantities as ε_r', ε_r'' and σ, are

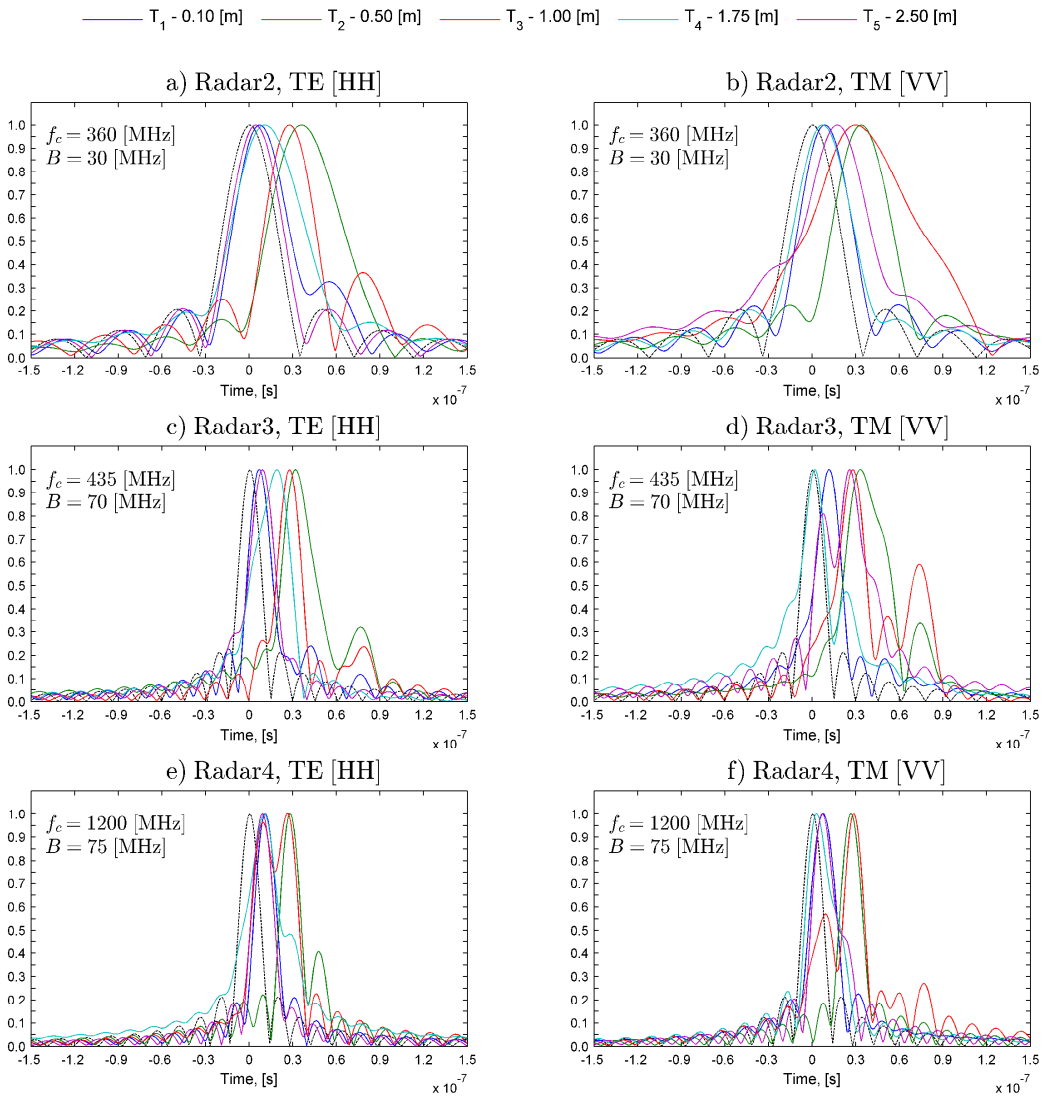

Figure 2.21 Normalized output of matched filtering for various SAR systems for incident angle of $\theta_i = 40°$ and horizontal polarization (left) and vertical polarization (right): Radar2 (top), Radar3 (middle) and Radar4 (bottom).

highly related to geological structure of the soil and moisture profile as well as frequency (Eq. 2.32, 2.40, 2.41). Hence, the geologically- and hydrologically-motivated approach for estimation of its value seems to be the correct procedure, in particular, when the soil cannot be assumed as a totally arid or semi-arid area. Therefore, the real geological databases are a valuable source of information about the soil textural composition in the depth dimension. Moreover, about the soil distribution over similar areas (i.e., parcels). In particular, such information is a key parameter in the planning of the AGPR mission over a vast area. Although the problem of moisture profile estimation is outside the scope of this dissertation, a simple numerical calculation shows that moisture profile is strongly dependent on soil type (its hydrological parameters) and its distribution in soil horizons, in particular, in depth dimension.

Furthermore, because of the dispersion, frequency-dependent attenuation and strongly curved propagation path (inward and outward refraction) through soil inhomogeneities, the backscattered signal is distorted. Irregular and frequency-dependent attenuation disfigure the envelope of backscattered pulse. Moreover, the dispersion deform its instantaneous frequency

and changes the effective duration time of the pulse. Thus, both effects in consequences, lead to energy dissipation and pulse distortion strongly affecting the output of the matched filtering and significantly degrading the spatial (range/depth) resolution. Envelope modulation of the backscattered signal leads to the ghost targets, which introduce ambiguity in the evaluation of the scatterer depth (location). Besides, depending on the EM properties and presumed height of consecutive layers, the length of the propagation path (and thus the two-way time delay) of the pulse through the soil structure depends on the incident angle at the soil surface. The correct assessment of the true target location is a major problem, in particular, for subsurface imaging at oblique incidence, where the relative depth misplacement can be relatively high compared to the true target location. Due to oblique incidence, the target misplacement occurs both in depth dimension as well in ground plane.

Finally, for backscattered pulse envelope, both effects of dispersion and frequency-dependent attenuation demonstrate the *cumulative-in-time* manner. Targets are affected twice in downward and upward propagation through soil layers, hence, the longer a signal travels in the medium (to deeper targets), the more it is distorted from the original pulse, whose replica is used in matched filtering aimed at maximization of the Signal-to-Noise Ratio (SNR).

CHAPTER 3

TIME-REVERSAL TECHNIQUE FOR SUBSURFACE IMAGING

This chapter validates the Time-Reversal (TR) hypothesis in inhomogeneous, dispersive and lossy medium. After a short introduction to the Time-Reversal technique for EM waves, the differences and limitations are presented. The dispersion and loss effects are described through an analysis of the spectrum of backscattered pulses at different carrier frequencies. Then, the TR-based focusing algorithm is described along the hypothesis of its application. A TR measurements scheme is proposed for the airborne system using for subsurface imaging in monostatic pulse-echo configuration. Differences, potential development and expectations regarding to the proposed method of measurement are discussed. The proposed acquisition methods has been verified over one soil structure from developed in ***Chapter 2****. Later, developed algorithm is numerically validated for six buried point-like targets freely distributed in the soil structure. Finally, the refocusing phenomenon is presented for all considered soil structure with the same location of the objects and for different radar parameters.*

3.1 Time-Reversal Concept

The Time-Reversal (TR) [88,90,92,95–99] technique utilizes the multipath propagations in a highly scattering medium to achieve supperresolution and to enhance detection performances. Supperresolution in the sense of resolution which is better than the classical diffraction limit (i.e., Rayleigh limit) [91]. In frequency domain, TR is equivalent to phase conjugation. However, phase conjugation applies to monochromatic waves whereas TR operates on pulsed broadband signals [97–99] in time domain. Hence, by acting in the time domain TR can operate at UWB, simultaneously providing the deeper penetration and the higher resolution in to lossy media [103] (for example, wide bandwidth centralized around low carrier frequencies). This refocusing concept exploits the reversibility (in other words, reciprocity) of the propagation medium, which means that a field and its time symmetric form can both propagate in this medium. The time domain Maxwell's equations in lossless and stationary media can be written, with taking into account the constitutive relations, where $\bar{B}(\bar{r},t) = \mu(\bar{r})\bar{H}(\bar{r},t)$ and $\bar{D}(\bar{r},t) = \epsilon(\bar{r})\bar{E}(\bar{r},t)$, as

$$\nabla \times \bar{E}(\bar{r},t) = -\frac{\partial}{\partial t}\mu(\bar{r})\bar{H}(\bar{r},t) \tag{3.1}$$

$$\nabla \times \bar{H}(\bar{r},t) = \frac{\partial}{\partial t}\varepsilon(\bar{r})\bar{E}(\bar{r},t) \tag{3.2}$$

where $\bar{E}$ is electric field intensity (volts/meter), $\bar{H}$ is magnetic field intensity (amperes/meter), $\bar{D}$ is electric flux density (coulombs/square meter) and $\bar{B}$ is magnetic flux density (webers/square meter). Moreover, $\varepsilon(\bar{r})$ is permittivity, $\mu(\bar{r})$ is permeability, t is time and $\bar{r} = \hat{x}x + \hat{y}y + \hat{z}z$ is the spatial coordinate. Solving this system of equations in terms of $\bar{E}$ electric field leads to the wave equation

$$\nabla^2\bar{E}(\bar{r},t) - \mu(\bar{r})\epsilon(\bar{r})\frac{\partial^2}{\partial t^2}\bar{E}(\bar{r},t) = 0 \tag{3.3}$$

The invariance of wave equation under TR stands that for Eq. 3.3 the time-reversed (time-symmetric) version of vector electric field $\bar{E}(\bar{r},t)$, i.e., $\bar{E}(\bar{r},-t) = T[\bar{E}(\bar{r},t)]$, is also a solution of this equation, for time-invariant $\varepsilon(\bar{r})$ permittivity and $\mu(\bar{r})$ permeability. Taking into account the intrinsic definition of four vectorial fields describing the EM waves, the TR operator $T[\ ]$ [96] transforms these fields as follows:

$$\begin{aligned} T[\bar{E}(\bar{r},t)] &= \bar{E}(\bar{r},-t), \quad T[\bar{H}(\bar{r},t)] = -\bar{H}(\bar{r},-t), \\ T[\bar{D}(\bar{r},t)] &= \bar{D}(\bar{r},-t), \quad T[\bar{B}(\bar{r},t)] = -\bar{B}(\bar{r},-t). \end{aligned} \tag{3.4}$$

As results from the reciprocity theorem, the time-reversed fields $\bar{E}(\bar{r},-t)$, $\bar{D}(\bar{r},-t)$, $-\bar{H}(\bar{r},-t)$ and $-\bar{B}(\bar{r},-t)$ are solution of the same set of Maxwell's equations as $\bar{E}(\bar{r},t)$, $\bar{D}(\bar{r},t)$, $\bar{H}(\bar{r},t)$ and $\bar{B}(\bar{r},t)$. Furthermore, reversibility implies that a pair of fields $\{\bar{E}(\bar{r},t), \bar{E}(\bar{r},-t)\}$, $\{\bar{D}(\bar{r},t), \bar{D}(\bar{r},-t)\}$, $\{(\bar{H}(\bar{r},t), -\bar{H}(\bar{r},-t)\}$ and $\{(\bar{B}(\bar{r},t), -\bar{B}(\bar{r},-t)\}$ can both propagate in medium characterized by $\varepsilon(\bar{r})$ permittivity and $\mu(\bar{r})$ permeability. The propagation of time-reversed electric field $\bar{E}(\bar{r},-t)$ corresponds to watching the initial propagation of original electric field $\bar{E}(\bar{r},t)$ in backwards mode, i.e., for backwards time. That means, that for wave propagating away from the source located at $\bar{r}_0$ to transceiver located at $\bar{r}_i$, via linking them propagation path $h_{r_0,r_i}(t)$, exists a wave which, during its propagation from $\bar{r}_i$, can precisely retrace the initial propagation path and reach the source location at $\bar{r}_0$. From reciprocity results $h_{r_i,r_0}(t) = h_{r_0,r_i}(t)$. In other words, re-transmission of initially acquired signal in time-reversed mode by transceiver mapped the LIFO (Last-In, First-Out) memory. By retracing the propagation path the energy of initially transmitted wave converge around initial source location $\bar{r}_0$.

Reciprocity features of the medium is used in TR measurements. Regardless of the relative position of the source and Time-Reversal Array (TRA) and its aperture size, the TR measurement scheme can be literally considered as the three steps linked to each other. These steps are: *Forward Propagation*, *TR Operation* and *Backward Propagation*. The first (*Forward Propagation*) and third (*Backward Propagation*) steps involve the independent transmission of EM wave through "reversible" medium and its registration. However, in *Backward Propagation* the initial receivers located in TRA aperture change its role and become a transmitters of new probing pulse. The second (*TR Operation*) step involves distinctive conversion of the initially recorded signal, and transforms it into a new probing signal. Sometimes, this step is considered as a part of the *Backward Propagation* - as a preparation of a new probing signal. These steps and the links between them are described in details in Appendix B for the measurements configuration consisting of active directional source and TRA with N elements, and where source and TRA are located on the opposite sides of the investigated area in time-independent medium homogeneous medium with the set of discrete scatterers (target and secondary scatterers).

3.1.1 TR Measurements Configurations

Within the last years, several different configurations of mutual co-location between transmitter (single antenna) and transceiver(s) (single antenna or TRA) were used in UWB TR imaging experiments, either in experimental indoor measurements or numerical considerations. Mostly, the TR experiments have been carried out as indoor measurements for short range radars and in frequency domain (rarely with pulsed signal) using the Vector Network Analyzer (VNA) as radar unit (for instance, as in [97, 99–102, 110, 111, 120]). Besides the large number of indoor measurements, UWB TR experiments were performed numerically by using the FDTD solution of Maxwell's equations in various media (for instance, as in [98, 104–106, 122, 123]). Furthermore, special attention should be given towards the TR measurement schemes which have been successively realized in limited scenario, i.e., in bistatic mode with two independent antennas (point source and point transceiver) [100] or even in monostatic mode by single antenna [99, 100, 112, 118]. In all these configurations, TR experiment involves re-transmission of the primary recorded wave with the assumption that time-reversed signal propagate towards multi-reflection and multi-refraction, as it underwent in forward transmission, will constructively interfere and focus around the location of the initial source. Moreover, as results from these experiments, TR focusing can take place at original source location (active antenna) or at the passive scatterers (illuminated by an active antenna or secondarily illuminated by surrounding scatterers).

3.1.2 TR Focusing and Effective Aperture

The Rayleigh resolution d_c is limited by relation between the wavelength λ, the real antenna aperture L_R and the distance L_d between source and target. Hence, the d_c equals

$$d_c = \alpha_a \frac{\lambda}{L_R} L_d \approx \theta_{az} L_d \tag{3.5}$$

To improve d_c at distance L_d, the antenna of longer real aperture or operating at a higher frequency (shorter wavelength) are required. However, for some radar systems, either increase operational frequency or antenna aperture is inadvisable due to design and functional constraints as well characteristic of medium under investigation. Alternatively, d_c can be improved using L_S synthetic aperture instead of L_R real aperture. While $L_S \gg L_R$, d_c significantly improves. In conventional SAR systems (Fig. 3.1(a)) operating on a direct reflection

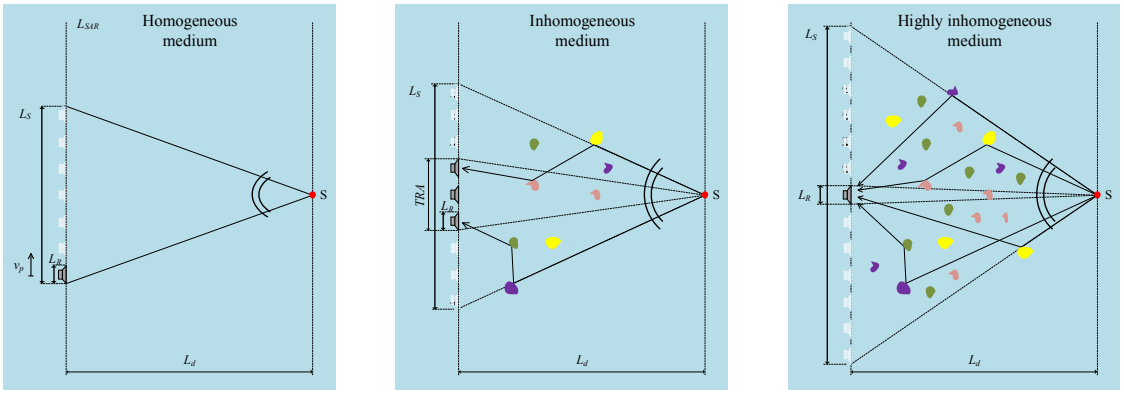

(a) Conventional SAR (b) TRA (c) TR by single antenna

Figure 3.1 Effective aperture length in different media: (a) SAR imaging in homogeneous medium along L_{sar}, (b) TRA imaging in homogeneous medium with set of discrete scatterers, (b) single antenna TR imaging in highly cluttered medium.

and neglect multipaths, the finer d_c is obtained by movement of the L_R real aperture along the synthetic aperture line L_{sar} with the platform velocity v_p. The length of synthetic aperture L_S (or *effective* aperture) correspond to total movement of radar system along L_{sar}.

In TR measurements with TRA of finite length L_{TR} (limited number of independent simultaneous transceivers) (Fig. 3.1(b)), the effective aperture length of TRA elongates as any component of the wave re-transmitted by TRA converge coherently to refocusing area centred at initial source location. The effective aperture of TRA can be identified with angular aperture, i.e., range of angles from which incoming wave components contribute in coherent refocusing. For a homogeneous medium with small number of discrete scatterers (Fig. 3.1(b)), the effective aperture is longer than for conventional SAR imaging in homogeneous medium (Fig. 3.1(a)), although the total length of TRA aperture L_{TR} is shorter than length of aperture synthesised by SAR during its movement. In highly inhomogeneous media the propagation channel can be decomposed into a large number of independent subchannels (multiple paths) [111]. Increase in the number of wave components reaching the scattering centres through sets of independent subchannels improves significantly the effective aperture length. While wave components can coherently converge from a wider range of angles at scatterer location, the TRA can be reduced to single antenna (Fig. 3.1(c)). Although the use of single antenna, the effective aperture is longer than for TRA imaging in medium with smaller number of scatterers in investigated medium (Fig. 3.1(b)). Hence, increase in the number of scatterers localized around the target under investigation results in better space and time resolution provided by a larger number of constructive interferences at the original source location.

3.1.3 Clutter Channel Characterization

Presence of clutter (radar returns from secondary scatterers) provides complex propagation medium where multipath components can arbitrarily propagate and coherently interfere around the focal point. In the majority of TR experiments the inhomogeneities were identified with different amount of discrete scatterers randomly distributed in investigated homogeneous medium (as depicted in Fig. 3.1). These scatterers are gathered around a certain area and surround the object under investigation (for instance, see [97, Fig. 2.18], [99, Fig. 3.1] or [101, Fig. 1]). Moreover, in these measurement configurations the radar operates in the same homogeneous medium as the objects and secondary scatterers are located. Slightly different model of clutter channel, used in numerical consideration [122, Fig. 1] [123, Fig. 3], divides

the space in which radar operates at two half-space, i.e., free-space and material half-space. In first half-space radar is located, and it illuminates the second half-space. Such a configuration correspond to well-known GPR system, where radar unit is located in free-space and it illuminates object placed inside soil structure through an air-ground interface. However, in these numerical experiments the soil (material) half-space is considered as homogeneous medium where only objects and secondary scatterers have different properties than surrounding half-space. In more complex versions of the TR numerical experiment, the material half-space have been modelled as continuously random media with pointwise fluctuation in its constitutive properties [98]. Then, the TR numerical experiments were carried out when TRA was located inside continuously random medium and also above it. Moreover, in some consideration the TRA was separated from investigated area contained discrete scatterers by single-layered or multi-layered plane wall, while both radar and scatterers are located in homogeneous media [119, 120]. The results of all these experiments show that the scatterers density (object and clutter) and their distribution in investigated area affects the TR performances which also depend on the operating frequencies and bandwidth of the probing signal.

Different models of rich cluttered medium was developed in Chapter 2 (Section 2.1.3), where constitutive properties of the soil structure were approximated based on geologically- and hydrologically-motivated soil model. The inhomogeneities are represented by piecewise fluctuations in the height of consecutive, geological non-identical and thin soil layers leading to piecewise fluctuations of constitutive properties. Moreover, in this model the target can be considered as an isotropic point scatterer located at the interface between two consecutive layers and with constitutive parameters as in the lower layer. Since TR experiment in medium modelled in such a way may look like Through-The-Wall (TTW) imaging, in fact it is more like a situation where object is located not behind the multi-layer wall, in free space, but inside the multi-layer wall (see Fig. 2.13) and where in front of (above) and behind (below) it a lot of layers are present. The maximum considered depth of the soil structure Z_{max} represents the total thickness of multi-layer wall, and its consecutive geological layers $l_n \in [z_n, z_{n+1})$ represent the layers forming up the wall. However, while TTW imaging process is performed in very short distances to the investigate area (much shorter than its largest dimension) and in frequency domain, the subsurface imaging by AGPR over soil surface (volume, in fact) in TR-based mode is performed at a height much longer than the maximum considered depth in soil model and at oblique incident angle.

3.1.4 Summary

Within the last year, the Time-Reversal (TR) technique have been included in many remote sensing method causing an increase in their efficiency (detection and imaging capabilities, as presented in the Section 1.2), mostly in imaging scenario. Apart from the increased efficiency, the use of TR technique led to new application and measurement methods, even in scenarios which were previously considered as unsuitable and potentially unsuccessful for remote sensing imaging.

The experimentally confirmed advantages of TR technique, derived from physical retransmission of initially recorded signals, has led to a rapid increase of TR application in many fields (as thoroughly surveyed in [103]). However, application of TR technique for airborne subsurface imaging requires intensified efforts in signal processing algorithm and necessary modifications of imaging methods. Given that the SAR missions are very costly and, for TR imaging, can require proper preparation of mission plan and modification on radar resources, the dissertation is focused on the numerical considerations on the envelope of the pulse backscattered by a theoretical point scatterer in TR imaging from airborne platform over realistic models of subsurface soil structure.

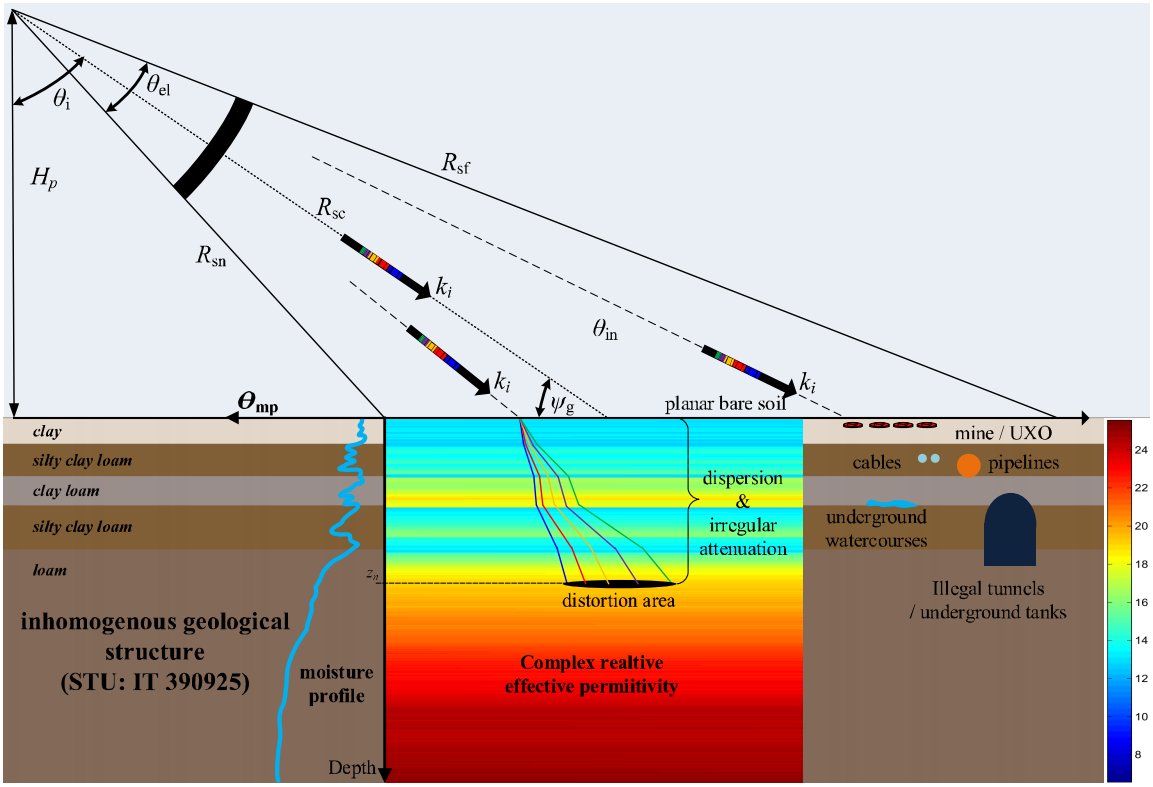

Figure 3.2 The geometry of TR-AGPR mission over non-arid area (*IT* 390925): the incident plane and intersection of soil structure.

3.2 Time-Reversal Technique for Imaging of Buried Target

Up to day, the problem of TR-based SAR imaging of buried structures located in non-arid areas from airborne platform has not been addressed either in experimental measurements or numerically. So far, however, the SAR imaging process of buried targets from airborne platforms has been performed experimentally over arid areas [63–70, 72–75] or was considered numerically [46, 78–84]; the TR-based Spotlight SAR imaging process [116] was applied for change detection at the soil surface [118] and GPR imaging process has been extended by TR procedure [122, 123]. Therefore, when the SAR technique is well known and widely used in airborne or space-borne mission, its extension by the TR technique for subsurface imaging is a new approach that requires special efforts in processing of the backscattered signals as well as in radar system modelling and designing. The signal acquisition is fraught with challenges and requires appropriate selection of radar parameters to avoid additional costs and unplanned repetition of the Time-Reversal Airborne Ground Penetrating Radar (TR-AGPR) mission [124]. The numerical considerations require relevant models of soil (as modelled in Section 2.1) and EM wave propagation inside its subsurface structure.

Let us consider the situation where the TR-AGPR operates in the low frequency (P- or L-band) and performs the strip-map SAR mission (monostatic mode, SLAR configuration) over bare surface of vast and non-arid soil volume (as in Fig. 2.11) along synthetic aperture line L_{sar}. The mission is performed at the H_p height with the υ_p platform velocity. The look angle is θ_i, and θ_{az} and θ_{el} are antenna 3dB beam-width in azimuth and elevation, respectively. Fig. 3.2 shows the incident plane and relevant geometry. The near, centre and far slant range to soil surface is R_{sn}, R_{sc} and R_{sf}, respectively. The soil is assumed as non-arid in investigate area, and the moisture profile is a function of depth (as shown in Section 2.1.2). The θ_i may vary in the range of $[25°, 55°]$, and the $\theta_{az} \in [10°, 40°]$ and $\theta_{el} \in [10°, 40°]$. During

Table 3.1 Time-Reversal Airborne Ground Penetrating Radar parameters of radar LFM pulse (up- or down-chirp, and in HH or VV polarization).

Radar Unit	f_c [GHz]	B_f [MHz]	τ [μs]	a_f [MHz][μs^{-1}]	$B_f\tau$ [–]	P_0 [kW]	ΔR [m]
Radar P1	0.400	100	1.25	80.00	125.00	1.0	1.499
Radar P2	0.400	150	1.25	120.00	187.50	1.0	0.999
Radar P3	0.400	200	1.25	160.00	250.00	1.0	0.749
Radar L1	1.200	100	1.25	80.00	125.00	1.0	1.499
Radar L2	1.200	150	1.25	120.00	187.50	1.0	0.999
Radar L3	1.200	200	1.25	160.00	250.00	1.0	0.749

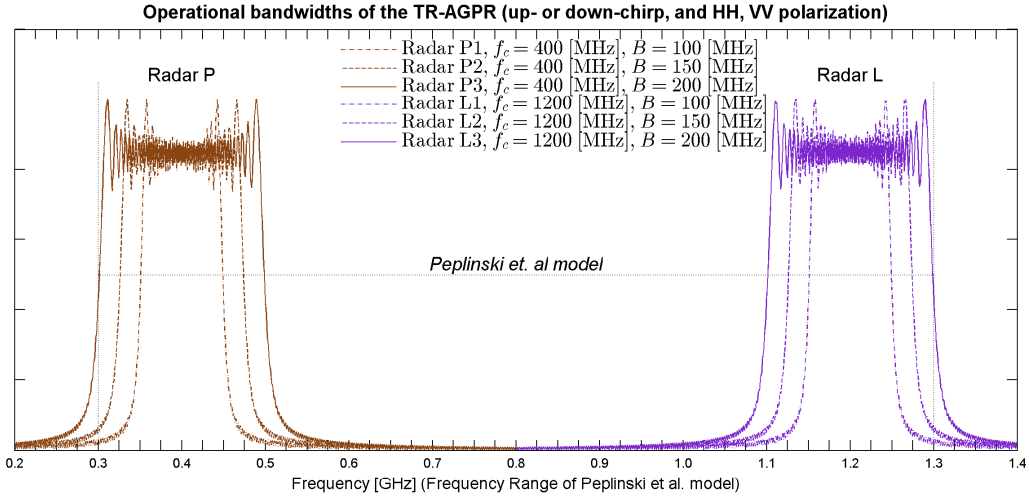

Figure 3.3 Operational frequency range of TR-AGPR

an acquisition over soil area, the TR-AGPR sends the LFM pulse (about $B_f\tau$ product, either up- or down-chirp and in two possible polarization: HH or VV) and records the backscattered signal consisting of a signal reflected from soil surface (as conventional SAR) and a weak echo from soil structure (see Section 2.3.5, Eq. 2.90). The operational parameters of TR-AGPR are presented in Tab. 3.1 and Fig. 3.3 shows the operational bandwidths of TR-AGPR, located around two assumed carrier frequencies, i.e., $f_c = 400$ MHz and $f_c = 1200$ MHz. The reconfigurable bandwidths of TR-AGPR are 100 MHz, 150 MHz and 200 MHz, which correspond to slant resolution of 1.5 m, 1.0 m and 0.75 m, respectively. Narrower bands are not taken into account because of low slant resolution, too coarse for subsurface imaging, while wider are not taken into consideration because for assumed carrier frequency the wider bandwidth leads to an overflow of considered frequency range (below 0.3 GHz or over 1.3 GHz). For such a radar resources variability, soil imaging can be performed with differentiated accuracy and under various conditions.

3.2.1 Soil Effect

The reciprocity theorem is broken in the soil due to its lossy and dispersive nature. A non-zero value of the conductivity $\sigma(\bar{r})$ and dependence of medium permittivity on frequency, $\varepsilon(\bar{r},t) = \mathcal{F}^{-1}[\varepsilon(\bar{r},f)]$, where $\mathcal{F}^{-1}[\,]$ is the inverse Fourier transform, leads to the wave equation [98]

$$\nabla^2\bar{E}(\bar{r},t) - \mu(\bar{r})\frac{\partial^2}{\partial t^2}\Big(\varepsilon(\bar{r},t)*\bar{E}(\bar{r},t)\Big) - \mu(\bar{r})\sigma(\bar{r})\frac{\partial}{\partial t}\bar{E}(\bar{r},t) = 0 \tag{3.6}$$

Comparison of Eq. 3.6 and Eq. 3.3 shows the presence of the additional term with first derivation of the $\bar{E}(\bar{r},t)$. Thus, the conventional TR operator cannot be directly applied into a lossy media. In addition, the attenuation in dispersive media, affecting each frequency component of $\bar{E}(\bar{r},t)$, depends on the medium properties. Let us describe the influence of dispersion and irregular (frequency-dependent) attenuations on the common radar LFM pulse which propagates in subsurface soil structure. For the sake of simplicity, in analysis the number of considered point scatterers (targets) is reduced to two, i.e., T_1 and T_2. The location of theoretical point scatterers is assumed as in Section 2.3.5, they lie in one vertical line, beneath each other at different depths, where $d_1 < d_2$.

Having regard to the wide variability of radar parameters, the effects of frequency-dependent attenuation and dispersion are shown separately. Taking into account the nature of Complex Relative Effective Permittivity (CREP) (Fig. 2.8), the frequency-dependent attenuation is discussed for Radar L (for B_1, B_2 and B_3, in VV polarization), where relative change of CREP is small and attenuation at its carrier frequency is higher than for Radar P. Later, conversely, the dispersion is discussed for Radar P (for B_1, B_2 and B_3, in HH polarization), where relative change of CREP is significant and attenuation at its carrier frequency is lower than for Radar L. When target imaging is performed at radio frequency, the analysis of these effects is presented on normalized envelope and spectrum of backscattered signals down-converted to baseband. Moreover, when these effects are analysed separately, in both case the refraction (inward and outward) and transmission losses at interfaces between layers are taken into account.

Frequency-Dependent Attenuation (in ideal non-dispersive medium)

Let assume the CREP (defined in previous chapter, Eq. 2.42) in non-dispersive form

$$\varepsilon_r(z,f) = \varepsilon_r'(z,f_c) - \left[\varepsilon_r''(z,f) + \frac{\sigma_{dc}(z)}{2\pi f \varepsilon_0}\right] i \tag{3.7}$$

where $\varepsilon_r'(z,f_c)$, and $\sigma_{dc}(z)$ depend only on depth and frequency-dependent attenuation is expressed through $\varepsilon_r''(z,f)$ and f term in imaginary part of Eq. 3.7. Moreover, $\varepsilon_r'(z,f_c)$ in considered radar bandwidth equals to values at carrier frequency. Hence, all frequency component of LFM pulse have the same phase velocity and both polarization and conductivity loss are taken into account. The frequency-dependent attenuation separately affects the amplitude of each frequency component of the LFM pulse. Depending on the attenuation properties of the medium (i.e. uniform or non-uniform attenuation), the amplitude of LFM characteristic spectra can change to any other shape. Fig. 3.4 shows a normalized envelope and normalized spectra of backscattered LFM pulse (both up- and down-chirp) irregularly attenuated in soil structure, for two point scatterers located at different depths. The pulse duration is assumed as $\tau = 1.25$ µs, whereas the signal bandwidth increases, as shown in Tab. 3.1. While the manner of frequency-dependent attenuation cannot be directly distinguished in time domain (left column) without knowing the frequency slope α_f of radar pulse. Therefore, the attenuation characteristic in the frequency domain can be obtained based on comparison between the initial spectrum and the attenuated signal spectrum. Comparing the normalized spectrum, it is clearly seen that a reduction of the signal bandwidth minimize the useful information about the selective nature of investigated medium. Operating in narrow bands (Fig. 3.4(a)-(b)) may mistakenly lead to assumptions of uniform (frequency independent), linearly changing (increasing or decreasing) or piecewise nature of attenuation. After increasing the operating bandwidth (Fig. 3.4(c)-(d), Fig. 3.4(e)-(f)), it appears that the attenuation oscillates and acts very selectively on the propagating pulse. However, despite the fact that irregular attenua-

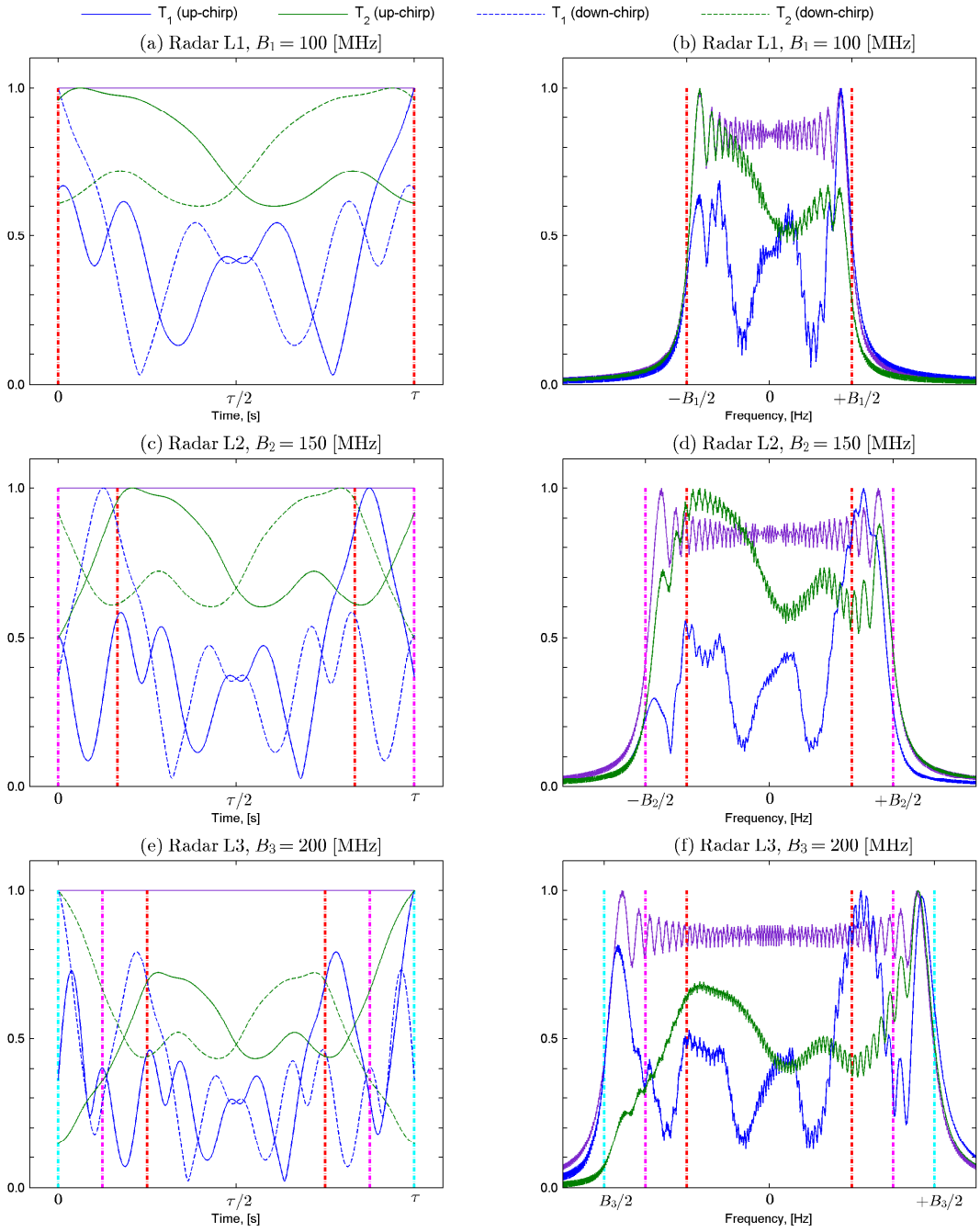

Figure 3.4 LFM pulse of Radar L (up- and down-chirp) irregularly attenuated in non-dispersive medium for three different bandwidth and frequency slope.

tion strongly degrades the output of matched filtering (see Fig. 2.20) due to the mismatch between replica of transmitted signal and received echoes, the irregularly attenuated spectrum of backscattered signal reveals important information about the selective nature of the investigated area. While $d_2 > d_1$, for $B_1 = 100$ MHz, the lower frequencies are attenuated relatively less than higher frequencies for T_2 and conversely for T_1. However, for $B_2 = 150$ MHz and $B_3 = 200$ MHz, in lower part of this bands the lower frequency are attenuated relatively stronger for deeper target T_2 than shallower T_1, and in the upper part additional oscillations occurs. Therefore, the attenuation characteristic of material medium should be acquired (or known) in a wide range of frequency and much below the presumed maximum depth of imaging. This information can be re-used in future investigations, for instance, in selective

amplification of selected frequency component through bandwidth of probing signal. Nevertheless, a priori knowledge of attenuation properties (for instance, based on the physical soil model, as shown in Section 2.1.3) can be used to selectively amplify the attenuated frequency components in order to reach the desired shape of backscattered pulses envelope.

Dispersion (in ideal uniformly attenuated medium)

Let modified the CREP (defined previous by Eq. 3.7) to constant attenuation form

$$\varepsilon_r(z,f) = \varepsilon_r'(z,f) - \left[\varepsilon_r''(z,f_c) + \frac{\sigma_{dc}(z)}{2\pi f_c \varepsilon_0}\right] i \cong \underbrace{\varepsilon_r'(z,f) - \left[0 + \frac{0}{2\pi f_c \varepsilon_0}\right] i}_{\text{lossless medium}} \tag{3.8}$$

where $\varepsilon_r''(z,f_c)$ in assumed radar bandwidth equals to values at carrier frequency, and f_c term is assumed in imaginary part of Eq. 3.8, hence, both losses are taken into account but as constant over the considered frequency band. In ideal lossless medium $\varepsilon_r''(z,f_c) = 0$ and $\sigma_{dc}(z) = 0$. Dispersive characteristic of the medium reveals within $\varepsilon_r'(z,f)$. In a dispersive medium, each wave component has a different phase velocity, decrease as the square root of $\varepsilon_r'(z,f)$ in comparison to the c speed of light in vacuum. Depending on the dispersion characteristic of the medium and frequency slope α_f of transmitted LFM pulse, the duration of backscattered signal can either increase or decrease. Thus, the LFM pulse (whether up- or down-chirp) travelling through the dispersive medium does not maintain a constant time-frequency form ($B_f\tau$, as defined at the time of its generation). Fig. 3.5 shows the real part and normalized spectrum of two backscattered LFM pulses (up- and down-chirp) dispersed in soil structure (for Radar P with B_1, B_2 and B_3). For the modelled CREP (see Fig. 2.6-Fig. 2.9), when the higher frequency components travel slower than those of lower frequency, then the duration time of up-chirp increases (Fig. 3.5(a)-(c)-(e)) while for down-chirp it decreases (Fig. 3.5(b)-(d)-(f)). For up-chirp shorter wavelengths lagging behind longer, and for down-chirp longer wavelength catching up shorter. While dispersive effect cumulates in time, and affects LFM pulse during downward and upward propagation, the change of backscattered signal duration (increase or decrease) is greater for deeper objects, $d_2 > d_1$. In the modelled structure, for the same $B_f\tau$ and opposite α_f, compression of the inner frequency structure of the pulse is slightly stronger for down-chirp ($\alpha_f < 0$) than its extension for up-chirp ($\alpha_f > 0$) (clearly visible in the lower limit of the pulse band). The dispersion effects, in addition to changing the inner time-frequency structure of signal, leads to the periodically oscillations of LFM spectrum (Fig. 3.5(g)-(h)-(i)), which enhance around low frequencies with increasing signal bandwidth. Similarly, as for frequency-dependent attenuation in non-dispersive medium, extension of the signal bandwidth reveals influence of dispersion in wider range than analysis of narrower signals. These changes are also proportional to the operational frequency of the radar system, as well the sampling frequency affects the possibility of its registration. While in the considered frequency range, the variation of CREP decreases with increasing frequency (for both parts), for the same operational bandwidth B_f located at opposite ends of frequency range defined by Peplinski *et al.* model, the inner time-frequency form of received backscattered pulse is less deformed for higher carrier frequency (smaller variations of phase velocity over constant bandwidth).

3.2.2 TR technique for soil structure

In soil structure, besides the inward or outward refraction at interfaces between layers, frequency-dependent attenuation and dispersion occur simultaneously, so they should be

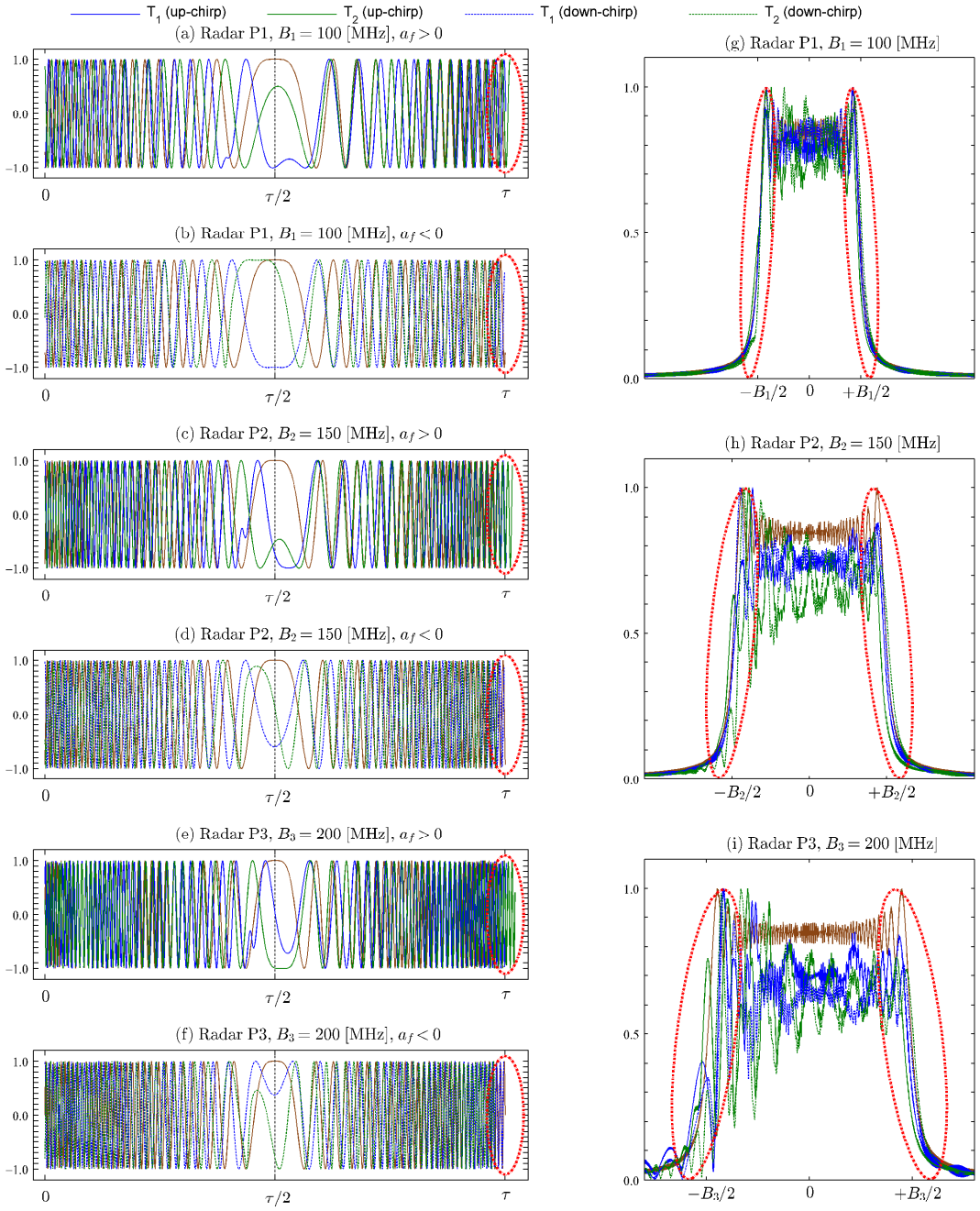

Figure 3.5 LFM pulse of Radar P (up- and down-chirp) dispersed in regularly attenuated medium for three different bandwidths and frequency slopes.

together taken into account in the consideration of EM wave propagation. The backscattered signal registered from buried point scatterer, at d depth, provide an information about both effects on envelope and inner time-frequency form of the transmitted pulse. Considering above-described effects, the three aspects are crucial for use of the Time-Reversal based technique for subsurface imaging:

- Comparing Fig. 3.4, attenuation does not depend on frequency slope α_f and acts in the same way on up-chirp ($\alpha_f > 0$, rising frequency) and down-chirp ($\alpha_f < 0$, falling frequency).

- Comparing Fig. 3.5, dispersion acts nearly inversely in the time-frequency structure of the propagated pulse. For constant (in time) medium constitutive parameters, it causes an increase in the pulse duration for up-chirp ($\alpha_f > 0$) or a decrease in the pulse duration for down-chirp ($\alpha_f < 0$).
- Unfortunately, when the attenuation strongly affects higher frequencies and the dispersion dominates in lower frequencies, the UWB signals suffer twice their impact leading to unforeseen modulation of backscattered pulse envelope and changes in its time-frequency inner structure.

Therefore, taking both previously described effects into account, it can be assumed that the mirrored (time-revered) re-transmission of the once irregularly attenuated and dispersed signal through the same medium, with selective amplification of each frequency components, allows restoration of the initial pulse (its inner time-frequency structure) with very high precision. Based on the attenuation characteristics obtained in a first transmission with initial LFM pulse, in re-transmission each frequency component can be selectively over-amplified (i.e., amplified twice as initially attenuated) to provide shape of re-attenuated LFM pulse spectrum as similar as the characteristic spectrum of the initial LFM pulse. Hence, the once changed shape can be retrieved with a fairly high accuracy after re-transmission through the same medium but with reversed internal frequency changes (down- or up-chirp). Since the soil affects the probing pulse from shallower layers and the effective propagation distance of pulse is twice as surface-target distance (taking into account the number of inward and outward refractions), the restoration should start when the re-transmitted pulse enters into the soil upper layers and stop exactly when pulse backscattered by the buried target leaves the upper soil layers. Hence, the restoration, similarly as distortion, takes place in *cumulative-in-time* manner, and in both cases the pulse reflection from the buried objects does not stop the propagation, only reverses its direction.

Furthermore, signal used in re-transmission is preferably matched to the investigated medium, since it has been created based on an information acquired directly in the initial transmission. Contrary to a priori information assumed about the soil structure, that may be limited, information acquired in initial probing is obtained in strictly defined frequency range as well as in the mission geometry (platform height H_p, incident angle θ_i, etc.), and therefore its potential value is far-reaching for soil imaging. Additional acquisition in time-reversed manner provides the method for optimal adaptation of the radar waveform to the medium under investigation (i.e., radar waveform diversity for optimal use of radar resources [193] and propagation and scattering phenomenon to reveal a certain information about the investigated medium). As shown in [194], the shape of radar pulse, and not only its energy distribution along, can have a significant effect on targets detection, where their backscattered response $s_r(t)$ cannot be modelled as a simple time-delay t_D and amplitude-scaled α copy of transmitted signal $s_t(t)$, $s_r(t) \neq \alpha \cdot s_t(t - t_D)$. For soil imaging, since the assumption about point target is valid under certain conditions, the propagation and scattering phenomenon is complex, and $s_r(t) = \alpha(t, \bar{r}) \cdot s_t(t - t_D(t, \bar{r}))$. Hence, searching of the optimal waveform for buried target imaging seems to be rational, and re-use of initially gained information is the best way for optimal waveform designing, that is self-adapted to each soil structure and complex buried targets scenario.

However, this hypothesis assumes an unchanging medium as well as the same location of the transmitter and receiver in the initial transmission and the secondary re-transmission. The first condition of invariant medium is valid since the TR-AGPR acquisition along L_{sar} (understood as a single flight) takes up less than few minutes, and thus, the geological and hydrological parameters impacting the value of CREP can be assumes as a constant. Unfortunately, since the radar is in motion, at the altitude H_p and with v_p velocity, the second

condition is not satisfied. However, proper selection of PRF, antenna beam-width (θ_{az}, θ_{el}), and consideration of the fact that $H_p \gg Z_{max}$ (and $Z_{max} \gg h_n$), where Z_{max} is maximum depth of penetration determined by the purpose of the mission, allow the presumption that radar motion at H_p slightly affect the (re-)focusing effect. Since the radar platform velocity v_p is much slower than speed of light in free space c as well in soil, the backscattered returns are recorded almost at the same position as transmission occurred. As shown in [110], the relative motion in measurement scenario can be identified with changing media, and where minor perturbation in measurement position, relative to inhomogeneous medium, have few effects on TR imaging.

Moreover, this hypothesis does not assume dispersion compensation [195] performed on initially recorded backscattered signals before its re-transmission, since the goal of re-transmission in TR manner is to accurately restore the initial pulse instead of focusing the buried target at its location. In such a defined way, the pulse restoration is presumed simultaneously from all scatterers in entire observed soil area (inside swath defined by antenna footprint on the ground, and down to presumed imaging depth) not only in small soil sub-areas (soil sub-volumes, as in [196]), i.e., region of interest extracted from investigated soil where targets are expected. Nonetheless, even supposed information about type, material, location and orientation of objects under investigation as well about the surrounding soil structure, may be essential for mission planing (i.e., geometry, antenna pattern and gain, radar parameter, ect.) and use of radar resources.

3.3 TR-Based Refocusing Algorithm

The formulation presented here refers to an acquisition at fixed position u_n along L_{sar}. Whereas, as in conventional SAR imaging, it is repeated N_s times along L_{sar} over a distance resulting from the $u_n = n{\cdot}v_p{\cdot}\mathrm{PRF}^{-1}$, where $n = 0, 1, ..., N_s - 1$.

3.3.1 Description

As results from TR principles, TR measurement schemes is organized as two successive and implicitly linked probing (see, for example, Appendix B), where a single probing is composed of its own signal transmission and registration. Thus, TR measurements scheme for TR-AGPR can be in general represented as two pairs of signals:

- the first pair of $[s_t^f(t),\ s_r^f(t)]$ representing the transmitted $s_t^f(t)$ and recorded $s_r^f(t)$ signal in Forward Probing (hereafter referred as FP), and
- the second pair of $[s_t^{tr}(t),\ s_r^{tr}(t)]$ representing the transmitted $s_t^{tr}(t)$ and recorded $s_r^{tr}(t)$ signals in Time-Reversal Probing (hereafter referred as TRP).

Furthermore, $s_t^{tr}(t)$ depends directly on $s_r^f(t)$ as follow

$$s_t^{tr}(t) = \mathcal{F}^{-1}[K_a S_r^{*f}(\omega)] \tag{3.9}$$

where K_a is an energy normalization factor, $S_r^f(\omega) = \mathcal{F}[s_r^f(t)]$, $\mathcal{F}[\ ]$ is the Fourier transform and * denotes conjunction. As previously mentioned, this time-frequency dependence between $s_t^{tr}(t)$ and $s_r^f(t)$ is aimed at retracing the signal propagation path and coherent energy restoration phenomenon. Hence, the two remaining signals, i.e. $s_t^f(t)$ and $s_r^{tr}(t)$, represent an input and an output of TR measurement scheme, performed at fixed position u_n along L_{sar}. The first of them, $s_t^f(t)$ is a well-known radar waveform with $B_f\tau$ product. In original

form of TR measurements scheme, the second, $s_r^{tr}(t)$ is supposed to represent the temporal and spatial refocused energy. However, for TR-AGPR, it is supposed to represent the signal with temporally and spatially restored envelope and inner structure, highly similar to the initially transmitted pulse. Therefore, the (re-)focusing algorithm consists of Matched Filtering (MF) performed on a restored signal, i.e., the backscattered signal, and replica of initially transmitted signal $s_t^f(t)$ for providing a high resolution (inversely proportional to the signal bandwidth) and maximizing Signal-to-Noise Ratio (SNR). More precisely, the three different MF may be carried on all signals registered in two steps of TR-based measurements and performed in the baseband frequency range. Namely, arranging chronologically:

1. after FP, between its own $s_t^f(t)$ input and $s_r^f(t)$ output,
2. after TRP, between its own $s_t^{tr}(t)$ input and $s_r^{tr}(t)$ output,
3. Cross Matched Filtering (CMF), between $s_t^f(t)$ input and $s_r^{tr}(t)$ output of TR measurement scheme.

In this operations, (1) correspond to range compression typical for SAR imaging. Although, important in terrain reflectivity imaging, it can be omitted in TR-AGPR, whereas only $s_r^f(t)$ is used for optimal waveform designing, i.e., $s_r^f(t) \Rightarrow s_t^{tr}(t)$ (Eq. 3.9). Second operation (2), can be also identified as range compression, and similarly as (1) can be omitted. Both FP and TRP are not fully independent probing. Unlike to them, (3), which components does not come from one probing in the strict sense, represents a proper CMF performed in order to ensure range compression, i.e., (re-)focusing objects on their true (slant) distance from the platform.

In addition, while $s_t^f(t)$ represents initial radar pulse, the $s_r^f(t)$, $s_t^{tr}(t)$ and $s_r^{tr}(t)$ can represent general radar returns in FP, new probing signal and general radar returns in TRP, respectively, or, they can be identified within a more thorough analysis as signals related to a one buried point.

3.3.2 Measurement Scheme

Since the proposed algorithm is described, let analyse its exemplary scheme shown in Fig. 3.6 in some aspects. This figure presents a possible time-schedule of TR-AGPR functionality at a particular position along the synthetic aperture with the use of only one antenna for transmission and registration. Naturally, other schedules of TR scanning and methods of its execution can be assumed. For example, adding a second antenna, which will be addressed later.

Forward Probing (FP): In usual transmission of pulse-echo SAR systems, backscattered signals are recorded in time t_w between T_{sn} and T_{sf}, corresponding to the near and far slant range, R_{sn} and R_{sf} (see Fig. 3.2), respectively

$$T_{sn} \leq t_w \leq T_{sf} \Longrightarrow \frac{2 \cdot H_p}{c \cos\left(\theta_{in} - \frac{\theta_{cl}}{2}\right)} \leq t_w \leq \frac{2 \cdot H_p}{c \cos\left(\theta_{in} + \frac{\theta_{cl}}{2}\right)} \tag{3.10}$$

Therefore, the time period T_w, intended for the terrain returns registration is $T_w = T_{sf} - T_{sn}$. However, T_w should be increased by a term τ added to fully record whole backscattered returns from the far slant range R_{sf}, hence, $T'_w = T_w + 2\tau$. In same scenario, the time period T'_w can be too short for registration of the sufficient amount of backscattered energy derived from internal reflections inside the soil on its inhomogeneities, as

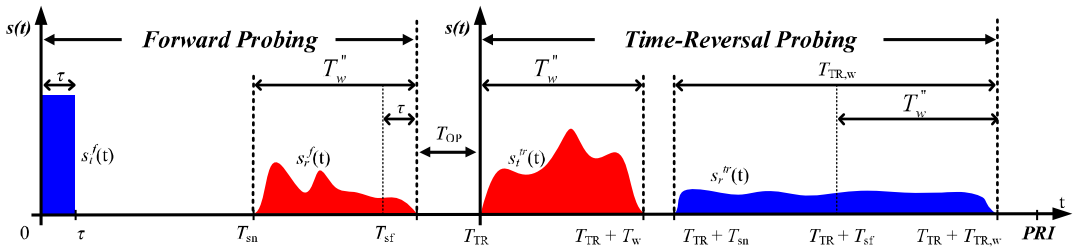

Figure 3.6 Schedule of proposed TR-based acquisition at a given position along synthetic aperture line.

well as from the buried objects (structures). In fact, as outlined in Section 2.1.3, variations of the relative complex dielectric constant ϵ_r result in changes of wave propagation velocity v_s in soil, which is locally in layer l_n given by $v_{s,n} = c/\sqrt{\epsilon_{r,n}}$. In consequence, variation of v_s affects the effective depth of propagation. Moreover, we have to consider what effective depth of penetration it is possible to achieve and what effective depth of penetration is desirable from the mission point of view. For mine detection, small penetration depths are sufficient (to tens of centimetres), but for pipeline monitoring or ancient remains, higher depths are required (to several meters). Therefore, T_w' should be further increased by the term representing the Sufficient Penetration Time T_{sp}, and now, $T_w'' = T_w' + T_{sp}$. The value of T_{sp} should be selected according to the TR-AGPR application and a priori information about the type of soil, as seen in Section 2.1.3. In addition, this problem is gaining importance when the ratio of T_w''/T_{sp} decreases and T_{sp} has greater contribution T_w'', i.e., for low incident angles θ_i with a small θ_{el}. An appropriate choice of time window T_w'' and its location at the time axis is one of several issues in proper selection for TR-based buried object imaging, that is dependent on the assumed SLAR geometry.

Time-Reversal Operation (TRO): This step is the formation of a new radar waveform based on the backscattered signal recorded in the previous step. All tasks in this step consist only of signal processing in the baseband frequency range. Effective duration of this step T_{OP} is dependent on the hardware performance of the radar and the efficiency of signal processing algorithms. As previously presented, TR operation is equivalent to a mirror operation, i.e. last in first out, and performed in time window T_w. In the frequency domain, this operation corresponds to the spectrum conjugation (as defined by Eq. 3.9). Energy Normalization (EN) provides compensation for energy losses and keeps average energy at a constant level [100]. The normalization factor is given by $K_a = \sqrt{\frac{E_s}{E_w}}$, where E_s is total energy of the transmitted radar signal and E_w is total backscattered energy from soil structure.

Time-Reversal Probing (TRP): This key step starts at T_{TR} (see Figure 3.6) and consists of re-transmission and backscattered returns registration. The duration of signal transmitted in TRP is equal to T_w''. Additionally, $T_{sn} \gg T_w''$, has to be satisfied in order to prevent signals overlapping and uncertainty of returns registration. Due to $T_w \gg \tau$, the radar blind zone for TRP is greater than for FP. In this acquisition, the time period $T_{TR,w}$ intended for backscattered returns registration is considerably longer than T_w.

An analysis of Fig. 3.6 have shown that the radar parameters (i.e., pulse time τ and peak power P_0) and mission geometry (as H_p, θ_i and θ_{el}), used in this initial transmission and acquisition, determine further performances of the second transmission and acquisition in Time-Reversal Probing (TRP).

3.3.3 Differences, Challenges and Expectations

Before the numerical verification of the proposed algorithm for different locations of buried point scatterer in various soil types and radar parameters, let us describe the differences, challenges and expectations related to the proposed TR-based acquisition methods and restoration (refocusing) algorithm, both in relation to conventional SAR acquisition and TR technique.

Most of all, the extended measurement times at individual positions along synthetic aperture line L_{sar}, more than twice that of the conventional SAR, due to $T_{sf} \leq (T_{sn} + T_{TR,w})$, decrease the value of PRF. For TR-AGPR mission value of PRF is considerably lower than in conventional SAR missions. A decreasing PRF value may result in the less precise reconstruction of the azimuth reference signal, and thus, deterioration of the azimuth resolution of synthesised images. Hence, a proper selection of PRF is the important issue in the TR-AGPR system, in particular, to perform the accurate synthesis of the antenna along the radar track. Since PRF depends on the radar parameters and mission geometry (see Eq. 2.52, Eq. 2.53), it also depends on the radar hardware performance (via T_{OP}). Therefore, assuming the full ability to control these parameters within certain ranges, the PRF may be properly selected in relation to the mission purposes. Besides that, current SAR systems work with PRF being much higher than its lower limit, as well as lower than its upper limit. Hence, proper selection of PRF is crucial for single antenna configuration. When two antennas are considered, in the front and rear part of airborne platforms, spaced by a distance of L_{TRO}, this problem becomes potentially easier to resolve by task separation. Front antenna is used only in FP and rear antenna only in TRP. Then, each probing is performed in monostatic configuration. Assuming a sufficient length of the airborne platform and appropriately selected velocity v_p and PRF, the TRP can be repeated exactly in the same place where related FP was initially made. Moreover, the upper limit on the time T_{OP} devoted to perform the Time-Reversal Operation (TRO) equals $T_{OP} = L_{TRO} \cdot v_p^{-1}$, and is higher than that obtained with only one antenna. On the other hand, the use of two antenna requires separation between FP at u_l position and TRP at u_k position, where $N_s - 1 > l > k > 0$, because both antennas transmit and receive signals within the same bandwidth. Another advantage of the task separation is possible to use two different transmitting and receiving microwave circuits of various gains and dynamic range, which may be different during a mission but controlled by the same radar unit.

Moreover, the TR experiment in the original form (see Appendix B), specifies location of the transmitter and receiver on opposite sides of the scattering environment (regardless of whether two single antennas or two TRA are used). Such a configuration is not appropriate for soil imaging from airborne platform, as well for GPR measurements, due to natural impracticality. Within the last years, several configurations of TR experiment (various transmitter-receiver configurations) were used: monostatic pulse-echo [115, 116] or bistatic pulse-echo [109, 123]. Having regard to the assumed TR-AGPR mission configuration (i.e., one antenna for signal transmission and backscattered echo registration), the TR experiment for an airborne platform can be carried out only in the pulse-echo configuration, either in single antenna or two antennas monostatic manner. Whereas the aim of TR approach is a pulse reconstruction instead of energy focusing at buried target location, the TR reflection mode is naturally suitable for airborne subsurface imaging than transmission mode (which is described in Appendix B).

Furthermore, the scheme of TR-based acquisition, proposed in previous section, differs considerably from a typical scheme of TR-based experimental measurements often encountered in the literature (for example, as in [99–101]) in one field. Namely, the conventional TR scheme assumes an additional (pre-initial) probing of the clutter channel as measure of the

clutter response only, i.e. when the target is absent in the investigated scene. In the case of TR-AGPR, the presence of objects in the soil is difficult to identify due to their invisibility and buried nature, only some assumptions can be undertaken about its presence (based on terrain maps or other information). Nonetheless, an additional flight and pre-acquisition over terrain, with the drawback of increasing the cost of the TR-AGPR mission, may provide some useful information about backscattered terrain returns, σ^0, which are identified as clutter (as defined in Section 2.2 and Section 2.3.4).

In spite of these differences and challenges, the expectations of the TR approach for AGPR imaging remains the same. Due to complex scattering phenomena in soil structure, the time-reversed signal (selectively over-amplified) should coherently cover and exploit the original multipath propagation, as underwent in initial propagation, to provide a temporal and spatial backscattered pulse restoration in dispersive and loss medium, which in turn should result in energy focusing and resolution improving.

3.4 Results and Discussion

This section validates the proposed refocusing algorithm at particular position u_n along L_{sar} with regard to the envelope of pulse backscattered by a buried point target, separately for each of them. However, for verification of the TR-based algorithm the platform height $H_p = 2$ km and $\theta_{az} = 5°$ were purposely assumed in unrealistic way, in particular, in relation to θ_{az}.

3.4.1 TR-AGPR Simulation Setup

Let us assume the situation where the six buried point targets T_i are present in observed area at different coordinates $(x_i,\ y_i,\ z_i)$ (arbitrarily arranged in z depth with $\Delta_z \approx 0.275$ m and randomly in the x and y, i.e., at various observation and azimuth angles from the position u_n) as shown in Fig. 3.7 and Tab. 3.2. In general, for a assumed H_p and θ_{az}, the $\theta_i = 40°$ and $\theta_{el} = 40°$. Hence, the incident angles range equals $20° - 60°$ (maximum possible) and grazing angle ψ_g decreases from 70° to 30°. The lines representing R_{gn}, R_{gc} and R_{gf} are marked at soil surface, in both approximated soil structure (Fig. 3.7(a)) and CREP (Fig. 3.7(b)). The buried points location is projected onto the corresponding cross-section of soil substructure as well inside the footprint at soil surface. The dashed lines indicate the ground range between location of target at surface $(X_{TSL},\ Y_{TSL},\ 0)$ and nadir platform location $(0,\ u_n,\ 0)$. For assumed pulse duration, $\tau = 1.25$ µs (Tab. 3.1), the slant time t_w, during which the backscattered signal is recorded in FP, is limited as follows

$$T_{sn} \leq t_w \leq T_{sf} + 2\tau + T_{sp} \tag{3.11}$$

in accordance with the considerations outlined in Section 3.3.2. Substituting assumed values, the intervals $T_w \in [14.202,\ 26.691]$ µs, $T''_w \in [14.202,\ 28.266]$ µs, $T_{sp} \approx 0.325$ µs and $T_{sn} > T''_w$, the ratio $T''_w/T_{sp} \approx 43.27$. Since soil is assumed as a planar structure and locally infinite in x and y, for assumed platform height, observation and azimuth angles, the slant range $r(t)$ from platform to target can be considered along flat distance from nadir platform positions at ground plane $(0,\ u_n,\ 0)$ to target location at soil surface $(X_{TSL},\ Y_{TSL},\ 0)$. Therefore, applying Pythagoras' theorem to layered medium with multiple inward and outward refraction (see Fig. 2.13), slant range can be decomposed as the sum of two factors

$$r(t) = \sqrt{H_p^2 + D_{TSR}^2(t)} + \sum_{0 \leq n < z_t} \sqrt{h_n^2 + D_n^2(t)} \tag{3.12}$$

Table 3.2 Coordinates of buried points scatterers located in observed area. Dimension subscribed as $_{TSL}$ is a coordinate on the ground plane XY, when $z_i = 0$ (see Fig. 2.13).

Target	T_1	T_2	T_3	T_4	T_5	T_6
x_i $[m]$, $[X_{TSL}]$	1739.19	1051.01	2283.20	3103.36	3177.98	828.80
y_i $[m]$, $[Y_{TSL}]$	299.67	298.12	298.56	298.58	299.38	298.36
z_i $[m]$, *depth*	0.102	0.385	0.654	0.929	1.202	1.483
$\theta_{i,TSL}$ [°]	41.01	27.72	48.78	57.20	57.82	22.51

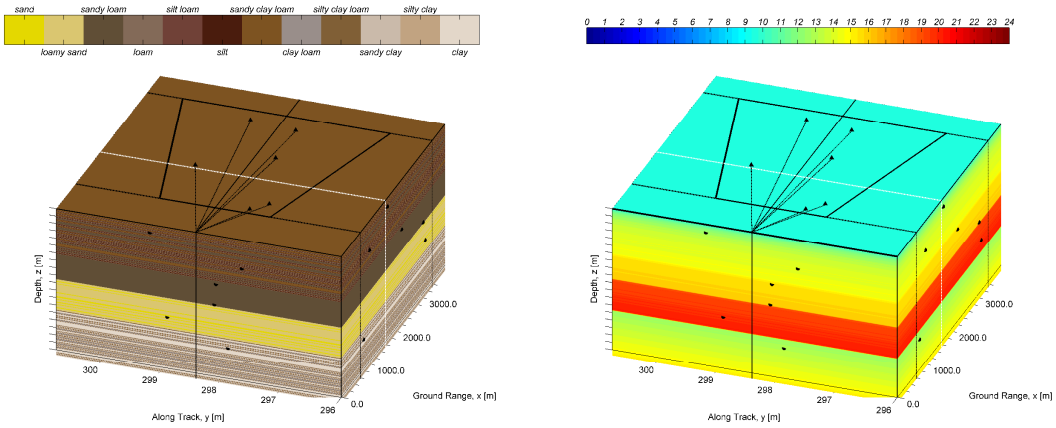

(a) Segment of approximated soil strucutre (b) Corresponding CREP (at carrier frequency)

Figure 3.7 Target location in soil structure (the proportions between x, y, z are purposely disfigured).

where $D_{TSR}(t)$ is a flat distance (on the soil surface) from platform $(0,\ u_n,\ 0)$ to refraction point at the soil surface $(X_{TSR},\ Y_{TSR},\ 0)$, that varies in general with t, incident angle θ_i and u_n platform position. The second term $\sum_{0\leq n<z_t}$ represents the total travelled distance in the soil structure, from refraction point at surface $(X_{TSR},\ Y_{TSR},\ 0)$, through successive refraction point at consecutive soil interfaces $(X_{TSR,n},\ Y_{TSR,n},\ -z_n)$ and to true target location $(X_{TSL},\ Y_{TSL},\ -z_d)$. The $D_n(t)$ is a flat distance on a flat interface between to consecutive soil layer l_n and l_{n+1}.

While X_{TSL} and Y_{TSL} are constant during acquisition, the X_{TSR} and Y_{TSR} changing depending on the target location $(X_{TSL},\ Y_{TSL},\ -z_d)$. In two half-space medium, with constant $\varepsilon_r(z, f) = \varepsilon_r$ (as modelled in [58, 78, 79, 81, 196]), Eq. 3.12 simplifies to two terms, without $\sum_{0\leq n<z_t}$ term, where only one inward refraction occurs at the soil surface. Since $D_{TSR}(t)$ at the soil surface is changing, the incident angle $\theta_i(t)$ at the soil surface is changing as well, $\theta_i(t) = \theta_{i,a}(t) = \arctan(D_{TSR}(t)/H_p)$. As result of Snell law, the propagation angle $\theta_{i,n}$ in l_n layer can be derived from

$$\theta_{i,n}(t) = \arcsin\left(\frac{\sqrt{\varepsilon_{r,a}}}{\sqrt{\varepsilon_{r,n}}}\sin\theta_{i,a}(t)\right) \tag{3.13}$$

Substituting $\varepsilon_{r,a} = 1.0 - 0i$ into Eq. 3.13, leads to

$$\theta_{i,n}(t) = \arcsin\left(\frac{1}{\sqrt{\varepsilon_{r,n}}}\sin\left(\arctan(D_{TSR}(t)/H_p)\right)\right) \tag{3.14}$$

Furthermore, when $\sqrt{h_n^2 + D_n^2(t)} = R_n(t) = h_n(\cos\theta_{i,n}(t))^{-1}$, Eq. 3.12 changes as follow

$$r(t) = \sqrt{H_p^2 + D_{TSR}^2(t)} + \sum_{0}^{z_t} h_n \left[\cos(\arcsin((\sqrt{\varepsilon_{r,n}})^{-1} \sin(\arctan(D_{TSR}(t)/H_p)))) \right]^{-1} \quad (3.15)$$

Since the estimation of $r(t)$ it laborious, it is carried out in an iterative manner for each buried point and at each position u_n along L_{sar}. Moreover, the calculation are performed when the refraction point at soil surface (X_{TSR}, Y_{TSR}, 0) leading to buried object location (X_{TSL}, Y_{TSL}, $-z_d$) lies inside the antenna footprint at the soil surface. Thus, at constant slant range, the deeper located targets are observed longer than shallowly located targets.

Throughout all the simulation, two radars are used, i.e., Radar P3 and Radar L3 (see Tab. 3.1), both of $B = B_3 = 200$ MHz (for a finer resolution). The tapers parameter r of the $\mathrm{w}_t(t)$ time-window function (see Eq. 2.93) equals $r \approx 0.21$. The proposed algorithm was verified for:

- two different chirp slopes ($\alpha_f > 0$ (α_f^+) up-chirp and $\alpha_f < 0$ (α_f^-) down-chirp),
- two different polarizations (HH and VV),
- six approximated soil structures (see Fig. 2.4 and Fig. 2.10).

In addition, while for imaging radar, the Signal-to-Clutter Ratio (SCR) plays often more important role than the SNR [13], for clutter modelling the surface standard deviation s was assumed equal to $s = \sigma_h$ (i.e., standard deviation of soil layers, see Section 2.1). The σ^0 was calculated with model presented in [189, 190], and clutter area A_c (see Fig. 2.12(b) and Eq. 2.92) has been divided into smaller areas equal to the theoretical SAR resolution cell area, i.e., $c/(2B_f) \times D_{az}/2$. Due to the large number of considered configurations, the successive stages of proposed scanning method (as described in Section 3.3.2) are presented for the two configurations, i.e., Radar P3 (up-chirp, HH) and Radar L3 (up-chirp, HH), and for the same soil structure (*HU* 360084) and objects location (Fig. 3.7). The same chirp slope α_f^+ and polarization HH were assumed for comparison of the clutter level. Then, the pulse restoration and refocusing phenomenon are presented taking into account other soil structures (Fig. 2.4, Fig. 2.10). While the results are presented jointly on the following figures, the analysis and processing of backscattered envelopes have been carried out separately for each buried point.

3.4.2 Forward Probing (FP)

Results of Forward Probing (FP) (i.e., conventional SAR imaging over terrain) are presented in Fig. 3.8. An analysis of this figure leads to the following observations:

- Fig. 3.8(A): For Radar P3 the spectrum of backscattered envelopes is deformed in more regular (predicted) way than that for Radar L3. Since for Radar P3, the spectrum is generally more attenuated for high-frequency components with the oscillations proportional to the angle of observation. For Radar L3 irregular oscillations appear with different levels of intensity (amplitude). However, since spectrum oscillations for Radar L3 are higher than for Radar P3, the normalized spectrum is more similar to LFM spectrum flattened by a tapered cosine window, and in some frequency regions of the considered bandwidth higher frequency component are more distinct than lower.
- Fig. 3.8(B-C): Spectrum shape affects the result of the matched filtering (MF), which is performed in the base band with the replica of transmitted LFM pulse. In general, outputs of MF show two effects, firstly the broader main lobe and ghost targets, secondly

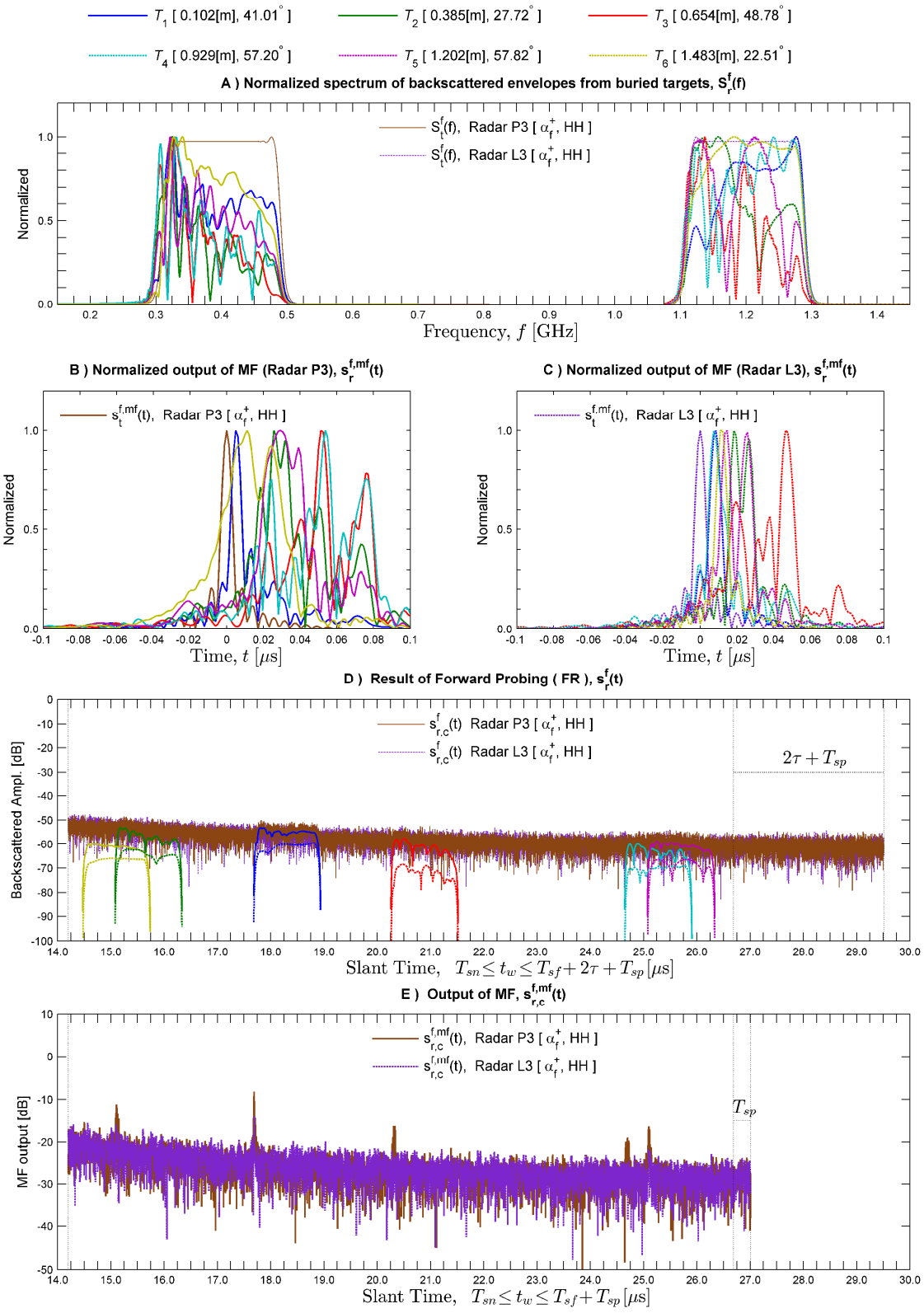

Figure 3.8 Results of Forward Probing (FP) over assumed soil structure with buried point targets: in (A)-(E) targets are marked by colour lines, dashed for Radar P3 and solid for Radar L3; in (D) and (E) plots are marked as in Fig. 3.3; targets colour, their depth and θ_{tsl} are presented at the top of the figure.

the relative shift with respect to the expected position at time axis (as in Fig. 2.21). Meanwhile, more regular (more attenuated but less dispersed) spectrum of Radar L3 results in less degradation of MF results. This can be easily explained by analysis of CREP model used in simulation (Fig. 2.6 - Fig. 2.8). In used frequency ranges, i.e., 0.3 GHz – 0.5 GHz for Radar P3 and 1.1 GHz – 1.3 GHz for Radar L3, the CREP considerably decreases in Radar P3 bandwidth and slightly decreases in Radar L3 bandwidth (plots for *HU* 360084). Moreover, as presented in Section 3.2.1, attenuation is stronger for higher frequencies, Over the same bandwidths, dispersion affects more strongly on these, which are centred around lower carrier frequency. Thus, taking into account both effects, the results for Radar L3, although their envelope is more attenuated (see Fig. 3.8(D)), are relatively less defocused (narrower main lobes and lower level of ghost targets) and less shifted in comparison to Radar P3. Moreover, in comparison with the Fig. 2.21, the distortion level (i.e., number of ghost target and their level in relation to the main lobe, as well the shift on the time axis in relation to the expected position) of MF outputs increases with increasing signal bandwidth. The bandwidths of Radar2 (345 MHz – 375 MHz) and Radar3 (400 MHz – 470 MHz) are contained in the bandwidth of Radar P3, and bandwidth of Radar4 (1162.5 MHz – 1237.5 MHz) in bandwidth of Radar L3. Further, comparing these figures, the distortion of internal signal structure strongly affects the result of MF than the attenuation level. Results for Radar L3 are more regular, or similar (excluding T_3), when for Radar P3 the regularity (similarity) does not exist. Without paying attention to time-shift of maximum from the expected position, the outputs of MF for Radar P3 are highly irregular (expect of the slight similarity between T_3 and T_4). Which confirms that the different types of soil affect the signal envelopes in different ways.

- Fig. 3.8(D): While the bandwidth of both radars is the same, due to the different carrier frequency the clutter level is slightly higher for Radar L3. For both radars, clutter decreases with an increasing incident angle (over slant registration interval $T_{sn} \leq t_w \leq T_{sf} + 2\tau + T_{sp}$). Comparing the regions of slant time in which backscattered signals return to radar, the difference in attenuation level are clearly visible in relation to the objects between each other and with regard to the level of clutter. Moreover, the rising and falling edges of the envelopes, due to the smoothing window $\mathrm{w}_t(t)$ with $r \approx 0.21$, are visible. For a particular target, the slight difference in the arrival time of the backscattered echo results from different propagation path and various propagation velocity in soil. In general, the backscattered envelopes of Radar P3 (solid lines) are stronger (dashed attenuated) than for Radar L3 (solid lines). When for Radar L3, the amplitude of backscattered envelopes are less than clutter level (over 10 dB less than surface clutter), for Radar P3, these envelopes are partially blended into clutter, and the envelope from the shallowest target T_1 slightly rises above the clutter level.

- Fig. 3.8(E): When the internal time-frequency structure of backscattered signals for Radar L3 are less deformed, their higher attenuation implies that the MF is not able to recover them all on a background of the clutter. Only the shallowest target T_1 was correctly detected, others are not so different from background. On the contrary, strongly deformed backscattered signals for Radar P3, that are at a similar level as the clutter, all have been recovered by processing based on MF, however, their main lobes are broader. Even T_6 has been correctly recovered and slightly rises above background, although that, due to its location in near slant ranges, it was hidden in strong clutter background. Looking more closely at peaks positions of the object T_1, the peak for Radar L3 appears later than this for Radar P3 and shift is about $\Delta^t_{T_1} = 3.66$ ns (i.e., slant distance shift $\Delta^r_{T_1} = 0.55$ m in free space). The difference in amplitude is about 5.79 dB in favour of Radar P3.

An analysis of Fig. 3.8 shows that the level of the backscattered signal from buried targets can be such low that the proper detection of buried targets is impossible. The shallowly located objects (down to few centimetres) can be detected on different carrier frequencies, while lower frequencies significantly improve the detection of deeper objects (lower attenuation and clutter level). The clutter level decreases with incident angle and there are not significant differences between the level of the backscattered signal at different incident angles, hence, higher observation angles also enhance the detection of buried objects.

3.4.3 Time-Reversal Operation (TRO)

In TR-besed measurement procedure, before re-transmission of initially recorded backscattered signal through soil structure in time-reversed manner, the backscattered signal is energy normalized due to losses resulting from propagation. Considering the attenuated envelopes from buried point targets, the over-amplification characteristic is derived from the comparison between the initial pulse and the irregularly attenuated envelopes with respect to relation between the time duration τ of initial pulse and time duration of dispersed backscattered returns. Ray-tracing method allows to perform pulse comparison for each considered buried scatterers. Then, the Energy Normalization (EN) can be performed twice to amplify the signal before its re-transmission in that way, that signal restored in TRP obtain fairly constant amplitude. In original form of the TR experiment, the EN by factor K_a simply compensate energy losses and keeps average energy at a constant level. However, K_a expresses normalization coefficient which is valid only in the medium where the attenuation does not depend on the frequency, i.e., in non-dispersive medium. In soil, loss compensation must be performed rather in a adaptive frequency manner (as depicted in Fig. 3.4) than average compensation.

Therefore, let analyse and compare the total cumulative energy, denoted as $E_{ct}(t_i)$, of backscattered signals calculated over duration t_i of the envelope of target T_i. In general, the energy E_s of the signal $s(t)$ is given by

$$E_s = \underbrace{\int_{-\infty}^{+\infty} |s(t)|^2 \, dt = \frac{1}{2\pi} \int_{-\infty}^{+\infty} |S(\omega)|^2 \, d\omega}_{\text{Parseval's theorem}} < \infty \tag{3.16}$$

The envelope of the signal backscattered by buried point target, $s_r^f(t)$ (see Fig. 3.8(D)), lies between T_d and $T_d + t_i$, where T_d is two-way time delay, t_i depends on several factors and is different for various target T_i, i.e., $T_d(T_i)$ and $t_i(T_i)$. The whole radar returns (surface clutter and backscattered signals), $s_{r,c}^f(t)$, occur between T_{sn} and $T_{sf} + 2\tau + T_{sp}$. Therefore, the energy of radar signal (defined by Eq. 2.93) is given by

$$E_t^f = \int_0^{\tau} |s_t^f(t)|^2 \, dt \tag{3.17}$$

and the total energy of radar returns (clutter and backscattered signals) are expressed by

$$E_{r,c}^f = \int_{T_{sn}}^{T_{sf}+2\tau+T_{sp}} |s_{rc}^f(t)|^2 \, dt \tag{3.18}$$

that contains the total energy of backscattered signals from N_T buried targets T_i, given by

$$E_{r,N_T}^f = \sum_{i=1}^{N_T} E_{r,T_i}^f = \sum_{i=1}^{N_T} \int_{T_d(T_i)}^{T_d(T_i)+t_i(T_i)} |s_r^{f,T_i}(t)|^2 \, dt \tag{3.19}$$

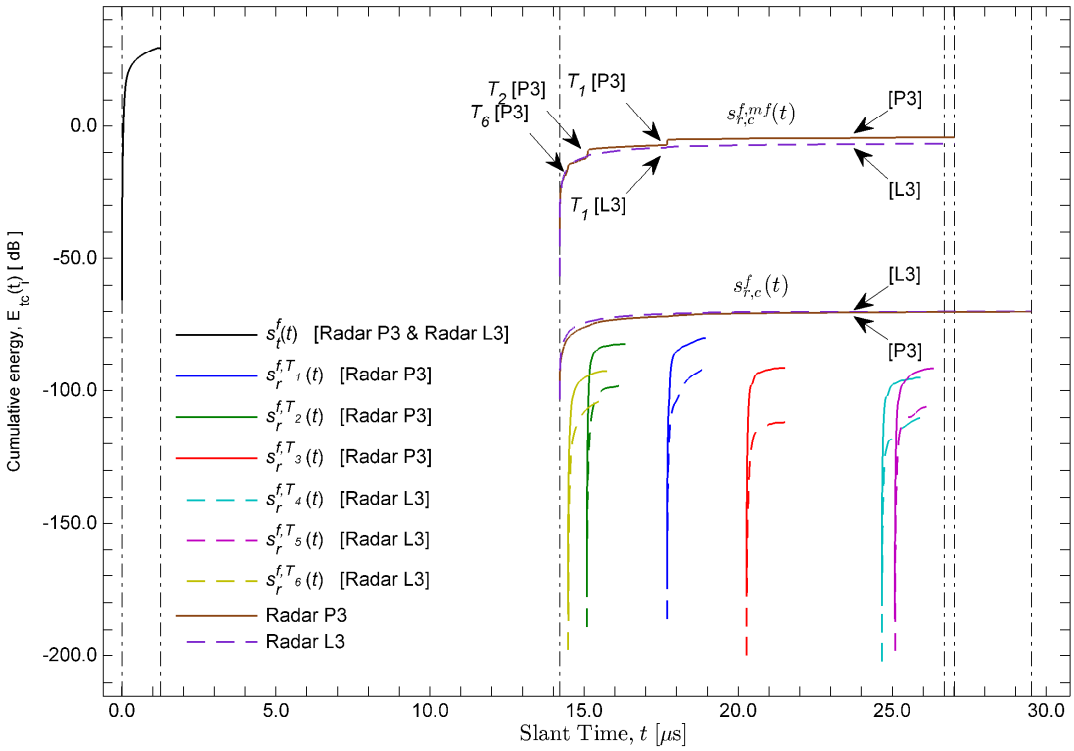

Figure 3.9 The changes of cumulative energy in respective intervals of time for both radars: separately for the probe signal $s_t^f(t)$, backscattered pulses $s_r^{f,T_i}(t)$, whole radar returns $s_{r,c}^f(t)$ and MF outputs $s_{r,c}^{f,mf}(t)$.

The total energy of MF outputs is given by

$$E_{r,c}^{f,mf} = \int_{T_{sn}}^{T_{sf}+T_{sp}} |s_{rc}^{f,mf}(t)|^2 \, dt \tag{3.20}$$

While the Eq. 3.17 - Eq. 3.20 are limited and calculated over the entire duration of the radar source, radar returns and backscattered envelopes, respectively, the cumulative energy $E_{ct}(t)$ is a function of time. Fig. 3.9 shows the cumulative energy of radar source $s_t^f(t)$, radar returns $s_{r,c}^f(t)$, results of MF $s_{r,c}^{f,mf}(t)$ and backscattered signals $s_r^{f,T_i}(t)$ from the six buried targets and the two radars. While the cumulative energy of transmitted pulse increases linearly and is the same for both radars (same bandwidth and peak power), the stronger attenuation for higher frequencies leads to lower values of cumulative energy of backscattered signals for Radar L3 (dashed lines) than Radar P3 (solid lines), lower about 20 dB comparing theirs maximum values at $T_d(T_i) + t_i(T_i)$. Due to the high clutter level, the contribution of backscattered energy from buried targets is not so significant within the total radar returns $s_{rc}^f(t)$ (compare with Fig. 3.8(D)). In particular, in case of Radar L3, where strongly attenuated signals are not visible within the background of strong clutter. Although the strongly backscattered signals for Radar P3 contribute to lower clutter level, the cumulative energy of Radar P3 returns does not increase over the cumulative energy of Radar L3 through entire registration time window $T_{sn} \leq t_w \leq T_{sf} + 2\tau + T_{sp}$. However, the MF approach ($T_{sn} \leq t_w \leq T_{sf} + T_{sp}$) pulls out objects from clutter and results in significant increases in the shape of the curve representing the total cumulative energy calculated over the outputs of MF, $s_{rc}^{f,mf}(t)$ (compare with Fig. 3.8(E)). These increases are clearly visible for T_1 and T_2 in Radar P3 and slightly for T_1 in Radar L3. While at near slant ranges (small incident angles) the cumulative energy of MF output for Radar L3 slightly exceeds that of Radar P3, due to the detection of objects

(even T_6) the cumulative energy of MF output for Radar P3 clearly overpass that Radar L3 and does not decrease below it.

Furthermore, looking more closely at changes of cumulative energy only along the envelope duration of backscattered signal $t_i(T_i)$ from considered scatterers, i.e., between $T_d(T_i)$ and $T_d(T_i) + t_i(T_i)$. For simplification, let's assume $T_d(T_i) = 0$ for all the objects regardless to their location. The cumulative energy of the pulse backscattered by buried targets, $E_{ct}^{T_i}(t)$, can be expressed (in time domain) as

$$E_{ct}^{T_i}(t) = \int_0^t |s_r^{f,T_i}(t')|^2 \, dt', \quad 0 \leqslant t \leqslant t_i(T_i), \quad 0 \leqslant t' \leqslant t \tag{3.21}$$

Fig. 3.10 (A,B) shows a comparison of cumulative energy of radar pulse and cumulative energy of backscattered signals derived from buried targets, respectively, for Radar P3 and Radar L3. Due to the backscattered pulse elongation, the maximum of cumulative energy is reached at the time $t_i(T_i) > \tau$. While the Fig. 3.10(A) and Fig. 3.10(B) show an instantaneous increase of the cumulative energy over the envelope duration $t_i(T_i)$, Fig. 3.10 (C,D) shows the normalized-to-maximum values

$$\frac{E_{ct}^{T_i}(t)}{max\{\ E_{ct}^{T_i}(t)\ \}} = \frac{E_{ct}^{T_i}(t)}{E_{ct}^{T_i}(t_i(T_i))} \tag{3.22}$$

and highlight derogation from the linear rising of cumulative energy, which is characteristic for radar pulses with constant amplitude, but it is not revealed in the normalized cumulative energy calculated based on the irregularly attenuated envelope of backscattered signals. However, due to the use of time window $\mathrm{w}_t(t)$ ($r \approx 0.21$), cumulative energy at the begin and the end of both radar pulses and backscattered signals increases non-linearly, when in the centre of radar pulses it grows linearly. Despite the irregularities of the MF outputs for both radars (see Fig. 3.10(B,C)) normalized cumulative energy of all backscattered pulses for Radar P3 grows stronger at the beginning of the pulse (in particular, for T_2, T_3, and T_4) than at the end of the pulses. While for both radars $\alpha_f > 0$, i.e., α_f^+, instantaneous frequency increase along pulse duration, the envelope of backscattered pulses is more strongly attenuated at the end of the pulse than at the begin. Thus, in the frequency domain (see Fig. 3.8 and Eq. 3.16), while the lower frequencies of the considered bandwidth have higher amplitudes they contribute more strongly to cumulative energy. When the envelope of backscattered pulses fluctuates irregularly with local minims and maxims (as well as the spectrum magnitude in Fig. 3.8(A)), the (normalized) cumulative energy also grows irregularly with periodic fluctuations. On the other hand, for Radar L3, due to the more diversified attenuation of the backscattered envelope than for Radar P3, the cumulative energy grows either of two ways. For T_2, T_3 and T_5, it grows stronger at the beginning of the pulses than at the end (similarly as in all targets for Radar P3). However, for T_1, T_4 and T_6 the spectrum magnitude of which is stronger for higher frequencies (located at the end of the pulse, Fig. 3.8(A))), the cumulative energy grows slightly at the beginning of the pulse and then it begins to grow faster depending on the irregularly distorted spectrum of backscattered signals.

As mentioned previously, the aim of the TRO is to prepare a new radar signal. Under the assumption about unchanging medium, the mirrored retransmission is intended to restore the inner signal structure (linearisation of frequency changes and restoration of the proper pulse duration) and over-amplification aims to align the amplitude to the same constant level. These two efforts are designed to matched the new backscattered signal to replica of initially transmitted radar pulse and to achieve the refocusing effect at the output of MF. While cumulative energy of backscattered pulses arise non-linearly, thus, the EN should amplify the amplitudes of backscattered pulses in non-linear way before its retransmission in time-reversed matter. Let's $K_a^{T_i}(t)$ denotes a normalization coefficient of the envelope of T_i target,

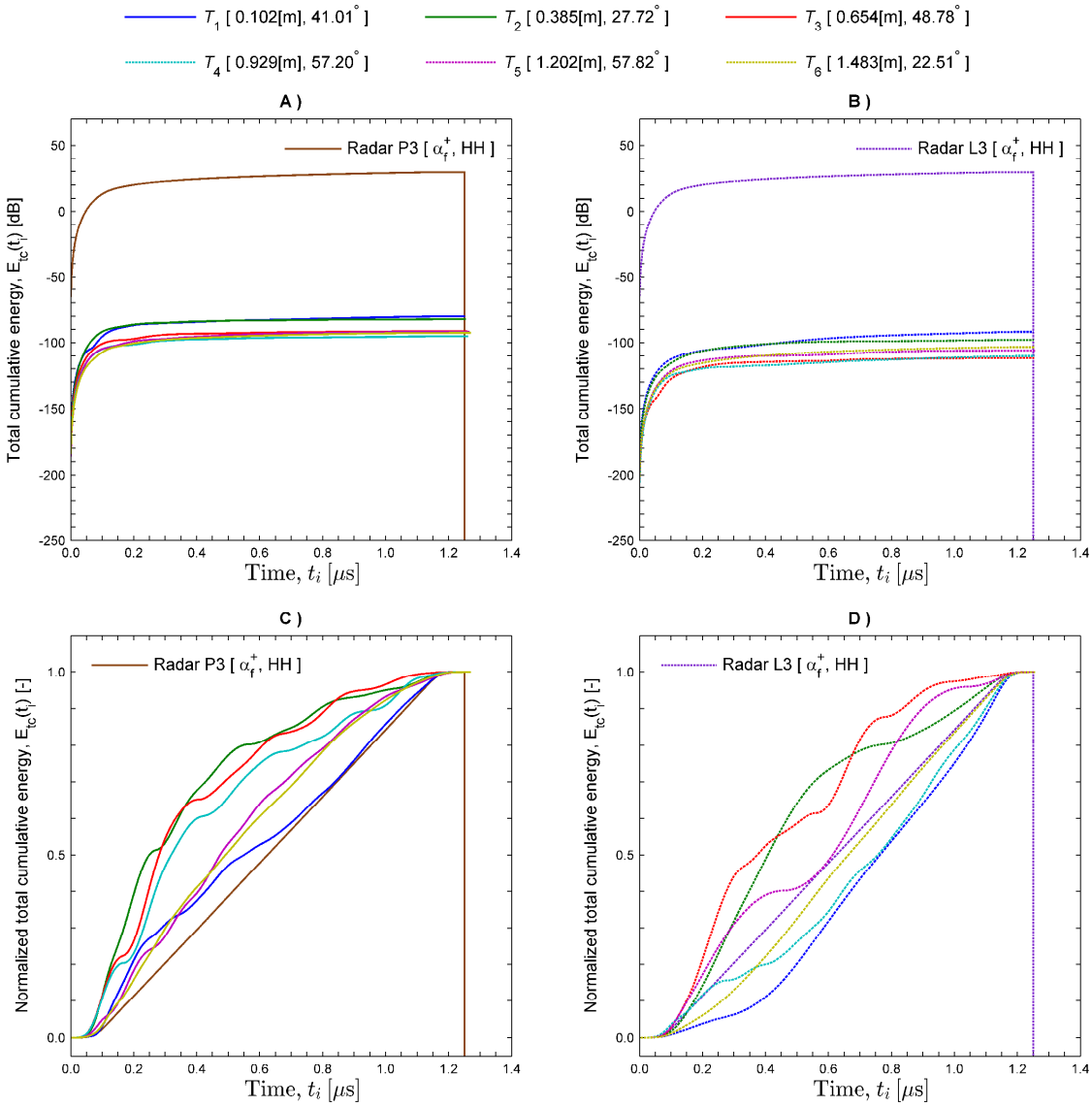

Figure 3.10 A comparison of cumulative energy through the envelope duration for Radar P3 (left column) and Radar L3 (right column): increase of the cumulative energy (top), comparison of the normalized-to-maximum values of cumulative energy (bottom).

which is defined as

$$K_a^{T_i}(t) = \frac{E_t^f(t)}{E_{ct}^{T_i}(t)} = \frac{\int_0^{t_t} |s_t^f(t)|^2 \, dt}{\int_0^{t_r} |s_r^{f,T_i}(t)|^2 \, dt}, \quad \begin{matrix} 0 \leqslant t_t \leqslant \tau \\ 0 \leqslant t_r \leqslant t_i(T_i) \end{matrix}, \quad \tau \neq t_i(T_i) \tag{3.23}$$

and expresses the ratio of cumulative energy of transmitted signal, $E_t^f(t)$, to cumulative energy of backscattered pulse, $E_{ct}^{T_i}(t)$. However, when $\tau \neq t_i(T_i)$, the $K_a^{T_i}(t)$ must take into account different time intervals over which the cumulative energy (and average power) is calculated. While EN equalizes the average power level

$$\frac{1}{\tau} \, E_t^f(\tau) = K_a^{T_i}(t_i(T_i)) \cdot \frac{1}{t_i(T_i)} \, E_{ct}^{T_i}(t_i(T_i)) \tag{3.24}$$

and

$$K_a^{T_i}(t_i(T_i)) = \frac{t_i(T_i)}{\tau} \frac{E_t^f(\tau)}{E_{ct}^{T_i}(t_i(T_i))} \tag{3.25}$$

hence, $K_a^{T_i}(t)$ (Eq. 3.23) should be modified as follows

$$K_a^{T_i}(t) = \frac{E_t^f(t)}{E_{ct}^{T_i}(t)} = \frac{t_r}{t_t} \frac{\int_0^{t_t} |s_t^f(t)|^2 \, dt}{\int_0^{t_r} |s_r^{f,T_i}(t)|^2 \, dt}, \quad \begin{matrix} 0 \leqslant t_t \leqslant \tau \\ 0 \leqslant t_r \leqslant t_i(T_i) \end{matrix}, \quad \tau \neq t_i(T_i) \tag{3.26}$$

Therefore, before its retransmission, the envelope of backscattered pulse must be further enhanced, i.e., normalized twice, in other words, over-amplified. When the EN only changes the amplitude of backscattered pulse, it can be expressed as

$$s_t^{tr,T_i}(t) = s_r^{f,T_i}(t) \cdot K_a^{T_i}(t) \cdot K_a^{T_i}(t) \tag{3.27}$$

where $s_t^{tr,T_i}(t)$ is a new radar pulse. While a single multiplication equalizes the envelopes only, a double multiplication reinforces them non-linearly in order to provide the constant level of envelopes after their re-attenuation in TRP. Fig. 3.11 shows the $K_a^{T_i}(t)$ and $s_t^{tr,T_i}(t)$ for both radars and six buried point targets. When, apart the smoothing window $w_t(t)$, before transmission the $s_t^f(t)$ is amplified by $A(t) = \sqrt{P_0}$, the $K_a^{T_i}(t)$ reaches a significant value compared to level of the backscattered pules envelope $s_r^{f,T_i}(t)$. Local minima and maxima through the backscattered pules envelope cause fluctuation of $K_a^{T_i}(t)$, which are highly evident at its beginning. Higher attenuations for Radar L3 induce in higher value of $K_a^{T_i}(t)$ for this radar. According to Eq. 3.27, over-amplification reinforces the new probing signal to an unreachable level for the dynamic range of radar. Assuming maximum amplitude level as $A_m = 30$ dB, the new probing signals $s_t^{tr,T_i}(t)$ after over-amplification were all normalized to that level, however, keeping the amplitude fluctuation determined by over-amplification. In Fig. 3.11, the $s_t^{tr,T_i}(t)$ are time-reversed and symmetrically reversed around a $t = 0$. While in $s_t^f(t)$ the frequency increases linearly over $0 \leqslant t \leqslant \tau$, in $s_t^{tr,T_i}(t)$ it decreases over $-t_i(T_i) \leqslant t \leqslant 0$. Local minima, occurring through $s_r^{f,T_i}(t)$, have been changed into local maxima through $s_t^{tr,T_i}(t)$ after the over-amplification. For comparison, local minima in $s_t^f(t)$ of T_3 (for example, in Radar P3: about $t_m = 0.16$ µs and $t_m = 0.42$ µs; in Radar L3: about $t_m = 0.56$ µs and $t_m = 0.74$ µs) and T_4 (for example, in Radar P3: about $t_m = 0.17$ µs and $t_m = 0.44$ µs; in Radar L3: about $t_m = 0.28$ µs and $t_m = 0.39$ µs) increase maxima in $s_t^{tr,T_i}(t)$ of T_3 and T_4 at $t_M = -t_m$. Hence, in TRO, the six new probing signals $s_t^{tr,T_i}(t)$ are formed on the basis of the amplitude level of six backscattered pulses $s_r^{f,T_i}(t)$ and in comparison with the initial radar pulse $s_t^f(t)$.

3.4.4 Time-Reversal Probing (TRP)

Aiming to investigate the $s_t^{tr,T_i}(t)$ behaviour in TRP along the same propagation path as $s_r^{f,T_i}(t)$ underwent in FP, the $s_t^{tr,T_i}(t)$ is considered separately within the same propagation model as in FP (Section 3.4.2), which is based on backward-propagating matrix $B_{(n,n+1)}$ (Eq. 2.75). Results of TRP are presented in Fig. 3.12 (in the same order as in Fig. 3.8). Whereas in Section 3.3.2 (Fig. 3.6) the TRP starts at T_{TR}, where $T_{TR} = T_{sf} + T_{sp} + 2\tau + T_{OP}$, for comparison of FP and TRP results at the same position u_n along L_{sar}, the $T_{TR} = 0$. An analysis of this figure leads to the following observations:

- Fig. 3.12(A): The shape of the spectrum of backscattered signals $S_r^{tr,T_i}(f)$ have been restored with fairly high accuracy for both radar. Either the frequency shift and mag-

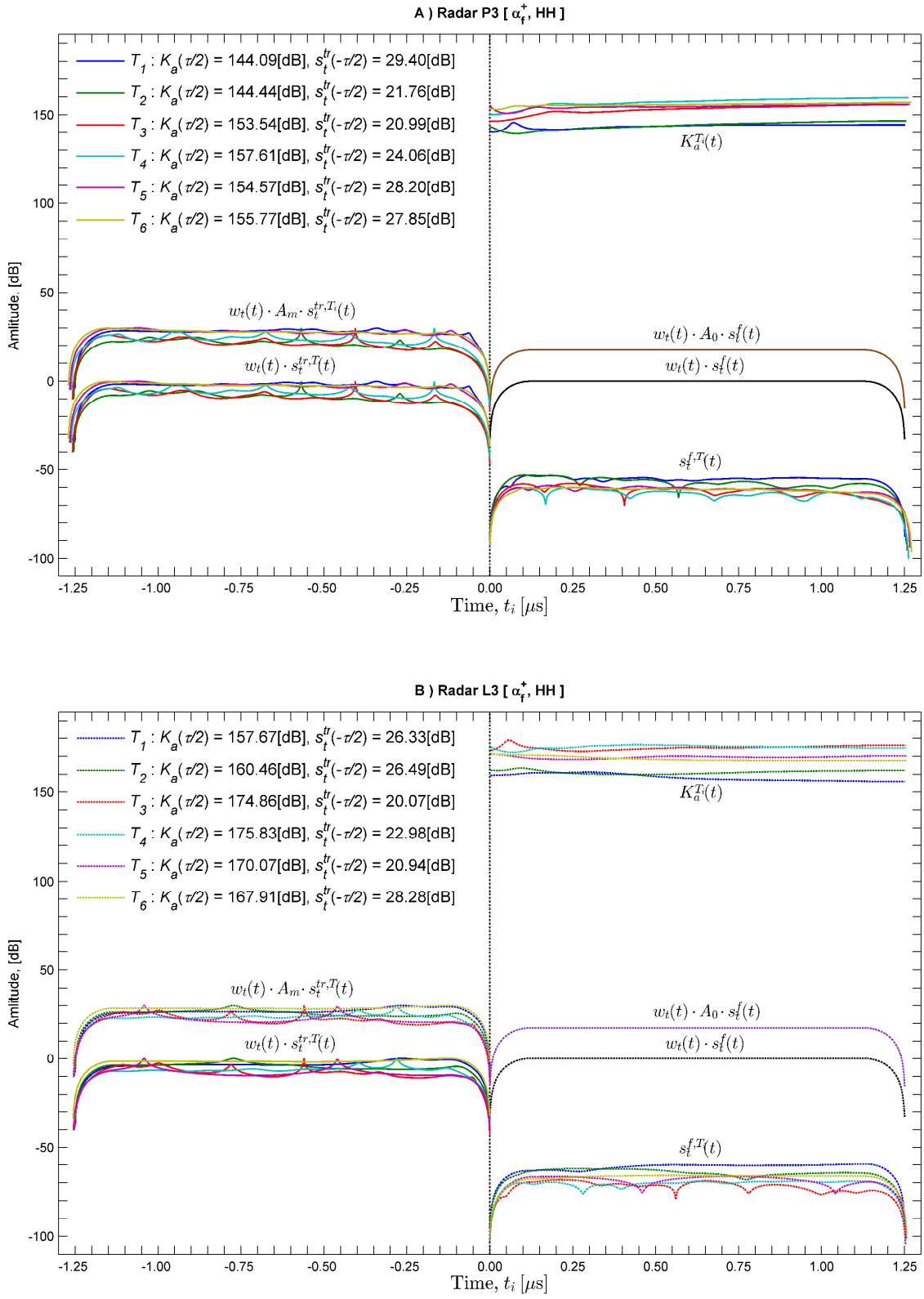

Figure 3.11 Derivation of the energy normalization factor $K_a^{T_i}(t)$ and a comparison of signal levels in FP and TRP for Radar P3 (top) and Radar L3 (bottom).

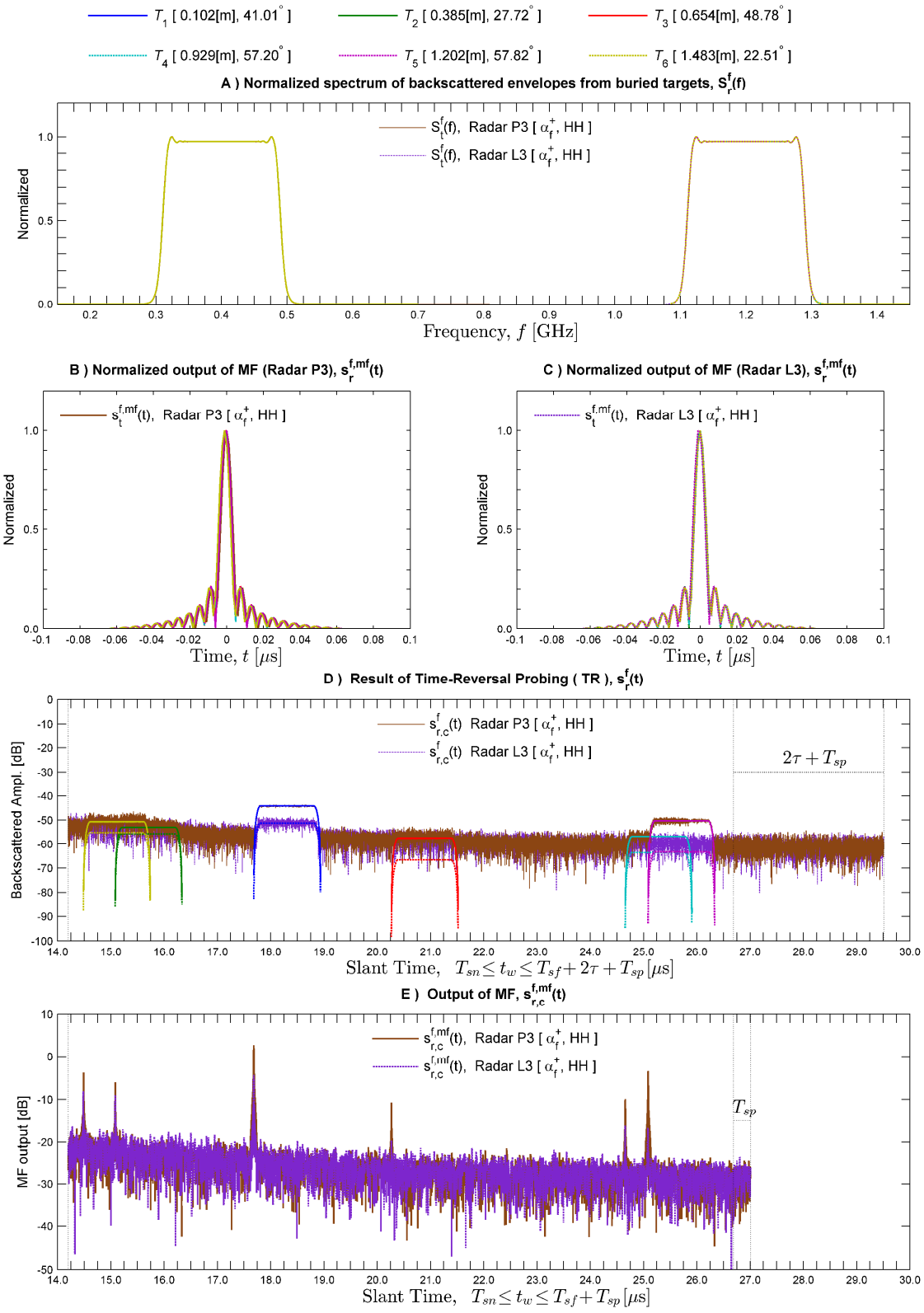

Figure 3.12 Results of Time-Reversal Probing (TRP) over assumed soil structure with buried point targets: in (A)-(E) targets are marked by colour lines, dashed for Radar P3 and solid for Radar L3; in (D) and (E) plots are market as in Fig. 3.3 and Fig. 3.8; targets colour, their depth and θ_{tsl} are presented at the top of the figure.

nitude fluctuations were compensated (see Fig. 3.8(A)). By comparing the normalized spectrum of these signals with $S_t^f(f)$ (slightly smoothed by $W_t(f)$) the differences are negligible and plots overlap on each other.

- Fig. 3.12(B-C): While $s_t^{tr,T_i}(t)$ is a radar pulse in TRP, the matched filter approach uses $s_t^f(t)$ as a reference signal in place of $s_t^{tr,T_i}(t)$, i.e., Cross Matched Filtering (CMF) approach (see Section 3.3.1). The MF outputs for both radar are correctly reconstructed with one dominant main lobe at $t = 0$ and symmetrical level of side lobes as well as without ghost targets (apparent objects) (for comparison, see Fig. 3.8(A)). Without considering the amplitude level of $s_t^{tr,T_i}(r)$, the normalized outputs of MF are fairly similar and overlapping.

- Fig. 3.12(D): The same mission geometry as in FP causes the same phenomenon of wave scattering in air (is taken into account in calculation of the amplitude of the signal at soil surface before its entrance to soils structure, and later, in calculation of the signal amplitude which reaches the radar antenna after leaving the soil). Furthermore, clutter behave similarly and decreases with increasing angle of observation. However, while $s_t^{tr,T_i}(t)$ are stronger than $s_t^f(t)$ (about A_m/A_0) at antenna transmission input, the backscattered signals $s_r^{tr,T_i}(t)$ are generally stronger than the $s_r^{f,T_i}(t)$. And, what is the most important, their amplitude are uniformly flat in the middle of the envelopes and smoothed at their ends. Identical attenuation in soil structure, the same as in FP, resulted in similar relationships in the level of the envelope for the same object T_i between Radar P3 and Radar L3 as in FP. These relationship are slightly disturbed by the differences in $s_r^{tr,T_i}(t)$ between Radar P3 and Radar L3 (see Fig. 3.11), whereas in FP $s_t^{f,T_i}(t) = s_t^f(t)$ are the same for six targets and two radars. In comparison to Fig. 3.8(D), now the T_1 strongly rises above the clutter level in $s_{r,c}^{tr}(t)$ for both radars as well T_5 but only for Radar P3. The targets T_2 and T_3 are revealed slightly in $s_{r,c}^{tr}(t)$ despite the fact that they are surrounded by a strong clutter (low incident angles).

- Fig. 3.12(E): A stronger contribution of the backscattered pulses $s_r^{tr,T_i}(t)$ into $s_{r,c}^{tr}(t)$ affects the result of MF approach, resulting in that the objects are firstly better extracted from clutter and they have a higher amplitude in $s_{r,c}^{tr,mf}(t)$, for both radars. All six objects have been detected by Radar P3 (even T_6), five objects were recovered correctly for Radar L3 where the T_3 is located at clutter level. Furthermore, reconstruction of the internal signal structure makes disappear the ghost targets in $s_{r,c}^{tr,mf}(t)$ and main lobes (or peaks) of detected targets have a thin form. Still, however, the $s_{r,c}^{tr,mf}(t)$ is lower for Radar L3 than for Radar P3. And a shift between a maximum locations of T_i in $s_{r,c}^{tr,mf}(t)$ still occurs, the same as in FP, but now it is much lower. The difference in the amplitude of T_1 is 7.04 dB in favour of Radar P3, and is higher over 1.2 dB than this for FP.

In general, an analysis of Fig. 3.12 shows that a fairly accurate restoration of the internal signal structure is possible. Hence, in combination with selective over-amplification aimed at unifying the signal level, the time-reversal (mirrored) retransmission results in significantly improved of the buried targets detection capability. Providing a high signal power in TRP, even slightly higher than in FP (see Fig. 3.11), also enhance the imaging capabilities of buried targets.

For comparison of the MF outputs between FP and TRP, in Fig. 3.13 the $s_{r,c}^{f,mf}(t)$ and $s_{r,c}^{tr,mf}(t)$ are both normalized to $max\{s_{r,c}^{tr,mf}(t)\}$ and presented separately for Radar P3 (top) and Radar L3 (bottom). For both radars the results are more accurate for TRP than for FP. While normalized clutter background is higher around 8 dB for Radar L3, the peaks amplitude are similar for some targets (as T_4, T_6). Whereas the refocused peaks in TRP are narrow for all of defect objects, in the results of FP for Radar P3 they are lower, highly

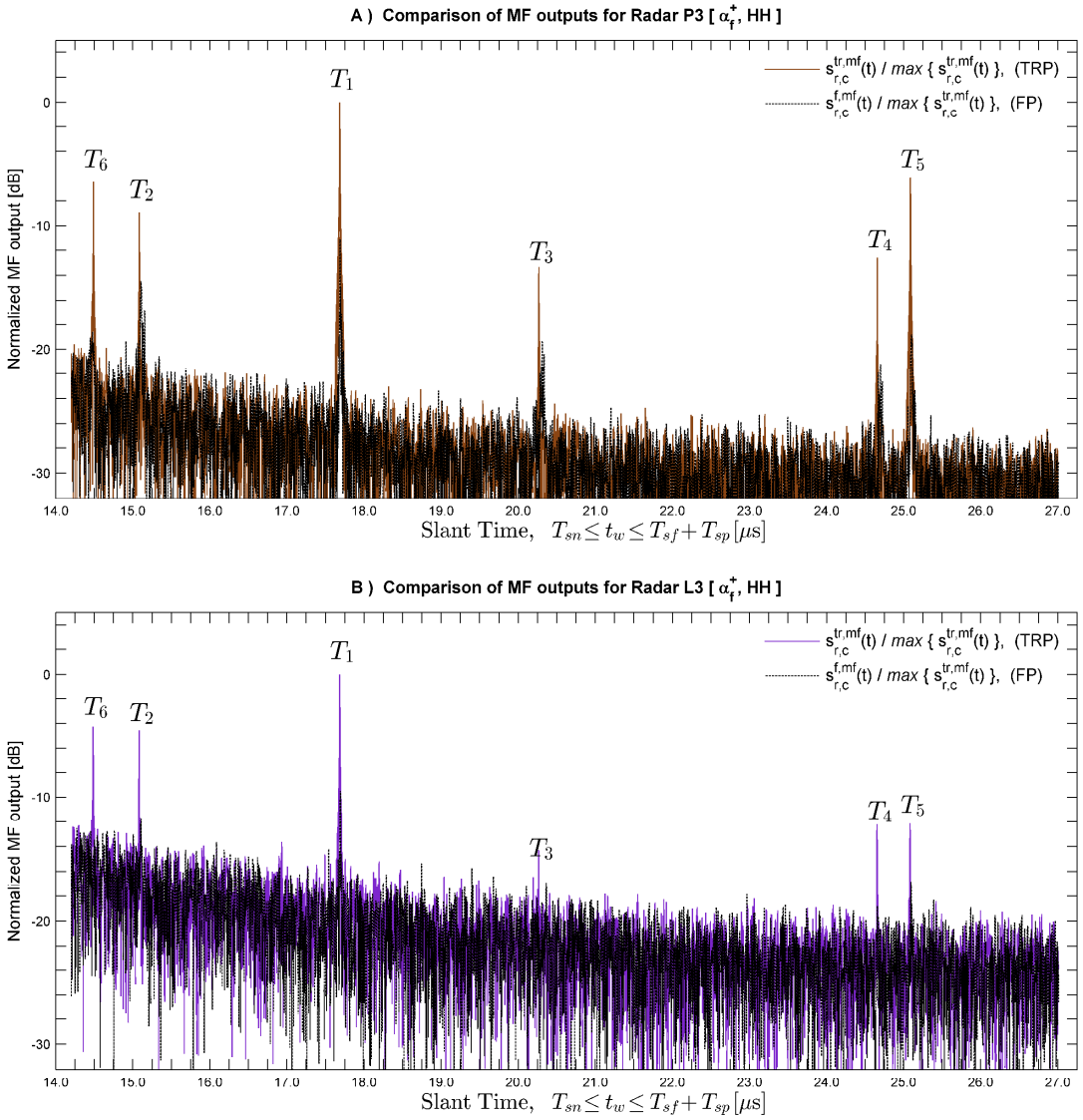

Figure 3.13 A comparison of the MF outputs for Radar P3 (top) and Radar L3 (bottom).

broader and slightly shift from maximum location of TRP result (in particular, T_2 and T_3). In the result of FP for Radar L3, the peak for T_1 is narrower than for Radar P3, however, other objects are hidden in clutter background (due to the higher attenuation). The slight shift in maximum of T_1 (and between other relevant peaks) occurs between Radar P3 and Radar L3 in TRP results. For both radars this shift is determined by the frequency components that formed up the leading edge of the radar signal. When the distortion of the internal pulse structure depends on the bandwidth of radar pulse (frequency slope as well) as well as a carrier frequency and turns into a delay or acceleration of the trailing edge (see, for instance, Fig. 2.20), the pulse delay is determined by the leading edge. Hence, while in TRP the pulse slope α_f is mirrored compared to FP, the delays of backscattered pulses are different and therefore the energy is refocused at slightly different slant time-delay (or slant range).

3.4.5 Pulse Restoration and Refocusing

In the previous subsections, we have presented results of a single probing in accordance with the proposed scheme (Fig. 3.6) of TR measurements over a one soil structure, this subsection

provides a comparison of refocusing effect through the all considered soil structures (Fig. 2.4) and for different configuration of TR-AGPR mission. The location of the buried object inside a soil structure (incident and observation angles) and operational bandwidth of considered radars remain the same, whereas the polarisation and LFM slope are changed.

Fig. 3.14 and Fig. 3.15 present a normalized results of pulse refocusing for Radar P3 and up-chirp LFM, separately for horizontal (Fig. 3.14) and vertical polarisation (Fig. 3.15), for each buried target T_i (from left to right) and each soil structure (from top to bottom). Each chart contains lines representing the results of the three different MF operation, which can be performed separately during TR measurements (as depicted in Section 3.3.1, and in [124]). Namely, the MF outputs after FP $[s_t^f(t),\ s_r^{f,T_i}(t)]$ are presented in colour lines (according to the colour used previously). The MF outputs after TRP $[s_t^{tr,T_i}(t),\ s_r^{tr,T_i}(t)]$ are presented in black lines for all targets and soil structures, whereas the CMF outputs $[s_t^f(t),\ s_r^{tr,T_i}(t)]$ are presented in uniform colour (such as defined for Radar P3). Mainly, these two figures show in a wide range the impact of soil structure and target location on the MF outputs, which are disfigured by distortion of the internal pulse structure. A comparison of FP $[s_t^f(t),\ s_r^{f,T_i}(t)]$ results (lines in targets colour) between different structures and targets show how the pulse distortion is irregular, in particular, in relation to deeply located targets or objects, which are located under highly changing soil structure. Strong variation of the main lobe maximum and amount of ghost target (apparent objects) as well the asymmetrical shape of MF outputs indicate the selective nature of the soil. Furthermore, the TRP results $[s_t^{tr,T_i}(t),\ s_r^{tr,T_i}(t)]$ (black lines) are also disfigured by pulse distortion with shifting of the main lobe maximum and different amount of ghost targets. When $s_t^{tr,T_i}(t)$ is preferably matched to soil structure (along propagation path), the $s_r^{tr,T_i}(t)$ represents renewed signal structure, thus, those signals are mismatched and MF outputs after TRP probing are distorted as well. However, while in FP $\alpha_f > 0$ and in TRP $\alpha_f < 0$ (reversed frequency), the pulse distortion in TRP is different than in FP and also depends from target depth and soil structure. Meanwhile, the results of CMF $[s_t^f(t),\ s_r^{tr,T_i}(t)]$ (colour as Radar P3) are fairly well refocused regardless to the soil structure and target depth.

Similarly, Fig. 3.16 and Fig. 3.17 present a normalized results of pulse refocusing for Radar L3 and down-chirp LFM, separately for horizontal (Fig. 3.16) and vertical polarisation (Fig. 3.17), for each buried target T_i (from left to right) and each soil structure (from top to bottom). Again, each chart contains lines representing the results of the three different MF operation. While the results of FP and TRP are marked the same as in Fig. 3.14 or Fig. 3.15, the CMF outputs are presented now in uniform colour defined for Radar L3. The same as for Radar P3, the results of FP $[s_t^f(t),\ s_r^{f,T_i}(t)]$ (lines in targets colour) are affected by pulse distortion. However, due to the different changes of CREP in the operational bandwidth of Radar L3, they are narrower with lower amount of energy and level of ghost targets. Moreover, the low disfiguration level remains the same for TRP results $[s_t^{tr,T_i}(t),\ s_r^{tr,T_i}(t)]$ (black lines), whose for some objects have almost the same maximum location and the same level of ghost targets as in FP. In Fig. 3.16 and Fig. 3.17, for FP $\alpha_f < 0$ and for TRP $\alpha_f > 0$. Meanwhile, the results of CMF $[s_t^f(t),\ s_r^{tr,T_i}(t)]$ (colour as Radar L3) are again fairly well refocused.

Despite the lower distortion level for Radar L3, the different attenuations of the backscattered pulse envelope (in favour of the Radar P3) should be taken into consideration in comparison of CMF results between Radar P3 and Radar L3. Moreover, various incident angles also contribute to level of focused target maximum after each step. The plots shown in Fig. 3.18, compare the magnitude level of considered targets after the FP and CMF for two radars (Radar P3 and Radar L3) in two configuration, i.e., α_+ HH and α_- VV. The difference in the attenuation between Radar P3 and Radar L3 is clearly visible in these plots (for both configurations). Mainly for all targets, the CMF mainly provides greater magnitude level than FP. However, since proposed method of EN (see Section 3.4.3) re-amplifies in non-linear way

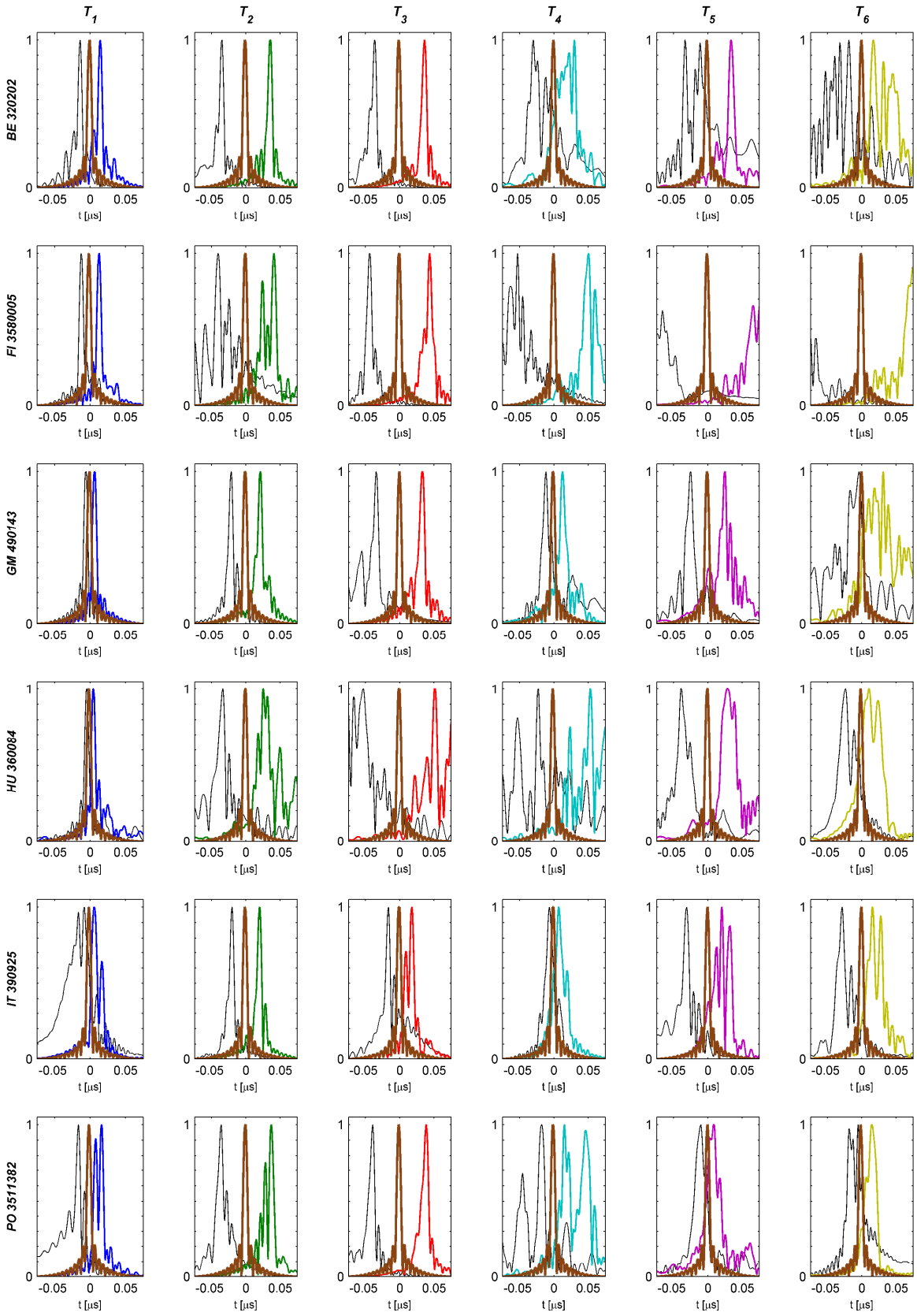

Figure 3.14 A comparison of the pulse refocusing for Radar P3 (α_+, HH) for six buried targets (from left to right) and six considered soil structures (from top to bottom): FP results in target's colour, TRP results on black and CMF results in Radar P3 colour.

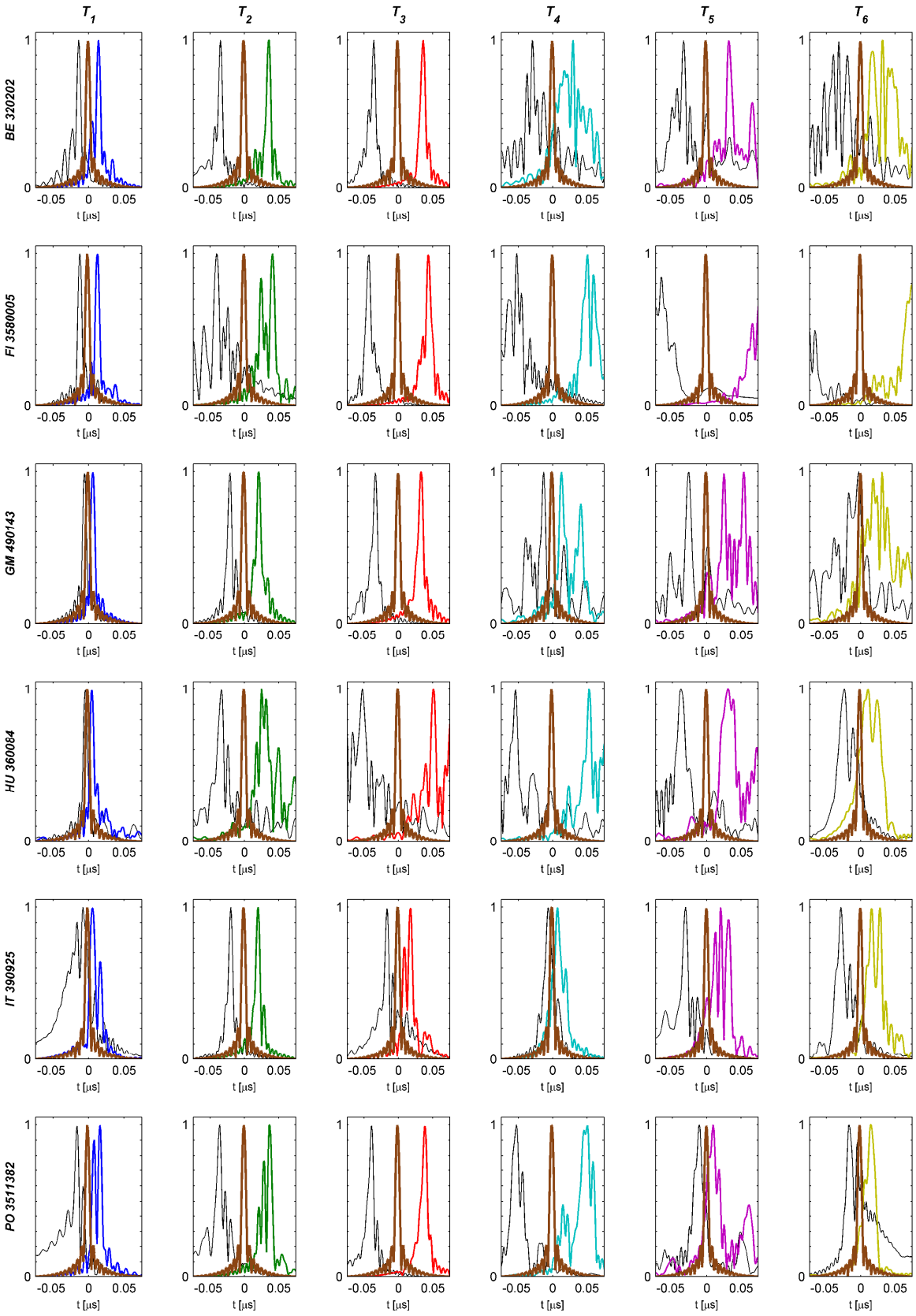

Figure 3.15 A comparison of the pulse refocusing for Radar P3 (α_+, VV) for six buried targets (from left to right) and six considered soil structures (from top to bottom): FP results in target's colour, TRP results on black and CMF results in Radar P3 colour.

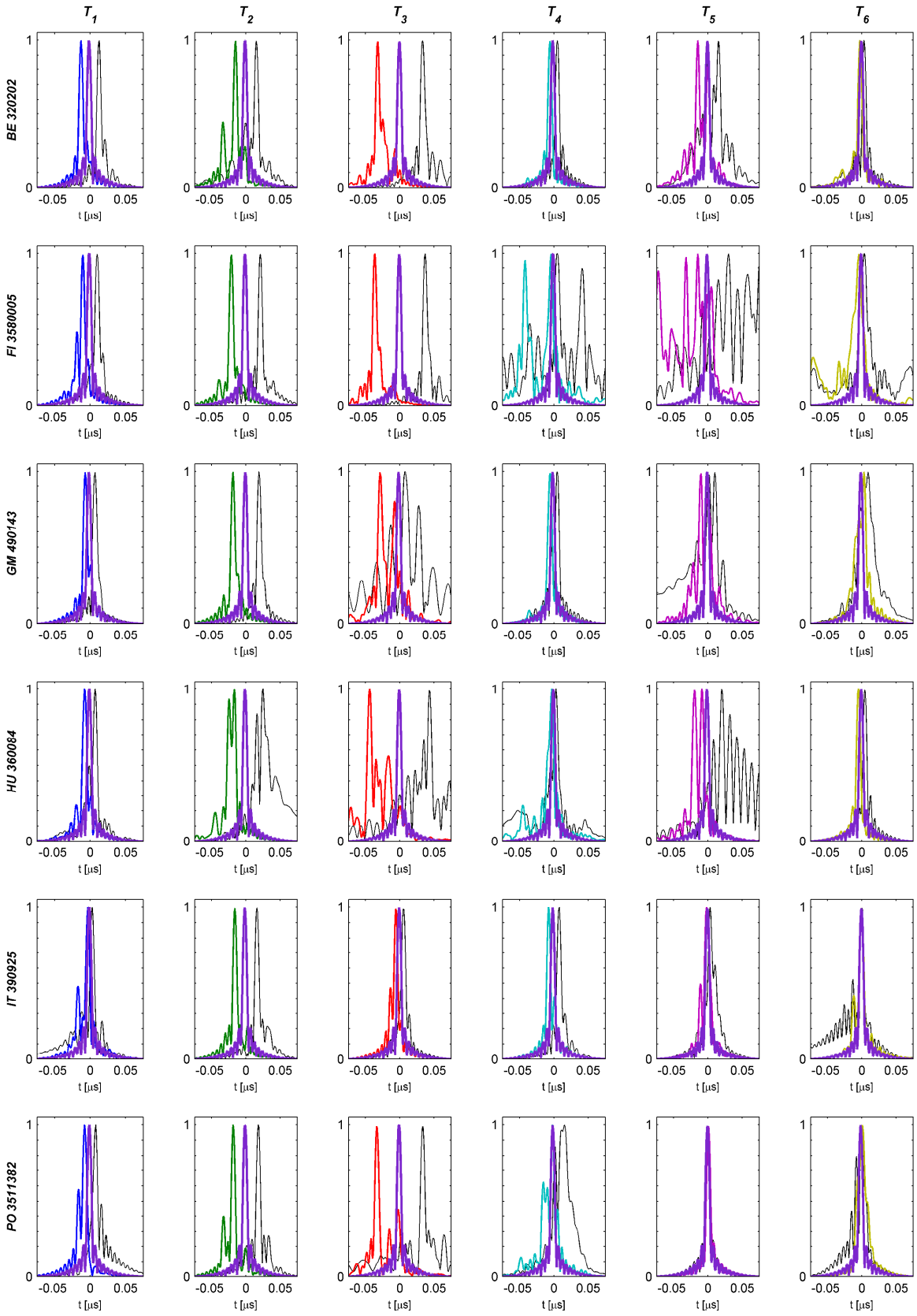

Figure 3.16 A comparison of the pulse refocusing for Radar L3 (α_-, HH) for six buried targets (from left to right) and six considered soil structures (from top to bottom): FP results in target's colour, TRP results on black and CMF results in Radar L3 colour.

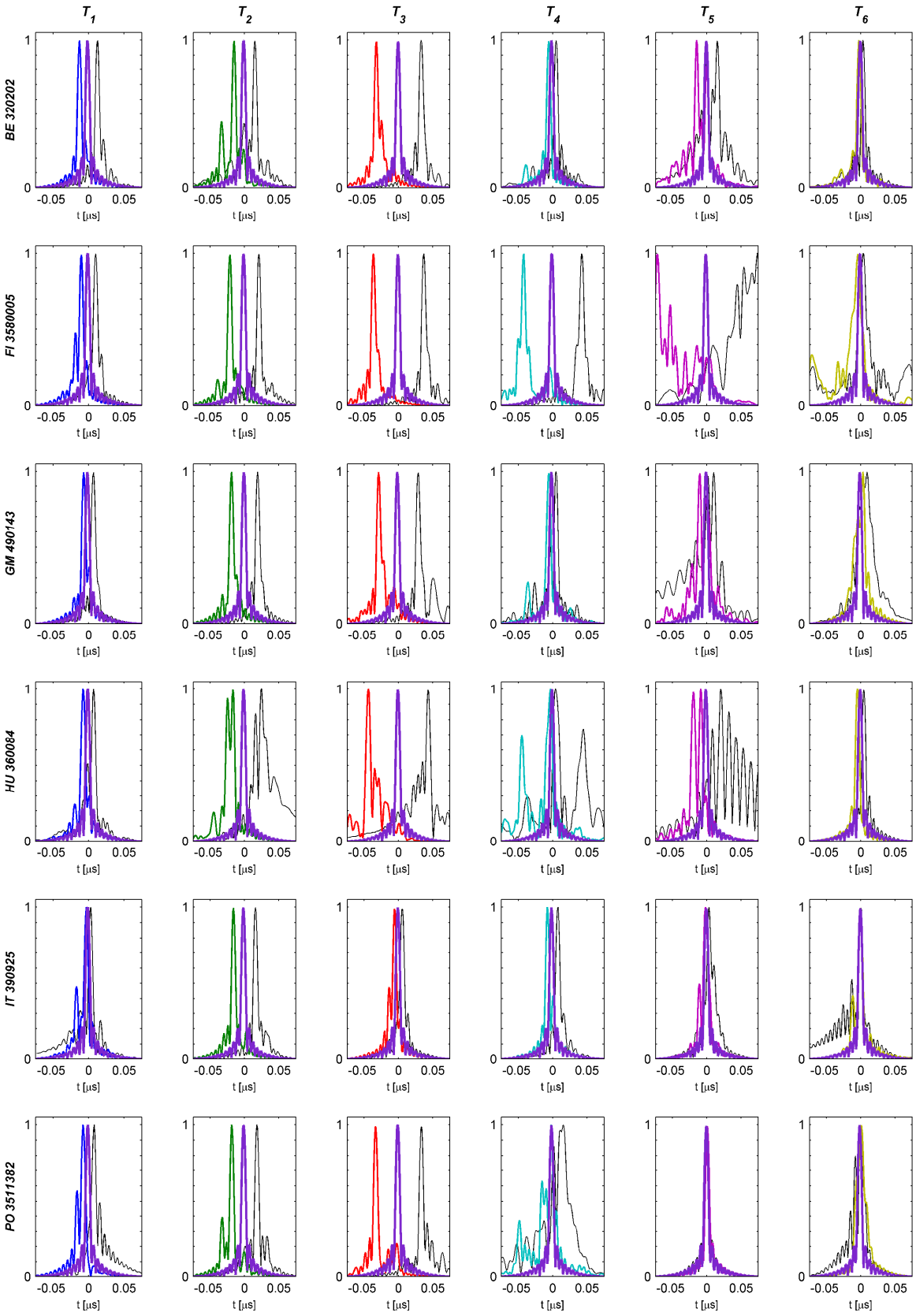

Figure 3.17 A comparison of the pulse refocusing for Radar L3 ($\alpha\_$, VV) for six buried targets (from left to right) and six considered soil structures (from top to bottom): FP results in target's colour, TRP results on black and CMF results in Radar L3 colour.

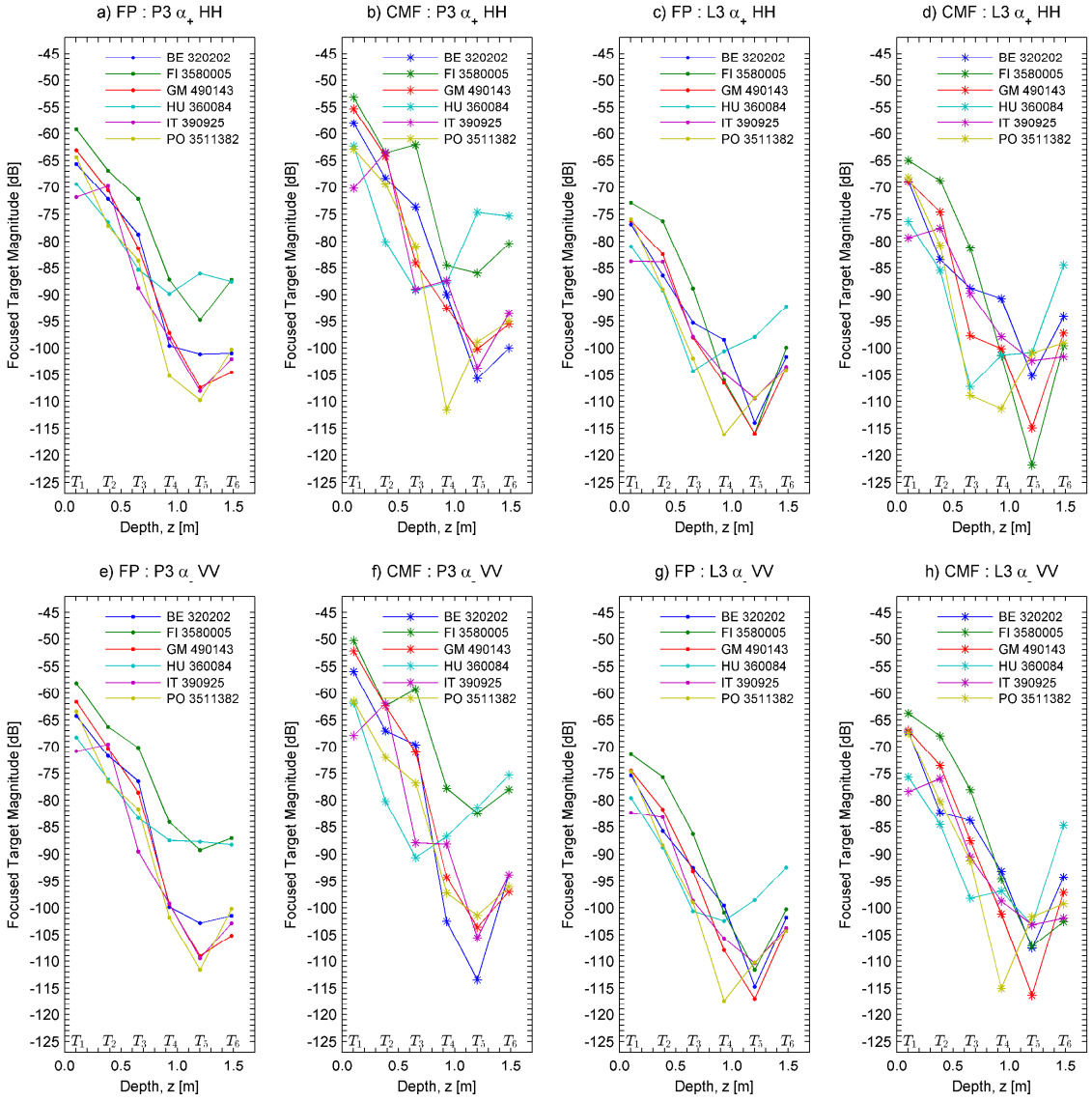

Figure 3.18 Magnitude level of the six focused target (at different depth and incident angle) after FP and CMF for two radars (Radar P3 and Radar L3) and two configurations (α_+ HH and α_- VV) in six considered soil structures.

the backscattered signals before its retransmission in the TRP, the curves of target magnitude for CMF are different and for certain targets the magnitude level is lower in CMF than in FP. Moreover, Fig. 3.19 shows the relative displacement of the focused target main lobe after the FP (solid lines) and TRP (dashed lines) for two radars (Radar P3 and Radar L3) and two configurations (α_+ HH and α_- HH) in six considered soil structures. For constant polarization and the slope α_a of initially transmitted pulse (Fig. 3.19, along rows), the relative focused target peak shift is lower for Radar L3 than for Radar P3 (with the drawbacks that attenuation is higher for Radar L3). For constant radar and polarization (Fig. 3.19, along columns), the relative shift is slightly lower when initially transmitted pulse has decreasing frequency slope (α_-). For all configuration, the relative main lobe shift between FP and TRP is nearly completely opposite (with a accuracy of the sampling period). Hence, pulse elongation (α_+) or shortening (α_-), which occurs in FP, is recovered in TRP, where pulses are re-transmitted in TR manner. Similar relationships occur for VV polarization. As shown in Fig. 3.14 - Fig. 3.17, the results of CMF are correctly re-focused and located at expected position, where relative main lobe shift equals one for each considered targets inside all con-

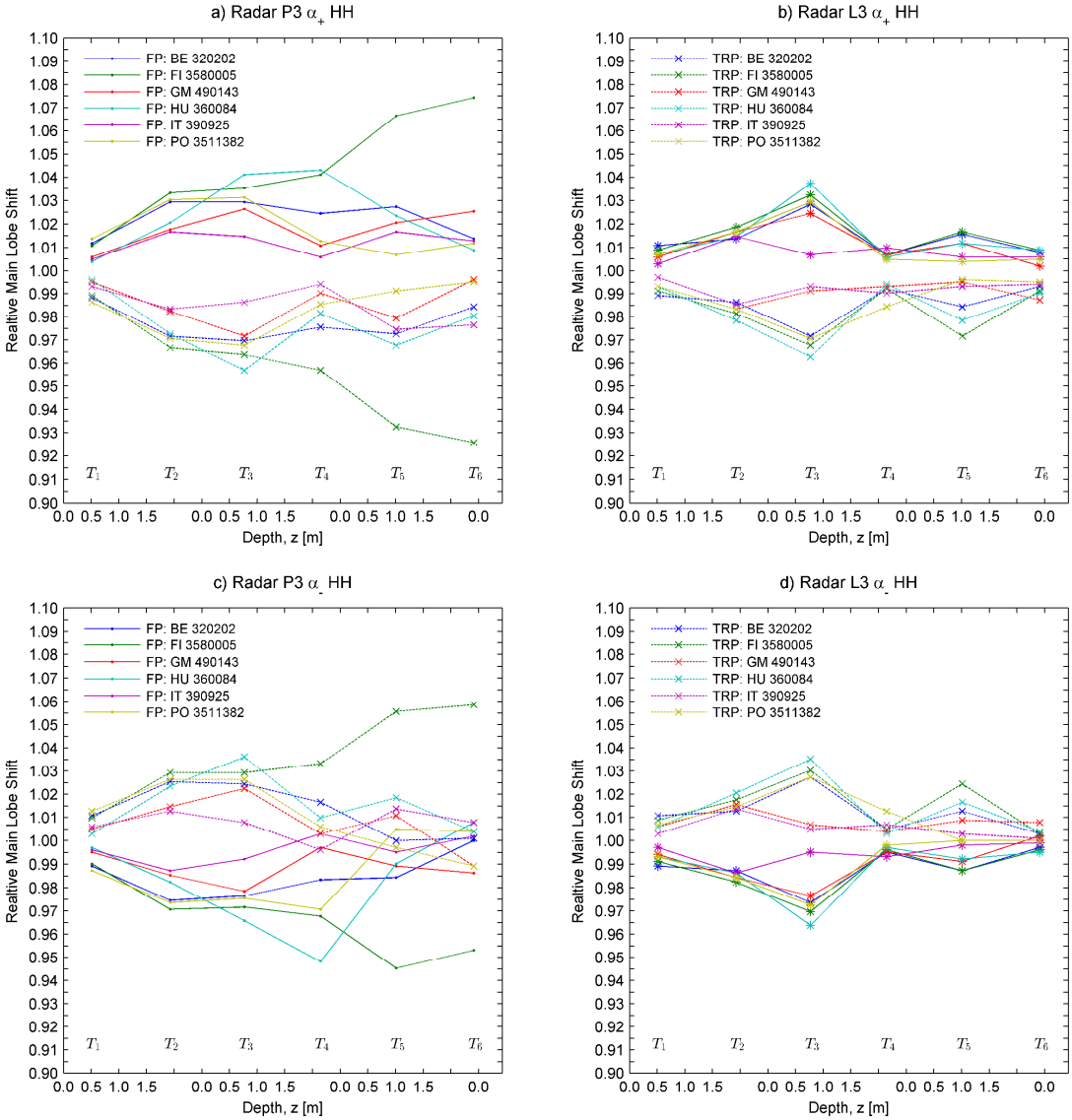

Figure 3.19 Relative main lobe shift from expected position after FP and TRP for two radars (Radar P3 and Radar L3) for two radars (Radar P3 and Radar L3) and two configurations (α_+ HH and α_- HH) in six considered soil structures.

sidered soil structures (and even these considered in [127], i.e., *BE* 320200 and *FI* 3580015).

Presented results show that the fairly accurate restoration of the internal signal structure through the initial propagation path occurs regardless of soil structures and its types in consecutive horizons as well composition in adjacent layers. In accordance with the proposed TR measurement assumptions, i.e., Eq. 3.9, the preferably matched signals $s_t^{tr,T_i}(t)$ were created on the basis of an analysis of backscattered pulse envelopes $s_r^{f,T_i}(t)$ without taking into account any corrections dependent on soil types in consecutive soil horizons. Therefore considering the soil structure as unknown system with spatially distributed targets, the pulse restorations and refocusing occurs unaffectedly. Hence, the proposed method becomes universal and independent of the type of soil since pulse refocusing occurs for different radars, polarization and LFM pulse slope. Furthermore, the extension of a conventional SAR system by additional acquisition in TR manner can provide a airborne radar system (possible to define as the TR-AGPR) with subsurface imaging capabilities of the unknown soil structures.

3.5 Chapter Summary

This chapter presents some considerations about TR approach for subsurface imaging from airborne platform. While the TR technique has been used successfully in a wide range of remote sensing systems (experimentally confirmed advantages), as results from foregoing considerations its application for high-resolution subsurface imaging requires necessary modifications of existing imaging methods and, what is most important, intensified efforts in developing accurate signal processing algorithms.

The impact of dispersions and losses has been discussed throughout the spectrum of backscattered pulse from two point-like targets imaged at two carrier frequencies with three different bandwidths. Extension of the signal bandwidth allows one to obtain more accurate information about tge soil nature which is conveyed in two effects, i.e., irregular attenuation of the backscattered pulse envelope as well in the distortion of the internal pulse structure. Moreover, a too narrow bandwidth is unsuitable for subsurface imaging, hence, the precise knowledge about the nature of the investigated medium enhance the choice of a larger frequency band and a carrier frequency for subsurface imaging. An analysis of these effects has led to the hypothesis that the reconstitution of initial prorogation path with a simultaneous adequate over-amplification lead to the restoration of internal pulse structure. The use of preferably matched signal to the investigated medium (with a suitable matched non-linear frequency variation and the envelope modulation) enhance the imaging capabilities. In addition to many differences with the conventional TR technique, it is applied based on the same expectation about propagation path reconstruction.

Additionally, the TR measurement scheme has been proposed for TR-AGPR system in a monostatic configuration and in TR reflection mode. This TR scheme, designed to verify the assumed hypothesis, differs significantly from the commonly used TR scenario performed in transmission mode, and its objective is different in relation to them. Namely, instead of energy focusing at target location, the aim is to obtain the *cumulative-in-time* pulse restoration. Proposed scheme has been validated over a approximated soil structure for two radars operating at two different carrier frequency both with 200 MHz bandwidth. Moreover, the refocusing phenomenon was confirmed for each considered soil structure and buried target location. It has been observed that, although different types of soil exhibiting a layered structure affect the pulse in their own way, the pulse restoration occurs independently if these structures.

Finally, an additional acquisition in TR mode, beyond reliance on signal acquired in initial probing, depends on the mission parameters defined for initial probing (conventional SAR acquisition). Hence, their proper selection is necessary for the TR-AGPR mission, which can be successfully carried out over any type of soil structure, in particular, over non-arid and large areas.

CHAPTER 4

SYNTHETIC APERTURE AND INTERFEROMETRY APPLICATION FOR BURIED POINT IMAGING

This chapter addresses the efforts of synthetic aperture application for focussing and interferometry of buried structure. Based on the introduction to SAR concept (Section 1.3), the motivations of TR-based SAR imaging of subsurface structures are presented. When the fine azimuth resolution requires the undistorted range resolution (regardless of its exact value depending of signal bandwidth), in inhomogeneous structures the TR reveals the azimuth resolution by restoration of the fine range resolution initially disturbed by impact of the soil. The imaging geometry in InSAR mode is presented with mission parameters as well the raw SAR images simulated in assumed geometry are shown and described. To verify the TR impact on image fomentation method the raw SAR images were focused with the Range-Doppler Algorithm (RDA) under the assumptions about the unknown soil parameters. As shown in ***Chapter 3****, when the TR impact on range compression enhance the range resolution, its applications along L_{sar} results in the narrowing and reinforcement of target trajectory over the clutter background. However, the parameters used for synthesis of azimuth reference function changed under TR acquisitions. Finally, based on the same assumption about the unknown soil, the InSAR method has been applied for soil structure reconstruction.*

4.1 TR-based Synthetic Aperture and Interferometry for Subsurface Imaging from Airborne Platform

As mentioned in Introduction (Section 1.2), SAR methods were extensively used for imaging the soil subsurface structure either from airborne platform (shuttle mission) or were combined with other techniques as GPR. The soil nature affects the results of application the SAR technique causing the problems, among others, related to range defocusing and misplacement ([87], and presented in Chapter 2). While, as results from SAR principles, the azimuth processing is coupled with range processing, hence, range defocusing encountered over several range (depth) cells distorts the azimuth resolution. Whereas fast-time processing is the first step leading to a two-dimensional high-resolution imaging, improvement of range compression is a necessary step to realize the full potential of SAR imaging, in particular, of the optically invisible soil structure. The works on the InSAR imaging of subsurface layers were started quite recently [86], whereas the interferometric technique for SAR-based GPR was presented much earlier [47].

As shown in the previous chapter, the use of TR technique enhance the range compression performed on the backscattered signal recorded at a particular position u_n along synthetic aperture line L_{sar}. Outside the drawbacks resulting from the extension of the effective time for range compression at u_n (see Fig. 3.6 and Section 3.3.3), the TR leads to focusing of target at one dominant range cells instead of spreading it into several cells, where a few of them can have a similar intensity (i.e., apparent targets, see Fig. 3.8). This, in turn, leads to range misplacement and wrong assessment of target location. Hence, while TR reinforces fast-time processing as seen in Chapter 3, its application also directly affects the quality of slow-time processing. This dissertation, among other issues, mainly addresses the problem of synthetic aperture and interferometry application for buried targets detection over non-arid areas, where the constitutive parameters of soil structure are considered as unknown and inhomogeneous in depth. In this chapter, the image formation method is applied for different configurations of radar systems. Later, complex SAR images are processed with phase interferometry methods for extraction of additional information (as detailed in Section 1.3.1).

4.1.1 Imaging Geometry

For a complete consideration of the raw data collection scheme, Fig 4.1 shows two spatially distributed radars (stereo imaging geometry), which are separate by the interferometric baseline B_{in} orthogonal to velocity vector and at an angle β_{in}. The perpendicular baseline B_p (also referred to as a effective baseline) is a projection of B_{in} to the slant range. Assuming different configuration of these radar, Fig 4.1 shows two different SAR missions. However, for an identical bandwidths and polarizations of these radars, it shows a InSAR configuration in two-pass mode in which the two coupled raw images can be simulated [21]. For the differentiation, in Fig 4.1 one radar is coloured (marked) as the Radar P, second as the Radar L (as used in the previous chapter, for instance, in Fig. 3.3, and defined in Tab. 3.1). In the case of considering only one radar, the Fig 4.1 is identical with Fig 2.13 and generally presents the same situation as in Fig 2.11 and Fig 2.12. The elevation θ_{el} and azimuth θ_{az} beam-width of antenna pattern are equal, i.e., $\theta_{el1} = \theta_{el2}$ and $\theta_{az1} = \theta_{az2}$, and the antenna gain is modulated by tapered cosine window along L_{sar} with tapers parameter $r_g = 0.15$. The spatial separation of radars (Master in $(0,\ u_n,\ H_p)$ and Slave in $(\Delta x,\ u_n,\ H_p + \Delta h)$) and assumed overlapping of the main axis of the antenna beam (the Line-of-Sight (LOS)) on the surface leads to different incident angle θ_i, i.e., $\theta_{i1} \neq \theta_{i2}$. Moreover, when the swath centres are co-registered, their width varies between radar and an effective area under observation is narrowed to the common part of swaths. Unlike to Fig 2.13, that addressed the geometry for particular po-

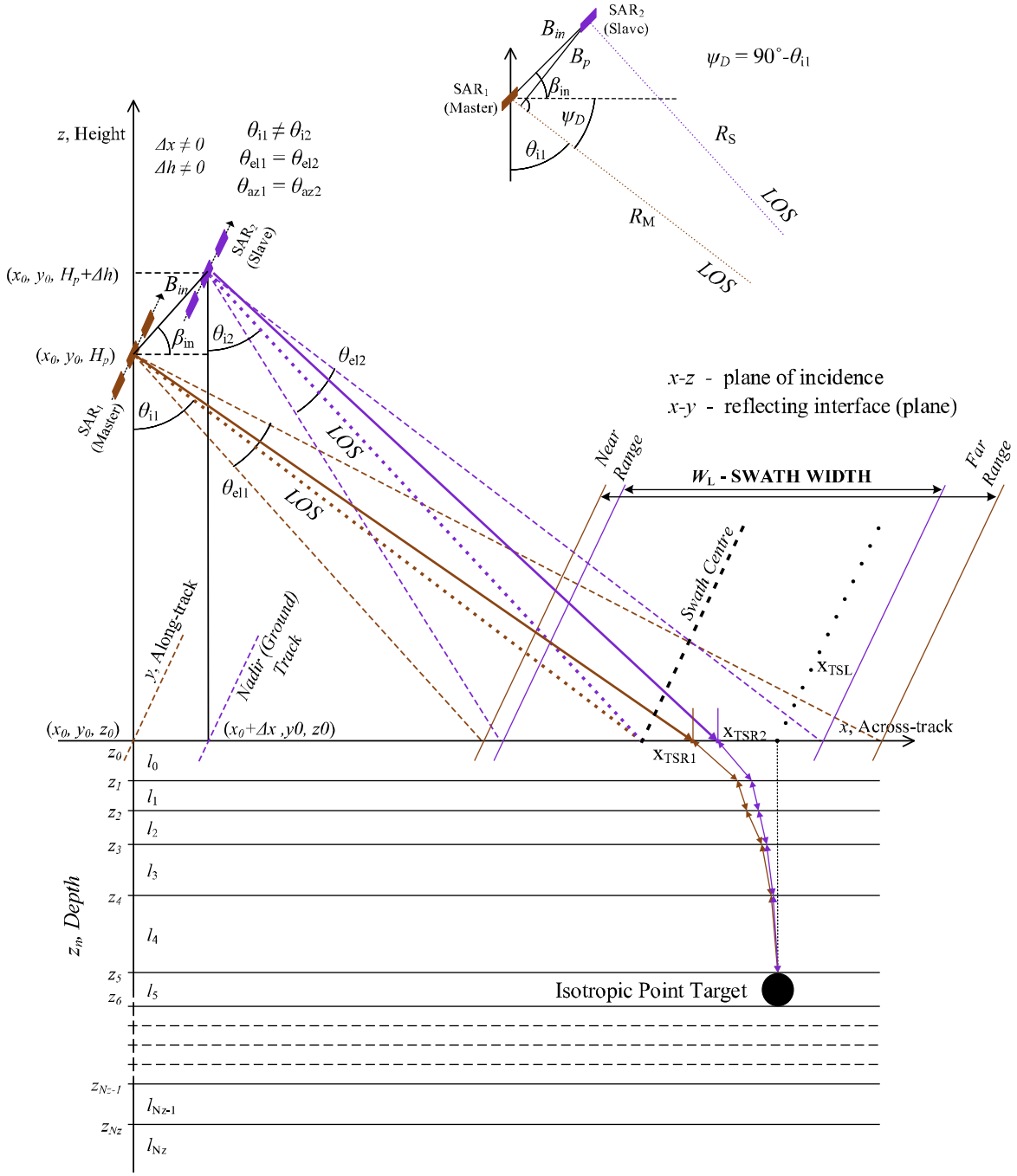

Figure 4.1 Geometry of the InSAR imaging over a stratified isotropic medium made up from N_z homogeneous, planar and thin layers (the relationship between platforms altitude and layers height is intentionally disrupted).

sition u_n, Fig 4.1 emphasizes problems for buried target imaging along the flight path of airborne platform (however, not all data have been placed in this figure, in comparison to Fig 2.13). As previously denoted, the x_{TSL} stands for target location at surface, and as the swath centre point (square markers), it determines the line (circular markers) at soil surface parallel to the velocity vector. The x_{TSR} denotes target surface refraction point, wherein wave enters the soil structure. As results from Fig 4.1, x_{TSR} is different for considered radars and moves along the parabolic curve during illumination. In conventional SAR data collection, where the target is located at terrain, the slant range changes parabolically with a minimum reached at the position $u_n = u_{cpa}$, at which the LOS intersects the target plane (x, u_{cpa}, z).

For subsurface imaging, where the target is buried in soil, the parabolically variations of the distance can be considered only in relation to x_{TSL} (located at surface). However, more interesting are the slant range changes to x_{TSR} along the flight path. Multiple inward and outward refractions at soil layers and change of the incident angle along L_{sar} result in variation of $[X_{TSR}(u_n), Y_{TSR}(u_n), 0]$ at terrain surface, in particular, in strongly inhomogeneous soil structure. In that structure, the slant range to target buried in soil (the horizontal and vertical planes), $r(t)$ (Eq. 3.15), can oscillates along the parabolic curve. Fig. 4.2 shows the changes of ground distance to x_{TSL} (top) as well as to x_{TSR} (middle) along L_{sar} for six different targets located at depth z_i. Three of these targets (T_1, T_2, T_3) are buried under each other, the others three (T_4, T_5, T_6) are distributed at the same depth as the shallowest target of the previous ones along the constant u_n position. Apart from the exact values of mission geometry, Fig. 4.2 shows only a trends in the changes. When it may seem that the curves of x_{TSL} (top) and x_{TSR} (middle) overlap, x_{TSR} is slightly shifted toward the radar. It is shown in Fig. 4.2 (bottom), where variation x_{TSL} and x_{TSR} has been concentrated on targets T_1, T_2, and T_3, which lie vertically below each other. Whereas the black lines (solid for Radar P, and dashed for Radar L) represent the ground range to x_{TSL}, the coloured lines represent the ground range to x_{TSR} for three buried targets (solid for Radar P, and dashed for Radar L). Due to the higher altitude of Radar L ($H_{p2} > H_{p1}$), the dashed lines are wider (broader footprint on the ground), further they are more curved as well due to lower incident angle ($\theta_{in2} < \theta_{in1}$). Fig. 4.2c shows that at u_{cpa} the spacing between x_{TSR} tracks increases for deeper targets. For these targets, the curve of x_{TSR} moves away from x_{TSL} towards the nadir radar track. For InSAR, where the CREP (Fig. 2.8) is the same for both radars (same operational bandwidth), the drift of x_{TSR} depends on the θ_i, which varies along the L_{sar}. For two various bandwidth, where the CREP is different, outside depending on the θ_i, the drift of x_{TSR} depends also on the relative refractive index $n_{n,n+1}$ at soil surface and at interfaces between soil layers. The contribution of the travelling time in soil increases for lower incident angle, where the relation between travelling time in air to the travelling time in soil decreases.

4.1.2 Simulation Setup

When the mission geometry is known (Fig 4.1), let analyse the mission parameters. Among others, for azimuth processing the most important are the v_p, the PRF and a number of position (scans) along L_{sar}, i.e., N_s. These parameters, together with the θ_i, θ_{el} and θ_{el}, affect both the swath size and the quality of azimuth processing. Too low PRF combined with a small number of scans N_s and a too high v_p lead to an acquisition of the phase history over a too coarse grid point. Moreover, as presented in Section 2.2, the range of possible PRF values is determined by mission geometry and parameters as well by radar waveform length. Given that the higher observation angles result in surface clutter minimization (for example, see the level of clutter for further slant distances in Fig 3.13 or the σ^0 in Fig. 2.18), the θ_{i1} (for Master radar) was assumed as $\theta_{i1} = 60°$, where typically, for airborne SAR systems, the θ_i increases from 45° to around 80°. Furthermore, for the analysis of slow-time processing, the $\theta_{el1} = \theta_{el2} = 2.0°$. Although this value can be considered as small, from Master radar altitude $H_p = 3000$ m it allows one to cover a swath about the ground width of (see Fig. 4.1)

$$W_{L1} = H_p \left[\tan(\theta_{i1} + \frac{\theta_{el1}}{2}) - \tan(\theta_{i1} - \frac{\theta_{el1}}{2}) \right] \approx 419.30 \text{ m} \tag{4.1}$$

which is adequate for the needs of the assumed mission objectives. For registration of the phase history in a fairly wide angle, the $\theta_{az1} = \theta_{az2} = 10.0°$. At assumed θ_{i1}, the dwell time along swatch centre (square points in Fig. 4.1) equals $T_{dwell1} \approx 14.00$ s for Master radar and assumed platform velocity $v_p = 75.0$ m/s (reachable for the typical light airborne SAR

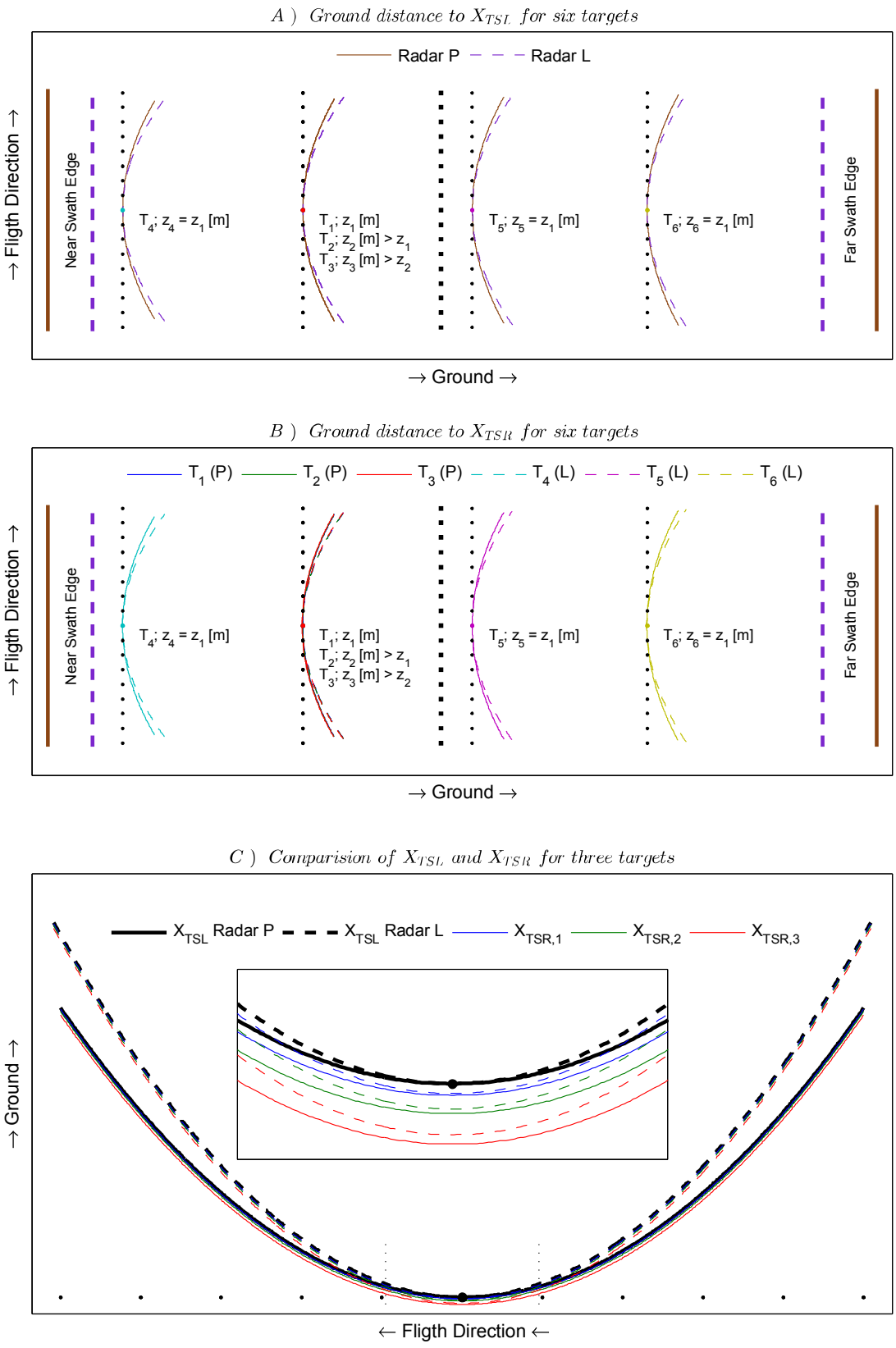

Figure 4.2 The variation of the ground distance to x_{TSL} (top) and to x_{TSR} (middle) for six buried targets. A comparison of x_{TSL} and x_{TSR} (bottom) for three objects linearly located in depth.

platform). For the SAR_1 the range of possible PRF values equals (see Eq. 2.52 and Eq. 2.53)

$$27 \text{ Hz} < PRF_1^P < 203132 \text{ Hz} \tag{4.2}$$

$$81 \text{ Hz} < PRF_1^L < 203132 \text{ Hz} \tag{4.3}$$

for Radar P3 and Radar L3, respectively. For the same geometry, the upper limit (Eq. 2.53) is constant, whereas the higher carrier frequency of Radar L3 (three times as for the Radar P3) reduces the size of the antenna in the azimuth direction L_R, and hence, the lower limit (Eq. 2.52) increases threefold.

Foremost, in the default configuration for independent SAR imaging the Slave radar (always located in SAR_2) is spatially separated from Master about $\Delta h = 50$ m in height and $\Delta x = 500$ m in ground range in order to verify the TR impact on images acquired at different angles. Almost the horizontal displacement of sensors have reduced the observation angle to

$$\theta_{i2} = \arctan\left[\frac{H_p \tan(\theta_{i1}) - \Delta x}{H_p + \Delta h}\right] \approx 56.998° \tag{4.4}$$

under which σ^0 (see Fig. 2.18) considerably changes. The interferometric baseline B_{in} is derived from the Pythagorean theorem

$$B_{in} = \sqrt{\Delta h^2 + \Delta x^2} \approx 502.49 \text{ m} \tag{4.5}$$

and the angle between B_{in} and the ground plane is equal to

$$\beta_{in} = \arctan\left(\frac{\Delta h}{\Delta x}\right) \approx 5.7° \tag{4.6}$$

The perpendicular baseline B_p equals (refer to additional sketch in Fig. 4.1) [22, 23]

$$B_p = B_{in} \sin(\psi_D + \beta_{in}) \approx 293.30 \text{ m} \tag{4.7}$$

for the $\theta_{i1} = 60°$, where $\psi_D = \pi/2 - \theta_{i1}$. In general, Eq. 4.4 - Eq. 4.7 show the impact of Slave radar shift, which in turn affects the dwell time along swath centre. For Slave radar the $T_{dwell2} \approx 13.06$ s for constant v_p. The swath width for Slave radar equals $W_{L2} \approx 359.16$ m, (Eq. 4.1 with the $H_p + \Delta h$ and θ_{i2} instead of H_p and θ_{i1}, respectively) and is located inside the swath of Master radar (as shown in Fig. 4.2). For SAR_2, the PRF range equals (see Eq. 2.52 and Eq. 2.53)

$$27 \text{ Hz} < PRF_2^P < 221740 \text{ Hz} \tag{4.8}$$

$$81 \text{ Hz} < PRF_2^L < 221740 \text{ Hz} \tag{4.9}$$

respectively, for Radar P3 and Radar L3. The lower limits of possible PRF values are constant for both radars, whereas the shift toward the swath reduced the slant range to its near and far edges. Hence, as results from Eq. 2.53, the upper limits increase for both radars to 221740 Hz. In order to ensure uniform sampling along the L_{sar} $PRF = 150$ Hz was assumed for both radars (also to reduce computational effort and memory saving). The $N_s = 1500$ uniformly spaced point (linear collection) results in a flight distance equals 750 m for the assumed PRF and v_p. Therefore, considering the move of the LOS along the L_{sar}, the SAR_1 observes a swath of 750 m x 419.30 m and the SAR_2 of 750 m x 293.30 m. The mission duration time equals $T_s = 10.0$ s.

When this section provides only a general description of the mission parameters related to its geometry, the radar and waveform parameters are given in Section 3.2 (Fig. 3.3, Tab. 3.1). For ensuring a fine range resolution and investigation of TR refocusing capability

in a wide frequency range, the Radar L3 and Radar P3 were selected, both of 200 MHz bandwidth. Each of them can be used as Master and Slave radar unit in a configuration as in Fig 4.1. Finally, the $N_T = 10$ isotropic buried targets were randomly located in soil structure (from Fig. 2.4) to the depth of a 1.5 m and with a random distribution in y along-track and x across-track dimension. Conversely to conventional SAR simulations, the simulations of backscattered returns from buried targets starts as soon as the antenna footprint cover the $[X_{TSR}(u_n), Y_{TSR}(u_n), 0]$ and stops when it over passed that coordinates. So the effective exposure time (or dwell time) is longer than follows from theoretical considerations (Eq. 2.50).

4.1.3 Raw Data Analysis and Comparison

Fig. 4.3 and Fig. 4.4 present the raw data $s(t, u)$ simulated for Radar P3 and Radar L3, respectively, over six different soil structures (from Fig. 2.4). The Fig. 4.3 compares results of the Forward Probing (FP) (left column) and the Time-Reversal Probing (TRP) (right column) simulated for Radar P3 (in geometry of SAR_1 in Fig. 4.1). Further, the Fig. 4.4 compares results of the FP (left column) and the TRP (right column) simulated for Radar L3 (in geometry of SAR_2 in Fig. 4.1). The brighter areas in these images represent a stronger backscattered echoes from buried targets. However, for the set of isotropic targets, the level (intensity) of backscattered returns mainly depends on the soil effect. White dots represent the target location at soil surface $[X_{TSL}(t_i), Y_{TSL}(t_i), z = 0]$. As shown in the first chapter (Fig. 2.15 and Fig. 2.16), the deeply located targets are more attenuated and blurred by the clutter. For a given radar (Radar P3 or Radar L3), the differences between the magnitude of raw images of SAR_1 and SAR_2 are slightly different (also within the polarization). However, the additional figures are not supplemented for comparison, i.e., Radar P3 in SAR_2 and Radar L3 in SAR_1. Since the HH polarization provides the higher penetration depth δ (Eq. 2.86) because of the lower interference backscattering (see Fig. 2.18), results for the HH polarization are only used in following section of this chapter. Moreover, while in previous chapter the Fig. 3.8D and Fig. 3.12D present and compare the raw slant range profile of illuminated scene (i.e., results before range compression) after FP and TRP, the Fig. 4.3 and Fig. 4.4 present and compare the total raw data $s(t, u)$ before their two-dimensional compression. Vertical lines in the charts represent the near swath edge, swatch centre line and far swath edge, respectively, all being parallel to flight direction. Extension of the raw data beyond far swath edge shows the delay of backscattered echoes from objects located in far swath area. Hence, the adjusted value of PRF (significantly lower than upper limit defined by Eq. 2.53) allows their correct registration. The background colour in these figures represents the first layer of soil (refer to the colour scale in Fig. 2.4). For both radar and acquisitions, the influence of antenna gain on backscattered signal level is apparent in images and the envelope variation and distortion along the azimuth direction is weak. Results shown in these figures are presented in linear scale and compared within a given soil structure to prove the impact of TR technique on the raw data magnitude. Generally, the incorporation of TR technique into a raw data acquisition scheme (Fig. 3.6) enhanced data collection over almost all soil structures for Radar P3 (Fig. 4.3) (except the *IT* 390925) and for majority of these structures for Radar L3 (Fig. 4.4) (except the *HU* 360084 and *IT* 390925). Outside these structures, the raw data magnitudes for acquisition in TR mode are more intense and have a uniform level for particular objects. The backscattered echoes from the buried objects are unified in amplitude level along their duration (compare Fig. 3.8D and Fig. 3.12D). However, the true difference between the intensity of Radar P3 and Radar L3 images is distorted by the different ranges of intensity scale used in these figures. Finally, taking into account the different colour scales, these two figures indicate the advantages of P band over L band for buried structures imaging, even considering only a results of FP acquisition.

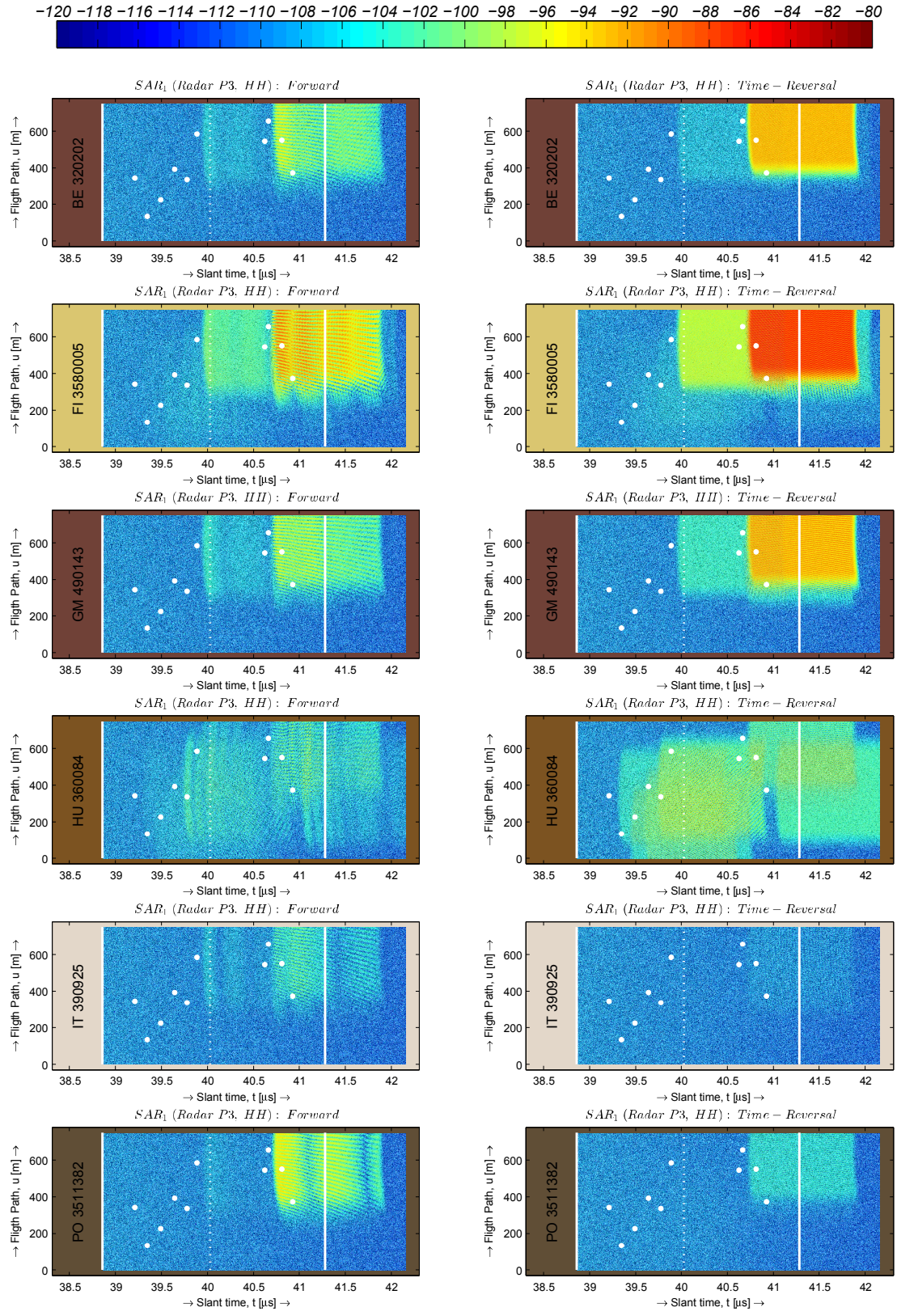

Figure 4.3 Raw data (in [dB]) comparison for Radar P3 (SAR_1) between FP (left) and TRP (right) for six considered soils structures.

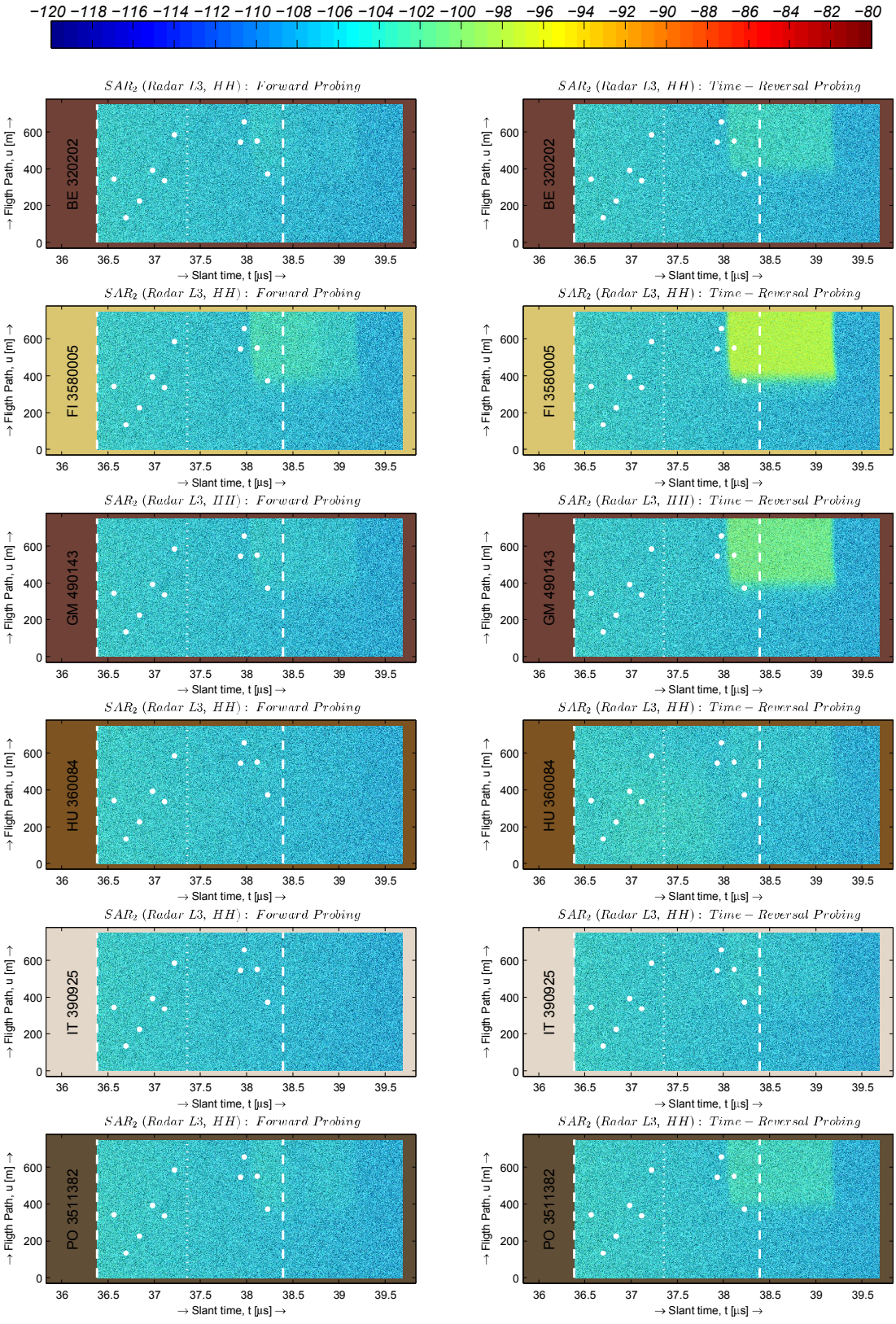

Figure 4.4 Raw data (in [dB]) comparison for Radar L3 (SAR_2) between FP (left) and TRP (right) for six considered soils structures.

Radar P3 ($f_c = 400$ MHz, $B = 200$ MHz, HH) (SAR_1 in Fig. 4.1): For this configuration, expect the raw data for *HU* 360084, the FP acquisition (left column) gives one dominant backscattered echoes for the shallowest target, which is slightly modulated by other objects (interference). For *HU* 360084, backscattered echoes from more than one dominant target are visible. The TRP acquisition (right column) resulted in an increase of the dominant backscattered echo and slightly enhances at least one weaker target from background clutter for *BE* 320202, *FI* 3580005 and *GM* 490143. For *HU* 360084, the backscattered returns for six targets are uniformly enhanced. However, for *IT* 390925 and *PO* 3511382, TRP acquisition reduced the dominate scatterer and other shallow objects. As shown in the Fig. 3.11, energy normalization by factor $K_a(t)$ depends on envelope attenuation, and for strongly deformed backscattered signals (due to their high envelope fluctuation) the envelope of time-reversed signals is inverted both in the time (mirror reflection) and highly in amplitude (minima changed in maxima and oppositely). Therefore, in time-reversed radar waveform only one peak have the highest level equal to A_m (see Fig. 3.11), and the average signal level is significantly lower that this maximum, even though the other peaks appear locally in envelope. Strongly amplified frequency components are in TRP acquisition still attenuated more than the others, hence, the envelope is aligned to the level of low-reinforced components. When the different soil attenuated the signal envelope in various way, the smoothed envelopes can be lower for TRP than for FP acquisition, as for *IT* 390925 and *PO* 3511382.

Radar L3 ($f_c = 1200$ MHz, $B = 200$ MHz, HH) (SAR_2 in Fig. 4.1): Expect a single dominant backscattered echo in the *FI* 3580005, the FP acquisition (left column) does not revealed the dominant scatterers in other considered structures. Comparing with FP acquisition for Radar P3, the L band is mostly not suitable for almost all considered structures, except for these which contain more sand in the upper layers as *FI* 3580005. Hence, a preliminary information about the area intended for imaging support carrier frequency selection. Besides that, TRP acquisition (right column) reveals a single dominant backscattered returns in *BE* 320202, *GM* 490143 and *PO* 3511382 as well reinforce that in *FI* 3580005. For the other two structures, i.e., *HU* 360084 and *IT* 390925, TRP acquisition does not reinforced the backscattered returns level. Similarly as for Radar P3, the $K_a(t)$ is calculated based on initially attenuated envelope in FP. Hence, beside that the attenuation mechanism are differed between radars (i.e., operational bandwidth), their constant nature in TRP acquisition aligns the envelope to the level of low-reinforced components. And in *HU* 360084 and *IT* 390925 the backscattered signals are aligned but not reinforced over clutter background.

In the next section the SAR technique is applied for image formation. However, raw data for both radars are further processed, although the P-band showed higher capabilities to penetrate the considered structures than L-band.

4.2 Synthetic Aperture Application with TR

In a very simplified manner, the image formation by SAR processor can be identified with two-dimensional processing along orthogonal dimension recognized as the range and azimuth. As mentioned in Section 1.3, the range compression is based on the MF approach, that used a replica of transmitted signal as a reference function, and the range resolution is determined by radar waveform bandwidth. In azimuth direction, the reference function is synthesised as the expected Pulse Spread Response (PSR) along the L_{sar}, and the azimuth compression can also be based on the MF approach. In the two compressions, the MF approach correlates an appropriate reference function with the range or azimuth line. Whereas the range reference

function is constant for each range line, the azimuth reference function changes for each azimuth line from near to far slant range (see the chirp rate K_u and the exposure time T_{dwell} denoted by Eq. 1.12 and Eq. 1.14, respectively, both depending on the slant range r_s).

Up to day, dozens of algorithms have been developed both in the time and frequency domain. Their derivation and comparison can be found in [5,10,14], among others. The oldest image formation technique, defined as the Doppler Beam Sharpening (DBS) [3], evolved into a series of algorithms, which make certain mathematical approximation and exploit a PSR to focus a spread energy from point target over a series od 1-D range profiles into a point-like returns in focused image. However, nowadays, these well-defined algorithms are rather improves and modified, through phase correction related to the unstable platform trajectory or other methods in general leading to better resolution in azimuth, than completely new algorithm are developed. In addition, there are also attempts to match the reconstruction algorithm to illuminated subsurface structure with perfectly known and constant parameters as [46]. Various data collection modes are closely related to image formation methods. For broadside Stripmap SAR mode, as assumed in this dissertation (for instance, see Fig. 2.11 and Fig. 2.12), the Range-Doppler and Fourier image formation methods are considered as preferably tailored. These methods include algorithms such as the Range-Doppler Algorithm (RDA), the Range Migration Algorithm (RMA) and the Chirp Scaling Algorithm (CSA) [14]. The former algorithm, i.e., RDA, is the most common algorithm which uses the Doppler shift along L_{sar} to synthesize the azimuth reference function from near to far range and all operations are performed sequentially in one dimension only. The other two, i.e., RMA and CSA, are modified version of RDA, in which the full hyperbolic form of PSR is used instead of its parabolic approximation and where range and azimuth processing may intersect [10].

When the proposed data collection scheme (see Fig. 3.6) incorporates the TR technique, the raw data (simulated as depicted in Chapter 3) are processed with RDA to verify the impact of TR on the range and azimuth compression with MF approach. Whereas the approximated soil structures (developed in Chapter 2) are used in raw data simulation (to calculate backscattered signal from buried targets, i.e., deformed amplitude and phase, and to estimate its exact time delay), the hypothesis about unknown soil is assumed for image formation, hence, this ranks the work even more challenging than in the case when soil nature is totally known (or even partially). In the following discussion the slant range is directly determined based on time delay as $r_s = ct/2$, where $\Delta r_d = c/(2f_s)$, since radar operates in the time domain and f_s is sampling frequency. The processing on the backscattered signal is carried out as if it returns from terrain surface.

4.2.1 Range Compression with TR

After the FP, the MF approach uses the conjugated replica of initially transmitted signal $h^f(t) = s_t^{f*}(-t)$, and the range compression can be expressed in frequency domain as

$$s_{r,c}^{f,mf}(t) = \mathcal{F}^{-1}[\, S_{r,c}^{f}(\omega)\; H^f(\omega)\,] \tag{4.10}$$

where $s_{r,c}^{f,mf}(t)$ ia a 1-D complex range profile of illuminated scene derived from u_n, $S_{r,c}^{f}(\omega) = \mathcal{F}[s_{r,c}^{f}(t)]$ (for $s_{r,c}^{f}(t)$ see Fig. 3.8D), $H^f(\omega) = \mathcal{F}[h^f(t)]$, whereas the $\mathcal{F}[\,]$ and $\mathcal{F}^{-1}[\,]$ denote forward and inverse Fourier transform, respectively. As shown in figure Fig. 3.9E, the MF approach increase the SNR and some strong targets are detected (in case of *HU* 360084).

For the TRP, the Cross Matched Filtering approach also uses the replica of the transmitted signal. However in the TR scheme, whereas the $s_{r,c}^{tr}(t)$ contains backscattered returns derived from time-reversed signal (defined by Eq. 3.9), the reference function used in the

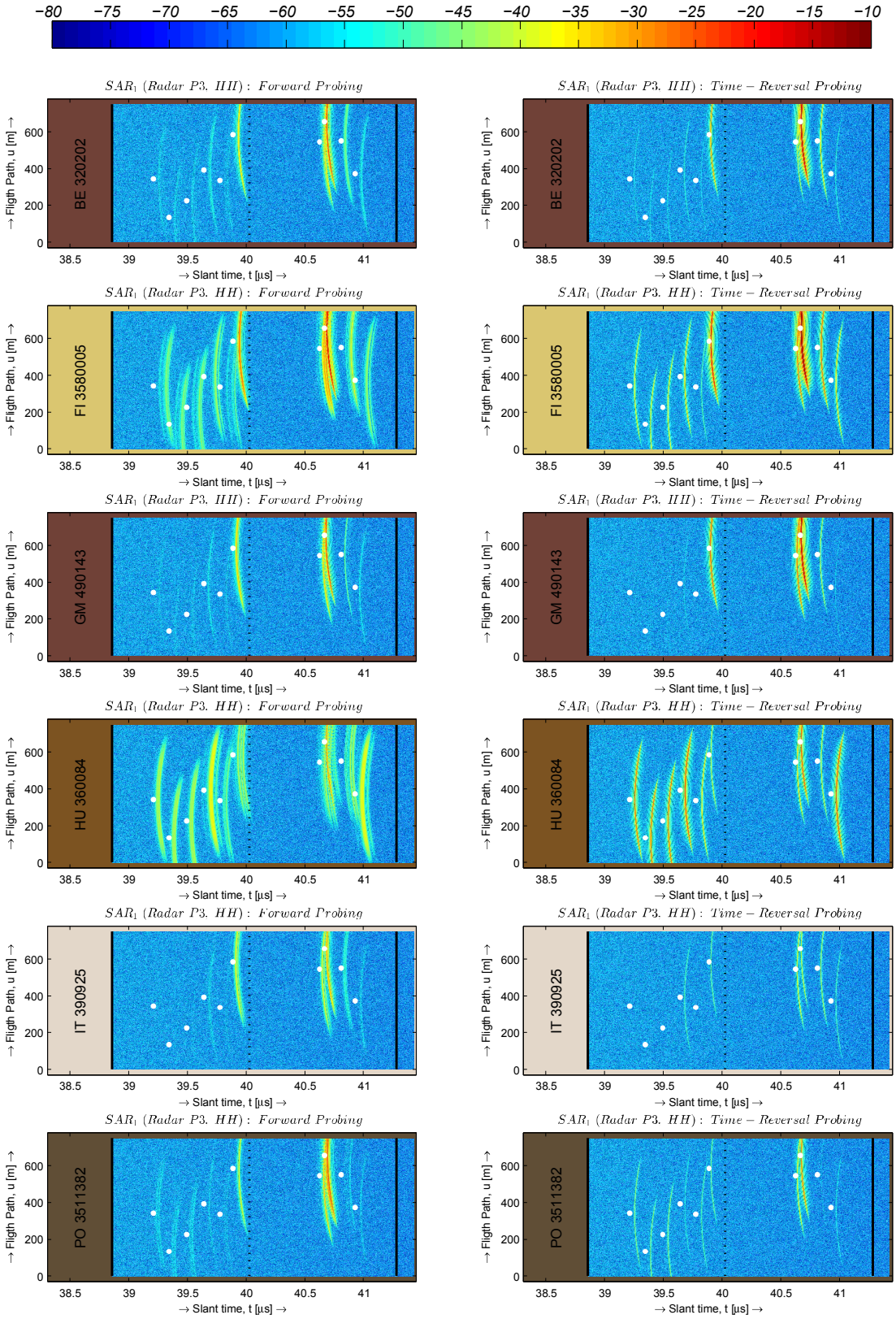

Figure 4.5 Range compressed data (in [dB]) for Radar P3 (SAR_1) after FP (left) and TRP (right) and for six considered soils structures.

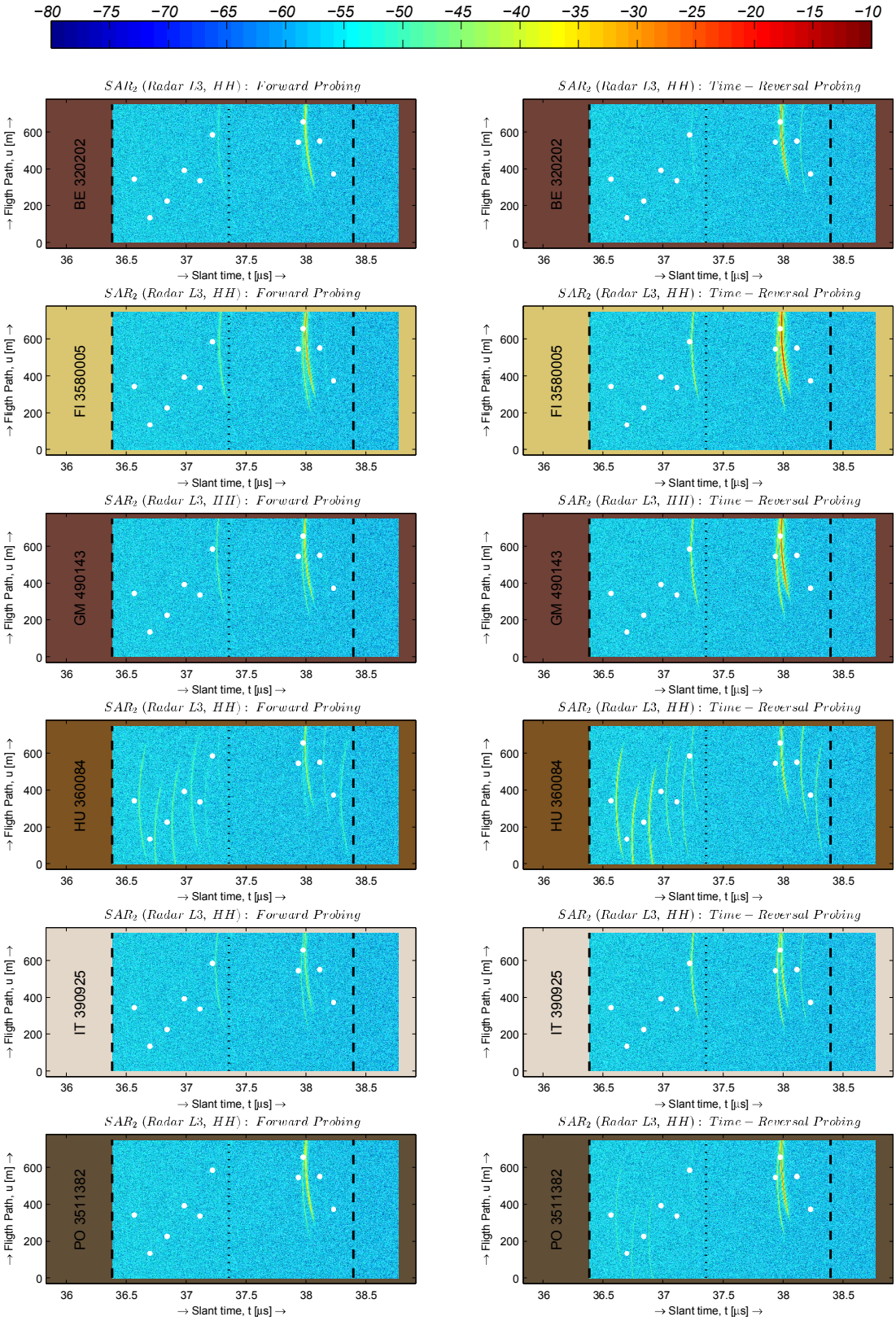

Figure 4.6 Range compressed data (in [dB]) for Radar L3 (SAR_2) after FP (left) and TRP (right) and for six considered soils structures.

range compression is the normal replica of initially transmitted signal $h^{tr}(t) = s_t^f(t)$. An additional conjugation leads to a convolution of two signals in which the frequency changes have the same slope, then the phase compensation does not occur. Similarly as for the FP, the range compression in each range line can be expressed in frequency domain as

$$s_{r,c}^{tr,mf}(t) = \mathcal{F}^{-1}[\ S_{r,c}^{tr}(\omega)\ H^{tr}(\omega)\ ] \tag{4.11}$$

where $s_{r,c}^{tr,mf}(t)$ ia a 1-D complex range profile of illuminated scene derived from u_n in TRP, $S_{r,c}^{tr}(\omega) = \mathcal{F}[s_{r,c}^{tr}(t)]$ (for $s_{r,c}^{tr}(t)$ see Fig. 3.12D), $H^{tr}(\omega) = \mathcal{F}[h^{tr}(t)]$. More targets (even the weaker ones) are now detected in Fig. 3.12E, even for Radar L3. Hence, an integration of the TR into a acquisition scheme beyond detection gain results in the use the direct copy of the transmitted signal $s_t^f(t)$ as a reference function in range compression instead of its conjugated time-reversed version $s_t^{f*}(-t)$. Fig. 4.5 and Fig. 4.6 present the result of range compression (in the same convention as Fig. 4.3 and Fig. 4.4). Left columns represents the range compression after FP, and right after TRP. The images are less extended beyond the far slant edge, and still, the images are compared within a given soil structure. The gain of TR is clearly evident in the right columns of both these figures. Firstly, as presented in previous chapter, TR narrows again the results of range compression, which are now distributed smoothly along parabolic curves without any apparent targets (side lobes). For FP, these curves are weaker and blurred (compare *HU* 360084 for Radar P3) and contain many apparent targets. Furthermore, whereas the range compression after TR groups together the diffuse energy in a one range cell with dominant level, the weaker targets are revealed and those existing are improved (compare *FI* 3580005 or *PO* 3511382 for Radar P3). And finally, when for some considered soils structures the raw data collected in TRP apparently seem to be worst than these for FP, the range compression after TRP gives better results in each soils structures, even if the number of revealed target is the same for FP and TRP.

4.2.2 Range Cell Migration with TR

As stated in Section 1.3, range and azimuth processing are coupled. The instantaneous slant range changes between radar and target, it not only results in quadratic phase variation along L_{sar} (see Fig. 1.3) but also leads to a range offset (delay) of backscattered echoes that can reach a few range cells. Before the azimuth compression, the target curve (target trajectory) need to be corrected into a straight line along the azimuth time and located in the same range cell within series of the 1-D range complex profile. The process of trajectory compensation is referred to as the Range Cell Migration (RCM). Whereas the target trajectory depends on slant range in slow-time domain (along azimuth) and for multiple targets at the same slant range their curves can intersect, in the range-Doppler domain, after $\mathcal{F}[\ ]$ along the slow-time, the Doppler spectrum is centralized along L_{sar}. Fig. 4.7 show the previously compressed-in-range images in range-Doppler domain after FP (left) and TRP (right). In order to present a general overview of the RCM, Fig. 4.7 shows the Doppler spectrum only for the one soil structure (PO 3511382) and the two radars, Radar P3 (in SAR_1, top) and Radar L3 (in SAR_1, bottom). Before the proper RCM, we have to analyse the figures containing the range-Doppler data. The Doppler frequency is defined as the first derivation of quadratic phase $\phi(u)$ (see Eq. 1.11)

$$f_D(u) = \frac{2v_p^2}{\lambda\ r_s} t_u \Big|_{t_u = u - u_c} = \frac{2v_p^2}{\lambda\ r_s}(u - u_c) = \frac{2v_p}{\lambda}\frac{v_p(u - u_c)}{r_s} = \frac{2v_p}{\lambda}\sin[\theta_f(u)] \tag{4.12}$$

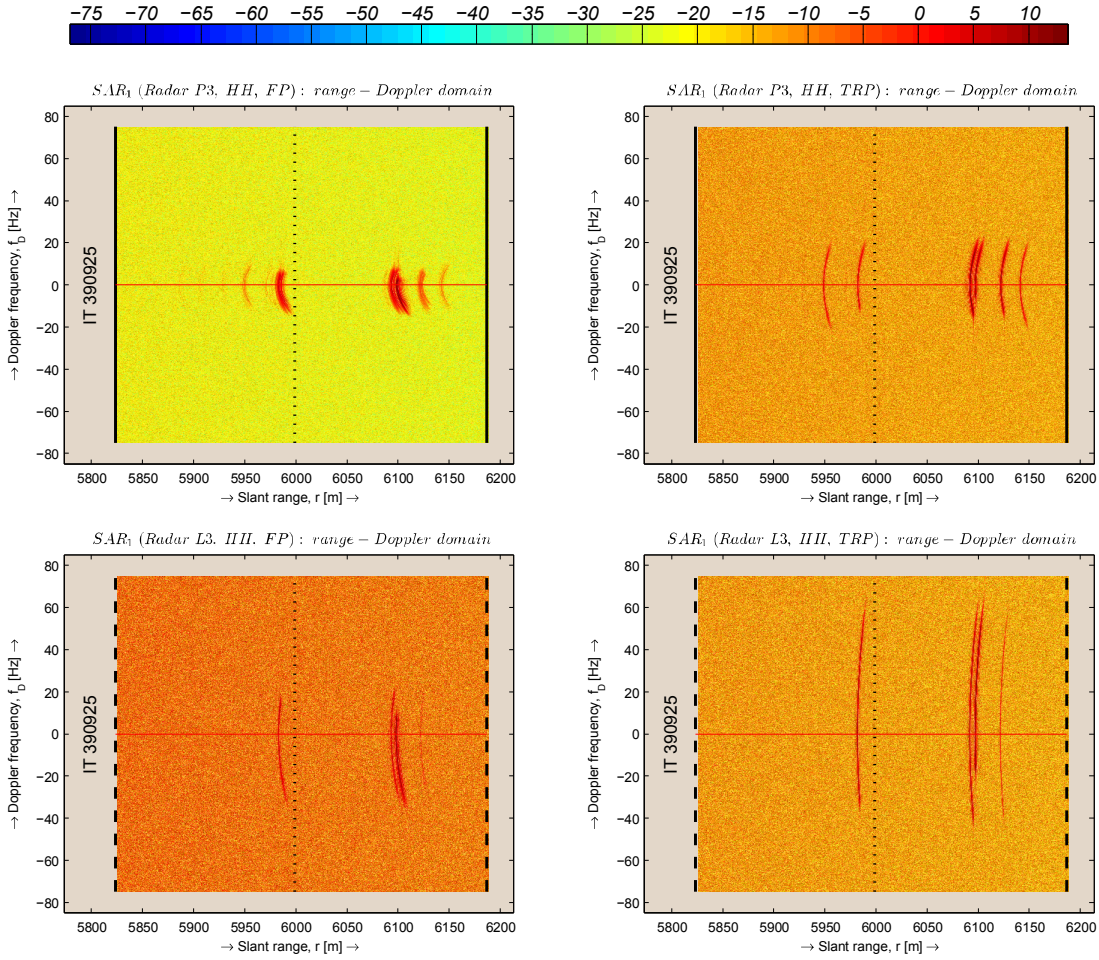

Figure 4.7 Range-Doppler (in [dB]) data for Radar P3 (SAR_1, top) and Radar L3 (SAR_1, bottom) after FP (left) and TRP (right) for *IT* 390925.

where $\theta_f(u)$ is an angle between ground range axis and the projection of the range line connecting radar and target at soil surface in FP. Three main issues are important for the RCM, and further, for azimuth compression. Namely:

- Whereas the lower frequencies are more distorted in soil, after the FP (left column) the Doppler spectrum of Radar P3 (top) is more deformed than Radar L3 (bottom). However, stronger attenuations of the higher frequencies induce the Doppler spectrum is intensive (for Radar P3) and contribution from more targets are evident (for Radar L3 the clutter contribute strongly into background). Additionally, random target location along the L_{sar} results in asymmetrical Doppler spectrum wider towards the object location (targets are not symmetrically illuminated).

- Considering the particular target at constant slant range, after the FP, Radar L3 has a wider Doppler spectrum (even these unsymmetrical) than Radar P3 due to a higher carrier frequency (see Eq. 4.12).

- Application of TR (right column) for both radars leads to wider Doppler spectrum for particular targets (the effective travelled distance by the radar waveforms is twice in TRP as in FP) which is conjugated in relation to FP (follows from TR assumption, Eq. 3.9). Moreover, the same degree of bend at both ends in range direction is spread widely in Doppler domain.

When the first two remarks can be derived after an analysis of Fig 4.5 and Fig 4.6 (irrespective of the soil structure), the last remark is not so obvious for range compressed data. The phase delay and Doppler shift appears at a distance between radar and target in the FP are not reset before the TRP, but, according to the TR assumptions (Eq. 3.9), these two quantities are further reproduced (intensified) over the same distance in TRP. Hence, for TRP the RCM and azimuth processing will be held with different parameters.

In general, the RCM in range-Doppler domain can be performed as a range shift and data approximation in constant range bins. The amount of range shift $\Delta R(u)$ [11] along L_{sar} equals

$$\Delta R(u) = r(u) - r_s = \frac{r_s}{\cos[\theta_f(u)]} - r_s \tag{4.13}$$

where $\theta_f(u)$ changes along L_{sar}. Based on the Pythagorean trigonometric identity, the Eq. 4.13 changes to

$$\Delta R(u) = r_s\left(1 - \left(\frac{\lambda_c f_D(u)}{2v_p}\right)^2\right)^{-1/2} - r_s \tag{4.14}$$

where $f_D(u)$ is defined by Eq. 4.12. Hence, defining a corrected slat range for each platform position, $R_n(u) = r_s + \Delta R(u)$, the $R_n(u)$ equals

$$R_n(u) = r_s\left(1 - \left(\frac{\lambda_c f_D(u)}{2v_p}\right)^2\right)^{-1/2} \tag{4.15}$$

where $f_D(u)$ varies between $-PRF/2$ and $PRF/2$ through N_s values.

For TRP, which is performed in the same position u_n as FP, the amount of range shift is defined by Eq. 4.13. However, when the distance between the radar and the target is traversed again, Eq. 4.12 (derived from Eq. 1.11) is multiplied as

$$f_D^{tr}(u) = 2 \cdot f_D(u) = 2 \cdot \frac{2\ v_p}{\lambda_c} \sin[\theta_f(u)] \tag{4.16}$$

Substituting Eq. 4.16 into Eq. 4.13 leads to

$$R_n^{tr}(u) = r_s\left(1 - \left(\frac{\lambda_c f_D(u)}{4v_p}\right)^2\right)^{-1/2} \tag{4.17}$$

which differs from Eq. 4.15 by the denominator. For both acquisitions, RCM depends on λ_c central wavelength, v_p platform velocity and f_D Doppler frequency. However, a wider Doppler spectrum in TRP data leads to the RCM with a smaller amount of range shift over wider Doppler bandwidth.

Fig. 4.8 presents the results of RCM (with same convention as Fig. 4.7). The RCM leads to correct results for the two radars (Radar P3 (top) and Radar L3 (bottom)) and the successive acquisitions (FP (left) and TRP (right)). The images in Fig. 4.8 are transformed back to the slow-time domain by the $\mathcal{F}^{-1}[\ ]$ inverse Fourier transform in azimuth direction. A comparison of Fig. 4.8 with the corresponding rows in the Fig. 4.5 and Fig. 4.6 shows that the trajectory of all revealed targets are correctly moved into a straight lines in azimuth direction (even these which intersect). Application of Eq. 4.14 into TRP data resulted in excessive range shift towards platform trajectory where both ends of target trajectory ahead their centre and appeared closer to the L_{sar}.

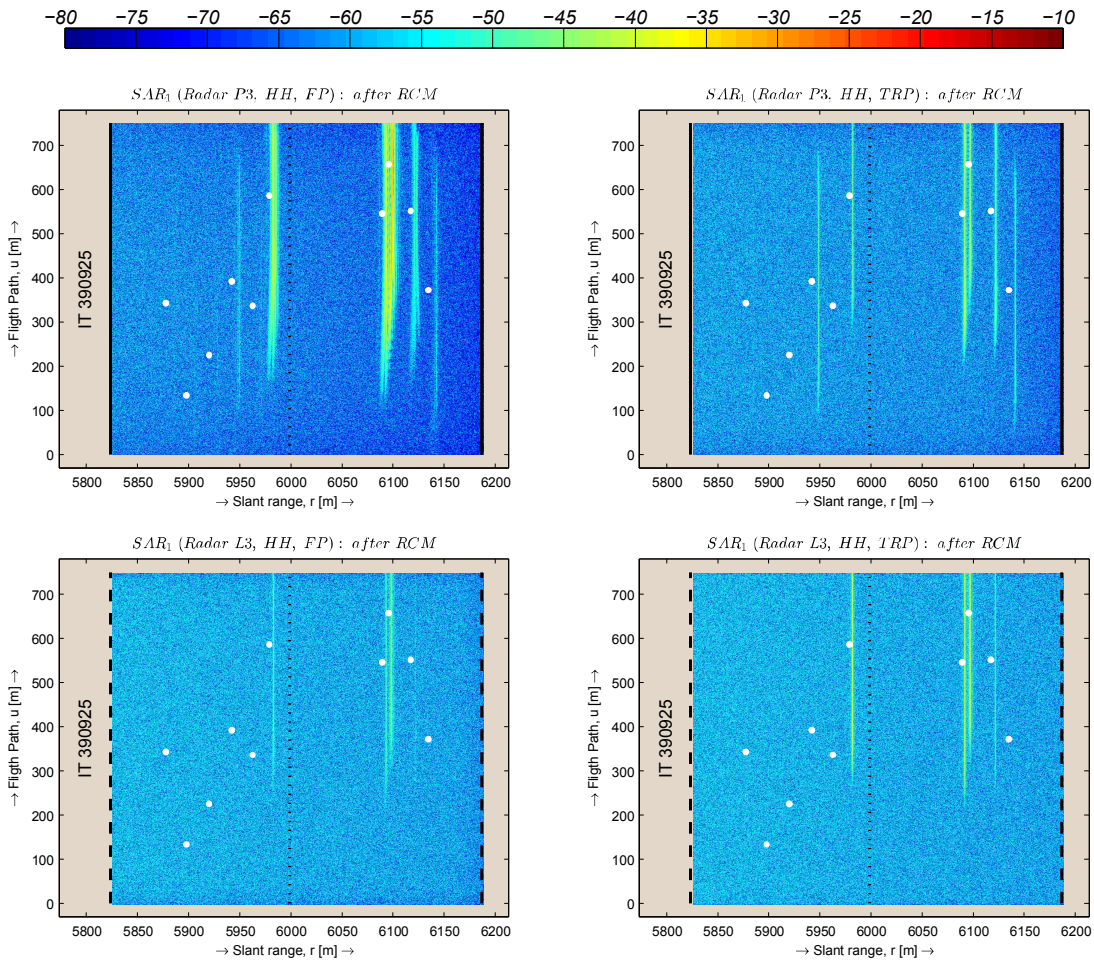

Figure 4.8 Data (in [dB]) after RCM for Radar P3 (SAR_1, top) and Radar L3 (SAR_1, bottom) after FP (left) and TRP (right) for *IT* 390925.

4.2.3 Azimuth Compression with TR

After the RCM, the azimuth compression can be performed in analogous ways as the range compression, i.e., in frequency domain by fast convolution. However, for azimuth compression the reference function is synthesized based on mission geometry and radar parameters. For a broadside SAR system the Doppler frequency changes linearly along L_{sar} and reaches the zero in the middle of L_{sar}. When the radar moves toward the object, f_D decreases and it increases when radar moving away. These changes are even with respect to centre of the L_{sar} and results from quadratic changes of phase delay in backscattered signals having a chirp character. Hence, in general, the azimuth reference function can be expressed in complex form as [5, 10]

$$h_a(u) = \exp(-\mathrm{j}\pi K_u t_u^2), \qquad \mid t_u \mid \leq T_{dwell} \tag{4.18}$$

which corresponds to demodulated baseband signal with LFM structure (compare with term of $\mathrm{j}\pi\alpha_f t^2$ in the Eq. 2.93). The K_u denotes the Doppler frequency rate and t_u varies over T_{dwell} dwell time. When for range compression the α_f and range of the t is strictly defined and constant for each u_n position (scan), in azimuth compression the K_u and T_{dwell} depend on slant range. Thus, the $h_a(u)$ has different length and chirp rate along the L_{sar} for each range cell from near to far range. The L_S synthetic aperture length varies within a slant

range r_s (or illumination angle θ_i) as (see Fig. 2.12)

$$L_s = 2\ r_s \tan\left(\frac{\theta_{az}}{2}\right) = 2\ \frac{H_p}{\cos\left(\theta_i\right)} \tan(\frac{\theta_{az}}{2}), \qquad \theta_{in} - \frac{\theta_{el}}{2} \leq \theta_i \leq \theta_{in} + \frac{\theta_{el}}{2} \tag{4.19}$$

Hence, the T_{dwell} dwell time (specifying the length of the reference function at r_s) is computed as (see Eq. 1.14)

$$T_{dwell} = \frac{L_s}{\upsilon_p} \tag{4.20}$$

and the number of h_a samples equals

$$N_a = T_{dwell} \cdot PRF = \frac{L_s \cdot PRF}{\upsilon_p} \tag{4.21}$$

Furthermore, the K_u (the chirp rate of h_a) equals (from Eq. 1.12)

$$K_u = -\frac{2\ \upsilon_p^2}{\lambda_c\ r_s} \tag{4.22}$$

Eq. 4.19 to Eq. 4.22 show how the mission geometry and the radar parameters affect the azimuth reference function (Eq. 4.18, its effective time length and bandwidth). However, similarly to RCM, the azimuth reference function for TRP is different from that of the FP, i.e., $h_a^{tr} \neq h_a$. For the same imaging geometry

$$L_s = L_s^{tr} \implies T_{dwell} = T_{dwell}^{tr} \implies N_a = N_a^{tr} \tag{4.23}$$

but wider and conjuncted Doppler spectrum (as shown in Fig. 4.7) leads to

$$K_u^{tr} = -2 \cdot K_u = 2 \cdot \frac{2\ \upsilon_p^2}{\lambda_c\ r_s} \tag{4.24}$$

Therefore, substituting Eq. 4.24 into Eq. 4.18 results in a pair of

$$h_a(u) = \exp(-\mathrm{j}\pi K_u t_u^2), \qquad \mid t_u \mid \leq T_{dwell} \tag{4.25}$$

$$h_a^{tr}(u) = \exp(\ \mathrm{j}2\pi K_u t_u^2), \qquad \mid t_u \mid \leq T_{dwell}^{tr} \tag{4.26}$$

taking into account relations indicated in the Eq. 4.23. Fig. 4.9 compares the azimuth reference functions synthesised for Radar P3 (SAR_1) in FP (top) and TRP (bottom) at near R_n, centre R_c and far R_f slant range of observed swath. The azimuth reference function is modulated by the antenna gain along L_{sar} (tapered cosine window with tapers parameter $r_h = 0.21$). When these functions have equal duration at constant range for FP and TRP (left column) the corresponding spectrum h_a^{tr} is twice wider as the h_a (right column). Since h_a and h_a^{tr} have the same sign of real parts, the Fig. 4.9 (left column) compares imaginary parts to reveal their conjugated character along L_{sar}. In slow-time domain, the duration of the azimuth reference function increases in accordance with the Eq. 4.20 for both acquisitions. In the Doppler frequency domain, the two spectra are centred around zero Doppler centroid (zero squint angle), but reference function at each range bins in TRP has a wider spectrum than for FP. Similarly to range compression, by applying the MF approach azimuth compression, in the frequency domain, is performed as

$$s_u^{f,mf}(u) = \mathcal{F}_u^{-1}[\ S_u^f(\omega_u)\ H_a^f(\omega_u)\ ] \tag{4.27}$$

$$s_u^{tr,mf}(u) = \mathcal{F}_u^{-1}[\ S_u^{tr}(\omega_u)\ H_a^{tr}(\omega_u)\ ] \tag{4.28}$$

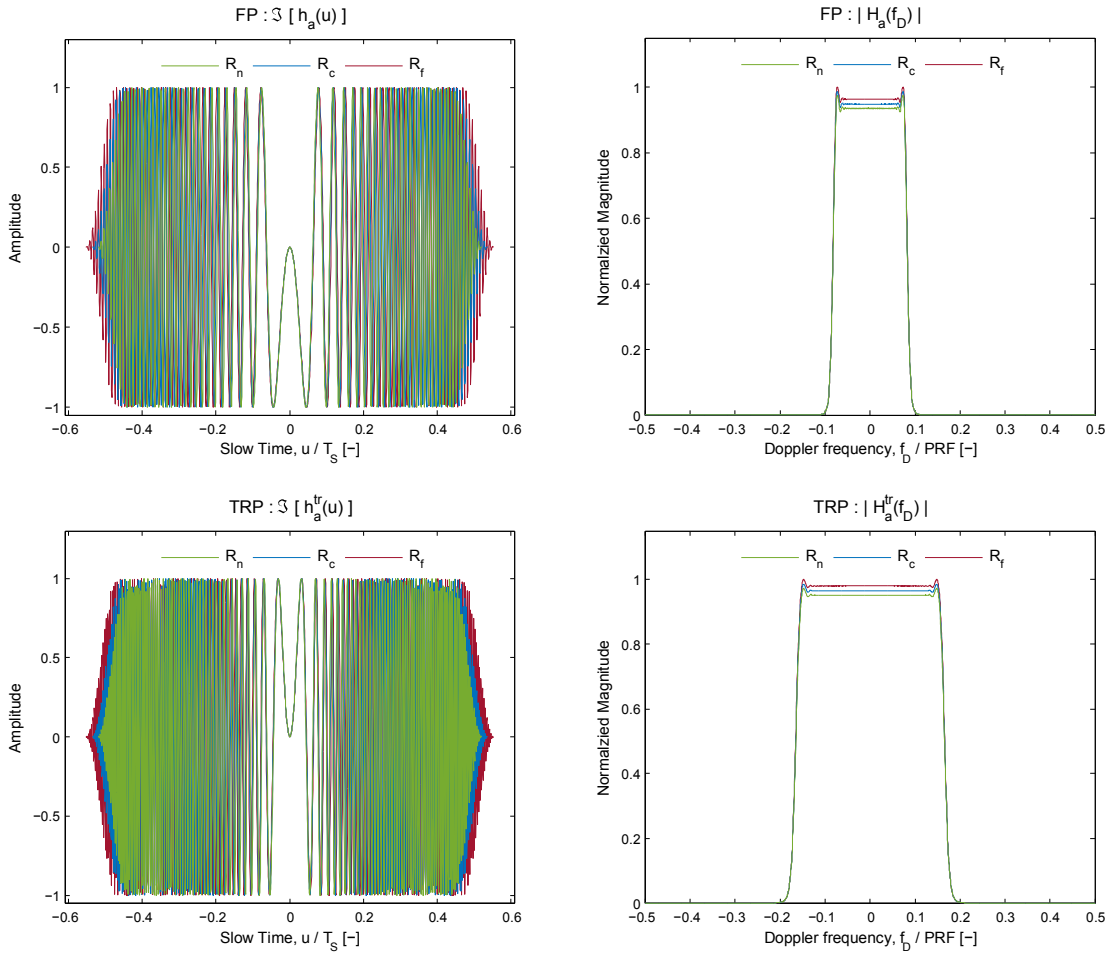

Figure 4.9 The azimuth reference function synthesised for Radar P3 for FP (top) and TR (bottom): comparison of the imaginary part (left), normalized spectrum magnitude (right).

where $S_u^f(\omega_u)$ ($S_u^{tr}(\omega_u)$) represents successive azimuth lines transformed by forward Fourier transform and $H_a^f(\omega_u)$ ($H_a^{tr}(\omega_u)$) represent azimuth reference function in frequency domain (their Fourier transform), respectively for FP and TRP.

Finally, applying the RCM and azimuth compression to the data presented in Fig. 4.5 and Fig. 4.6 the two-dimensional images are formed (shown in Fig. 4.10 and Fig. 4.11, in the same convention as the previous ones). For a complete comparison between the images, by taking into account the impact of the soil, images in these figures are not normalized to the most intense one within a given radar and the same colour scale is applied within a radar. When it seems that images for Radar L3 are batter focused (no sidelobes), in fact, they are weaker and sidelobes are hidden in the background interference (raw images for Radar L3 are more attenuated than for Radar P3). Maximum intensity peak for TRP and Radar P3 appeared in *FI* 3580005 and equals −4.85 dB whereas for Radar L3 in the same structure equals −15.04 dB. This difference is similar to the difference between raw data of considered radars (see Fig. 3.13), however, it has been slightly increased by azimuth processing. Similarly as for range compression, not all revealed objects in the FP appear in the TRP images (in particular, for Radar P3 and *GM* 490143) which is caused by assumed energy normalization method.

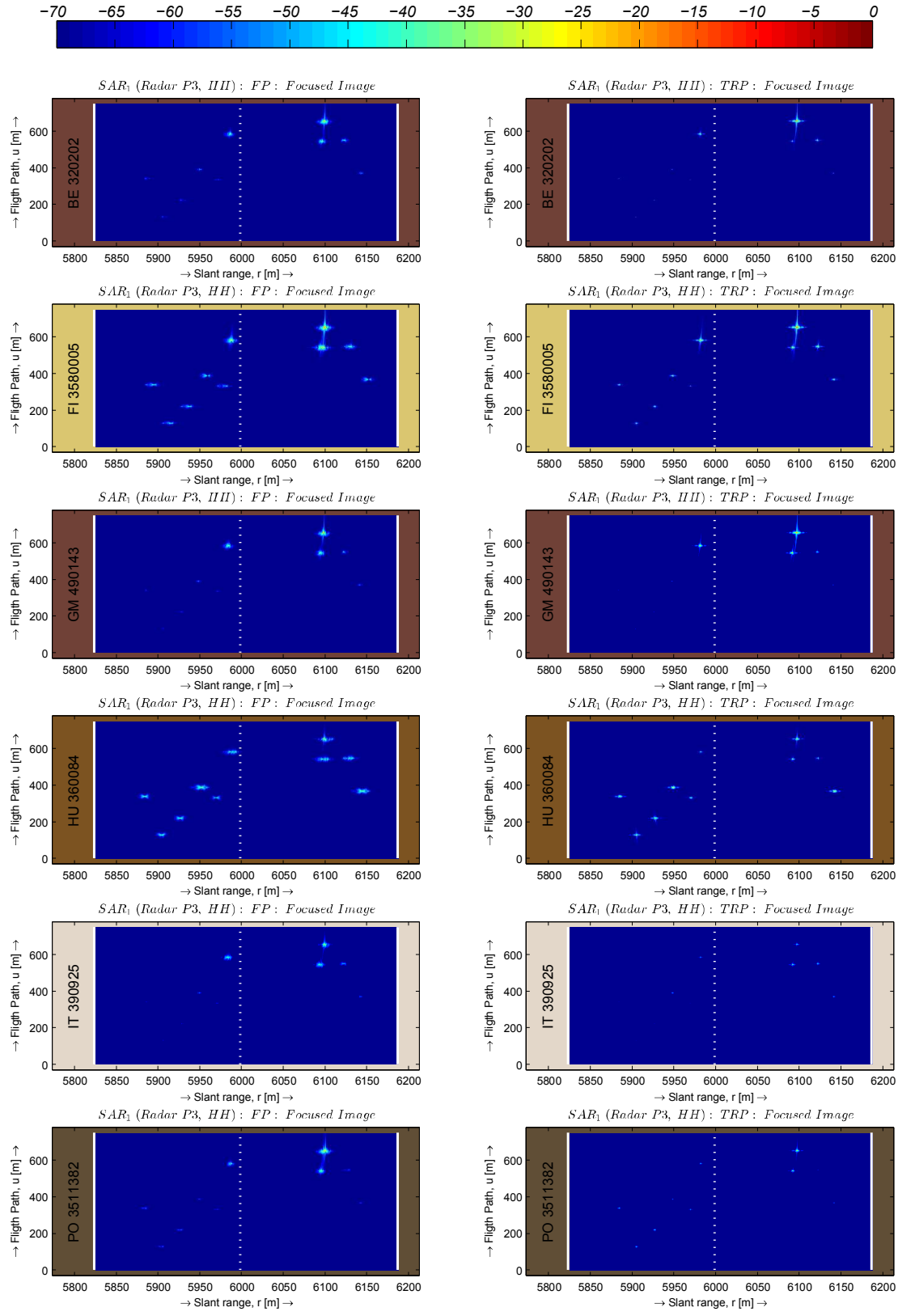

Figure 4.10 Focused images (in [dB]) for Radar P3 (SAR_1) after FP (left) and TRP (right) and for the six considered soils structures.

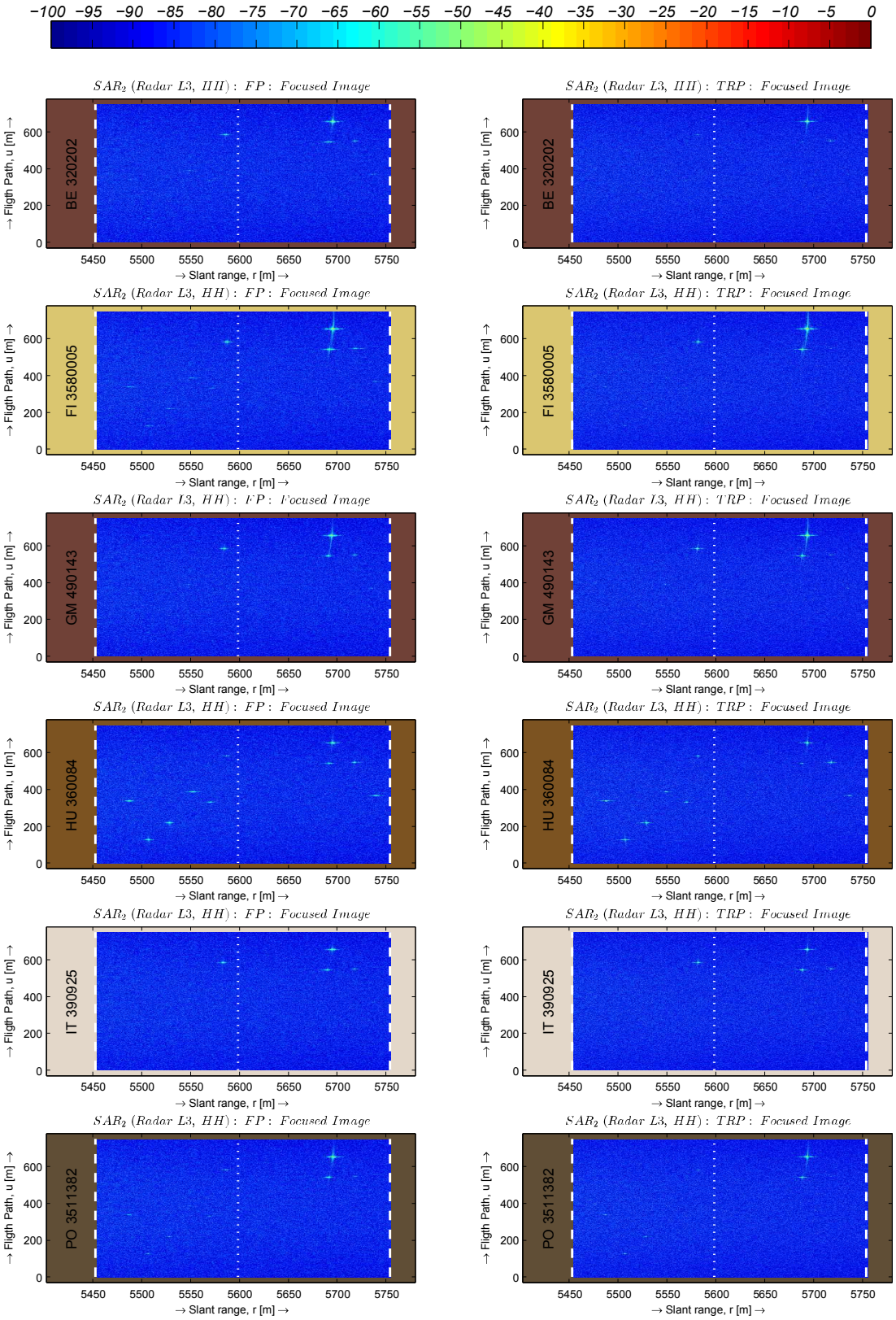

Figure 4.11 Focused images (in [dB]) for Radar L3 (SAR_2) after FP (left) and TRP (right) and for the six considered soils structures.

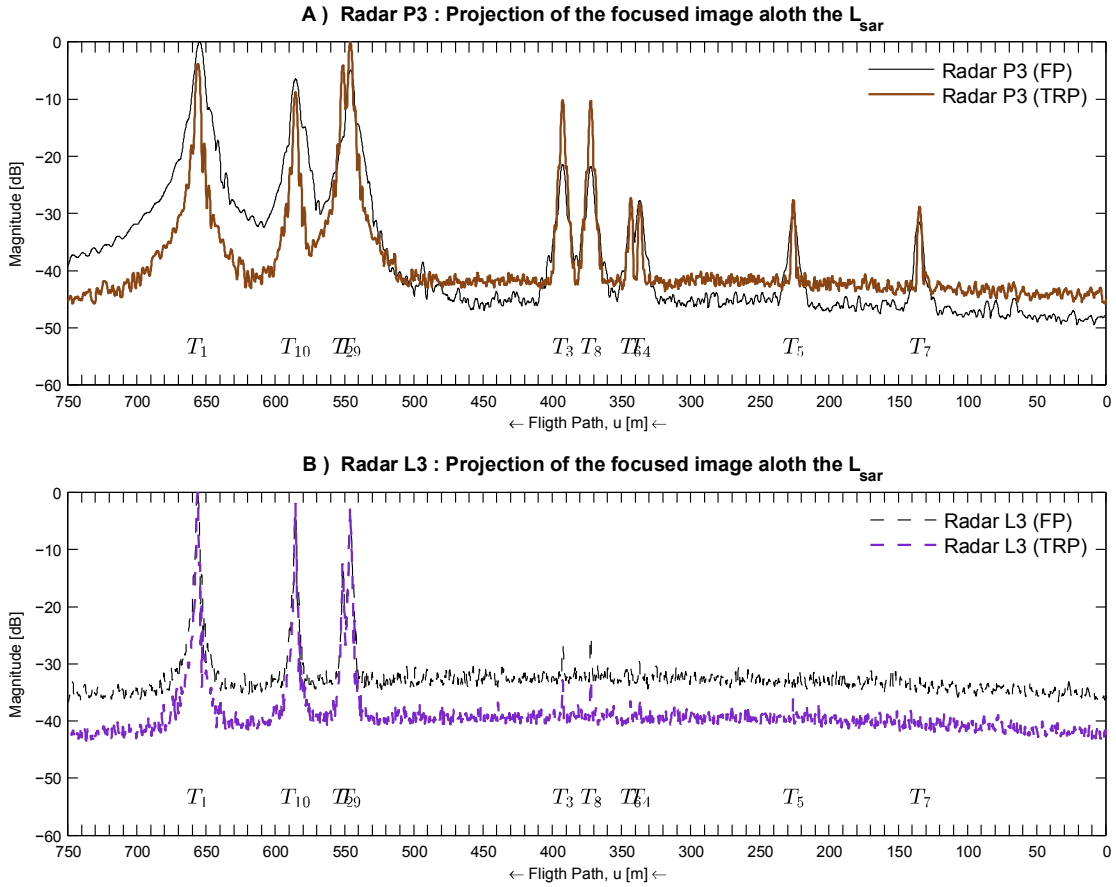

Figure 4.12 Comparison of the focused image projections along the L_{sar} for Radar P3 (top) and Radar L3 (bottom)

4.2.4 Discussion

The impact of the TR technique on range resolution and target location having been presented in Chapter 3 (Fig. 3.15). Fig. 4.12 shows the impact of TR on azimuth resolution by comparison of the projection of the focused imaged along the azimuth axis for one soil structure (PO 3511382) and for Radar P3 (top) and Radar L3 (bottom). In FP (black lines) the background level is higher for Radar L3 and not all the targets are revealed by this radar (T_7) and some are only barely seen (T_4, T_5 and T_6). When the pulse distortion is stronger for Radar P3 (top) the impact of TR is more visible for this radar. In general, for Radar P3 the TR leads to slightly narrower and higher targets peaks (for T_3 to T_8) and strongly narrower (for T_1 and T_{10}). In the case of T_2 and T_9, the TR helps in their separation where in FP the T_2 is masked in the T_9. Whereas the background level after TR is slightly higher for certain aperture lengths, the obtained azimuth resolution is significantly improved thus leading to the enhancement of the target detection. For Radar L3 (bottom), where pulse distortion is lower the target level (T_1, T_2, T_3 and T_{10}) is slightly higher after TRP. However, the azimuth resolution is slightly improved but not as much as for Radar P3 and the background level in lower in TRP along the entire aperture length. For both radars, the TR provides lower sidelobes level around revealed targets as well as higher mainlobe levels. These consideration can be generalized to other soil structures, with regard to a different number of objects to be detected and different magnitude.

The analysis of Fig. 4.12 shows the potential of TR. Whereas the fine range resolution is required for a fine azimuth resolution, the application of the TR does not improve the

azimuth resolution (directly) but enhances it by improving the range resolution (see Fig. 3.13). Moreover, although lower frequencies have greater potential to penetrate inside the soil (with drawbacks of stronger pulse distortion), the TR overcomes these drawbacks and allows us to use the lowest possible frequencies (collected over wide bandwidth) for deeper penetration depth and finer resolution. For higher frequencies, where the pulse distortion is weaker, the TR also enhance resolution, but deeper penetration is prevented by stronger attenuation. Hence, the TR makes the lower frequencies more attractive of subsurface imaging and buried object detection. However, still the soil affects their imaging and detection, in particular, when the first soil layers are formed up by highly clayey compositions (as the *IT* 390925).

4.3 Interferometry Application with TR

As mentioned at the beginning of the chapter and in the Introduction, the efforts to apply the InSAR processing for subsurface reconstruction have been taken fairly recently and are a relatively new issue in remote sensing domain.

The raw data compressed in previous section with RDA were simulated in the geometry which does not fully coincide with the modern airborne SAR systems with InSAR capabilities, where the baseline is much shorter (with respect to Fig. 4.1). Hence, for the InSAR imaging of subsurface structure, the previously assumed geometry is changed to fit to these systems. Foremost, the Slave radar is moved to common platform with Master radar, and baseline B_{in} is assumed as horizontal and equals now $B_{in} = 10$ m (to antennas at located under different plane wings). However, both radarss still operate with their own transmitter and receiver. For horizontal baseline the $\Delta h = 0$ m and $\beta_{in} = 0\ ^\circ$ (Eq. 4.7 and Eq. 1.25 simplified). The conventional SAR operates in free space over continuous terrain topography, and later, InSAR processing results in continuous terrain model not distorted by unexpected phases changes that influence the interferogram. For subsurface imaging, which depend on target depth, the soil parameters and incident angle, the phase may change unpredictably even for slightly different incident angles separated by a small baseline. Hence, to verify the InSAR, the number of point-like targets is limited to $N_T = 1$. It also allows us to reduce the InSAR processing over smaller area in compressed images. To simplify the discussion, the main steps of InSAR processing are presented for one soil structure after TRP and only for Radar P3.

Similarly to the SAR application, since the soil is assumed to be unknown, the InSAR is applied as if the focused images represent terrain returns.

4.3.1 Image Coregistration

Focused images presented in Fig. 4.10 and Fig. 4.11 are defined in azimuth displacement (flight path, which is the same for SAR_1 and SAR_2) and in relative slant range, which is different in the range but have the same grid (inversely proportional to the f_s radar sampling frequency). Moreover, the width of swath is different. Hence, for InSAR application, compressed image should be first narrowed to the common area and later coregistered in common grid in ground range dimension. The parallel and constant baseline does not impose coregistration in azimuth direction. The transformation to horizontal distance along the ground (with taking into account the slave radar shift Δx) is given by (compare with Eq. 2.51)

$$r_g = \Delta x + r_s \sin(\theta_i) = \Delta x + \frac{c\,t}{2}\sin(\theta_i), \qquad \theta_{in} - \frac{\theta_{el}}{2} \leq \theta_i \leq \theta_{in} + \frac{\theta_{el}}{2} \tag{4.29}$$

where $\Delta x = 0$ for SAR_1 and $\Delta x \neq 0$ for SAR_2. The result of ground range transformation

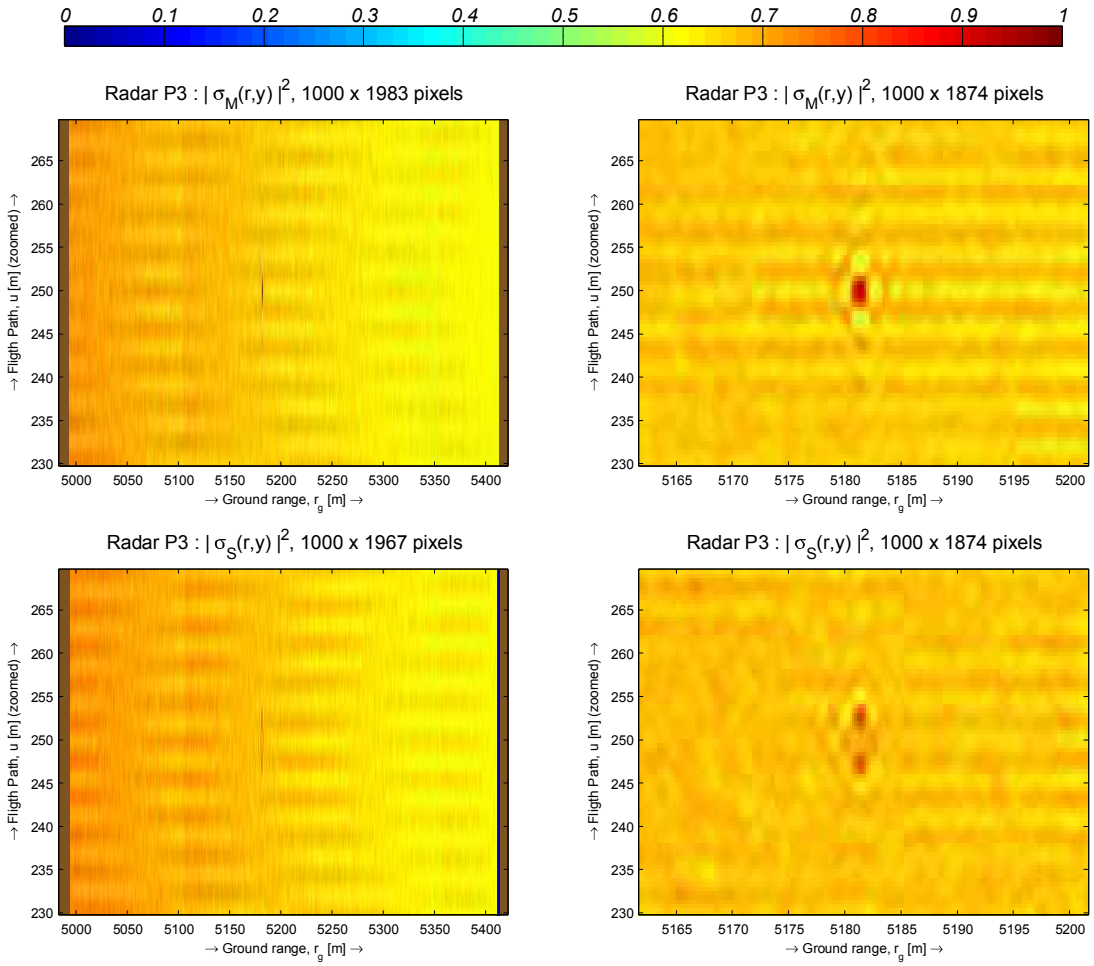

Figure 4.13 Results of image coregistration (normalized scale): original Master (top-left) and Slave (bottom-left) images and coregistred images. Unchanged and narrowed Master (top-right) and resampled and narrowed Slave (bottom-right) images.

of new SAR images (zoomed in azimuth direction) is presented in Fig. 4.13 (left column) for SAR_1 (top) and SAR_2 (bottom). When the baseline is small, the difference in ground range in not so evident. After transformation from the uniformly sampled slant range, since $\theta_{in1} > \theta_{in2}$ and $H_{p1} = H_{p2}$, the ground range for slave radar have larger grid step than for master radar. When the common area of both images is found (around the considered object), the ground range vector of SAR_1 (master image) is used as reference vector for slave image coregistration. In coregistration process, the master image remains unchanged, whereas the slave image is resampled and interpolated along ground axis to obtain the same grid as in reference vector. Final results of image coregistration are presented in Fig. 4.13 (right column, limited to the area with the objects).

4.3.2 Interferogram Generation

According to Eq. 1.19, the interferogram is produced by pixel-by-pixel multiplication of master image by conjugated slave image. The Fig. 4.14 (top-left) shows the ψ^{wr} interferometric phase difference (Eq. 1.20) of the $\chi(r, y)$ interferogram (Eq. 1.19) created based on the two previously coregistered images in changed geometry. The $\eta(r, y)$ coherence map evaluates the

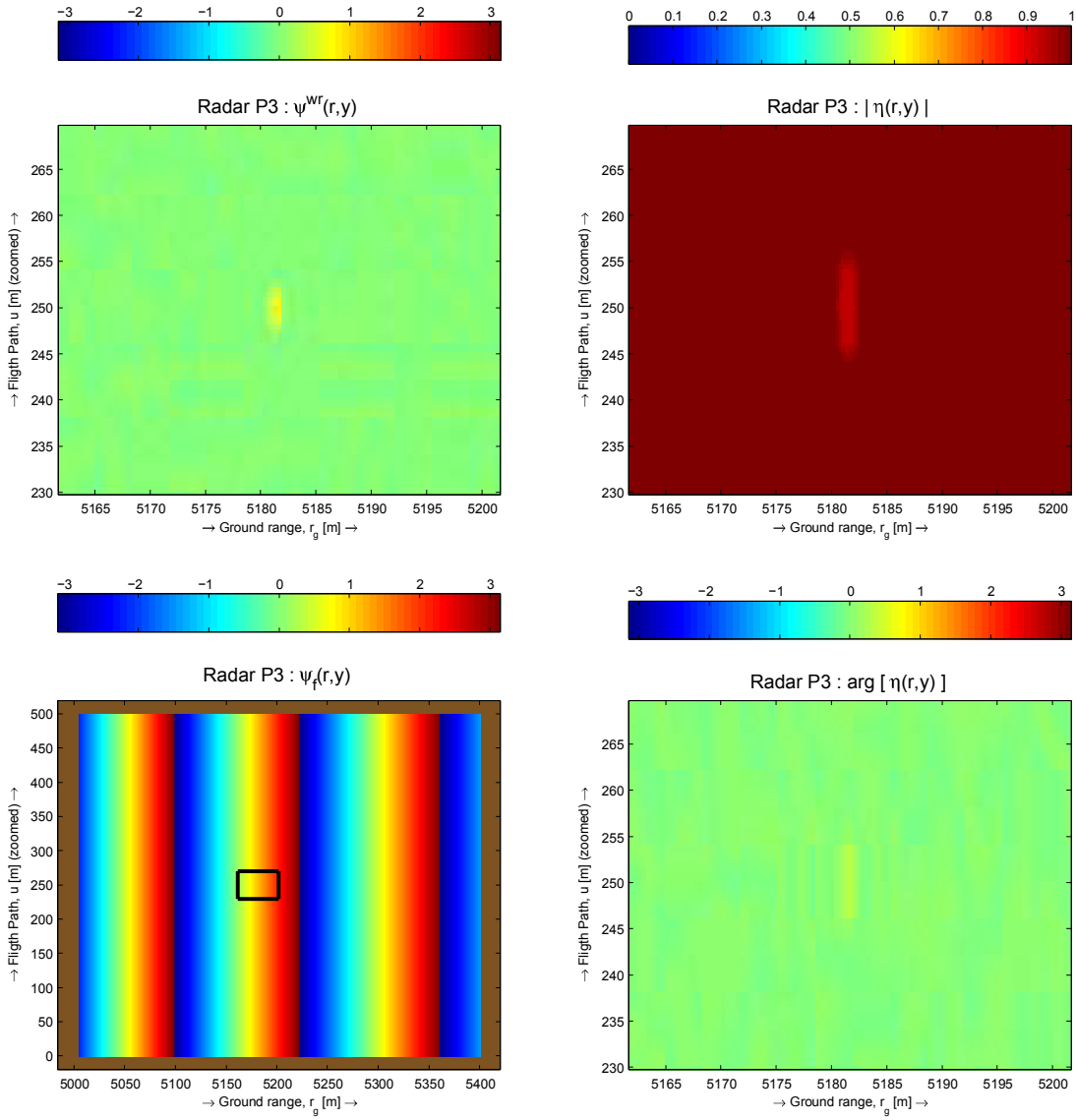

Figure 4.14 The step of interferogram generation: (top-left) the $\psi^{wr}(r,y)$ interferogram, (top-right) the module of coherence map $\eta(r,y)$ and its argument (bottom-right), the $\psi_f(r,y)$ flat-earth phase model (bottom-left).

correlation between compressed images [20, 23]

$$\eta(r,y) = \frac{\sum\limits_{(r,y)\in W} \left[\sigma_M(r,y)\sigma_M^*(r,y) \times \exp(\mathrm{j}\ \psi_f(r,y))\right]}{\sqrt{\sum\limits_{(r,y)\in W} \sigma_M^2(r,y) \sum\limits_{(r,y)\in W} \sigma_M^2(r,y)}} \tag{4.30}$$

over moving window W (number of pixels in each dimension is proportional to resolution cell size). Fig. 4.14 shows the module of $\eta(r,y)$ (top-right) and argument of $\eta(r,y)$ (bottom-right). Coherence map evaluate the normalized complex correlation between the acquisitions and its value varies from 0.0 (total decorrelation, the interferometric phase contains only the noise) to 1.0 (perfect correlation, the total absence of noise). Hence, the better coherence map the interferogram is more confident. In Eq. 4.30 $\psi_f(r,y)$ represents the model of flat earth phase (see Eq. 1.25) used for removal of phase fringes from the interferogram. For parallel flight path the phase variation are linearly dependent only on slant range (see Fig. 4.14 (bottom-left)).

For Radar L3, these fringes are more dense. In Fig. 4.14 (bottom-left), the black rectangle covers an area in which the InSAR processing is applied.

The phase changes in the $\psi^{wr}(r, y)$ interferogram oscillate around zero (soil surface is assumed as flat) with dominant phase value in target location. However, the characteristic fringes (as for terrain interferogram) are not present. For assumed baseline the $h_{amb} \approx 390$ m (similar to the swath width), and whereas the soil is assumed as flat (no topography) the phase shifts from π to $-\pi$ do not occur. Potentially, to significantly decrease h_{amb} (to few meters), the interferoemtric baseline B_{in} must be extended to several hundred meters, which can result in lower correlation between images. However, when the subsurface imaging is considered, the restrictions on baseline length are no longer applied. For constant homogeneous structures, where the phase shift is determine by β (see Eq. 2.83) the baseline length and the h_{amb} can be mutually matched. For inhomogeneous and unknown medium as the soil structure, where phase shifts in thin layer vary rapidly, the h_{amb} is impossible to determine before acquiring in InSAR mode. A possible solution consists of several (or dozen) independent flights correlated with an initial reference flight by changing baseline length and later analysis of the subsequent images. In the considered area, the coherence map reaches the maximum value. However, around target location the coherence slightly decreases. The moving window W has 3×9 pixels in range and azimuth (proportional to resolution cell size), respectively, hence, the slight decorrelation around target area is extended in azimuth direction.

4.3.3 Phase Unwrapping

The phase unwrapping step is considered as the key point of InSAR processing [23] and cannot be simply performed as one dimensional operation along the range or azimuth line in the complex and wide interferogram. According to Eq. 1.29, the phase unwrapping aims at adding the multiple value of 2π to wrapped phase. Whereas the SAR processing is still developing, the two-dimensional phase unwrapping is also an active research area, in particular, directed towards the generation of accurate DEM. However, development of a new method of phase unwrapping is beyond the scope of this dissertation.

For subsurface interferometry, the application of most commonly used phase unwrapping techniques is challenging. First of all, these methods need a predicable phase changes through the interferogram (result from changes in terrain topography). Even sudden changes in topography can be recreated in DEM with robust algorithms. Later, in the soil, where phase difference results from range to the entry point as well, what makes it the worst scenario, from cumulative-in-time (up and down) propagation in soil through multiple layers. Therefore, where relative path distance between radars and buried targets may differs multiples of 2π, the influence of soil introduces irregularity by unpredicted phase shifts which lead to false interferograms. Finally, when in terrain imaging, the presence of a dominant scatterer in a resolution cell is required for smooth interferogram changes, for subsurface imaging, the backscattered pulse is attenuated and it contributes to interferogram in a slight manner. However, taking this limitations into account, Fig. 4.15 shows the soils structure created based on argument of $\eta(r, y)$ (top) and interferogram (bottom) after FP (left) and TRP (right), respectively. The bottom of each figure represents soil surface. Structures obtained after FP (left column) contain two clear peaks (target energy split into two targets, original and ghost) whereas in the TRP (right column) one dominant peak occurs. Results created based on coherence map (top) are weaker and wider in azimuth direction, and target reconstructed after TRP is lower than after FP (results from assumed energy normalization factor). Targets reconstructed based on the interferograms (bottom) are finer and stronger. The application of TR leads to approximately twice stronger target reconstruction over conventional FP due to the intensified phase difference over the same propagation path. This

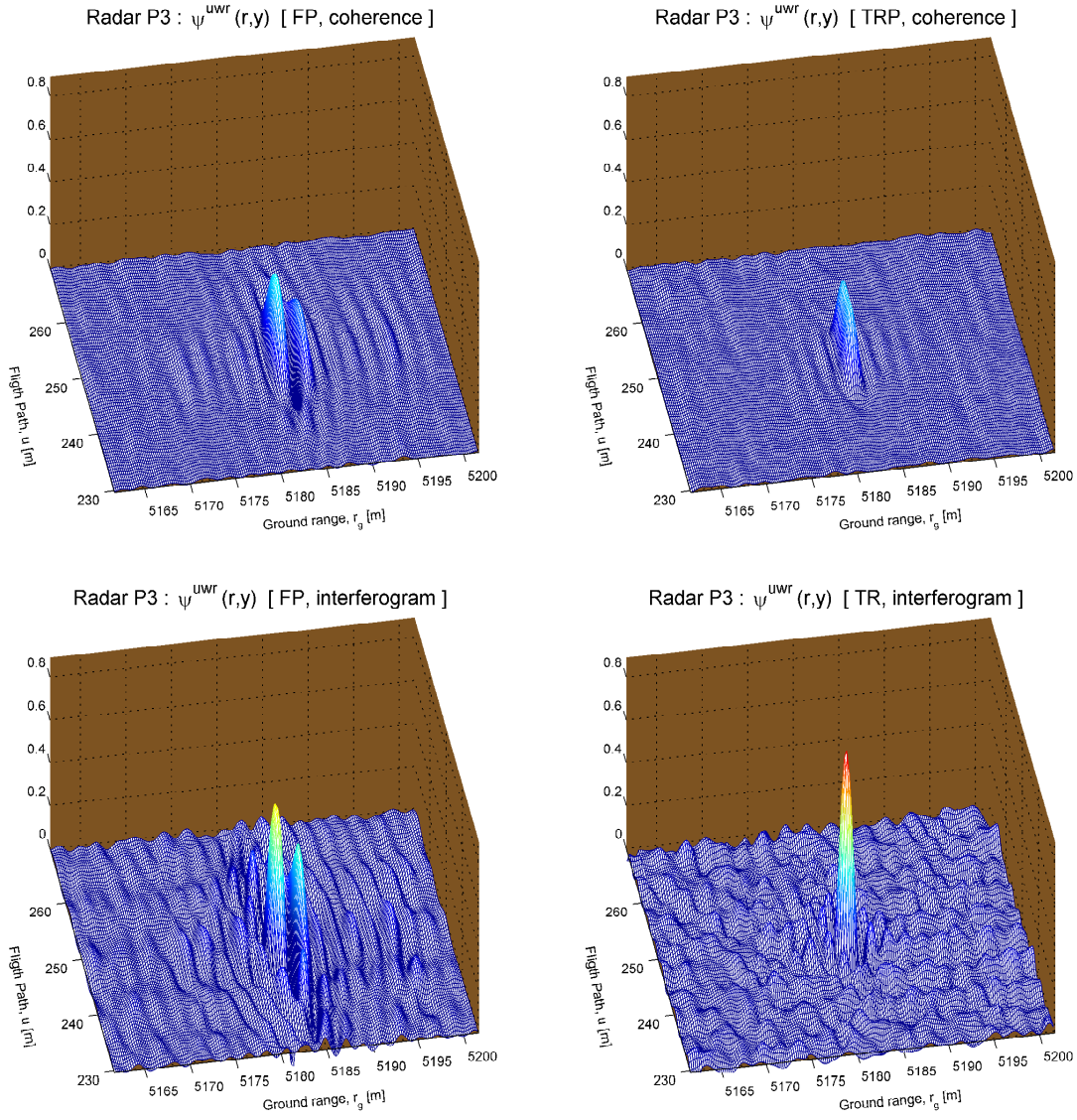

Figure 4.15 Reconstructed soil structure based on coherence map (top) and interferogram (bottom) for FP (left) and TRP (rigth).

comparison and analysis shows the potential of the TR technique in subsurface structure reconstruction. Similar results were observed for other considered soils structures.

4.3.4 Discussion

Application of the InSAR with TR processing for target reconstruction shows same promising results, in particular, comparing the result of FP and TRP processing. Similar results were obtained for other considered soil structures, where TRP enhances phase difference between coregistered images. When the phase of individual pixel results from range to entry point and effective propagation path in soil, the interferogram does not represent subsurface topography of soil structure but its shifted form. Moreover, beyond the different phase shift along the propagation path in soil, the phase of individual pixel in compressed images depends on the relative slant range to entry point. Where the entry points varies with incident angles, the additional phase shift affects the intergerofram $\psi^{wr}(r, y)$. Due to the refocusing ability, the TR technique reverses propagation path (targets are correctly focused) and intensifies

phase different that enhanced the interferograms, which leads to high potential for subsurface reconstruction.

To fully investigate the ability of InSAR processing, the differential InSAR method were applied for interferogram generation. When the topographic deformation can be identified as different target locations in the FP and TRP images formed for the same radar (SAR_1 or SAR_2), the different values of the parameters used in azimuth compression completely decorrelates the interferogram.

4.4 Chapter Summary

In this Chapter, the TR-based SAR were applied for subsurface imaging in inhomogeneous and unknown medium. Assuming that the imaging geometry and parameters of the AGPR as well as the soil dielectric constants are all sufficient to give acceptable ground penetration, the raw data were simulated with the use of six different soils structures and two radar (P and L band). The mission geometry in simulation has been adapted to existing systems in order to maximize the reality of the mission scenarios. For image formation, the soil was assumed as unknown However, in simulation the exact delay of backscattered pulse and its deformation (envelope and inner structure) were calculated with known soil parameters. As presented, the P band (Fig. 4.3) has higher potential for subsurface imaging than L band (Fig. 4.4). When in conventional subsurface imaging, the P band leads to a greater distortion than L band (which is the drawback of P band), its lower attenuations allows better acquisitions (stronger backscattered echoes). Hence, based on TR assumption, additional acquisitions in TR manner use the signals that are preferably matched to probing medium. The more signal is distorted in initial propagation the better it will restored in TR propagation (compare left and right columns in mentioned figures).

Common image formation method, the RDA, was applied to verify the impact of TR on the ability to synthesize of SAR image. As shown, when the range compression in performed with normal replica of transmitted signal, the RCM (Fig. 4.7, Fig. 4.8) and azimuth reference function (Fig. 4.9) requires a parameter change which take into account the intensification of phase shift in TRP. Therefore, TR affects both range and azimuth compression in image formation method (as shown on the basis of the RDA) and leads to better focused images (right columns in Fig. 4.10 and Fig. 4.11). Comparison of azimuth profiles shows that TR revealed the fine azimuth resolution by pulse recovering. The phase shift intensification will certainly affect other image formation algorithms, but thus analysis is left as future works. An application of the InSAR processing shows a potential advantages of TR approach in relation to the conventional SAR. Phase intensification introduced by TR approach reinforces phase difference in the intergerogram. With respect to single point scenario, the target reconstruction worked better for TRP than for FP. However, the analysis of complete potential of TR-based InSAR imaging requires a properly defined ambiguity height h_{amb} (depth) with respect to baseline length (to avoid image decorrelation). That analysis should be performed in relation to real data.

CHAPTER 5

CONCLUSIONS AND FUTURE WORK

5.1 Summary

Direct application of SAR techniques for subsurface imaging suffers image defocusing. While the fine range resolution is required for azimuth processing, the soil affects the radar waveform and backscattered pulse causing the pulse distortion and range defocusing. The refocusing ability of TR technique, successfully confirmed in many experiments in remote sensing, shows a potential in the pulse restoration and refocusing in inhomogeneous media such as the soil. In this work, the TR-based SAR imaging was proposed for focusing and interferometry of buried structures located in inhomogeneous soil. Firstly, we have presented the soil effects over the radar pulse in various ways appropriately to the soil texture as well signal bandwidth. When the soil structure is known (homogeneous and constant during acquisition) the refocusing algorithms can be matched to the investigated medium. However, the soils structure vary over the Earth and its parameters continuously change. Hence, the matched reconstruction algorithm works only in laboratory conditions. Therefore, to make the SAR imaging independent from investigated structure and the used operational bandwidth, we propose an imaging technique based on TR approach, for which the initially recorded signals are time-reversed and transmitted back towards the investigated medium. Whereas the acquisitions in such a way requires modification of mission parameters and also radar resources, the results show that time-reversed pulse is preferably matched to investigated medium and the pulse reconstruction occurs along the propagation path. The MF approach allows the energy refocusion and enhances the target detection after Time-Reversal Probing. An application of image formation method (a common RDA) leads to correct image synthesis with the use of modified parameters derived for the RCM and the azimuth compression. Finally, the InSAR processing for simple scenario has confirmed the potential of TR application for subsurface structure focusing and interferometry.

5.2 Contributions

The following sections outline the contributions of this dissertation which can be recognized as major and minor.

- The image formation method was proposed and verified for focusing the energy backscattered from buried target located inside inhomogeneous structure. The proposed method is independent from investigated medium and works well for targets located at different depth and incident angles. Moreover, proposed methods exploit the wider signal band-

width making the subsurface imaging much more efficient than conventional imaging, in particular, in lower frequencies where pulse distortion is stronger. By waveform diversity, the TR acquisition use the matched source signal for optimal probing of investigated structure. Reconstructed signals are correctly focused in range dimension.

- In azimuth direction, the proposed method enforces a modification of parameters used in azimuth compression. As shown based on the RDA, due the intensification of phase shift along the synthetic aperture the RCM and azimuth processing needs a modification of their parameters for correct focusing.

- Considerations presented through the work about proposed imaging method shows that incorporation of TR acquisition requires modification of the radar resources and mission parameters. Most of all, to ensure additional transmission and acquisition, the PRF must be suitable selected, also in relation to further azimuth processing. Secondly, the radar dynamic range should provide both correct registration of weak backscattered signals as well the transmission of strongly amplified signals in TR mode. This requirement may be slightly mitigated by highly directional antenna with the drawbacks of increasing its size. The considerations can be used to modify the actual airborne SAR system with interferometric capabilities.

- The modelled soil structure, based on real database, shows the diversity of subsurface soil geological structures as well their variety over particular countries. When simply precipitation history is assumed and used in water profile simulation, the presented results show that the dielectric constant of soil consist of similar values (grouped in horizons with various height) which mingle with each other. When in shallow depths the strong variation of water profile determinates strong variation of dielectric constant, in deeper depths, dielectric constant may increase or decrease in piecewise manner strongly related to soil texture.

5.3 Recommendation for Future Work

In additions to the studies presented through this dissertation, the work reveals direction of further investigations or experiments. Some of these directions are as follows:

- First and foremost, when the simulation adapted the mission geometry related to currently operating airborne SAR system with InSAR capabilities, the real mission must be carried out for data acquisition as well to validate the correct selection of mission parameters. The required modification of these system can be done based on the consideration presented through this work.

- First of possible investigation is an analysis of TR impact of other images formation algorithm, as the RMA or CSA. Where in the RDA the two-dimensional processing is separated, an application of TR may leads to more crucial modification introduced at various processing stages, which are overlapping. Therefore the use of these algorithms requires more attention when used in subsurface imaging in TR mode.

- Secondly, assuming the positive results of real missions over non-arid areas, the interferometric methods can be investigated over the real data. Beyond final structure reconstruction, the additional investigation should deduce a relationship between the parameters of the mission and both the ambiguous depth and baseline length. In order to support the subsurface structure reconstruction, the InSAR system may consist of two subsystems using TR mode and operating in two different bandwidth: one for terrain topography

and second for subsurface imaging (the solutions proposed in [86], where Ka-band system map the terrain topography and the VHF band system map the subsurface topography, however, both operate in conventional mode).

APPENDIX

A INTRODUCTION TO GEOLOGICAL SOIL TEXTURE

Soil is composed of the mineral particles, organic matter (both decomposed and undecomposed one), water and air [125, 126]. Organic matter originates from residues of plants or animals (pieces of bones or putrefying leaves), mineral particles originate from the degradation of rocks. This mixture, widespread in the Earth surface, is arranged in a structure with varied texture, different geological and hydrological parameters assigned to the spatial coordinates (x, y, z), which can be identified with displacement, i.e., x along and y across axis, and with z depth. An example of soil composition averaged over the sample soil volume, with 5%, 20%, 30% and 45% percentages of organic matter, air, water, and mineral particles, respectively, is shown in Fig. A.1. Their percentages vary with spatial coordinates (x, y, z) and can be transformed into one-, two- or three-dimensional profile for each component. Since Fig. A.1 represents only the averaged and quantitative information over sample soil volume, the Fig. A.2 shows the pictorial cross-section of the soil structure. It might seem that mineral particles touch each other, however, the space occurs between them. The spaces between mineral particles are called pores and they can be filled with air or water. For dry soil, the pores are mainly filled with air. However, after rainfall or irrigation and due to the water infiltration process, the air is forced out (replaced) by water. The fraction of space filled by water or air in the soil volume is defined as p porosity, or void fraction. Porosity can vary between 0 and 1, and also can be represented in percent terms. Moreover, porosity remains constant even when the amount of water and air changing in time.

While free water and air can move within the soil volume, due to the evaporation and infiltration process, the mineral particles mainly retain their location. Their distinctive size differ widely and is used in particles classification as follows: particles smaller than 0.002 mm are classified as clay; particles greater than 0.002 mm and smaller than 0.05 mm are classified as silt; particles greater than 0.05 mm and smaller than 2.0 mm are classified as sand. Also particles greater than 2.0 mm occurs and are classified gravel. Only the three first particle types are taking into account in determination of the soil texture. Sand is predominant in coarse textured soils (sandy soils), while in medium textured soils silt is predominant (loamy soils) and in fine textured soils clay is predominant (clayey soils). The fundamental method for classifying the soil types has been gathered in the form of soil textural triangle, based on the relationships between percentages of different particles size, i.e., clay, silt and sand, and where the axes are located on the sides of the triangle. Various texture classification systems are developed, and divide the soil textural triangle in varying numbers of differently shaped soil textural classes [133, Fig. 1]. For example, the soil textural triangle developed by the US

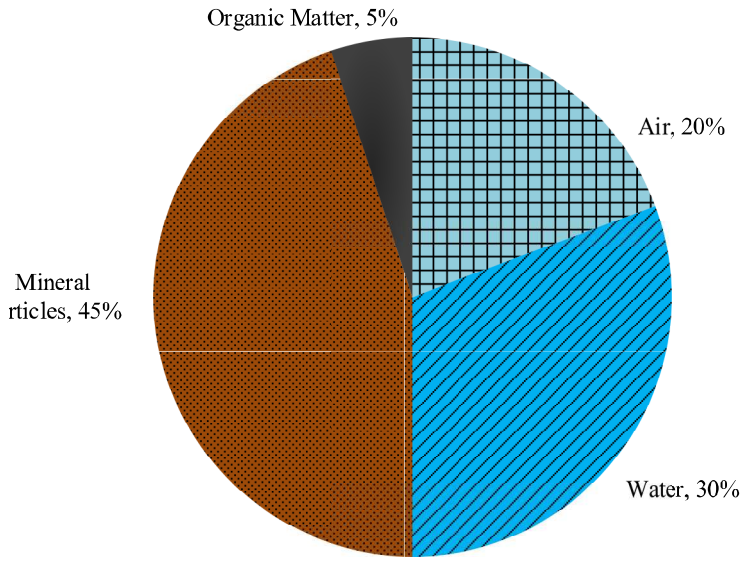

Figure A.1 An example of the averaged soil composition.

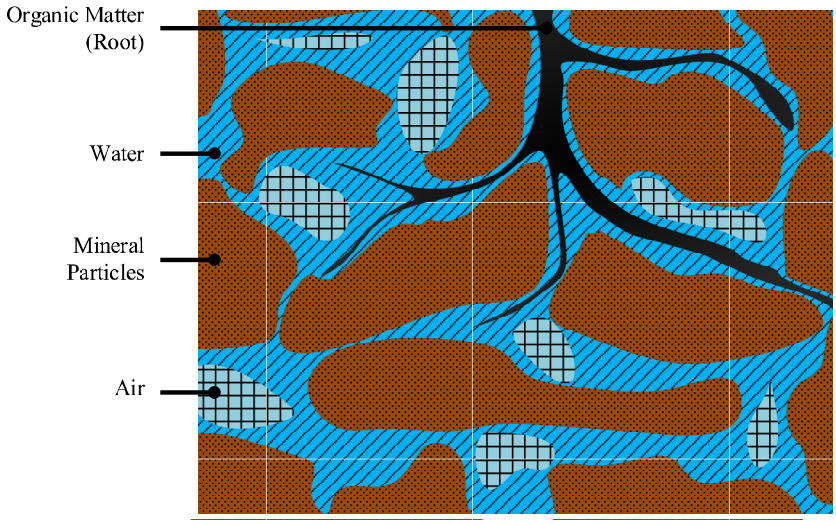

Figure A.2 The illustrative sketch of cross-section of the soil structure.

Department of Agriculture (USDA)[1] consists of the twelve classes of unequal areas, ranging from homogeneous (in the vertices of triangle: *sand*, *silt*, *clay*) to highly mixed (in the centre of triangle: *loam*). On the contrary to textural classification of soil type, the hydrologically motivated classification methods are also developed [133]. Overall, the strong variation of the soil across the world makes the measurements of soil physical parameters not possible, and mostly a statistical approach for its estimation is used [150]. Each group of soils have characteristic hydraulic parameters, for instance, infiltration rate, which is also dependent from the particles size. For coarse texture, i.e., with large particles and pores size, the water moves more easily into the soil than for fine textured soils. Moreover, infiltration rate depends on initial moisture profile.

Due to the natural land development process, the most significant and crucial changes of the soil structure are observed in z depth dimension, in which soil exhibits horizontal-layered structure (planar or rough) of different horizon heights. In remaining dimension,

[1] Soil Textural Triangle available at: http://ims.eid.org/homepage/Images/SoilTriangle.jpg

(a) The cross-section of soil profile (partially weathered) (b) Information board with the soil profiles

Figure A.3 Real geological soil profile (left) and comparison of examples one (right) in the protected reserve *Rezerwat Jata* (Łuków commune, Poland).

i.e. along x and across y axis, soil structure shows a less significant variations over considered soil polygon. Observation of the pit in the ground, down to few meters, gives an information about the horizontally arranged layers, different in height, composition and colour. These layers are called soil horizons. Fig. A.3 shows an example of soil profile (down to 1 m, partially weathered) in the protected reserve *Rezerwat Jata* (Łuków commune, Poland). Unfortunately, a vast land surface, about 29% of the Earth's, makes difficult to observe its geological texture. Thus, the soil texture profiles are prepared for representative polygon sites and stored in geological databases. One of a such soil database is the Soil Profile Analytical Database for Europe (SPADE-2) (Version 2.0 Beta, March 2009) [197, 198], which is created and provided on-demand by the European Commission Joint Research Centre (The Institute for Environment and Sustainability). The SPADE-2 contains the 3045 Soil Typological Unit (STU) profiles from the 17 European countries. The single STU contains averaged information about soil texture of the selected volume of ground, and is organized as a column vector defined in the depth dimension and presents information, among others, about percentage of clay c_l, percentage of silt s_t, percentage of sand s_d and bulk density ρ_b as well as about the nomenclature name and the upper z_{up} and lower z_{down} depth of the successive horizons. Moreover, STU contains information about the country of origin, organic carbon and acidity. Unfortunately, despite the similarities in the number of horizons between the STU profiles from different country, the STU profiles are limited in the maximum depth to which they are specified. This value is varying from 0.80 m to 2.00 m, according to the measuring standards in a given country. Single horizon in the STU represents distinguishable soil texture related to the depth range, limited between the upper z_{up} and lower z_{down} depth. In general, in certain STU, despite the clear differences in soil texture, the two consecutive horizons represent the same class of soil (for instance, *BE* 320202, *GM* 490143). In another one, slight differences in the soil texture, sometimes even just in the only one component, caused the change of soil class (for instance, *HU* 360084). The arrangements of soil horizons and the change of the soil type for six STU profiles were shown in Fig. A.4 and in Fig. A.5, respectively. When the depth is naturally identified with absolute value, the z depth axis in Fig. A.4 is presented in the negative convention. Fig. A.4 shows the arrangements of soil horizons for six arbitrary chosen STU profiles from SPADE-2, i.e., a) from Belgium *BE* 320202, b) from Finland *FI* 3580005, c) from Germany *GM* 490143, d) from Hungary *HU* 360084, e) from Italy *IT* 390925, and f) from Portugal *PO* 3511382. Each line on a single plot represents the percentages of *sand* (orange), *silt* (red), *clay* (blue) and bulk density (magenta), respectively, for each STU profile. The top x abscissa axis rep-

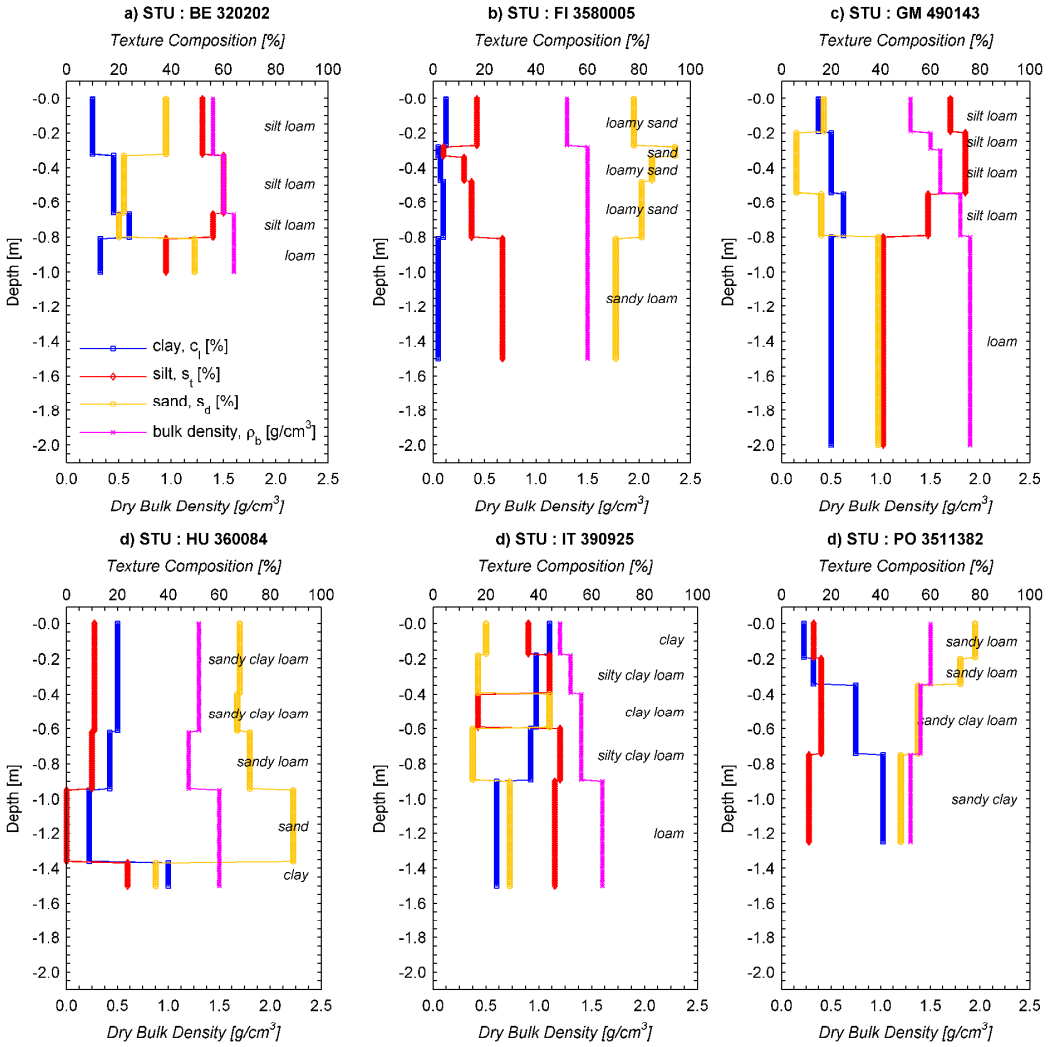

Figure A.4 Soil texture composition of six STU profiles from SPADE-2: percentage content of c_l clay, s_t silt and s_d sand, and value of bulk density ρ_b.

resents the percentages value of the soil texture (defined from 0% to 100%), while bottom x abscissa axis represents the value of the bulk density (from 0 g/cm^3 to 2.5 g/cm^3). As was mentioned, maximum depth of STU differ depending on the countries, and none information is given for the depth below maximum depth of the profile. Four of the six STU profiles contain five horizons with different texture, while two of them, i.e., *BE* 320202 and *PO* 3511382, are made up of only four horizons. Three STU profiles, i.e., *FI* 3580005, *HU* 360084 and *PO* 3511382, contain clearly dominant value of one particles size thorough all horizons, and for all of them *sand* is dominant. The remaining profiles present variable texture through horizons. STU *IT* 390925 shows the greatest variation of textures. Furthermore, the value of the bulk density changes within the profile. Generally, it changes between every horizon. But sometimes, it remains constant in two successive horizons (for instance, in third and fourth horizon of *BE* 320202, from second to fifth horizon of *FI* 3580005, ect.) and also it changing in spite of constant texture (as in second and third horizon of *GM* 490143). Moreover, the changes of soil horizons were plotted on the soil textural triangle and shown in Fig. A.5. The texture changes are strongly emphasized and the change of soil along STU profile is clearly visible. These two figures distinctly depict the complicated nature of the soil and its horizontally layered structure, which stems from centuries of natural soil-forming processes.

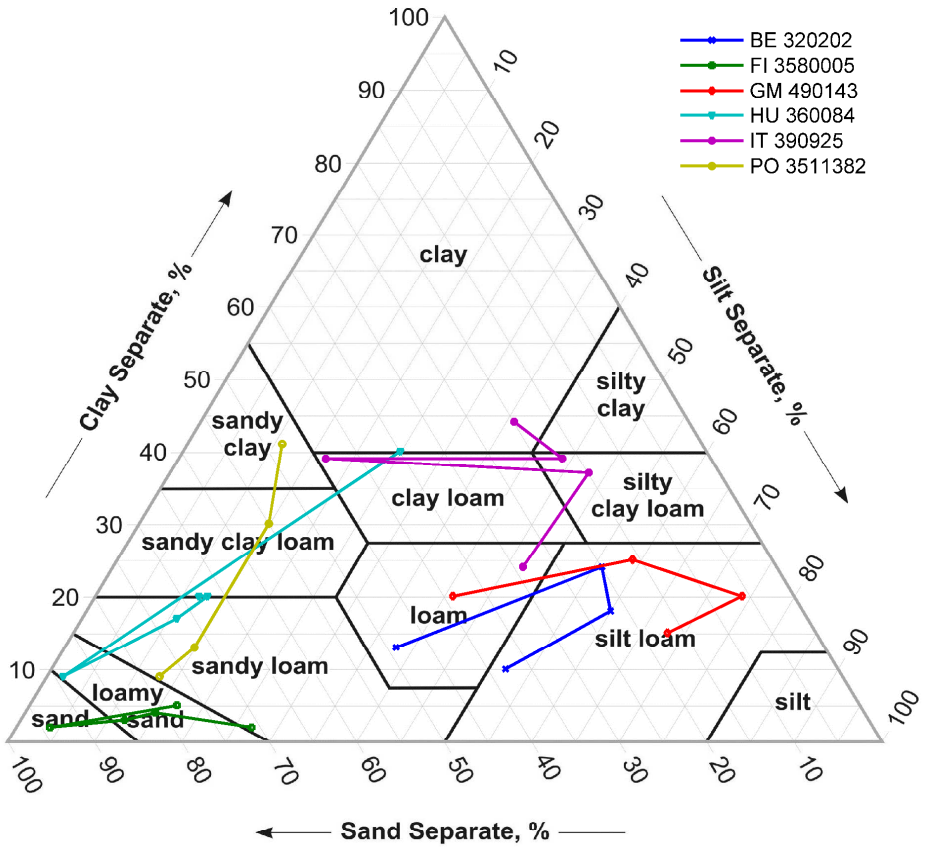

Figure A.5 Soil texture composition represented on the soil textural triangle.

The mentioned STU profiles were used in Chapter 1 for modelling of the subsurface soil structure, and later, for calculation of soil dielectric constant with the use of hydrologically- and geologically-motivated approach (by pedotransfer function proposed by Peplinski *et. al* [159]).

APPENDIX B

TIME-REVERSAL MEASUREMENT SCHEME

The prototype TR-based experiment [90] assumed the complete source surroundings by independent transceivers on each side (so-called full aspect configuration). This is equivalent of placing the omnidirectional source inside the sphere which is packed with these transceivers. From a theoretical point of view, it is possible, but in practice, for directional source it is unnecessary. Hence, in practice, the TR experiment is often performed by a set of independent transceivers, co-located to each other and creating the synthetic aperture, so-called Time-Reversal Array (TRA) [88–90, 92]. TRA acts like as spatial mirror, consisting of set of independent *point* mirror, which record (absorbs) EM wave and transmits its in the reverse order (as the LIFO memory). In detail, TR measurement consists of three steps linked to and performed directly after previous step. TR measurement scheme (transmission mode) in homogeneous medium with a set of discrete scatterers carried out by directional source and TRA is shown in Fig. 3.1 and composed as follows:

- **Forward Propagation (Fig. B.1(a))**: Point directional source located at r_o emits a UWB pulse $s(t)$, of E_s energy and τ duration, through homogeneous scattering medium. Simultaneously, transceivers, arranged into TRA of aperture length L_R and located at L_d distance, are starting to record the relevant part of the transmitted signal. Both the source and transceivers have the same time-line. In frequency domain, the signal recorded by transceiver $Y_i^F(\omega)$ located at $r_{t,i}$ is

$$Y_i(\omega) = S(\omega)H_{0,i}(\omega) \tag{B.1}$$

  where $S(\omega) = \mathcal{F}[s(t)]$ is Fourier transform of $s(t)$ transmitted signal. $H_{0,i}(\omega) = \mathcal{F}[h_{0,i}(t)]$ is Fourier transform of the $h_{0,i}(t)$ impulse response of the unique propagation path between source and transceivers. As shown in Fig B.1(a) $h_{0,i}(t)$ can have indefinite shape, and hence, a length of unique time delay. Besides the amount of energy absorbed (recorded) by set of transceivers, a part of energy, due to the multipath propagation, spreads beyond the TRA. This causes the information loss, and total energy recorder by TRA, i.e., $E_{TRA} = \sum_{i=1}^{N} E_i$, is smaller than E_s. Registration of transmitted signal is finished after a sufficiently long period T_r of time.

- **Time-Reversal Operation (Fig. B.1(b))**: Before re-transmission, the recorded signal is normalized (by factor K_i) and reversed in time ($T[\ ]$). Energy Normalization (EN)

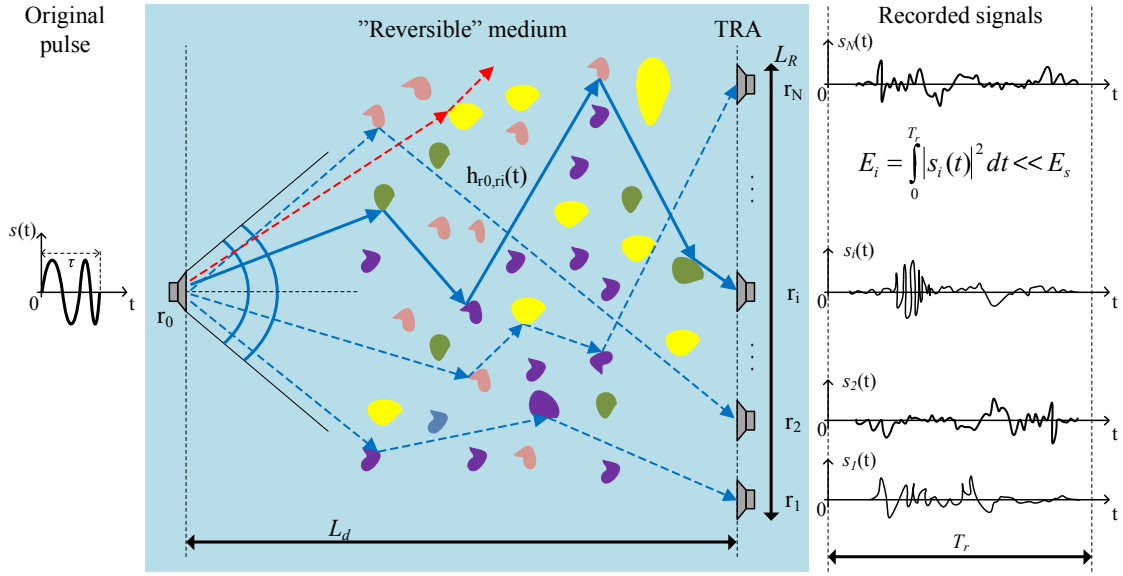

(a) Forward Propagation

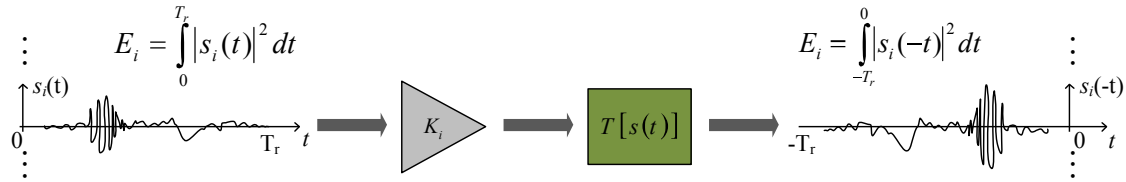

(b) TR Operation

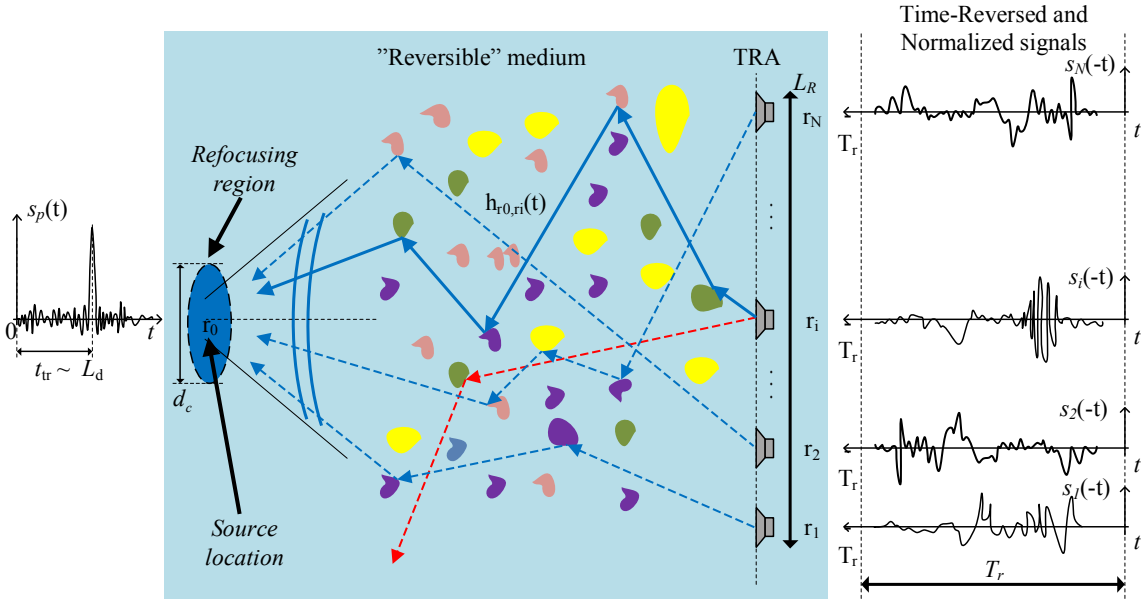

(c) Backward Propagation

Figure B.1 Time-Reversal measurements scheme with Time-Reversal Array (TRA) (created based on [88, 90, 92, 98, 103])

provides the signals re-transmitted by the TRA will have the same level of energy as E_s. After normalization and reversing in time, $y_i^{tr}(t)$ becomes a mirror reflection of $y_i(t)$, i.e., $y_i^{tr}(t) = y_i(T_r - t)$, which corresponds to phase conjunction

$$Y_i^{TR}(\omega) = Y_i^*(\omega) \tag{B.2}$$

- **Backward Propagation (Fig. B.1(c))**: At the same time, transceivers, located at $\bar{r}_i$, begin to re-transmit $y_i^{tr}(t)$. As results from reciprocity, $h_{r_i,r_0}(t) = h_{r_0,r_i}(t)$, hence, retransmitted signal should precisely retrace the path of original wave and converge to refocus in the region centred at the initial source location r_0. Moreover, during back-propagation any distortion of wave should be compensated. However, similarly as in the Forward Propagation, loss of information reappears.

BIBLIOGRAPHY

[1] C. A. Wiley, "Synthetic Aperture Radars: A paradigm for technology evolution," *IEEE Transactions on Aerospace and Electronic Systems*, vol. 21, pp. 440–443, May 1985.

[2] M. I. Skolnik, ed., *Radar Handbook*. New York: McGraw Hill, 3 ed., 2008.

[3] C. A. Wiley, "Pulsed Doppler Radar Methods and Apparatus," 1954.

[4] K. Tomiyasu, "Tutorial Review of Synthetic-Aperture Radar (SAR) with Applications to Imaging of the Ocean Surface," *Proceedings of the IEEE*, vol. 66, pp. 563–583, May 1978.

[5] J. C. Curlander and R. N. McDonough, *Synthetic Aperture Radar: Systems and Signal Processing*. Wiley Series in Remote Sensing and Image Processing, New York, NY: Wiley-Interscience, 1991.

[6] W. G. Carrara, R. S. Goodma, and R. M. Majewski, *Spotlight Synthetic Aperture Radar: Signal Processing Algorithms*. Artech House Remote Sensing Library. Boston: Artech Print on Demand, 1995.

[7] M. Soumekh, ed., *Synthetic Aperture Radar Signal Processing with MATLAB Algorithms*. New York: Wiley-Interscience, 1999.

[8] R. J. Sullivan, *Radar Foundations for Imaging and Advanced Concepts*. New York, NY: SciTech Publishing, 2004.

[9] A. Hein. *Processing of SAR Data: Fundamentals, Signal Processing, Interferometry*. Signals and Communication Technology, Berlin: Springer-Verlag, 2004.

[10] I. G. Cumming and F. H. Wong, *Digital Processing of Synthetic Aperture Radar Data: Algorithms and Implementation [With CDROM]*. Artech House Remote Sensing Library, Boston: Artech House Print on Demand, 2005.

[11] B.-C. Wang, *Digital Signal Processing Techniques and Applications in Radar Image Processing*. Information and Communication Technology Series, Berlin: Wiley-Interscience, 2008.

[12] J. A. Richards, *Remote Sensing with Imaging Radar*. Signals and Communication Technology, Berlin: Springer-Verlag, 2009.

[13] M. A. Richards, *Fundamentals of Radar Signal Processing*. McGraw-Hill Professional Engineering, Berlin: McGraw-Hill Professional. 2 ed., 2013.

[14] R. Bamler, "A Comparison of Range-Doppler and Wavenumber Domain SAR Focusing Algorithms," *IEEE Transactions on Geosciences and Remote Sensing*, vol. 30, pp. 706–713, July 1992.

[15] E. C. Zaugg and D. G. Long, "Generalized Frequency-Domain SAR Processing," *IEEE Transactions on Geosciences and Remote Sensing*, vol. 47, pp. 3761–3773, Nov. 2009.

[16] F. Argenti, A. Lapini, L. Alparone, and T. Bianchi, "A Tutorial on Speckle Reduction in Synthetic Aperture Radar Images," *IEEE Geoscience and Remote Sensing Magazine*, vol. 1, pp. 6–35, Sept. 2013.

[17] A. Moreira, P. Prats-Iraola, M. Younis, G. Krieger, T. Hajnsek, and P. Papathanassiou, "A Tutorial on Synthetic Aperture Radar," *IEEE Geoscience and Remote Sensing Magazine*, vol. 1, pp. 6–43, Mar. 2013.

[18] K. Ouchi, "Recent Trend and Advance of Synthetic Aperture Radar with Selected Topics," *Remote Sensing*, vol. 5. pp. 716–807. Feb. 2013.

[19] C. T. Allen, "Interferometric Synthetic Aperture Radar," *IEEE Geoscience and Remote Sensing Newsletter*, vol. 96, pp. 6–13, Sept. 1995.

[20] R. Bamler and P. Hartl, "Synthetic Aperture Radar Interferometry," *Inverse Problems*, vol. 14, pp. R1–R53. Aug. 1998.

[21] G. Franceschetti, A. Iodice, M. Migliaccio, and D. Riccio, "A Novel Across-Track SAR Interferometry Simulator," *IEEE Transactions on Geosciences and Remote Sensing*. vol. 36, pp. 950–962, May 1998.

[22] P. A. Rosen, S. Hensleyand, I. R. Joughin, K. L. Fuk, S. N. Madsen, E. Rodriguez, and R. M. Goldstein, "Synthetic Aperture Radar Interferometry," *Proceedings of the IEEE*, vol. 88, pp. 333–382, Mar. 2000.

[23] M. A. Richards, "A Beginner's Guide to Interferometric SAR Concepts and Signal Processing," *IEEE Aerospace and Electronic Systems Magazine*. vol. 22, pp. 5–29, Sept. 2007.

[24] L. Ferro-Famil, A. Reigber, E. Pottier, and W.-M. Boerner, "Scene Characterization Using Subaperture Polarimetric SAR Data," *IEEE Transactions on Geosciences and Remote Sensing*, vol. 41, pp. 2264–2276, Oct. 2003.

[25] D. Massonnet and J.-C. Souyris, *Imaging with Synthetic Aperture Radar*. London: EPFL Press, 2008.

[26] J. J. van Zyl, *Synthetic Aperture Radar Polarimetry*. London: Wiley, 2011.

[27] S. R. Cloude and F. P. Papathanassiou, "Polarimetric SAR interferometry," *IEEE Transactions on Geosciences and Remote Sensing*, vol. 36, pp. 1551–1565, Sept. 1998.

[28] Y. Lasne, P. Paillou, T. August-Bernex, G. Ruffie, and G. Grandjean, "A phase signature for detecting wet subsurface structures using polarimetric L-band SAR," *IEEE Transactions on Geosciences and Remote Sensing*, vol. 42, pp. 1683–1694, Aug. 2004.

[29] K. C. Kornelsen and P. Coulibaly, "Advances in soil moisture retrieval from synthetic aperture radar and hydrological applications," *Journal of Hydrology*, vol. 476, pp. 460–489, Jan. 2013.

[30] D. J. Daniels, *Ground Penetrating Radar*. IEE Radar Sonar Navigation and Avionics Series, London: The Institution of Engineering and Technology, 2 ed., 2004.

[31] H. M. Jol, *Ground Penetrating Radar: Theory and Applications*. Amsterdam: Elsevier Science, 2008.

[32] J. D. Taylor, *Ultrawideband Radar: Applications and Design*. London: CRC Press, 2012.

[33] A. Gunawardena and D. Longstaff, "A Matched Filter Based Synthetic Aperture Radar (SAR) Algorithm for Stepped Frequency Ground Penetrating Radar," in *Record of the IEEE 1995 International Radar Conference*, (Alexandria, VA), pp. 239–243, May 1995.

[34] A. Gunawardena and D. Longstaff, "Wave Equation Formulation of Synthetic Aperture Radar (SAR) Algorithms in the Time-Space Domain," *IEEE Transactions on Geosciences and Remote Sensing*, vol. 36, pp. 1995–1999, Nov. 1998.

[35] I. L. Morrow and P. van Genderen, "Effective Imaging of Buried Dielectric Objects," *IEEE Transactions on Geosciences and Remote Sensing*, vol. 40, pp. 943–949, Apr. 2002.

[36] V. Kabourek and P. Cerny, "SAR and Stolt Migration processing for plastic landmine detection," in *Proc. 2010 20th International Conference Radioelektronika (RADIOELEKTRONIKA)*, (Brno), pp. 1–4, Apr. 2010.

[37] J. I. Halman and K. S. G. T. Ruck. "SAR Processing of Ground-Penetrating Radar Data for Buried UXO Detection: Results from a Surface-Based System," *IEEE Transactions on Antennas and Propagation*, vol. 46, pp. 1023–1027, July 1998.

[38] C. Gilmore, I. Jeffrey, and J. LoVetri, "Derivation and Comparison of SAR and Frequency-Wavenumber Migration Within a Common Inverse Scalar Wave Problem Formulation," *IEEE Transactions on Geosciences and Remote Sensing*, vol. 44, pp. 1454–1461, June 2006.

[39] U. Uschkerat. "Application of 3D-SAR nearfield imaging algorithms to GPR data," in *Proc. IEEE 2007 International Geoscience and Remote Sensing Symposium, IGARSS 2007*, (Barcelona), pp. 452 – 455, July 2007.

[40] Z. Chun-Cheng, K. Ling-jiang, and Z. Zheng-ou, "Research on Fast Synthetic Aperture Imaging Method for Ground Penetrating Radar in Subsurface Object Detection," in *Proc. 2004 International Conference on Communications, Circuits and Systems (ICCCAS 2004)*, pp. 777–779 Vol.2, June 2004.

[41] K. Gu, G. Wang, and J. Li, "Migration Based SAR Imaging for Ground Penetrating Radar Systems," *IEE Proceedings Radar, Sonar and Navigation*, vol. 151, pp. 317–325, Oct. 2004.

[42] C. Ozdemir, S. Demirci, and E. Yigit, "Practical Algorithms to Focus B-Scan GPR Images - Theory and Application to Real Data." *Progress In Electromagnetics Research B*, vol. 6. pp. 109–122. Jan. 2008.

[43] L. Zhou and Y. Su, "GPR Imaging With RM Algorithm in Layered Mediums," *IEEE Geosciences and Remote Sensing Letters*, vol. 8, pp. 934–938, Sept. 2011.

[44] M. Sato and X. Feng, "GPR migration algorithm for landmines buried in inhomogeneous soil," in *Proc. 2005 IEEE Antennas and Propagation Society International Symposium*, (Washington, DC), pp. 206–209 vol. 1B, July 2005.

[45] S. M. Shrestha and I. Arai, "Signal Processing of Ground Penetrating Radar Using Spectral Estimation Techniques to Estimate the Position of Buried Targets," *EURASIP Journal on Applied Signal Processing*, vol. 2003, pp. 1198–1209, Dec. 2003.

[46] P. T. Gough and B. R. Hunt, "Synthetic aperture radar image reconstruction algorithms designed for subsurface imaging," in *Proc. 1997 IEEE International Geoscience and Remote Sensing Symposium, IGARSS 1997*, (Signapore), pp. 1588–1590, vol.4, Aug. 1997.

[47] C. Leuschen. N. Goodman, C. Allen, and R. Plumb, "An Interferometric Techniquef Synthetic Aperture Ground-Penetrating Radar," in *Proc. 1996 Geoscience and Remote Sensing Symposium, IGARSS '96*, (Lincoln), pp. 2033–2035, vol. 4, May 1996.

[48] A. van der Merwe and I. J. Gupta. "A novel signal processing technique for clutter reduction in GPR measurements of small, shallow land mines," *IEEE Transactions on Geoscience and Remote Sensing*, vol. 38, pp. 2627–2637, Nov. 2000.

[49] C. Rappaport, M. El-Shenawee, and H. Zhan, "Suppressing GPR Clutter from Randomly Rough Ground Surfaces to Enhance Nonmetallic Mine Detection," *Subsurface Sensing Technologies and Applications*, vol. 4, pp. 311–326, Oct. 2003.

[50] M. A. C. Tuncer and A. C. Gurbuz, "Ground Reflection Removal in Compressive Sensing Ground Penetrating Radars," *IEEE Geoscience and Remote Sensing Letters*, vol. 9, pp. 23–27, Jan. 2012.

[51] H. Brunzell, "Detection of Shallowly Buried Objects Using Impulse Radar," *IEEE Transactions on Geosciences and Remote Sensing*, vol. 37, pp. 875–886, Mar. 1999.

[52] J. Jenwatanavet and J. T. Johnson, "An analytical model for studies of soil modification effects on ground penetrating radar ," *IEE Transactions on Antennas and Propagation*, vol. 49. pp. 923–933, June 2001.

[53] J. B. Rhebergen, H. A. Lensen, R. van Wijk. J. M. H. Hendrickx, and R. van Dam and B. Borchers, "Prediction of Soil Effects on GPR Signatures," *Proc. SPIE*, vol. 5415, pp. 705–715, Sept. 2004.

[54] H. Nazli, E. Bicak, and M. Sezgin, "Experimental investigation of different soil types for buried object imaging using impulse GPR," in *Proc. 2010 13th International Conference on Ground Penetrating Radar (GPR)*, (Lecce). pp. 1–5, June 2010.

[55] R. Wu, G. Kunlong. L. Jian, M. Bradley, J. Habersat, and G. Maksymonko, "Propagation Velocity Uncertainty on GPR SAR Processing," *IEEE Transaction on Aerospace and Electronic Systems*, vol. 39, pp. 849–861, July 2003.

[56] A. Arvaniti, E. Orzeł-Tatarczuk, J. Popkowski, P. Kaczmarek, A. Kawalec, and M. Pasternak, "Mobilna platofrma z ultraszerokopasmowym radarem do wykrywania ukrytych w ziemiu niebiepiczenych obiektów," in *Urządzenia i Systemy Radioelektroniczne: Wybrane Problemy 2* (A. Kawalec, ed.), Warsaw, Poland: Military Univeristy of Technology, 2012. (in polish).

[57] T. Ton. D. Wong. and M. Soumekh, "ALARIC Forward-Looking Ground Penetrating Radar System With Standoff Capability," in *Proc. 2010 IEEE International Conference on Wireless Information Technology and Systems (ICWITS)*, pp. 1–4, Aug./Sept. 2010.

[58] J. Fortuny-Guasch, "A Novel 3-D Subsurface Radar Imaging Technique," *IEEE Transactions on Geosciences and Remote Sensing*, vol. 40, pp. 443–452, Feb. 2002.

[59] D. Eisenburger, Y. Krellmann, H. Lentz, and G. Triltzsch, "Stepped-Frequency Radar System in Gating Mode: An Experiment as a New Helicopter-Borne GPR System for Geological Applications," in *Proc. 2008 IEEE International Geoscience and Remote Sensing Symposium, IGARSS 2008*, (Boston, MA), pp. I–153–I–156. July 2008.

[60] N. Blindow, C. Salat, V. Gundelach, U. Buschmann, and W. Kahnt, "Performance and Calibration of the Helicoper GPR System BGR-P30." in *Proc. 2011 6th International Workshop on Advanced Ground Penetrating Radar (IWAGPR)*, (Aachen), pp. 1–5, June 2011.

[61] I. Catapano, L. Crocco, Y. Krellmann, G. Triltzsch, and F. Soldovieri, "Tomographic Airborne Ground Penetrating Radar Imaging: Achievable Spatial Resolution and on-Field Assessment," *ISPRS Journal of Photogrammetry and Remote Sensing*, vol. 92, pp. 69–78, 2014.

[62] M. D'Errico, S. Ponte. M. Grassi. and A. Moccia, "Preliminary Design of a Space System Operating a Ground-Penetrating Radar," *Acta Astronautica*, vol. 57, pp. 851–863, Dec. 2005.

[63] C. Elachi, W. E. Brown, J. B. Cimino, T. Dixon, D. L. Evans, J. P. Ford, R. S. Saunders, C. Breed, H. Masursky, J. F. Mccauley, G. Schaber, L. Dellwig, A. England, H. Macdonald, P. Martin-Kaye, and F. Sabins, "Shuttle Imaging Radar Experiment," *Science*, vol. 218, pp. 996–1003, Dec. 1982.

[64] J. F. McCauley. G. G. Schaber, C. S. Breed, M. J. Grolier, C. V. Haynes, B. Issawi, C. Elachi. and R. Blom, "Subsurface Valleys and Geoarcheology of the Eastern Sahara Revealed by Shuttle Radar," *Science*, vol. 218, pp. 1004–1020, Dec. 1982.

[65] J. Cimino, C. Elachi, and M. Settle, "SIR-B-The Second Shuttle Imaging Radar Experiment," *IEEE Transactions on Geosciences and Remote Sensing*, vol. 24, pp. 445–452, July 1986.

[66] G. L. Berlin, M. A. Tarabzouni, A. H. Al-Nazer, K. M. Sheikho, and R. W. Larson. "SIR-B Subsurface Imaging of a Sand-Buried Landscape: Al Labbah Plateau, Saudi Arabia," *IEEE Transactions on Geosciences and Remote Sensing*, vol. 24, pp. 595–602, July 1986.

[67] G. G. Schaber, J. F. McCauley, C. S. Breed, and G. R. Olhoeft, "Shuttle Imaging Radar: Physical Controls on Signal Penetration and Subsurface Scattering in the Eastern Sahara," *IEEE Transactions on Geosciences and Remote Sensing*, vol. 24, pp. 603–623, July 1986.

[68] T. G. Farr, C. Elachi, P. Hartl, and K. Chowdhury. "Microwave Penetration and Attenuation in Desert Soil: A Field Experiment with the Shuttle Imaging Radar," *IEEE Transactions on Geosciences and Remote Sensing*, vol. 24, pp. 590–594, July 1986.

[69] J. Shi, J. Dozier, and H. Rott, "Snow Mapping in Alpine Regions with Synthetic Aperture Radar," *IEEE Transactions on Geosciences and Remote Sensing*, vol. 32, pp. 1254–1266, Jan. 1994.

[70] J. J. Legarsky, S. P. Gogineni, and T. L. Akins, "Focused synthetic aperture radar processing of ice-sounder data collected over the Greenland ice sheet," *IEEE Transactions on Geosciences and Remote Sensing*, vol. 39, pp. 2109–2882, Oct. 2001.

[71] P. Dubois-Fernandez, O. R. du Plessis, D. L. Coz, J. Dupas, B. Vaizan, H. Dupuis, H. Cantalloube, C. Coulombeix, C. Titin-Schnaider, P. Dreuillet, J.-M. Boutry, J. P. Canny, L. Kaisersmertz, J. Peyret, P. Martineau, M. Chantelclerc, L. Pastore, and J. P. Bruyant, "The ONERA RAMSES SAR System," in *Proc. IEEE 2002 International Geoscience and Remote Sensing Symposium, IGARSS 2002*, (Toronto), pp. 1723–1725 vol.3, June 2002.

[72] P. Dreuillet, P. Paillou, H. Cantalloube, C. Titin-Schnaider, L. Pastore, H. Dupuis, V. Lafon, R. Garello, J.-M. L. Caillec, I. Champion, M. Dechambre, R. Chapoulie, M. Martinaud, C. Coulombeix, P. Dubois-Fernandez, and O. Duplessis, "P Band Data Collection and Investigations Utilizing the RAMSES SAR Facility," in *Proc. IEEE 2003 International Geoscience and Remote Sensing Symposium, IGARSS 2003*, (Toulouse), pp. 4262–4264 vol.7, July 2003.

[73] L. Pastore, *Imagerie Radar Par Synthese d'Ouverture en Basse Frequence*. PhD thesis, Universite Paris X, 2003.

[74] G. Grandjean, P. Paillou, P. Dubois-Fernandez, T. August-Bernex, N. N. Baghdadi, and J. Achache, "Subsurface Structures Detection by Combining L-Band Polarimetric SAR and GPR Data: Example of the Pyla Dune (France)," *IEEE Transactions on Geosciences and Remote Sensing*, vol. 39, pp. 1245–1258, June 2001.

[75] P. Paillou, G. Grandjean, N. Baghdadi, E. Heggy, T. August-Bernex, and J. Achache, "Subsurface imaging in south-central Egypt using low-frequency radar: Bir Safsaf revisited," *IEEE Transactions on Geosciences and Remote Sensing*, vol. 41, pp. 1672–1684, July 2003.

[76] "E-SAR - The Airborne SAR System of DLR."

[77] K. K. Williams and R. Greeley, "Modification of Radar Backscatter by Sand: Results From AIRSAR Data and Laboratory Experiments," in *Proc. IEEE 2000 International Geoscience and Remote Sensing Symposium, IGARSS 2000*, (Honolulu, HI), pp. 1516–1518 vol.4, Oct. 2000.

[78] A. W. Doerry, B. C. Brock, B. Boverie, and D. Cress, "Imaging Targets Embedded in a Lossy Half Space with Synthetic Aperture Radar." in *Proc. 1994 Geoscience and Remote Sensing Symposium, IGARSS 1994*, (Pasadena, CA), pp. 2508–2512, vol. 4, Aug. 1994.

[79] W. Gregorwich, "An Airborne Ground Penetrating Radar System," in *Proc. 1996 IEEE Aerospace Applications Conference*, (Aspen, CO), pp. 157–161, vol.1, Feb. 1996.

[80] R. S. Vickers, "Design and Applications of Airborne Radars in the VHF/UHF Band," *IEEE Aerospace and Electronic Systems Magazine*, vol. 17, pp. 26–26, June 2002.

[81] W. Zhai, Y. Zhang, and X. Zhang. "SAR Imaging Simulation for Subsurface Target Detection," in *Proc. 7th International Symposium on Antennas, Propagation and EM Theory (ISAPE'97)*, (Guilin), pp. 1–5, Oct. 2006.

[82] J. A. Martinez-Lorenzo, C. M. Rappaport, and F. Quivira, "Physical Limitations on Detecting Tunnels Using Underground-Focusing Spotlight Synthetic Aperture Radar," *IEEE Transactions on Geosciences and Remote Sensing*, vol. 49, pp. 65–70, Jan. 2011.

[83] S. Liu and Y. Feng, "Airborne GPR: Advances and Numerical Simulation," in *Proc. 2011 IEEE International Geoscience and Remote Sensing Symposium (IGARSS)*, (Vancouver, BC), pp. 3390–3340, July 2011.

[84] L. Fu, S. Liu, and L. Liu, "Numerical Simulations and Analysis for Airborne Ground Penetrating Radar," in *Proc. 2012 14th International Conference on Ground Penetrating Radar (GPR'12)*, (Shanghai), pp. 200–203, June 2012.

[85] L. Fu, S. Liu, L. Liu, and L. Lei, "Development of an Airborne Ground Penetrating Radar System: Antenna Design, Laboratory Experiment, and Numerical Simulation," *IEEE Journal of Selected Topics in Applied Earth Observations and Remote Sensing*, vol. 7, pp. 761–766, Mar. 2014.

[86] A. Elsherbini and K. Sarabandi, "Mapping of Sand Layer Thickness in Deserts Using SAR Interferometryn." *IEEE Transactions on Geosciences and Remote Sensing*, vol. 48, pp. 3550–3559, Sept. 2010.

[87] J.-M. Le Caillec, S. Redadaa, C. Sintes, B. Solaiman, and M. Benslama, "Focusing Problems of a Buried Point Scatterer Using a Low Frequency SAR," *IEEE Transaction on Aerospace and Electronic Systems*, vol. 47, pp. 438–453, Jan. 2011.

[88] M. Fink, C. Prada, F. Wu, and D. Casserau, "Self Focusing in Inhomogeneous Media with Time Reversal Acoustic Waves." in *Proc. IEEE 1989 Ultrasonics Symposium*, (Montreal, Que.). pp. 681–686 vol.2, Oct. 1989.

[89] M. Fink, D. Cassereau, A. Derode, C. Prada, P. Roux, M. Tanter, J. Thomas, and F. Wu, "Time-Reversed Acoustics," *Reports on Progress in Physics*, vol. 63, no. 12, pp. 1933–1995, 2000.

[90] M. Fink. "Time Reversal of Ultrasonic Fields - Part I: Basic Principles," *IEEE Transactions on Ultrasonics, Ferroelectrics and Frequency Control*, vol. 39, pp. 555–566, Sept. 1992.

[91] M. Born and E. Wolf, *Principles of Optics: Electromagnetic Theory of Propagation, Interference and Diffraction of Light.* Oxford: Pergamon Press, fourth ed., 1970.

[92] F. Wu, J.-L. Thomas, and M. Fink, "Time Reversal of Ultrasonic Fields - Part II: Experimental results," *IEEE Transactions on Ultrasonics, Ferroelectrics and Frequency Control*, vol. 39, pp. 567–578, Sept. 1992.

[93] Z. Wang, J. Li, and R. Wu, "Time-Delay- and Time-Reversal-Based Robust Capon Beamformers for Ultrasound Imaging," *IEEE Transactions on Medical Imaging*, vol. 24, pp. 1308–1322, Oct. 2005.

[94] J.-P. Fouque, J. Garnier, G. Papanicolaou, and K. Solna. *Wave Propagation and Time Reversal in Randomly Layered Media.* Stochastic Modelling and Applied Probability, Vol. 57, Berlin: Springer, 2007.

[95] G. Lerosey, J. de Rosny, A. Tourin. A. Derode, G. Montaldo, and M. Fink, "Time Reversal of Electromagnetic Waves," *IEEE Transactions on Antennas and Propagation*, vol. 92, pp. 193904–1–193904–3, May 2004.

[96] J. de Rosny, G. Lerosey, and M. Fink, "Theory of Electromagnetic Time-Reversal Mirrors," *IEEE Transactions on Antennas and Propagation*, vol. 58, pp. 3139–3149, Oct. 2010.

[97] A. G. Cepni, *Experimental Investigation of Time-Reversal Techniques using Electromagneti Waves.* PhD thesis, Carnegie Mellon Univeristy. 2005.

[98] M. E. Yavuz, *Time reversal based signal processing techniques for ultrawideband electromagnetic sensing in random media.* PhD thesis, The Ohio State University. 2007.

[99] Y. Jiang, *Time reversal technique in electromagnetic wave propagation.* PhD thesis, Carnegie Mellon Univeristy, 2008.

[100] J. M. F. Moura and Y. Jin, "Detection by Time Reversal: Single Antenna," *IEEE Transactions on Signal Processing*, vol. 55, pp. 187–201, Jan. 2007.

[101] Y. Jin and J. M. F. Moura. "Time-Reversal Detection Using Antenna Arrays," *IEEE Transactions on Signal Processing*, vol. 57, pp. 1396–1414, Apr. 2009.

[102] Y. Jin, J. M. F. Moura, Y. Jiang, D. D. Stancil, and A. G. Cepni, "Time Reversal Detection in Clutter: Additional Experimental Results," *IEEE Transactions on Aerospace and Electronic Systems*, vol. 47, pp. 140–154, Jan. 201.

[103] M. E. Yavuz and F. L. Teixeira, "Ultrawideband Microwave Sensing and Imaging Using Time-Reversal Techniques: A Review," *Remote Sensing*, vol. 1, pp. 466–495, Aug. 2009.

[104] P. Kosmas and C. M. Rappaport, "FDTD-Based Time Reversal for Microwave Breast Cancer Detection - Localization in Three Dimensions," *IEEE Transactions on Microwave Theory and Techniques*, vol. 54, pp. 1921–1927, June 2006.

[105] M. E. Yavuz and F. L. Teixeira, "Space-Frequency Ultrawideband Time-Reversal Imaging ," *IEEE Transaction on Geoscience and Remote Sensing*, vol. 46, pp. 1115–1124, Apr. 2008.

[106] Y. Jin and J. M. F. Moura, "Time Reversal in Multiple-Input Multiple-Output Radar," *IEEE Journal of Selected Topics in Signal Processing*, vol. 4, pp. 210–225, Feb. 2010.

[107] C. Prada, Manneville, D. Spoliansky, and M. Fink. "Decomposition of the Time Reversal Operator: Detection and Selective Focusing on Two Scatterers," *The Journal of the Acoustical Society of America*, vol. 99, pp. 2067–2076, 1996.

[108] M. E. Yavuz and F. L. Teixeira, "Full Time-Domain DORT for Ultrawideband Electromagnetic Fields in Dispersive. Random Inhomogeneous Media," *IEEE Transaction on Antennas and Propagation*, vol. 54, pp. 2305–2315, Aug. 2006.

[109] J. M. F. Moura and Y. Jin, "Time Reversal Imaging by Adaptive Interference Canceling," *IEEE Transactions on Signal Processing*, vol. 58, pp. 233–247, Jan. 2008.

[110] D. Liu, G. Kang, L. Li, Y. Chen, S. Vasudevan, W. Joines, L. Q. Huo, J. Krolik, and L. Carin, "Electromagnetic Time-Reversal Imaging of a Target in a Cluttered Environment," *IEEE Transactions on Antennas and Propagation*, vol. 53, pp. 3058–3066, Sept. 2005.

[111] D. Liu, S. Vasudevan, J. Krolik, G. Bal, and L. Carin. "Electromagnetic Time-Reversal Source Localization in Changing Media: Experiment and Analysis," *IEEE Transactions on Antennas and Propagation*, vol. 55, pp. 344–354, Feb. 2007.

[112] Y. Jiang, J.-G. Zhu, D. D. Stancil, J. Moura, A. G. Cepni, B. Henty, and Y.-W. Jin, "Single Antenna Target Detection Using Broadband Frequency Selection Time Reversal Method," in *Proc. 2006 IEEE Antennas and Propagation Society International Symposium*, (Albuquerque, NM), pp. 699–702, July 2006.

[113] H. Lev-Ari and A. J. Devaney, "The Time-Reversal Technique Re-Interpreted: Subspace-Based Signal Processing for Multi-Static Target Location," in *Proc. 2000 IEEE Sensor Array and Multichannel Signal Processing Workshop*, (Cambrige, MA), pp. 509–513, Mar. 2000.

[114] Y. Jiang. J.-G. Zhu, and D. D. Stancil, "Synthetic Aperture Radar Ghost Image Cancellation Using Broadband Time Reversal Averaging Techniques," in *Proc. 2007 IEEE/MTT-S International Microwave Symposium*, (Honolulu, HI), pp. 1479–1482, June 2007.

[115] Y. Jin and J. M. F. Moura, "TR-SAR: Time Reversal Target Focusing in Spotlight SAR," in *Proc. IEEE International Conference on Acoustics, Speech and Signal Processing*, (Honolulu, HI), pp. II–957–II–960, Apr. 2007.

[116] Y. Jin, J. M. F. Moura, N. O'Donoughue, M. T. Mulford, and A. A. Samuel, "Time Reversal Synthetic Aperture Radar Imaging In Multipath," in *Proc. 2007 41nd Asilomar Conference on Signals, Systems and Computers*, (Pacific Grove, CA), pp. 1812–1816, Nov. 2007.

[117] Y. Jiang and J.-G. Zhu, "Time reversal SAR technique for imaging extended target shielded from line-of-sight ," in *Proc. 2007 IEEE Antennas and Propagation Society International Symposium*, (San Diego, CA), pp. 1–4. July 2008.

[118] N. O'Donoughue, J. M. F. Moura. and Y. Jin, "Signal-Domain Registration for Change Detection in Time-Reversal SAR," in *Proc. 2008 42nd Asilomar Conference on Signals, Systems and Computers*, (Pacific Grove. CA), pp. 505–509, Oct. 2008.

[119] W. Zheng, Z. Zhao, and Z.-P. Nie, "Application of TRM in the UWB Through Wall Radar," *Progress In Electromagnetics Research*, vol. 87, pp. 279–296, 2008.

[120] A. Cresp, I. Aliferis. M. J. Yedlin, C. Pichot, and J.-Y. Dauvignac, "Investigation of Time-Reversal Processing for Surface-Penetrating Radar Detection in a Multiple-Target Configuration," in *Proc. 5th European Radar Conference (EuRAD 2008)*, (Amsterdam), pp. 144–147, Oct. 2008.

[121] R. Dubroca, N. Fortino, J.-Y. Dauvignac, L. Bellomo, S. Pioch, M. Saillard, T. Lepetit, J. de Rosny. C. Prada, P. Millot, N. Maaref, and B. Boudamouz, "Time Reversal-Based Processing for Human Targets Detection in Realistic Through-the-Wall Scenarios," in *Proc. 2011 European Radar Conference (EuRAD)*, (Manchester), pp. 1–4, Oct. 2011.

[122] C. J. Leuschen and R. G. Plumb, "A Matched-Filter-Based Reverse-Time Migration Algorithm for Ground-Penetrating Radar Data," *IEEE Transactions on Geosciences and Remote Sensing*, vol. 39, pp. 929–936, May 2001.

[123] F. Foroozan and A. Asif, "Time Reversal Ground Penetrating Radar: Range Estimation With Cramer Rao Lower Bounds." *IEEE Transactions on Geosciences and Remote Sensing*, vol. 48, pp. 3698–3708, Oct. 2010.

[124] R. Kedzierawski, J.-M. Le Caillec, and W. Czarnecki, "The Time-Reversal Technique for SAR Focusing of Buried Targets: Theoretical improvements and practical limitations," *IEEE Signal Processing Magazine*, vol. 32, pp. 99–109, July 2014.

[125] FAO - Food and Agriculture Organization of the United Nations, Rome, Italy, *Irrigation Water Management: Training Manual No. 1 - Introduction to Irrigation*, 1985.

[126] J. Behari, *Microwave Dielectric Behaviour of Wet Soils*. Remote Sensing and Digital Image Processing, Vol. 8, New York: Springer, 2005.

[127] R. Kedzierawski. J.-M. Le Caillec, W. Czarnecki, and M. Pasternak, "Subsurface Soil Modeling Based on Geological Database for Simulation of Electromagnetic Wave Propagation," in *Proc. 2012 13th International Radar Symposium (IRS '12)*, (Warsaw), pp. 441–445, May 2012.

[128] S. Lambot, E. C. Slob, I. van den Bosch, B. Stockbroeckx, and M. Vanclooste. "Modeling of Ground-Penetrating Radar for Accurate Characterization of Subsurface Electric Properties," *IEEE Transactions on Geosciences and Remote Sensing*, vol. 42, pp. 2555–2568, Nov. 2004.

[129] A. Tabatabaeenejad and M. Moghaddam, "Bistatic Scattering From Three-Dimensional Layered Rough Surfaces," *IEEE Transactions on Geosciences and Remote Sensing*, vol. 44, pp. 2102–2114, Aug. 2006.

[130] C.-H. Kuo and M. Moghaddam. "Electromagnetic Scattering From Multilayer Rough Surfaces With Arbitrary Dielectric Profiles for Remote Sensing of Subsurface Soil Moisture." *IEEE Transactions on Geoscience and Remote Sensing*, vol. 45, pp. 349–366, Feb. 2007.

[131] A. Tabatabaeenejad, *Forward and Inverse Models of Electromagnetic Scattering From Layered Media With Rough Interfaces.* PhD thesis, The University of Michigan. 2008.

[132] H. Zhong-hua and Y. Yan, "Deconvolution of the Impulse Response of Rough Ground," in *Proc. 2010 3rd International Conference on Advanced Computer Theory and Engineering (ICACTE) (Volume:5)*, (Chengdu), pp. V5–470–V5–474. Aug. 2010.

[133] H. Bormann, "Towards a Hydrologically Motivated Soil Texture Classification," *Geoderma*, vol. 157, pp. 142–153, July 2010.

[134] J. R. Birchak, C. G. Gardner, J. E. Hipp, and J. M. Victor, "High Dielectric Constant Microwave Probes for Sensing Soil Moisture," *Proceedings of the IEEE*, vol. 62, pp. 93–98, Jan. 1974.

[135] T. J. Schmugge, "Remote Sensing of Soil Moisture: Recent Advance," *IEEE Transactions on Geosciences and Remote Sensing*, vol. 21, pp. 336–344, July 1983.

[136] R. B. Keam and J. R. Holden, "Determination of Soil Moisture Profile from Surface Reflection Coefficient Measurements," *Subsurface Sensing Technologies and Applications.* vol. 1, pp. 453–471, Oct. 2000.

[137] A. Tabatabaeenejad and M. Moghaddam, "Radar Retrieval of Surface and Deep Soil Moisture and Effect of Moisture Profile on Inversion Accuracy," *IEEE Geosciences and Remote Sensing Letters*, vol. 8, pp. 478–482, May 2011.

[138] R. A. van Overmeeren, S. V. Sariowan, and J. C. Gehrels, "Ground Penetrating Radar for Determining Volumetric Soil Water Content; Results of Comparative Measurements at Two Test Sites," *Journal of Hydrology*, vol. 197, pp. 316–338, Oct. 1997.

[139] F. T. Ulaby and P. C. D. J. van Zyl. "Radar Mapping of Surface Soil Moisture," *Journal of Hydrology*, vol. 184, pp. 57–84, Oct. 1994.

[140] G. Satalino, F. Mattia, M. Davidson, T. L. Toan, G. Pasquariello, and M. Borgeaud, "On current limits of soil moisture retrieval from ERS-SAR data ," *IEEE Transactions on Geosciences and Remote Sensing*, vol. 40, pp. 2438–2447, Nov. 2002.

[141] P. J. Ross, "Modeling Soil Water and Solute Transport - Fast, Simplified Numerical Solutions," *Agronomy Journal*, vol. 95, pp. 1352–1361, Nov. 2003.

[142] N. Varado, I. Brauda, P. J. Rossd, and R. Haverkampa, "Assessment of an Efficient Numerical Solution of the 1D Richards' Equation on Bare Soil," *Journal of Hydrology*, vol. 323, pp. 244–257. May 2006.

[143] F. T. Tracy, "Three-dimensional analytical solutions of Richards' equation for a box-shaped soil sample with piecewise-constant head boundary conditions on the top," *Journal of Hydrology*, vol. 336, pp. 391–400. Apr. 2007.

[144] R. H. Brooks and A. T. Corey, *Hydraulic Properties Of Porous Media.* Fort Collins: Colorado State Univeristy, 1964.

[145] L. A. Richards, "Capillary conduction of liquids through porous mediums," *Physics*, vol. 1, pp. 318–333, June 1931.

[146] D. H. Lee and L. M. Abriola, "Use of the Richards equation in land surface parameterizations," *Journal of Geophysical Research: Atmospheres*, vol. 104, pp. 27519–27526, Nov. 1999.

[147] M. Inouea, J. Simunek, S. Shiozawac, and J. Hopmansd, "Simultaneous Estimation of Soil Hydraulic and Solute Transport Parameters From Transient Infiltration Experiments," *Advances in Water Resources*, vol. 23, pp. 677–688, June 2000.

[148] Y. Pachepskya, D. Timlin, and W. Rawls. "Generalized Richards' equation to simulate water transport in unsaturated soils," *Journal of Hydrology*, vol. 272, pp. 3–13, Mar. 2003.

[149] X. Chen and Q. Hu, "Groundwater Influences on Soil Moisture and Surface Evaporation," *Journal of Hydrology*, vol. 277, pp. 285–300, Sept. 2004.

[150] B. J. Cosby, G. M. Hornberger. R. B. Clapp, and T. R. Ginn, "A Statistical Exploration of the Relationships of Soil Moisture Characteristics to the Physical Properties of Soils." *WATER RESOURCES RESEARCH*, vol. 20, pp. 682–690, June 1984.

[151] L. R. Leung, M. Huang, Y. Qian, and X. Liang, "Climate-soil-vegetation control on groundwater table dynamics and its feedbacks in a climate model," *Climate Dynamics*, vol. 36, pp. 57–81, Jan. 2011.

[152] J. F. Mahfouf and J. Noilhan, "Comparative Study of Various Formulations of Evaporations from Bare Soil Using In Situ Data," *Journal of Applied Meteorology*, vol. 30, pp. 1354–1365, Sept. 1991.

[153] D. Wobschall, "A Theory of the Complex Dielectric Permittivity of Soil Containing Water: The Semidisperse Model," *IEEE Transactions on Geoscience Electronics*, vol. 15. pp. 49–58, Jan. 1977.

[154] J. R. Wang. "The Dielectric Properties of Soil-Water Mixtures at Microwave Frequencies," *Radio Science*, vol. 15, pp. 977–985, Sept. 1980.

[155] J. R. Wang and T. J. Schmugge, "An Empirical Model for the Complex Dielectric Permittivity of Soils as a Function of Water Content," *IEEE Transactions on Geoscience and Remote Sensing*, vol. 18, pp. 288–295, Oct. 1980.

[156] M. T. Hallikainen, F. T. Ulaby, M. C. Dobson, M. A. El-Rayes, and W. Lil-Kun, "Microwave Dielectric Behavior of Wet Soil - Part I: Empirical Models and Experimental Observations," *IEEE Transactions on Geosciences and Remote Sensing*, vol. 23, pp. 25–34, Jan. 1985.

[157] M. C. Dobson, F. T. Ulaby, M. T. Hallikainen, and M. A. El-Rayes, "Microwave Dielectric Behavior of Wet Soil - Part II: Dielectric Mixing Models ," *IEEE Transactions on Geosciences and Remote Sensing*, vol. 23, pp. 35–46, Jan. 1985.

[158] W. A. Wensink, "Dielectric Properties of Wet Soils in The Frequency Range 1-3000 MHZ," *Geophysical Prospecting*, vol. 41, pp. 671–696, Aug. 1993.

[159] N. R. Peplinski, F. T. Ulaby, and M. C. Dobson, "Dielectric Properties of Soils in the 0.3-1.3 GHz Range," *IEEE Transactions on Geosciences and Remote Sensing*, vol. 33, pp. 803–807, May 1995.

[160] V. L. Mironov, M. C. Dobson, V. H. Kaupp, S. A. Komarov, and V. N. Kleshchenko. "Generalized Refractive Mixing Dielectric Model for Moist Soils," *IEEE Transactions on Geoscience and Remote Sensing*, vol. 42, pp. 773–785, Apr. 2004.

[161] V. L. Mironov, L. G. Kosolapova, and S. V. Fomin, "Physically and Mineralogically Based Spectroscopic Dielectric Model for Moist Soils," *IEEE Transactions on Geoscience and Remote Sensing*, vol. 47, pp. 2059–2070, July 2009.

[162] R. C. Schwarz, S. R. Evett. M. G. Pelletier, and J. M. Bell, "Complex Permittivity Model for Time Domain Reflectometry Soil Water Content Sensing: I. Theory." *Soil Science Society of America Journal*, vol. 73, pp. 886–897, May-June 2009.

[163] R. C. Schwarz, S. R. Evett, and J. M. Bell, "Complex Permittivity Model for Time Domain Reflectometry Soil Water Content Sensing: II. Calibration," *Soil Science Society of America Journal*, vol. 73, pp. 898–909, May-June 2009.

[164] W. G. Fano and V. Trainotti, "Dielectric Properties of Soils," in *Proc. 2001 Annual Report Conference on Electrical Insulation and Dielectric Phenomena*, (Kitchener, Ont.), pp. 75–78, Oct. 2001.

[165] T. Meissner and F. J. Wentz, "The complex dielectric constant of pure and sea water from microwave satellite observations," *IEEE Transactions on Geoscience and Remote Sensing*, vol. 42, pp. 1836–1849, Sept. 2004.

[166] T. J. Kelleners, D. A. Robinson, P. J. Shouse, J. E. Ayars, and T. H. Skaggs. "Frequency dependence of the complex permittivity and its impact on dielectric sensor calibration in soils," *Soil Science Society of America Journal*, vol. 69, pp. 67–76, Jan.-Feb. 2005.

[167] K. Zhang and D. Li, *Electromagnetic Theory for Microwaves and Optoelectronics*. Berlin: Springer-Verlag, 2008.

[168] R. L. van Dam, B. Borchers, and J. M. H. Hendrickx, "Methods for prediction of soil dielectric properties: a review," *Proc. SPIE - Detection and Remediation Technologies for Mines and Minelike Targets X*, vol. 5794, pp. 188–197, July 2005.

[169] A. Stogryn, "Equations for Calculating the Dielectric Constant of Saline Water," *IEEE Transactions on Microwave Theory and Techniques*, vol. 19. pp. 733–736, Aug. 1971.

[170] J. D. Irving and R. J. Knight, "Removal of Wavelet Dispersion From Ground-penetrating Radar Data," *GEOPHYSICS*, vol. 68, pp. 960–970, May/June 2003.

[171] M. Loewer, J. Igel, and N. Wagner, "Frequency-Dependent Attenuation Analysis of Soils Using Broadband Dielectric Spectroscopy and TDR," in *Proc. 2014 15th International Conference on Ground Penetrating Radar (GPR 2014)*, (Brussels, Belgium), July 2014.

[172] J. R. Holdem, R. B. Keam, and J. A. Schoonees, "Estimation of the Number of Frequencies and Bandwidth for the Surface Measurement of Soil Moisture as a Function of Depth," *IEEE Transactions on Instrumentation and Measurement*, vol. 49, pp. 964–970, Oct. 2000.

[173] J. M. H. Hendrickx, R. van Dam, B. Borchers, J. Curtis, H. A. Lensen, and R. Harmon, "Worldwide Distribution of Soil Dielectric and Thermal Properties," *Proc. SPIE*, vol. 5089, Sept. 2003.

[174] Y. Lasne, P. Paillou, A. Freeman. T. Farr, K. C. McDonald, G. Ruffie, J.-M. Malezieux, B. Chapman, and F. Demontoux, "Effect of Salinity on the Dielectric Properties of Geological Materials: Implication for Soil Moisture Detection by Means of Radar Remote Sensing," *IEEE Transactions on Geosciences and Remote Sensing*, vol. 46, pp. 1674–1688, June 2008.

[175] V. K. Gupta and R. A. Jangid, "The Effect of Bulk Density on Emission Behavior of Soil at Microwave Frequencies," *International Journal of Microwave Science and Technology*, vol. 2011, pp. 1–6, 2011.

[176] J. O. Curtis, "Moisture Effects on the Dielectric Properties of Soils," *IEEE Transactions on Geosciences and Remote Sensing*, vol. 39, pp. 125–128, Jan. 2001.

[177] J. E. Hipp, "Soil Electromagnetic Parameters as Functions of Frequency, Soil Density, and Soil Moisture," *Proceedings of the IEEE*, vol. 63, pp. 98–103, Jan. 1974.

[178] F. Lavoue, Brossier, S. Garambois, J. Virieux, and L. Metivier, "2D full waveform inversion of GPR surface data: Permittivity and conductivity imaging," in *Proc. 2013 7th International Workshop on Advanced Ground Penetrating Radar (IWAGPR)*, (Nantes), pp. 1–6, July 2013.

[179] J. A. Kong, *Electromagnetic Wave Theory*. Hoboken, NJ: Wiley, 4986.

[180] W. C. Chew, *Waves and Fields in Inhomogenous Media*. New York: Wiley-IEEE Press, 1999.

[181] S. J. Orfanidis, *Electromagnetic Waves and Antennas*. Piscataway: Rutgers University, 2008.

[182] C. A. Balanis, *Advanced Engineering Electromagnetics*. New York: Wiley, 2012.

[183] G. H. Spencer and M. V. R. K. Murty, "General Ray-Tracing Procedure," *Journal of the Optical Society of America*, vol. 52, pp. 672–676, June 1962.

[184] G. Sun and K. J. Ranson, "A Three-Dimensional Radar Backscatter Model of Forest Canopies," *IEEE Transactions on Geoscience and Remote Sensing*, vol. 33, pp. 37–382, Mar. 2002.

[185] F. T. Ulaby, *Microwave Radar and Radiometric Remote Sensing*. Michigan: University of Michigan Press, 2013.

[186] F. T. Ulaby, P. P. Batlivala, and M. C. Dobson, "Microwave Backscatter Dependence on Surface Roughness. Soil Moisture, and Soil Texture: Part I - Bare Soil," *IEEE Transactions on Geoscience Electronics*, vol. 16, pp. 286–295, Oct. 1978.

[187] F. T. Ulaby, G. A. Bradley, and M. C. Dobson, "Microwave Backscatter Dependence on Surface Roughness. Soil Moisture, and Soil Texture: Part II - Vegetation-Covered Soil," *IEEE Transactions on Geoscience Electronics*. vol. 17, pp. 33–40, Apr. 1979.

[188] M. C. Dobson and F. T. Ulaby, "Microwave Backscatter Dependence on Surface Roughness, Soil Moisture, and Soil Texture: Part III - Soil Tension," *IEEE Transactions on Geoscience and Remote Sensing*, vol. 19, pp. 51–61, Jan. 1981.

[189] Y. Oh, K. Sarabandi, and F. T. Ulaby, "An empirical model and an inversion technique for radar scattering from bare soil surfaces." *IEEE Transactions on Geosciences and Remote Sensing*, vol. 30, pp. 370–381, Mar. 1992.

[190] Y. Oh, K. Sarabandi, and F. T. Ulaby, "Semi-empirical model of the ensemble-averaged differential Mueller matrix for microwave backscattering from bare soil surfaces ," *IEEE Transactions on Geosciences and Remote Sensing*, vol. 40, pp. 1348–1355, June 2002.

[191] F. J. Haris, "On the Use of Windows for Harmonic Analysis with the Discrete Fourier Transform," *Proceedings of the IEEE*, vol. 66, pp. 51–83, Jan. 1978.

[192] D. K. Barton, *Radar Equations for Modern Radar*. Artech House Radar Series, London: Artech House, 2012.

[193] R. Calderbank, S. D. Howard, and B. Moran, "Waveform Diversity in Radar Signal Processing," *IEEE Signal Processing Magazine*, vol. 26, pp. 32–41, Jan. 2009.

[194] M. R. Bell, "Information Theory and Radar Waveform Design," *IEEE Transactions on Information Theory*, vol. 39, pp. 1578–1597, Sept. 1993.

[195] M. E. Yavuz and F. L. Teixeira, "Frequency Dispersion Compensation in Time Reversal Techniques for UWB Electromagnetic Waves," *IEEE Geoscience and Remote Sensing Letters*, vol. 2, pp. 233–237, Apr. 2005.

[196] T. Jin and Z. Zhou, "Refraction and Dispersion Effects Compensation for UWB SAR Subsurface Object Imaging," *IEEE Transactions on Geosciences and Remote Sensing*, vol. 45, pp. 4059–4066, Dec. 2007.

[197] J. A. Hannam, J. M. Hollis, R. J. A. Jones, P. H. Bellamy. S. E. Hayes, A. Holden, M. H. V. Liedekerke, and L. Montanarella, "SPADE-2: The soil profile analytical database for Europe, Version 2.0 Beta, Version March 2009." Unpublished Report.

[198] P. Panagos, M. V. Liedekerke, A. Jones, and L. Montanarella, "European Soil Data Centre: Response to European Policy Support and Public Data Requirements," *Land Use Policy*, vol. 29, pp. 329–338, 2012.

Résumé

Ce manuscrit aborde le problème de l'application de la synthèse d'ouverture radar et des techniques d'interférométrie, pour des radars (sur satellites ou aéroporté) ayant pour but d'imager la sous surface de zones non-arides (en général inconnues) pour des applications de défense et civiles. Les résultats expérimentaux, publiés jusqu'ici, montrent que les radars à synthèse d'ouverture aéroportés peuvent atteindre des profondeurs de pénétration de plusieurs mètres dans un sol homogène et sec. Cependant, de telles zones se rencontrent rarement dans la nature, et donc l'intérêt d'appliquer les techniques usuelles d'imagerie RSO décroît fortement pour les autres types de sol à cause des distorsions de l'enveloppe de l'onde électromagnétique par les effets de dispersion et d'atténuation. Si l'on considère le sous sol comme un milieu inhomogène et qu'on lui applique conjointement un modèle basé sur une fonction de pedotransfert, l'approche par Renversement Temporel, grâce à ses capacités de refocalisation adaptative peut être utilisée pour la régénération de l'impulsion électromagnétique afin de préserver la résolution radiale la plus haute possible comme cela est nécessaire pour obtenir une résolution azimutale satisfaisante.

Une première partie de ce manuscrit est consacrée à la modélisation du sol basée sur des données géophysiques réelles et en supposant un historique météorologique connu. Les constantes diélectriques et la conductivité sont alors déduites par une approche par fonction de pédotransfert. La géométrie d'acquisition est alors définie et les caractéristiques de l'image du sous sol sont ensuite analysées. Le manuscrit se poursuit par une présentation du concept de renversement temporel ainsi que de ses limitations pour un milieu inhomogène. Le concept de RSO basé sur ce concept est alors proposé. La méthode ainsi proposée a été testée pour deux radars (en bande P et L). Les effets de restauration de l'impulsion et de sa refocalisation sont présentés pour tous les types de sol et d'objets. Quand la méthode proposée permet la refocalisation radiale, les acquisitions sont répetées le long de la ligne de synthèse d'antennes sur des sols nus présentant des inhomogénéités le long de l'axe vertical. La méthode de formation de l'image est alors appliquée afin de vérifier l'impact du renversement temporel sur la refocalisation le long de la direction azimutale. Finalement, la méthode de reconstruction des images est appliquée sur deux images interférométriques afin de vérifier la reconstruction sur de structures étendues dans le sous sol.

Bien que nous ayons considéré l'imagerie à partir des algorithmes proposés et toutes les contributions présentées ici peuvent directement être adaptées pour des images d'imageries satellitaires ou modifiée pour des systèmes GPR.

Mots-clés : Radar à synthèse d'ouverture, Imagerie de cibles enfouies, Modélisation du sol, Traitement du signal

Abstract

This dissertation addresses the problem of the application of synthetic aperture and interferometry techniques for low frequencies (VHF, UHF, P, L bands) airborne/satellite borne radars imaging over non-arid (in general, unknown) areas for civilian and defence applications. The experimental results, published so far, shown that the airborne Synthetic Aperture Radar (SAR) reached the sufficient penetration depth in soil structure down to several meters in homogeneous and dry soil. Hence, whereas such areas with homogeneous sand dry soil rarely occur in natural environment, the convenience of SAR application decreases significantly due to the soil effect on electromagnetic wave as pulse distortion and envelope deformation caused by dispersion and frequency-dependent attenuation. When soil is considered as inhomogeneous medium and modelled based on the pedotransfer (geologically and hydrologically-motivated) approach, the Time-Reversal (TR) technique, through its refocusing ability, can be used for pulse regeneration and for restoration of undisturbed range resolution required for the essential azimuth processing by SAR methods.

We start by soil modelling based on the real geological data and assumed meteorological history to obtain as realistic as possible soil structures. Using the pedotransfer approach, the dielectric constants and conductivity are modelled. Then the mission geometry is defined and features related to subsurface imaging are analysed. We continue with the TR concept and its limitations for inhomogeneous media. The TR-based acquisition method is proposed for airborne platform with the analysis of its differences, challenges and expectations. Then, the proposed method of scanning is investigated in two different radar band (P, L) under several assumptions. The refocusing and pulse restoration effects are presented for all considered soil structures and location of buried objects. When the proposed algorithm is verified, the acquisitions is repeated along the synthetic aperture line over bare and flat soil with inhomogeneous-in-depth properties. The image formation method is applied to verify the TR impact on SAR processing in azimuth direction. Finally, interferometric phase method is applied for soil structure reconstruction.

Although we only consider imaging from airborne platform, the proposed algorithm and all contributions presented in this dissertation can be directly adapted for satellite-borne system or modified for Ground Penetrating Radar (GPR) systems.

Keywords : Synthetic Aperture Radar, Buried Target Imaging, Soil Modeling, Signal Processing

TELECOM Bretagne

n° d'ordre : 2016telb0383

Télécom Bretagne

Technopôle Brest-Iroise - CS 83818 - 29238 Brest Cedex 3

Tél : + 33(0) 29 00 11 11 - Fax : + 33(0) 29 00 10 00